SYNTHESIS, CHARACTERIZATION AND CATALYTIC PROPERTIES OF MESOPOROUS MOLECULAR SIEVES

A THESIS

SUBMITTED TO THE

UNIVERSITY OF PUNE

FOR THE DEGREE OF

DOCTOR OF PHILOSOPHY

(IN CHEMISTRY)

BY

KARUNA CHAUDHARI

(M. Phil.)

CATALYSIS DIVISION

NATIONAL CHEMICAL LABORATORY

PUNE – 411 008, INDIA

(MAY 2000)

DEDICATED

TO

MY BELOVED SISTERS

Certificate

Certified that the work incorporated in the thesis "**Synthesis, Characterization and Catalytic Properties of Mesoporous Molecular Sieves"** submitted by **Miss Karuna Chaudhari,** for the degree of Doctor of Philosophy, was carried out by the candidate under my supervision in the Catalysis Division, National Chemical Laboratory, Pune, India. Materials obtained from other sources have been duly acknowledged in the thesis.

[Dr. (Mrs.) Asha J. Chandwadkar]

(Research Guide)

Acknowledgments

I express my profound gratitude to my research guide, Dr. (Mrs.) Asha J. Chandwadkar, Scientist, National Chemical Laboratory, Pune, for her invaluable guidance, numerous discussions and constructive suggestions through out the course of this investigation.

I am grateful to Dr. A.V. Ramaswamy, Head, Catalysis Division, NCL, for providing me all facilities required for my work.

It gives me a great pleasure to express my deep sense of gratitude and indebtedness to Dr. S. Sivasanker, Deputy Director, NCL for his expert and inspiring guidance and suggestions in carrying out the research work.

I owe my special thanks to Dr. H.S. Soni, Dr. D. Srinivas Dr. P. Rajmohanan, Dr. S.G. Hegde, Dr. R. Vetrivel, Miss N. Jacob, Miss Agashe, Dr. S. Awate, Dr. A. A. Belhekar, Dr. Mirajkar, Dr. B.S. Rao, Dr. Satyanarayan Dr. V. Ramaswamy, and all other scientific and nonscientific staff in the Catalysis Division and Dr. (Mrs.) Mitra (Physical Chemsitry Division), NCL, for their help and cooporation given to me in completing my research work successfully.

I am grateful to Prof. K. Lazar and Prof. Schay, Institute of Isotopes, Budapest, Hungary for analyzing samples by Mossbauer Spectroscopy and XPS.

I take the opportunity to thank my friends, Tapan, Raja, Mantri, Subho, Suman, Annyt, Chitto, Bikas, Suresh, Anil, Sindhu, Ranjeet, Sharda, Vandana, Priyo, Dinu, Subhash, Tomal, Sourav, Nepu, Krishanu, Debalina, Suvarno, Saptarshi, Manna, Eric, Chloe, Siddesh, Suhas, Bhavana, Anand, and many others, and my family members, Rajubhai, Niranjan, Shipu, Mrudula, Salil and Popeye, from whom I have received invaluable help and moral support.

Finally, my thanks are due to Dr. P. Ratnasamy, Director, NCL, for allowing me to carry out the research at NCL and to submit the work in the form of a thesis for the award of the Ph. D. degree and to the Council of Scientific and Industrial Research (CSIR), New Delhi, India, for providing me a research fellowship.

[Karuna Chaudhari]

CONTENTS

2. SYNTHESIS

5 SUMMARY AND CONCLUSIONS

Chapter I

INTRODUCTION

1.1 GENERAL BACKGROUND

Porous solids have extensive commercial applications as adsorbents, catalysts and catalyst supports due to their high surface areas. According to IUPAC definition[1] porous materials may be divided into three types based on their pore dimensions:

Type		Pore Size (Å)
Microporous	:	< 20
Mesoporous	:	20-500
Macroporous	:	> 500

Well known microporous materials are zeolites[2] and aluminophosphate molecular sieves[3] which are inorganic composites having a crystalline three-dimensional framework woven with tetrahedral atoms (T-atoms) like aluminium, silicon, phosphorous etc. bridged by oxygen atoms. These materials possess uniform channels or cavities circumscribed by rings of a definite number of T-atoms. The exploitation of the architectural features of zeolites resulting in different acid sites and acid strengths, exchangeable ions, shape and size selective channels and pores etc. has been well established by now. Modification of the framework and extra-framework composition makes these materials useful for catalyzing organic reactions. Till 1990 heterogeneous catalysis available with zeolites was restricted to the use of materials with pore sizes less than 20 Å and consequently the reactant molecules trapped and transformed inside them were also small. Thus the usefulness of the microporous molecular sieves in processing high molecular weight reactants of increasing importance was limited by their pore size (~ 7Å). Hence there has been an ever-growing interest in expanding the pore sizes of the zeotype materials from the micropore region to mesopore region. The requirement of adsorbing larger molecules at the catalytic sites has led the development of molecular sieves with pore diameters larger than those of the traditional zeolites.

In order to preserve the remarkable catalytic properties of the zeolites while expanding their use to process bulkier molecules, new synthesis routes have been undertaken to increase their pore diameters. This approach has led to the synthesis of ultra large pore molecular sieves. In 1982 Wilson and co-workers[4] synthesized a novel crystalline, microporous aluminophosphate ($AlPO_4$) material with a pore diameter of about 8 Å. Later, in 1988, Davis *et al.*[5] reported the synthesis of VPI-5, an $AlPO_4$ molecular sieve with 18 tetrahedral atoms that could sorb molecules about 12 Å in size. Since then, microporous materials with pore openings containing 20 tetrahedral atoms have been synthesized (Table 1.1). They include cloverite[6], which is a gallophosphate and JDF-20, which is an $AlPO_4$[7]. Recently a 14-membered ring (MR) unidirectional zeolite (UTD-1) was synthesized using a cobalt organometallic complex as the template[8]. However, these materials lack the required thermal stability and catalytic activity because their frameworks are electrically neutral. Table 1.1 lists a few examples of zeolites and molecular sieves.

Table 1.1 Examples of zeolites/molecular sieves (Pore diameter < 20 Å)[9]

Definition	Typical material	Ring size	Pore diameter (Å)	Ref.
Small pore	CaA	8	4.2	10
	SAPO-34	8	4.3	11
Medium pore	ZSM-48	10	5.3×5.6	12
	ZSM-5	10	5.3×5.6	13
			5.1×5.5	
Large pore	Faujasite	12	7.4	14
	$AlPO_4$-5	12	7.3	15
	ZSM-12	12	5.5×5.9	16
Ultralarge pore	Cloverite	20	6.0×13.2	6
	JDF-20	20	6.2×14.5	7
	VPI-5	18	12.1	5
	$AlPO_4$-8	14	7.9×8.7	17
	UTD-1	14	7.5×10	8

Researchers have taken significant efforts to synthesize mesoporous materials such as silicas[18], transitional aluminas[19] or pillared clays and silicates[20,21]. However the pores in these materials are generally irregularly spaced and broadly distributed in size. Synthesis of amorphous silica-alumina with a narrow pore size distribution in the presence of tetraalkylammonium cations[22] has been reported, where the average pore diameter was related to the size of the tetraalkylammonium cations. Although, these materials were found to be active for acid catalyzed organic reactions, they were not thermally stable at high temperatures.

In 1992 researchers at Mobil Research and Development Corporation reported the synthesis of a new family of silicate/aluminosilicate mesoporous molecular sieves (M41S) with exceptionally large uniform pore structures[23-29]. These materials possess well-defined mesopores whose diameters can be tailored in the range of 15-100Å. The understanding about the synthesis of these materials and the corresponding mechanism has opened up a new era of molecular engineering. The most outstanding feature of the preparation of these materials is the role of the templating agents. The template molecules used are not single solvated organic cations as used in zeolite synthesis, but a self assembled surfactant molecular array around which the main structure is built up (Fig. 1.1). Surfactants are large organic molecules having a long hydrophobic tail of variable length (e.g. alkyltrimethylammonium cations with formula $C_nH_{2n+1}(CH_3)_3N^+$, where n > 8) and a hydrophilic head.

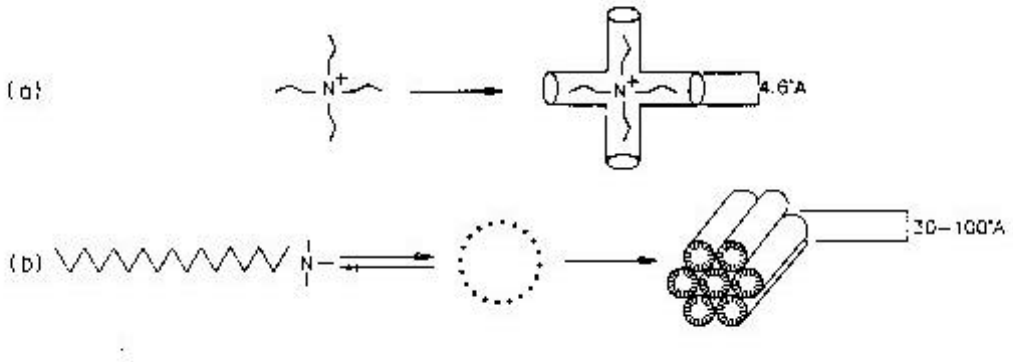

Fig. 1.1 (a) Formation of microporous molecular sieves using individual short alkyl chain quaternary ammonium compounds**.**

(b) The formation of mesoporous molecular sieves using long chain alkyl quaternary ammonium compounds (ref. 30)

1.2 FORMATION MECHANISM

Different synthesis mechanisms have been proposed in the literature to explain the formation of mesoporous materials. A few of them are described below:

1.2.1. Liquid Crystal Templating (LCT) Mechanism

Because of the similarity between the different M41S phases and known liquid-crystal phases, the first mechanism proposed for the synthesis of these materials was the liquid crystal templating mechanism[23, 28-30]. In aqueous solution, surfactant molecules exist as randomly dispersed monomolecules at low concentrations. With increasing concentration, the surfactant molecules aggregate with their hydrophobic tails together exposing their polar heads to the aqueous solution to reach a minimum energy configuration and thus form spherical micelles decreasing the system entropy. The lowest concentration at which

monomolecules aggregate to form spherical isotropic micelles is called critical micellization concentration (CMC1). There exists a second critical concentration CMC2 corresponding to the further aggregration of spherical into cylindrical or rod-like micelles. There are three main liquid crystalline phases with hexagonal, cubic and lamellar structures. The hexagonal phase is the result of hexagonal packing of cylindrical micelles, the lamellar phase corresponds to the formation of surfactant bilayers and the cubic phase may be regarded as a bicontinuous structure. The structure of the mesophase depends on the composition of the mixture, the pH and the temperature[31].

Two possible pathways have been proposed[28] for the LCT mechanism which are schematically shown in Fig. 1.2. In the first pathway, it is considered that first there is a formation of the surfactant hexagonal liquid-crystal phase around which the growth of the inorganic materials is directed. The $C_nH_{2n+1}(CH_3)_3N^+$surfactant micelles aggregate to form hexagonal arrays of rods. Silicate anions present in the reaction mixture interact with the surfactant cationic head groups. Condensation of the silicate species leads to the formation of an inorganic polymer.

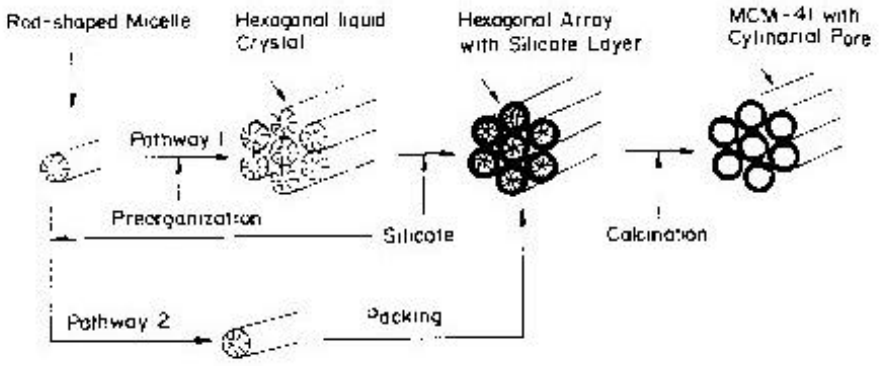

Fig. 1.2 Possible mechanistic pathways for the formation of MCM-41: (1) liquid crystal phase initiated and (2) silicate anion initiated (ref. 28).

On calcination, the organic template is burnt off, leaving inorganic hollow cylinders in hexagonal arrangement. However, this pathway did not get much support in the literature. It has been observed that at lower concentrations only micelles exist in solution[32]. Moreover, in situ ^{14}N-NMR spectra revealed that the hexagonal liquid-crystalline phase of CTMA ions was not present at any time during MCM-41 formation[33]. Thus the first synthesis scheme proposed by Beck *et al.*[28] was abandoned (Fig. 1.2).

In the second pathway, it has been proposed that the randomly ordered rodlike micelles interact with silicate species by coulombic interactions in the reaction mixture to produce approximately two or three monolayers of silicate around the external surfaces of the micelles. These randomly ordered composite species spontaneously pack into a highly ordered mesoporous phase with an energetically favourable hexagonal arrangement, accompanied by silicate condensation. With the increase in heating time, the inorganic wall continues to condense. The investigation on the formation mechanism[33,34] using XRD, ^{29}Si NMR, *in situ* ^{14}N NMR, and thermogravimetric analysis (TGA) techniques proves the absence of hexagonal liquid crystalline mesophases, either in the synthesis gel or in the surfactant solution used as template. It was therefore, concluded that formation of MCM-41 phase is possibly *via* pathway 2 (Fig. 1.2) rather than pathway 1.

Initially three different mesophases in M41S family were reported, *viz.*; lamellar[35], hexagonal[28] and cubic[36] (Fig. 1.3), in which the hexagonal mesophase MCM-41 possessed highly regular arrays of uniform-sized channels. Later additional phases such as SBA-1 (cubic phase with the space group *Pm3n*[31,37], SBA-2[38] (three dimensional hexagonal symmetry (*P6$_3$/mmc*) with super cages instead of unidimensional channels and MSU-*n* having highly disordered hexagonal like array of channels with diameters in the nanometer range[39] were reported.

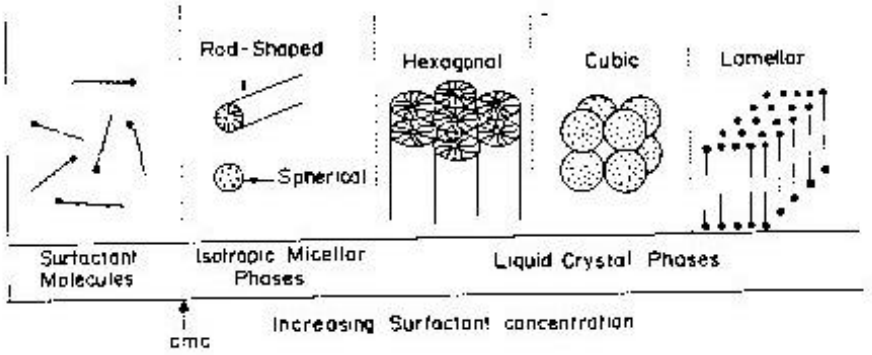

Fig. 1.3 Different mesophases in M41(S) family; hexagonal (ref. 28); cubic (ref. 36) and lamellar (ref. 35).

1.2.2 Transformation Mechanism from Lamellar to Hexagonal Phase

It has been proposed that[31,40,41] in a surfactant/silicate aqueous mixture with relatively low pH, low degree of polymerization of silica species, and low temperatures, small silica oligomers (three to eight silicon atoms) interact with surfactant cations by coulombic interactions at the interfaces forming multidentate binding between them. These subsequently polymerize to form larger ligands, enhancing the binding between the surfactant and silicate species. These surfactant silicate multidentate ligands lead to a lamellar biphase governed by the optimal surfactant average head group area (A). As the polymerization of silicate species proceeds, the average headgroup area of surfactant assembly increases due to the decrease in the charge density of larger silicate layers and ultimately results in the hexagonal mesophase precipitation (Fig. 1.4).

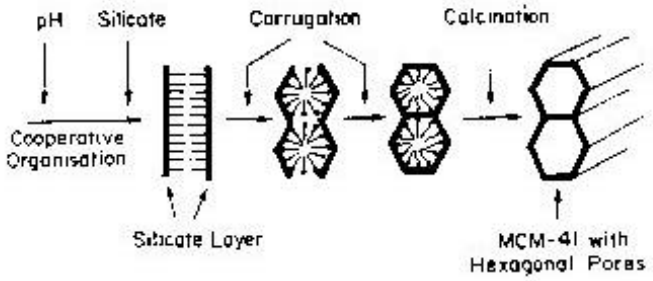

Fig. 1.4 Transformation mechanism from lamellar to hexagonal phase (ref. 40).

1.2.3 Folded Sheet Mechanism

Yanagisawa *et al.*[20] and Inagaki *et al.*[42,43] synthesized crystalline mesoporous silicate and aluminosilicate materials designated as FSM-16 (Folded Sheet Mesoporous Materials). They proposed a folded sheet mechanism (Fig. 1.5) for the formation of mesostructures derived from kanemite (layered silicate). The surfactant cations intercalate into the bilayers of kanemite by ion-exchange process. The transformation to the hexagonal phase occurs during hydrothermal treatment by condensation of silanol groups. MCM-41 and FSM-16 are similar but show slightly different properties in adsorption[29] and surface chemistry[44].

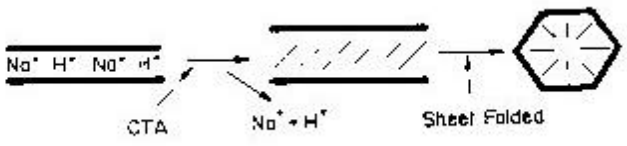

Fig. 1.5 Folded sheet mechanism (ref. 43).

1.3 SYNTHESIS OF MESOPOROUS MOLECULAR SIEVES

Similar to zeolite and molecular sieves syntheses, mesoporous molecular sieves are hydrothermally synthesized by mixing organic molecules (surfactants), silica, and/or silica-alumina source to form a gel which is then crystallized at a temperature between 70-150°C for a selected period of time. Surfactant molecules function as templates forming an ordered organic-inorganic composite material[45]. The product obtained after crystallization is filtered, washed with water and dried at ambient temperature. Surfactant molecules are removed by calcination leaving porous silicate/aluminosilicate network.

The structure of mesoporous materials can be altered by varying the surfactant/SiO_2 ratio[28]. It has been found that[36] as the surfactant/silica molar ratio increased, the siliceous products obtained could be classified into four groups as presented in Table 1.2.

Table 1.2 Classification of Mesoporous Molecular sieves

Surfactant/silica	**Phase**
< 1.0	Hexagonal (MCM-41)
1.0-1.5	Cubic (MCM-48)
1.2-2.0	Thermally unstable materials
2.0	Cubic octamer $[(CTMA)SiO_{2.5}]_8$

One of the most unique and useful features of M41S family materials is the ability to tailor the pore diameter (15–100Å). This can be achieved in three different ways; (i) by varying the chain length of alkyl groups (from 8 to 22 atoms) in surfactant molecules[23,28], (ii) by adding auxiliary chemicals such as 1,3,5 trimethylbenzene[23,28,31,46] which dissolve in the

hydrophobic region of the micelles, thus increasing their size, or (iii) by aging a sample prepared at a lower temperature in its mother liquor at a higher temperature for different periods of time[47]. Besides, the pore diameter of mesoporous molecular sieves also depends on other factors such as temperature, pH and crystallization time[9,48].

Eversince the first report on the synthesis of mesoporous molecular sieves in alkaline medium appeared[23-29], a large number of publications on synthesis of mesoporous materials, mainly MCM-41 have been reported[49-53]. The synthesis of mesoporous materials has also been done in acidic and neutral medium. Huo *et al.*[31,37] reported the synthesis of mesoporous silica under acidic conditions, while Tanev and Pinnavaia[54] proposed a neutral templating synthesis mechanism based on hydrogen bonding between primary amines and neutral inorganic species (Table 1.3). Such mesoporous molecular sieves are named as HMS (hexagonal mesoporous silica).

Table 1.3 Routes for synthesis of mesoporous molecular sieves

Surfactant	**Example**	**PH**	**Resulting Phase**	**Reference**
S^+I^-	Cetyltrimethyl ammonium ions + silicate species	10-13	Hexagonal, cubic and lamellar	24
$S^+X^-I^+$	Cetyltrimethyl ammonium ions + silicate species	< 2	Hexagonal	31
S^0I^0	$C_{12}H_{25}NH_2 + (C_2H_5O)_4Si$	< 7	Hexagonal	54

S = surfactant species; I = inorganic species (Si); X =Cl, Br or OH

1.4 MODIFICATION OF MESOPOROUS SILICA

Pure siliceous mesoporous molecular sieves possess a neutral framework, which limits their applications. In order to provide molecular sieves with potential catalytic applications,

it is possible, as in the case of zeolites, to modify the nature of the framework by introduction of heteroatoms, by hydrothermal methods. Besides, other elements can also be incorporated on the surface of the materials by grafting or impregnation.

1.4.1 Incorporation of Heteroatoms by Hydrothermal Methods

When trivalent cations like Al^{3+}, B^{3+}, Ga^{3+} and Fe^{3+} [55-61] substitute for silicon in the walls of the mesoporous silica, the framework possesses negative charges that can be compensated by protons providing acid sites. The number of acid sites and strength depend on the amount and nature of the incorporated metal. Such materials are used in acidic reactions and have potential applications in various petroleum refining processes[62,63]. When other cations like Ti^{4+}, V^{4+} etc.[64-67] are incorporated, the corresponding mesoporous materials are used in oxidation reactions. The Ti and V containing MCM-41 molecular sieves have been used in a variety of oxidation reactions of bulky molecules using either H_2O_2 or TBHP as oxidant[63,65,68-71]. A few reports describe the synthesis and characterization of mesoporous silica modified by metals like Cr[72-74], Mn[53] or Mo[73]. Cr-MCM-41[74] has been found to be catalytically active in the hydroxylation of phenol, 1-naphthol and oxidation of aniline with aqueous H_2O_2.

1.4.2 Grafting of Heteroatoms

In addition to variable pore diameters and large surface area, mesoporous molecular sieves have a number of surface silanol groups, which can be functionalized by introducing functional organic groups. This is normally achieved through attachment of silane-coupling agents to the mesoporous walls of previously synthesized and calcined materials[75]. In one of the methods, functionality is directly introduced through reaction of silanol groups[76,77]. In another method, a transition metal, metal oxide or a bimetal complex is grafted on the wall without the use of intermediate silane complex agent. Hence, surface hydroxyl groups are

directly reacted with the metal species. Ti grafted MCM-41 sample showed higher catalytic activity for the epoxidation of alkenes than other supports containing Ti in their framework[78]. Mesoporous materials anchored with $AlCl_3$, $SnCl_2$, $Zn(O_2CMe)_2$ or $Mn(O_2CMe)_2$ have high stablity and catalytic activity alongwith ion-exchange capacity[79].

1.4.3 Impregnation of Heteroatoms

Certain reactions such as hydroisomerization and aromatization are carried out on bifunctional catalysts possessing acid functionality of the molecular sieves and the hydrogenation-dehydrogenation property of the metal impregnated on the surface of the molecular sieves. Such catalysts are usually prepared by loading the metals (Ni, Co, Pt, Pd, W etc.) by impregnation methods.

It has been reported that sulfided Co and Mo impregnated Al-MCM-41 catalyst shows higher hydrogenation and hydrocracking activities than Co-Mo/Al_2O_3 catalysts[80]. Cu impregnated MCM-41 has been used in the liquid phase oxygenation of benzene to phenol using O_2 as an oxidant and they have been found to be more active than Cu Supported ZSM-5, MgO, TiO_2, SiO_2, NaY, KL etc.[81]. Cs impregnated MCM-41 has been reported to be a good basic catalyst for Michael addition of diethylmalonate to neopentyl glycol diacrylate and high regioselectivity was obtained in contrast to bulk cesium oxide[82]. Impregnation of binary Cs-La oxide on MCM-41 has been found to produce a useful base catalyst for the Knoevenagel additiion of enolates to benzaldehyde and for liquid phase Michael addition of ethyl cyanoacetate to ethyl acrylate[83]. Pt impregnated MCM-41 has been used for naphthalene hydrogenation[84].

1.5 ACIDITY IN MESOPOROUS MOLECULAR SIEVES

The acidity of mesoporous molecular sieves arises from the presence of accessible intrachannel hydroxyl groups associated with 4-coordinated framework metal atoms, such as

Al(III), as well as from the presence of octahedral metal species. Based on TPD studies of ammonia carried out on aluminium containing MCM-41 samples, Corma *et al.*[85] and Chen *et al.*[33] concluded that the acidity of these samples is comparable to that of amorphous silica-alumina and much lower than the acidity of zeolites such as USY or H-mordenite. Pyridine adsorption spectra reveal that Al-MCM-41 possesses both Brönsted acid sites (band at 1540 cm^{-1}) and Lewis acid sites (band at 1450 cm^{-1})[85-88]. It has been further reported that aluminium containing MCM-41 contains at least three types of acid sites:

(1) Acid sites due to extra-framework Al species located within the channels of the mesostructure,

(2) Acid sites at the surface of the pores (i.e. the channel walls), whose strength is comparable to the strength of bridging hydroxyl in zeolites, and

(3) Acid sites sandwiched between the various Si(IV) layers that form the wall[89].

The nature, size, concentration and ease of hydrolysis of Al precursors control Al incorporation and location within the structure and, therefore the acidity of the samples.

1.6 PHYSICO-CHEMICAL CHARACTERIZATION

A number of techniques are used to characterize mesoporous molecular sieves. Among these, x-ray powder diffraction, transmission electron microscopy (TEM) and adsorption measurements are the essential ones to identify the structure of the mesoporous molecular sieves. Infrared spectroscopy, ultra violet spectroscopy, nuclear magnetic resonance spectroscopy and electron spin resonance spectroscopy have also been applied to obtain additional structural information about molecular sieves.

1.6.1 X-ray diffraction

Powder x-ray diffraction is used to identify the structure, phase purity, degree of crystallinity, unit cell parameters and crystallite size. It also helps in the study of the kinetics

of crystallization of molecular sieves. As the powder pattern is the finger print of the molecular sieve structure, phase purity and percent crystallinity of the synthesized molecular sieve can be ascertained by comparing with the standard pattern for the molecular sieve under investigation. XRD patterns of mesoporous phases exhibit peaks in the low angle region the most intense peak being the (100) reflection. In the case of MCM-41 the wall thickness of hexagonal channels is usually calculated by subtraction of the inside pore diameters obtained by gas adsorption from the unit cell dimensions determined by XRD. Isomorphous substitution of a heteroatom in the framework of the molecular sieves results in changes in the unit cell parameters and unit cell volume. This is one of the ways to confirm isomorphous substitution.

1.6.2 Adsorption measurements

Molecular sieves have the ability to adsorb probe molecules of different sizes. Sorption capacities for probe molecules such as n-hexane, water, benzene, nitrogen etc. yield information about the hydrophilicity/hydrophobicity, pore dimensions and pore volume of the molecular sieves.

The Braunauer-Emmett-Teller (BET) volumetric gas adsorption technique using nitrogen, argon, etc. is a standard method for the determination of the surface areas and pore size distribution of finely divided porous samples[90]. The relation between the amount adsorbed and the equilibrium pressure of the gas at constant temperature is defined by the adsorption isotherm. N_2-adsorption-desorption isotherms of MCM-41, MCM-48 and FSM-16 are of the type IV isotherm. The steep increase in N_2 adsorption (within the P/P_0 range between 0.2 to 0.4) corresponds to capillary condensation within uniform pores. The sharpness and the height of this step reflects the uniformity of the pore size and the pore volume respectively. The wall thickness of hexagonally packed silicates (MCM-41 and HMS) was determined as

the difference between the repeat distance $a_0 = 2d_{100}/\sqrt{3}$ (from XRD) and the Horvath-Kawazoe[91] pore diameter using N_2 adsorption.

1.6.3 Transmission Electron Microscopy (TEM)

TEM is used to elucidate the pore structure of mesoporous molecular sieves[23,28,32,33,37,45,92,93]. It provides topographic information of materials at near atomic resolution. However, the exact analysis of pore sizes and thickness of the pore walls is very difficult and not possible without additional simulations because of the 'focus' problem. More than one model with a hexagonal array of large cylindrical pores with thin walls gives a similar XRD pattern, but TEM gives a direct, precise and simultaneous measurement of the pore diameter and pore thickness. HRTEM can be successfully used to examine the microstructural feature of mesoporous molecular sieves[92,93]. In addition to structural characterization, it can also be used to detect the location of metal clusters and heavy cations in the framework[93].

1.6.4 Thermal Analysis

Thermal analysis is widely used to study the structural stability of as-synthesized forms of molecular sieves. It provides information about the temperature required for the removal of adsorbed water, decomposition of the occluded organic cations in the pores and channels of molecular sieves and dehydroxylation at higher temperatures to produce Lewis acid sites. Data obtained from TG, DTA and DTG study are useful in evaluating the thermal properties of molecular sieves[94]. The shape and splitting of the endotherms (low temperature) helps to identify the location of water molecules and also helps in studying the kinetics of dehydration. The temperature at which an exotherm appears in the DTA after the loss of water molecules, gives helpful information about the temperature required to remove the template molecules from the pores of the molecular sieves during calcination. Phase

transformations (if any) can also be understood from the exotherms obtained at higher temperatures.

1.6.5 Infrared spectroscopy

Framework infrared spectroscopy provides additional information about the structural details of the molecular sieves. It can be used to confirm acidic nature and isomorphous substitution in molecular sieves. Flanigen[95] has discussed the i.r. spectra of the hydroxyl group region of zeolites. Maroni *et al.*[96] and Janin *et al.*[97] have used different probe molecules to study the acidity of molecular sieves. The IR spectrum in the range 200-1300 cm^{-1} is used to characterize and to differentiate framework structures of different molecular sieves.

Isomorphous substitution of metal ions such as B, Fe, Ga etc, for Al and Ti, Ge, V etc. for Si also lead to shift in band positions. An additional band at 960 cm^{-1} may be observed for Ti or V substituted molecular sieves. The IR bands around 3600-3700 cm^{-1} confirm the presence of the silanol groups[98,99] or bridged hydroxyl groups in the molecular sieves and their Brönsted acidities can be compared.

1.6.6 Nuclear Magnetic Resonance

Lippmaa *et al.*[100] were the first to demonstrate the use of ^{29}Si MAS-NMR (Magic Angle Spinning Nuclear Magnetic Resonance) spectra in determining the nature and chemical environment of the atoms. Since then this technique has been found to be very useful in understanding the structural and physicochemical properties of molecular sieves. ^{29}Si and ^{27}Al MAS-NMR spectra provide information on Si/Al ordering[101], crystallographically equivalent and non-equivalent Si and Al ions in various sites[102,103], framework silica to alumina ratio[104], coordination of Si and Al[105,106], spectral correlation with Si-O-T bond angles[107] and Si-O bond lengths[108]. Solid state MAS-NMR spectroscopy of ^{27}Al can prove

the presence of tetrahedrally coordinated atoms in the zeolite lattice[101,102] and also reveal extraframework octahedral Al if present in the pores of the molecular sieves. ^{29}Si MAS NMR has been extensively used for the characterization of M41S silicates[48,109]. The broad ^{29}Si NMR spectra of mesoporous samples closely resemble those of amorphous silica.

1.6.7 Diffuse Reflectance UV-visible spectroscopy

This technique measures the scattered light reflected from the surface of samples in the UV-visible range (200-800 nm). For most of the isomorphously substituted molecular sieves, transitions in the UV region (200-400) nm are of prime interest. This spectroscopic technique is used to determine the coordination state of transition metal ions substituted in the matrix of the molecular sieves, involving ligand-to-metal charge transfer transitions at ~ 200-220 nm.

1.6.8 Electron Spin Resonance Spectroscopy

Electron Spin Resonance (ESR) spectroscopy is the resonance absorption of the electromagnetic (microwave) radiation by magnetically split states of unpaired electrons. In the case of some paramagnetic molecules, the formation of a charge-transfer complex can be determined by this technique. It is possible when the electron of donor molecule interacts with the nuclear spin of the electron-acceptor site. Thus, this technique provides valuable information on the redox site and the intermediate species formed in the catalytic reaction. With the help of this information it is easier to focus on the status of framework and non-framework species formed in the transition metal incorporated molecular sieves.

The formation mechanism of MCM-41 and MCM-50 has been studied by in situ EPR spectroscopy[110,111]. ESR studies of Mn-containing MCM-41 materials have revealed the presence of Mn(II) species in both extraframwork and framework sites[112]. The presence of different oxidation states of vanadium ions in as-synthesized and calcined MCM-41 has been

characterized by ESR spectroscopy[67,113, 114]. ESR spectroscopy has also been used to study isomorphous substitution of metal ions like Ni(I), Fe(III) and Cr(III) in MCM-41[115-117]. ESR characterization of Ti(III) species obtained by reduction of Ti(IV) by γ-irradiation and thermal activation has been found to be useful in characterizing the different Ti-sites in the structure of Ti-MCM-41[118].

1.6.9 X-ray Photoelectron Spectroscopy (XPS)

XPS is among the most frequently used techniques in catalysis. It gives information on the elemental composition and the oxidation state of the elements. It is an important tool for the characterization of the surface of zeolites and related materials[119]. Depth selective information can be obtained by varying the angle between the sample surface and analyzer.

Mesoporous molecular sieves containing different heteroatoms such as Al, Ti, V, Nb and Zr have been analyzed by XPS technique to obtain information about the dispersion of the heteroatom in the structure[120-123].

1.7 APPLICATIONS AND PROSPECTS

The high surface area and large pore size of MCM-41 favour high dispersion of the active species and provide easy accessibility to large feed stock molecules making it an attractive catalyst. Other potential applications for these novel materials are in sorption, separations, polymer chemistry etc. To date several mesoporous metallosilicates with significant catalytic properties have been synthesized. Some of the reactions studied on different metallosilicate molecular sieves are listed in Table 1.4.

Table 1.4 Reactions studied on mesoporous metallosilicate molecular sieves

No	Catalyst	Reaction	Ref.
1	Al-MCM-41	Alkylation of 2,4-di-ter. butyl phenol with cinnamyl alcohol	124
2	Al-MCM-41 and Al-MS	Cumene hydrocracking	87,88
3	Al-MCM-41	Conversion of plastic wastes into hydrocarbons with low aromatic content	125
2	Ni-MCM-41 and Mo-MCM-41	Hydrodenitrogenation, hydrodesulfurization and hydrocracking of gas oil	126
3	Ti-MCM-41 and Ti-HMS	Epoxidation of 1-hexene using H_2O_2, epoxidation of norbornene using TBHP as oxidant	65
	Ti-MCM-41, Ti-HMS and V-HMS	Oxidation of phenol and 2,6-di-*tert*-butyl phenol using H_2O_2 as oxidant	122, 127, 128
	Ti-MS and Zr-MS	Oxidation of aniline to azoxibenzene, epoxidation of cyclohexene, norbornene and oxidation of 2,6-di-*tert*-butyl phenol using H_2O_2 as oxidant	129
4	V-MCM-41	Oxidation of cyclodecane and 1-naphthol using H_2O_2 as oxidant	66
5	Cr-MCM-41	Oxidation of phenol, 1-naphthol and aniline using H_2O_2 as oxidant	74
6	Mn-MCM-41	Conversion of propene to CO_2	130
7	Na-MCM-41 and Cs-MCM-41	Knoevenagel condensation of benzaldehyde with ethyl cyanoacetate	131
8	Cs-MCM-41	Addition of diethyl malonate to neopentyl glycol	82
9	Cu- and Fe-phthalocyanine- MCM-41	Oxidation of n-hexane using TBHP as oxidant	132
10	Pt-MCM-41	Oxidation of carbon monoxide	133

1.8 SCOPE OF THE THESIS

It is evident from the literature survey on mesoporous molecular sieves, that these materials have opened new opportunities in the field of catalysis. The framework composition can easily be modified by incorporation of trivalent and tetravalent elements, thus providing solids with potential applications in acid or redox reactions. Metal species are usually highly dispersed in the silica framework making the otherwise chemically inert framework catalytically active. In the present work aluminium, tin and zirconium containing mesoporous molecular sieves MCM-41 have been synthesized, characterized and catalytically evaluated in few reactions.

Solid acid catalysts have been widely used in chemical industries, as they are non-corrosive, eco-friendly, easy to handle and reusable. In the present investigation, Pt loaded H-Al-MCM-41 molecular sieves have been catalytically evaluated in the hydroisomerization of n-hexane which is an important process in the petroleum refining industry for obtaining high octane gasoline blendstocks, and which has been investigated by earlier workers on molecular sieves such as Pt-Y[134], Pt-beta[135], Pt-mordenite[136] and Pt-ETS-10[137]. Liquid phase Beckmann rearrangement of cyclohexanone oxime using methanol and hexanol as solvents to prepare ε-caprolactam, which is the monomer of nylon-6 has been studied by Dai *et al.*[138]. They reported that the protonic form of mesoporous molecular sieves possessed high activity for the rearrangement. A comparative study of this reaction has been made over Si-MCM-41, H-Al-MCM-41 and Pt-H-Al-MCM-41. Linear alkyl benzenes (LAB) are important in the manufacture of detergents. The alkylation of benzene with long chain alkenes has been reported over heteropolyacids[139], clays[140], pillared clays[141] and ZSM-12[142] and a number of medium and wide pore zeolites[143]. In the present thesis a comparative study of the alkylation of benzene with long chain olefins over mesoporous Al-MCM-41, ReY and amorphous silica-alumina catalysts is being studied.

The incorporation of Ti and V into MCM-41 has been extensively studied and shown to result in active catalysts for the oxidation of larger molecules[64-67]. Systematic studies on the incorporation and characterization of Fe[55-61], Cr[72-74] and Mn[53] in MCM-41 have been reported. But, limited reports are available on the synthesis, characterization and catalytic evaluation of zirconium containing mesoporous molecular sieves[129,144,145]. Hence it was decided to study in detail the incorporation of zirconium in MCM-41. Substitution of aluminium by tin in the faujasites, mordenites and ZSM-5 by post synthesis[146-149] or by hydrothermal crystallization[150,151] and of silicon in Sn-silicalite-1[152] and Sn-silicalite-2[153] is known. Sn-silicalite-1 and Sn-silicalite-2 (medium pore zeolites) are catalytically active in the hydroxylation of small molecules such as phenol and cresol. So far there are no reports regarding the isomorphous substitution of tin in MCM-41 structure. This is now reported in this work[154]. These materials are found to be useful for the oxidation of large molecules such as 1-naphthol and norbornene.

1.9 OBJECTIVES OF THE PRESENT INVESTIGATION

The objectives of the present work are:

1. To synthesize MCM-41 and to optimize the synthesis procedures.

2. To synthesize Al-MCM-41, Sn-MCM-41and Zr-MCM-41 (metal incorporated MCM-41).

3. To study the effect of templating agents (surfactants) on the physico-chemical properties and morphology of MCM-41 and metal incorporated MCM-41 samples.

4. To characterize the synthesized samples in detail using various techniques and tools such as elemental analysis, XRD, TGA/DTA, N_2-adsorption measurements, electron

microscopy (TEM/SEM), pyridine-TPD, UV-visible, FT-IR, MAS NMR, ESR and Mössbauer spectroscopic methods.

5. To study the catalytic activity of H-MCM-41 in reactions such as the Beckmann rearrangement of cyclohexanone oxime, alkylation of benzene with long chain olefins and hydroisomerization of n-hexane over Pt-H-MCM-41.

6. To evaluate the catalytic activities of Sn-MCM-41 and Zr-MCM-41 samples in various oxidation reactions.

The thesis has been divided into five chapters.

Chapter I presents the general introduction and summarizes the available literature on mesoporous molecular sieves. It describes the synthesis strategies, the role of templating surfactants, the mechanism of synthesis, the characterization techniques used in the characterization of molecular sieves and the scope of the present work.

Chapter II gives an account of the synthesis of MCM-41 materials in two sections.

Section one deals with the synthesis of the pure silica MCM-41. The use of two templating agents (1) cetyltrimethyl ammonium chloride/hydroxide (CTMACl/OH) and (2) dodecyltrimethyl ammonium bromide (DTMABr) is described. The kinetics of crystallization is presented.

Section two describes the modification of MCM-41 by the incorporation of Al, Sn and Zr in the framework.

Chapter III deals with the physicochemical characterization of the samples synthesized by different methods. Chemical analysis and x-ray fluorescence (XRF) methods were used to determine aluminium, tin and zirconium contents. Transmission Electron Microscopy (TEM) and Scanning Electron Microscopy (SEM) have been used to determine the morphology of

the crystalline materials. Thermal analysis, N_2-sorption studies and FT-IR spectroscopy have been used to determine thermal stability, surface area and pore volume, and T-O-T bond status, respectively for all the samples, while pyridine desorption and H_2 chemisorption have been used to determine the acidity and Pt dispersion, respectively, in the case of the (Pt)Al-MCM-41 samples.

Solid state ^{29}Si and ^{19}Sn MAS NMR studies have been carried out to understand the Si/Sn environment. ^{27}Al MAS NMR studies were performed to study the nature of Al in Al-MCM-41 samples. The Sn-MCM-41 samples have been examined further by Mössbauer Spectroscopy. ESR studies have been performed on reduced Zr-MCM-41 samples.

Chapter IV describes the catalytic performances of different MCM-41 samples.

In the first part, acid catalyzed reactions viz., hydroisomerization of n-hexane over Pt-H-MCM-41, Beckmann rearrangement of cyclohexanone oxime over Si-MCM-41, H-Al-MCM-41 and Pt-H-Al-MCM-41 and alkylation of benzene with long chain olefins on H-Al-MCM-41 samples are reported.

In the second part of this chapter, Sn-MCM-41 and Zr-MCM-41 catalysts are evaluated for the hydroxylation of phenol and 1-naphthol and also for the epoxidation of norbornene.

Finally, in **Chapter V**, a summary of the results obtained and the conclusions drawn are presented.

1.10 REFERENCES

1. Sing, K.S.W., Everett, D.H., Haul, R.H.W., Moscou, L., Pierotti, R.A., Rouquerol, J., and Siemieniewska, T., *Pure Appl. Chem.*, **57** (1985) 603.
2. Breck, D.W., *"Zeolites Molecular Sieves"* Wiley, New York (1974).
3. Szostak, R., "*Molecular Sieves: Principles of Synthesis and Identification*" Van Nostrand Reinfold, New York (1989).
4. Wilson, S.T., Lok, B.M., and Flanigen, E.M., *U.S. Pat*., 4, 310, 440 (1982); Wilson, S.T., Lok, B.M., Messina, C.A., Cannon T.R., and Flanigen, E.M., *J. Am. Chem. Soc.*, **104** (1982) 1146.
5. Davis, M.E., Saldarriaga, C., Montes, C., Garces, J.M., and Crowder, J.A., *Nature*, **331** (1988) 698.
6. Estermann, M., McCusker, L.B., Baerlocher, C., Merrouche, A., and Kessler, H., *Nature*, **352** (1991) 320.
7. Jones, R.H., Thomas, J..M., Chen, J., Xu, R., Huo, Q., Li, S., Ma, Z., and Chippindale A.M., *J. Solid State Chem.*, **102** (1993) 204.
8. Freyhardt, C.C., Tsapatsis, M., Lobo, R.F., Balkus Jr., K.J., and Davis, M.E., *Nature*, **381** (1995) 369.
9. Zhao, X.S., (Max) Lu, G.Q., and Miller, G.J., *Ind. Eng. Chem. Res.*, **35** (1996) 2075.
10. Meier, W.E., and Olson, D.H., *Atlas of Zeolite structure Types;* Butterworth-Heinemann, London, (1987).
11. Lok, B.M., Messina, C.A., Lyle Patton, R., Gajek, R.T., Cannon T.R., Wilson, S.T., and Flanigen, E.M., *J. Am. Chem. Soc.*, **106** (1984) 6092.
12. Schlenker, J.L., Rohrbaugh, W.J., Chu, P., Valyocsik, E.W., and Kokotailo, G.T., *Zeolite*, **5** (1985) 355.
13. Van Koningsveid, H., Jansen, J.C., and van Bakkum, H., *Zeolite*, **10** (1990) 235.
14. Olson, D.H., *J. Phys. Chem.*, **74** (1970) 2758.
15. Bialek, R., Meier, W.M., and Davis, M.E., *Zeolite*, **11** (1991) 438.
16. Fyte, C.A., Gies, H., Kokotailo, G.T., Marler, B., and Cox, D.E., *J. Phys. Chem.*, **94** (1990) 3718.
17. Dessau, R.M., Schlenkar, J.L., and Higgins, J.B., *Zeolite*, **10** (1990) 522.
18. Iler, R.K., *The Chemistry of Silica*; J. Wilwy & Sons, Inc., 1979.
19. Wefers, K., and Misra, C., *Oxides and Hydroxides of Aluminium*; Alcoa Technical Paper No. 19, Revised, Alcoa Laboratories, 1987.

20. Pinnavaia, T.J., *Science*, **220** (1983) 365.
21. Yanagisawa, T., Schimizu, T., Kuroda, K., Kato, C., *Bull. Chem. Soc. Japan.*, **63** (1990) 988.
22. Corma, A., Pérez-Pariente, J., Fornés, V., Rey, F., and Rawlence, D., *Appl. Catal.*, **63** (1990) 145.
23. Kresge, C.T., Leonowicz, M.E., Roth, W.J., and Vartuli, J.C., *U.S. Patent*, 5,098,684 (1992).
24. Kresge, C.T., Leonowicz, M.E., Roth, W.J., Vartuli, J.C., and Beck, J.S., *Nature*, **359** (1992) 710.
25. Beck, J.S., Chu, C.T., Johnson, I.D., Kresge, C.T., Leonowicz, M.E., Roth, W.J., and Vartuli, J.C., *U.S. Patent*, 5, 108, 725 (1992).
26. Beck, J.S., Calabro, D.C., McCullen, S.B., Pelrine, B.P., Schmitt, K.D., and Vartuli, J.C., *U.S. Patent*, 5, 145, 816 (1992).
27. Beck, J.S., Kresge, C.T., Leonowicz, M.E., Roth, W.J., and Vartuli, J.C., *U.S. Patent*, 5, 264, 203 (1993).
28. Beck, J.S., Vartuli, J.C., Roth, W.J., Leonowicz, M.E., Kresge, C.T., Schmitt, K.D., Chu, C.T-W., Olson, D.H., Sheppard, E.W., McCullen, S.B., Higgins, J.B., and Schlenker, J.L., *J. Am. Chem. Soc.*, **114** (1992) 10834.
29. Vartuli, J.C., Kresge, C.T., Leonowicz, M.E., Chu, A.S., McCullen, S.B., Johnson, I.D., and Sheppard, E.W., *Chem. Mater.*, **6** (1994) 2070.
30. Vartuli, J.C., Roth, W.J., Beck, J.S., McCullen, S.B., and Kresge, C.T., *"Molecular Sieves, Science and Technology"*, Eds: Karge, H.G., Weitkamp, J., **1** (1998) 97.
31. Huo, Q., Margolese, D.I., Ciesla, U., Demuth, D.G., Feng, P., Gier, T.E., Sieger, P., Firouzi, A., Chmelka, B.F., Schüth, F., and Stucky, G.D., *Chem. Mater.*, **6** (1994) 1176.
32. Cheng, C.F., He, H., Zhou, W., and Klinowski, J., *Chem. Phys. Lett.*, **244** (1995) 117.
33. Chen, C.-Y., Burkett, S.L., Li, H.Y., and Davis, M.E., *Microporous Mater.*, **2** (1993) 27.
34. Steel, A., Carr, S.W., and Anderson, M.W., *J. Chem. Soc. Chem. Commun.*, (1994) 1571.
35. Dubois, M., Gulik-krzywicki, Th., and Cabane, B., *Langmuir*, **9** (1993) 673.
36. Vartuli, J.C., Schmitt, K.D., Kresge, C.T., Roth, W.J., Leonowicz, M.E., McCullen, S.B., Hellring, S.D., Beck, J.S., Schlenker, J.L., Olson, D.H., and Sheppard, E.W.,

Chem. Mater., **6** (1994) 2317.

37. Huo, Q., Margolese, D.I., Ciesla, U., Feng, P., Gier, T.E., Sieger, P., Leon, R., Petroff, P.M., Schüth, F., and Stucky, G.D., *Nature*, **368** (1994) 317.
38. Huo, Q., Leon, R., Petroff, P.M., and Stucky, G.D., *Science*, **268** (1995) 1324.
39. Bagshaw, S.A., Pouzet, E., and Pinnavaia, T.J., *Science*, **269** (1995) 1242.
40. Monnier, A., Schüth, F., Huo, Q., Kumar, D., Margolese, D.I., Maxwell, R.S., Stucky, G.D., Krishnamurthy M., Petroff, P., Firouzi, A., Janicke, M., and Chmelka, B.F., *Science*, **261** (1993) 1299.
41. Firouzi, A., Kumar, D., Bull, L.M., Besier, T., Sieger, P., Huo, Q., Walker, S.A., Zasadzinski, J.A., Glinka, C., Nicol, J., Margolese, D.I., Stucky, G.D., and Chmelka, B.F., *Science*, **267** (1995) 1138.
42. Inagaki, S., Fukushima, Y., and Kuroda, K., *J. Chem. Soc. Chem. Commun*. (1993) 680.
43. Inagaki, S., Fukushima, Y., and Kuroda, K., *Stud. Surf. Sci. Catal.*, **84** (1994) 125.
44. Ishikawa, T., Matsuda, M., Yasukawa, A., Kandori, K., Inagaki, S., Fukushima, T., and Kondo, S., *J. Chem. Soc., Faraday Trans.*, **92** (1996) 1985.
45. Beck, J.S., Vartuli, J.C., Kennedy, G.J., Roth, W.J., and Schramm, S.E., *Chem. Mater*., **6** (1994) 1816.
46. Beck, J.S., *U.S. Patent*, 5. 057, 296 (1991).
47. Khushalani, D., Kuperman, A., Ozin, G.A., Tanaka, K., Garcés, J., Olken, M.M., and Coombs, N., *Adv. Mater.*, **7** (1995) 842.
48. Chen, X., Huang, L., and Li, Q., *J. Phys. Chem. B*, **101** (1997) 8460.
49. Schimdt, R., Akporiaye, D., Stöcker, M., and Ellestad, O.H., *J. Chem. Soc., Chem. Commun.*, (1994) 1493.
50. Stucky, G.D., Monnier, A., Schüth, F., Huo, Q., Margolese, D.I., Kumar, D., Krishnamurthy M., Petroff, P., Firouzi, A., Janicke, M., and Chmelka, B.F., *Mol. Cryst. Liq. Cryst.*, **240** (1994) 187.
51. Koyoano, K.A., and Tatsumi, T., *Chem. Commun.* (1996) 145.
52. Ulagappan, N., Neeraj, Battaram, V.N.R., and Rao, C.N.R., *J. Chem. Soc., Chem. Commun.* (1996) 2243.
53. Zhao, D., and Goldfarb, D., *J. Chem. Soc., Chem. Commun.* (1995) 875.
54. Tanev, P.T., and Pinnavaia, T.J., *Science*, **267** (1995) 865.
55. Tuel, A., and Gontier, S., *Chem. Mater.*, **8** (1996), 114

56. Sayari, A., Moudrakovaski, I., Danumah, C., Ratcliffe C.I., Ripmeester, J.A., and Preston, K.F., *J. Phys. Chem.*, **99** (1995) 16373.
57. Oberhagemann, U., Topalovic, I., Marler, B., Gies, H., *Stud. Surf. Sci. Catal.*, **98** (1995) 17.
58. Liu, S., He, H., Luan, Z., Klinowski, J., *J. Chem. Soc., Faraday Trans.*, **92** (1996) 2011.
59. Cheng, C.-F., and Klinowski, J., *J. Chem. Soc., Faraday Trans.*, **92** (1996) 289.
60. Cheng, C.-F., He, H., Zhou, W., Klinowski, J., Sousa Goncalves, L.F., and Gladden, L.F., *J. Phys. Chem.*, **100** (1996) 390.
61. Yuan, Z.Y., Liu, S.H., Chen, T.H., Wang, J.Z., and Li, H.X., *J. Chem. Soc., Chem. Commun.*, (1995) 973.
62. Casci, J.L., *Stud. Surf. Sci. Catal.*, **85** (1994) 329.
63. Sayari, A., *Chem. Mater.*, **8** (1996) 1840.
64. Kresge, C.T., Leonowicz, M.E., Roth, W.J., and Vartuli, J.C., *U.S. Patent*, 5, 250, 282 (1993).
65. Corma, A., Navarro, M.T., and Perez-Pariente, J., *J. Chem. Soc., Chem. Commun*., (1994) 147.
66. Reddy, K.M., Moudrakovski, I.L., and Sayari, A., *J. Chem. Soc., Chem. Commun*., (1994) 1059.
67. Luan Z., Xu, J., He, H., Klinowski, J., Kevan, L., *J.Phys. Chem.*, **100** (1996) 19595.
68. Corma, A., Navarro, M.T., Perez-Pariente, and Sanchez, F., *Stud. Surf. Sci. Catal.*, **84** (1994) 69.
69. Pinnavaia, T.J., Tanev, P.T., Wang, J., and Zhang, W., *Mater. Res. Soc. Symp. Proc.*, **371** (1995) 53.
70. Tanev, P.T., Chibwe, M., and Pinnavaia, T.J., *Nature*, **368** (1994) 317.
71. Reddy, J.S., Liu, P., and Sayari, A., *Appl. Catal. A: General*, **148** (1996) 7.
72. Zhang, W., Pinnavaia, T.J., *Catal. Lett*., **38** (1996) 261.
73. Zhang, W., Wang, J., Tanev, P.T., and Pinnavaia, T.J., *Chem. Commun.*, (1996) 979.
74. Ulagappan, N., and Rao, C.N.R., *J. Chem. Soc., Chem. Commun.*, (1996) 1047.
75 Olson, D.H., Stucky, G.D., and Vartuli, J.C., *U.S. Patent*, 5, 364, 797 (1994).
76. Mercier, L., and Pinnavaia, T.J., *Adv. Mater.*, **9** (1997) 500.
77. Cauvel, A., Renard, G., and Brunel, D., *J. Org. Chem.*, **62** (1997) 749.
78. Maschmeyer, T., Rey, F., Sanker, G., and Thomas, J.M., *Nature*, **378** (1995) 159.

79. Ryoo, R., Jun, S., Kim, J.M., and Kim, M.J., *J. Chem. Soc., Chem. Commun.* (1997) 2225.
80. Song, S., and Reddy, K.M., *Appl. Catal. A: General*, **176** (1999) 1.
81. Okamura, J., Nishiyama, S., Tsuruya, S., and Masai, M., *J. Mol. Catal. A Chem*., **135** (1998) 133.
82. Kloestra, K.L., and Bakkum, H.van, *Stud. Surf. Sci. Catal.*, **105 A** (1997) 431.
83. Kloestra, K.L., and Bakkum, H.van, *J. Chem. Soc., Faraday Trans.*, **93** (1997) 1211.
84. Corma, A., Martinez, A., Martinez-Soria, V., *J. Catal.*, **169** (1997) 480.
85. Corma, A., Fornes, V., Navarro, M.T., and Perez-Pariente, J., *J. Catal.*, **148** (1994) 569.
86. Borade, R.B., and Clearfield, A., *Catal. Lett*., **31 (**1995) 267.
87. Mokaya, R., Zones, W., Luan, Z., Alba, M.D., and Klinowski, J., *Catal. Lett*., **37** (1996) 113.
88. Mokaya, R., and Zones, W., *Chem. Commun.* (1996) 983.
89. Occelli, M.L., Biz, S., Auroux, A., and Ray G.J., *Microporous and Mesoporous Mater*., **26** (1998) 193.
90. Brunauer, S., Emmett P.H., and Teller E., *J.Am. Chem Soc.*, **60** (1938) 309.
91. Horvath, G., and Kawazoe, K.J., *J. Chem. Eng. Jpn.*, **16** (1983) 470.
92. Alfredsson, V., Keung, M., Monnier, A., Stucky, G.D., Unger, K.K., and Schüth, F., *J. Chem. Soc., Chem. Commun.*, (1994) 921.
93. Chenite, A., Page, Y.L., and Sayari, *Chem. Mater.*, **7** (1995) 1015.
94. Barrer, R.M., and Langley, D.A., *J. Chem. Soc*., 3804, 3811, 3817 (1958).
95. Flanigen, E.M., *"Zeolite Chemistry and Catalysis"* ACS monograph (Rabo, J.A. EDS.) **171** (1976) 118.
96. Maroni, V.A., Martin, K.A., and Johnson, S.A., *ACS Sym. Ser*., **368** (1988) 85.
97. Janin, A., Lovally, J.C., Macedo, A, and Raatz F., *ACS Sym. Ser.*, **368** (1988) 85.
98. Topsoe, N., Pedersen, R., and Derouance, E.G., *J. Catal.*, **70** (1984) 369.
99. Jacobs, P.A., and Martier, W.Y., *Zeolites*, **2** (1982) 226.
100. Lippmaa, E., Magi, M., Samoson, A., Engelhardt, G., and Gummer, A.R., *J. Am. Chem. Soc.*, **102** (1980) 4889.
101. Lippmaa, E., Magi, M., Samoson, A., Tarmak, M., and Engelhardt, G., *J. Am. Chem. Soc.*, **103** (1981) 4992.
102. Fyfe, C.A., Gobbi, G.C., Klinowski, J., Thomas J.M., and Ramdas, S., *Nature*, **296**

(1982) 530.

103. Fyfe, *C.A., Gobbi, G.C., Klinowski, J., and Thomas J.M., J. Phys. Chem.*, **86** (1982) 1247.
104. Engelhardt, G., Lohose, U., Lippmaa, E., Tarmak, M., and Magi, M., *Anarg. Allg. Chem.*, **482** (1981) 49.
105. Mastikim, V.M., and Zamarev, K.I., *J. Phys. Chemie.*, **152** (1987) 332.
106. Muller, D., Gessnev, W., Behrens, H.S., and Schelev, G., *Chem. Phys. Lett*., **79** (1981) 159.
107. Thomas J.M., Fyfe, C.A., Ramdas, S., Klinowski, J., and Gobbi, G.C., *J. Phys. Chem.*,**86** (1982) 3061.
108. Ramdas, S., and Klinowski, J., *Nature*, **308** (1984) 521.
109. Steel, A., Carr, S.W., and Anderson, M.W., *Chem. Mater.*, **7** (1995) 1829.
110. Zhang, J., Zimmermann, H., Luz, Z., and Goldfarb, D., *Stud. Surf. Sci. Catal.*, **117** (1998) 535.
111. Zhang, J., Luz, Z., and Goldfarb, D., *J. Phys. Chem. B*, **101** (1997) 7087.
112. Xu, J., Luan, Z., Wasowicz, T., and Kevan, L., *Microporous Mesoporous Mater.*, **22** 1998, 179.
113. Chao, K.J., Wu, C.N., Chang, H., Lee, L.J., and Hu, S.-F., *J. Phys. Chem. B*, **101** (1997) 6341.
114. Luca, V., MacLachlan, D.J., and Morgan, K., *Chem. Mater.*, **9** (1997) 2720.
115. Chang, Z.; Zhu, Z.; and Kevan, L. *J. Phys. Chem., B*, **103** (1999) 9442.
116. Kosslick, M., Lischke, G., Walther, G., Storek, W., Martin, A., and Fricke, R., *Microporus Mater.*, **9** (1997) 13.
117. Yuan, Z.-Y., Zhang, H.-B., Chen, T.-H., Wang, J.-Z., and Li, H.-X., *J. Nat. Gas Chem.*, **6** (1997) 237.
118. Prakash, A.M., Hyung, M. S.-S., and Kevan, L., *J. Phys. Chem., B*, **102 (**1998) 857.
119. Stocker, M., *Microporous Mater.*, **6** (1996) 235.
120. Mokaya, R., and Jones, W., *J. Mater. Chem.*, **9** (1999) 555.
121. Mokaya, R., *J. Catal.*, **186** (1999) 470.
122. Reddy, J.S., Dicko, A., and Sayari, A., *Chem. Ind.*, **69** (1997) 405.
123. Sayari, A., Reddy, K.M., Moudrakovski, I., *Stud. Surf. Sci. Catal.*, **98** (1995) 19.
124. Armengol, E., Cano, M.L., Corma, A., Garcia, H., and Navarro, M.T., *J. Chem. Soc., Chem. Commun.*, (1995) 519.

125. Aguado, J., Serrano, D.P., Romero, M.D., and Escola, J.M., *J. Chem. Soc., Chem. Commun.*, (1996) 725.
126. Corma, A., Martínez, A., Martínez-Soria V., and Monton, J.B., *J. Catal.*, **153** (1995) 25.
127. Reddy, J.S., and Sayari, A.,*J. Chem. Soc., Chem. Commun.*, (1995) 2231.
128. Zhang, W., Fröla, M., Wang, J., Tanev, P.T., Wong, J., and Pinnavaia, T.J., *J. Am. Chem. Soc.*, **118** (1996) 9164.
129. Gontier, S., and Tuel, A., *Stud. Surf. Sci. Catal.*, **105** (1997) 1085.
130. Burch, R., Cruise, N., Gleeson, D., and Tsang, S.C., *J. Chem. Soc., Chem. Commun*., (1995) 1495.
131. Kloetstra, R.K., and Bekkum, H. van, *J. Chem. Soc., Chem*. *Commun*. (1995) 1005.
132. Ernst, S., Glaser, R., and Selle, M., *Stud. Surf. Sci. Catal.*, **105 A** (1997) 69.
133. Junges, U., Jacobs, W., Voigt-Martin, I., Krutzsch, B., and Schüth, F., *J. Chem. Soc., Chem. Commun*. (1995) 2283.
134. Gianetto, G. E., Perot, G.R., and Guisnet M.R., *Ind. Eng. Chem. Prod. Res. Dev*., **25** (1986) 481.
135. Leu, L.J., Hou, L.-Y., Kang, B-D, Li, C., Wu, S-T., and Wu, J-C., *Appl. Catal*., **69** (1991) 49.
136. Guisnet, M., Fouche, V., Belloum, M., Bournonville, J.P., and Travers, C., *Appl. Catal*., **71** (1991) 283.
137. Das, T.K., Chandwadkar., A.J., Soni, H.S., and Sivasanker, S., *Catal. Lett*., **44** (1997) 113.
138. Dai, L.-X., Koyama, K., and Tatsumi, T., *Catal Lett*., **53** (1998) 211.
139. Sebulsky, R.T., and Henke, A.M., *Ind. Eng. Chem. Process Dev*., **10** (1971) 271.
140. Berna, T., Jose, L., Moreno, D., and Alfonso, *EP Appl.*, 0, 353, 813 (1991).
141. He, Ming-Yuan, Zhonghui, L., and Enze, M., *Catal. Today*, **2** (1988) 321.
142. Young, L.B., *US Patent*, 4, 301, 317 (1981).
143. Sivasanker, S., Thangaraj, A., Abdulla R.A., and Ratnasamy, P., *Proc. 10th Int. Cong. Catal., 1992, Elsevier Science Publishers* (1993) 397.
144. Gontier, S., and Tuel., A., *Appl. Catal. A: General*, **143** (1996) 125.
145. Occelli, M.L., Biz, S., and Aurox, A., *Appl. Catal. A: General*, **183** (1999) 231.
146 Skeels, G.W., and Flanigen, E.M., *Stud. Surf. Sci. Catal.*, **49A** (1989) 331.
147. Skeels, G.W., and Flanigen, E.M., *US Patent*, 133 372 (1987).

148. Skeels, G.W., and Flanigen, E.M., *EP*, 321 177 (1989).
149. Vaughan, D.E.W., and Rice, S.B., *US Patent*, 4 933 161 (1990).
150. Dwyer, F.G., Jenkins, E.E., *US Patent*, 3 941 871 (1976).
151. Corcoran, Jr. E.W., and Vaughan, D.E.W., *US Patent*, 5 192 519 (1993).
152. Mal, N.K., and Ramaswamy, A.V., *J. Mol. Catal*., **105** (1996) 149.
153. Mal, N.K., Ramaswamy, V., Ganapathy, S., and Ramaswamy, A.V., *Appl. Catal. A: General*, **125** (1995) 233.
154. Chaudhari, K., Das, T.K., Rajmohanan, P.R., Lazar, K., Sivasanker, S., and Chandwadkar, A.J., *J. Catal.*, **183** (1999) 281.

Chapter II

SYNTHESIS

2.1 INTRODUCTION

MCM-41 (Mobil Crystalline Material-41) is one of the members of M41S molecular sieves first synthesized by researchers at Mobil Corporation[1-3]. It possesses a hexagonal array of unidimensional mesopores with pore diameter ranging between 15 to 100 Å, depending on the surfactant template used and synthesis conditions. Unlike other mesoporous materials such as intercalated clays, the pore size of MCM-41 molecular sieve is fairly uniform. Since the discovery of MCM-41, it has attracted considerable attention due to its large and uniform pore size distribution, high surface area (> 800 m^2/g) and distinct adsorption properties[1].

Several synthesis methods have been proposed and successfully used to synthesize mesoporous MCM-41 molecular sieves[4-8]. These materials are normally synthesized by hydrothermal procedures and their structures are obtained from amorphous inorganic silica walls around surfactant molecules. Kresge *et al.*[1,2] first synthesized mesoporous silicates and aluminosilicates in alkaline conditions. Huo and co-workers[4,9] reported the first synthesis of porous silicates in acidic conditions, while Yanagisawa *et al.*[10] pillared a layered silica with surfactant cations and after calcination obtained a mesoporous silica with uniform distribution of pores.

In order to impart catalytic activity to the chemically inert mesoporous silicate framework, substitution of Si^{4+} ions by other heteroatoms in the MCM-41 structure has been attempted. Modification of MCM-41 with heteroatoms such as Al[11,12], Ti[13-16], V[17] etc. has resulted in materials with considerable catalytic activity in reactions of bulky molecules like, 2,4-di-*tert*-butylphenol, naphthalene, norbornene, linalool, substituted phenols etc., which would not have been possible by the use of microporous materials due to their small pore sizes.

A survey of the literature on mesoporous materials which is briefly reviewed in chapter I, reveals that substitution of transition metals such as titanium and vanadium for silicon in the MCM-41 structure has been studied in detail. The substitution of zirconium (a transition metal from the same group as titanium) in the structure of MCM-41 is investigated in detail in this study. Also studies on the substitution of tin are reported for the first time[18]. Prior to the modification of the MCM-41 structure, the synthesis of the parent material, Si-MCM-41 was optimized by employing different synthesis conditions. The synthesis procedures were based on those described in the literature[3,19-21].

This chapter describes the synthesis of mesoporous MCM-41 and modified MCM-41 molecular sieves in two parts.

Part I

- Synthesis of siliceous MCM-41 in alkaline medium using the surfactants cetyl trimethylammonium chloride/hydroxide [$C_{16}H_{33}N(CH_3)_3Cl$/OH-**CTMACl/OH**], cetyl trimethylammonium bromide [$C_{16}H_{33}N(CH_3)_3Br$-**CTMABr**] and dodecyl trimethylammonium bromide [$C_{12}H_{25}N(CH_3)_3Br$-**DTMABr**] (on the basis of refs. 3,19,20).

- Studies on the crystallization of MCM-41 in alkaline medium using the surfactant CTMACl/OH under various synthesis conditions.

- Synthesis of siliceous MCM-41 in acid medium using the surfactant CTMABr[21].

- Synthesis of siliceous HMS (Hexagonal Mesoporous Silica) in neutral medium using the surfactant dodecyl amine [$C_{12}H_{25}NH_2$-**DDA**][21].

Part II

- Synthesis of Al-MCM-41 in alkaline medium using the surfactant $CTMABr^{20}$ and impregnation of Pt on H-Al-MCM-41 samples.
- Isomorphous substitution of Sn^{4+} for Si^{4+} ions in MCM-41 structure in alkaline medium using the surfactant, CTMACl/OH.
- Isomorphous substitution of Zr^{4+} for Si^{4+} ions in MCM-41 structure in alkaline medium using the surfactant, DTMABr.

2.2 PART–I: SYNTHESIS OF MCM-41

2.2.1 EXPERIMENTAL

Hydrothermal syntheses of MCM-41 samples were carried out in stainless steel autoclaves at autogenous pressure under static conditions. The chemicals used in syntheses and modifications of MCM-41 are listed in Table 2.1.

Table 2.1 Specifications of the chemicals used

Reagent (Source)	**Chemical formula or composition**	**Purity (%)**
Fumed silica (Sigma)	SiO_2	99
Fumed silica (Cab-O-Sil, Fluka)	SiO_2	99
Tetramethyl ammonium silicate - TMA silicate (SACHEM Inc., USA),	$(CH_3)_4NOH.2SiO_2$	10 wt.% silica solution, TMA/SiO_2 = 0.5
Tetraethyl orthosilicate – TEOS (Aldrich)	$Si(OC_2H_5)_4$	99

Cetyltrimethylammonium chloride/hydroxide – CTMACl/OH (Aldrich)	$C_{16}H_{33}N(CH_3)_3Cl/OH$ (17.9 wt.% Cl, 6.7 wt% OH)	Prepared in the laboratory by partial exchange of CTMACl (25 wt. % aqueous solution, Aldrich) over an ion exchange resin,
Ammonium hydroxide – NH_4OH (S.D. Fine Chemicals)	NH_4OH	25% solution in water
Sodium silicate (UCIL, India)	Na_2SiO_3	28.48% SiO_2, 9.03% Na_2O, 62.5% H_2O
Cetyltrimethylammonium bromide - CTMABr (Aldrich)	$C_{16}H_{33}N(CH_3)_3Br$	98
Dodecyltrimethylammonium bromide – DTMABr (Aldrich)	$C_{12}H_{25}N(CH_3)_3Br$	99
Dodecyl amine – DDA (SRL, India)	$C_{12}H_{25}NH_2$	96
Tetramethyl ammonium hydroxide – TMAOH (Aldrich)	$(CH_3)_4NOH$	99
Tetramethyl ammonium hydroxide – TMAOH (Aldrich)	$(CH_3)_4NOH$	25 wt.% solution in water
Mesitylene (Aldrich)	C_9H_{12}	99
Sodium hydroxide (S.D. Fine Chemicals, India)	NaOH	99
Aluminium sulphate (Merck)	$Al_2(SO_4)_3.18H_2O$	98
Ammonium nitrate (S.D. Fine Chemicals, India)	NH_4NO_3	99
Stannic chloride (Loba Chemie), Bombay, India)	$SnCl_4.5H_2O$	98
Zirconium butoxide (Aldrich)	$Zr[O(CH_2)_3CH_3]_4$	80 wt.% solution in 1-butanol
Isopropanol (S.D. Fine Chemicals, India)	$(CH_3)_2CHOH$	99
Tetraamine platinum(II) nitrate (Aldrich)	$Pt(NH_3)_4(NO_3)_2$	99

2.2.1.1 Synthesis of Si-MCM-41 in Alkaline Medium

2.2.1.1(i) Using CTMACl/OH

The molar composition of the synthesis gel in terms of oxides was as follows:

SiO_2 : 0.086 $(NH_4)_2O$: 0.089 $(CTMA)_2O$: 0.155 $(TMA)_2O$: 40 H_2O.

Ammonium hydroxide (1.8 g; 25% solution) diluted with water (12.5 g) was added to a solution of CTMACl/OH (16.7 g) with stirring. To this mixture, 2.08 g TMAOH dissolved in 12.5 g water was added followed by the addition of 13.6 g TMA silicate. The mixture was stirred for 20 minutes. Fumed silica (3.1 g, Sigma) was added slowly to the above gel under stirring and the mixture stirred further for 1 h. The pH of the final gel was 11.5. The gel was then transferred to a stainless steel autoclave and heated in an oven at 110°C for 96 h (4 days) for crystallization. After the crystallization, the product was filtered, washed with deionized water and dried at 100°C for 5 h. The product was finally calcined at 550°C for 1 h in nitrogen and then for 6 h in air.

2.2.1.1(ii) Using DTMABr

The molar compositions of the synthesis gels in terms of oxides were as follows:

SiO_2 : 0.086 $(NH_4)_2O$: 0.089 $(DTMA)_2O$: 0.155 $(TMA)_2O$: 40 H_2O.

In a typical synthesis of Si-MCM-41, ammonium hydroxide (1.8 g; 25% solution) diluted with water (12.5 g) was added to a solution of DTMABr (4.043 g) dissolved in 12.5 g water with stirring. To this mixture, tetramethylammonium hydroxide ($TMAOH.5H_2O$, 2.09 g,) dissolved in 12.5 g water was added. Fumed silica (3.1 g, Sigma) was added to the above mixture of organic templates and stirred for some time. This was followed by the addition of tetramethylammonium silicate (13.6 g). This thick gel was stirred for 20 minutes. The pH of the mixture was 11 – 11.5. The gel was then transferred to a stainless steel autoclave and

heated in an oven at 110°C for 96 h (4 days) for crystallization. After the crystallization, the product was filtered, washed with deionized water and dried at 100°C for 5 h. The product was finally calcined at 550°C for 1 h in nitrogen and then for 6 h in air.

2.2.1.1(iii) Using CTMABr

The molar compositions of the synthesis gels in terms of oxides were as follows:

SiO_2 : 0.086 $(NH_4)_2O$: 6.5 EtOH : 0.27 $(CTMA)_2O$: 0.13 $(TMA)_2O$: 60 H_2O.

In a typical synthesis, 18.9 g TMAOH (25% aqueous solution) was added to 16.86 g sodium silicate diluted with 100 g water. In another beaker 19.68 g CTMABr was dissolved in 50 g water and 30 g ethanol, and 1.9 g of aqueous ammonia (25%) was added to it (solution A). Solution A was added to the above mixture of sodium silicate and TMAOH and then 7.06 g fumed silica was added to it. The mixture was stirred for one hour. The gel formed (pH = 11.5) was then transferred to an autoclave and heated at 110°C in an oven for 120 h (5 days). The product was then filtered, washed with distilled water and dried at 100°C for 5 h. The sample was calcined at 550°C in nitrogen for 1 h and then in air for 6 h.

2.2.1.2 Synthesis of Si-MCM-41 in Acid Medium

The molar compositions of the synthesis gels in terms of oxides were as follows:

TEOS : 0.2 CTMABr : HCl : 150 H_2O.

In a typical synthesis, 7.289 g CTMABr was added to a solution of 3.65 g HCl in 270 g water and stirred. TEOS (20.83 g) was added to the above solution and stirred vigorously at ambient temperature for 18 h. The crystalline product was then filtered, washed with distilled water and dried at ambient temperature. The sample was calcined at 550°C in nitrogen for 1 h and then in air for 6 h.

2.2.1.3 Synthesis of Si-MCM-41 in Neutral Medium (using DDA)

The molar compositions of the synthesis gels in terms of oxides were as follows:

TEOS : 0.2 DDA : 6.0 EtOH : 150 H_2O.

In a typical synthesis, 3.86 g DDA was added to a solution of 27.6 g ethanol in 270 g water and stirred. TEOS (20.83 g) was added to the above solution and stirred vigorously at ambient temperature for 18 h. The crystalline product was then filtered, washed with distilled water and dried at ambient temperature. The sample was calcined at 550°C in nitrogen for 1 h and then in air for 6 h.

2.2.2 RESULTS AND DISCUSSION

2.2.2.1 Kinetics of Crystallization

The effect of different factors affecting the synthesis mechanism has been examined by preparing different samples of mesostructured materials hydrothemally in alkaline medium using CTMACl/OH. Since x-ray analysis and N_2-sorption data are required to characterize MCM-41 materials[22], both these techniques have been used to characterize the samples obtained during studies on kinetics of crystallization; the data obtained is also discussed in this chapter.

2.2.2.1(i) Effect of Temperature

To study the effect of temperature on the formation of mesoporous Si-MCM-41 molecular sieves, four samples were synthesized using the procedure described in section 2.2.1.1(i), at different temperatures in the range between room temperature (RT) and 150°C keeping the crystallization time constant (96h; 4 days). The gel composition and the pH (11.2-11.5) were similar for the synthesis of the samples. The molar composition of the synthesis gel in terms of oxides was as follows:

SiO_2 : 0.086 $(NH_4)_2O$: 0.089 $(CTMA)_2O$: 0.155 $(TMA)_2O$: 40 H_2O.

These samples were synthesized by keeping the gel at room temperature, 50°C, 110°C and 150°C and designated as Si-MCM-41(RT), Si-MCM-41(50°C), Si-MCM-41(110°C) and Si-MCM-41(150°C), respectively. After the crystallization, the products were filtered, washed with deionized water and dried at 100°C for 5 h. The products were finally calcined at 550°C for 1 h in nitrogen and then for 6 h in air. Formation of the materials has been evaluated by x-ray diffraction and nitrogen sorption studies.

The XRD profiles of as-synthesized and calcined samples are shown in Fig. 2.1(A) and Fig. 2.1(B), respectively. As-synthesized forms of Si-MCM-41(RT), Si-MCM-41(50°C) and Si-MCM-41(110°C) exhibit a typical four peak pattern[3] with a very strong (100) reflection at low angle and three weaker (110), (200) and (210) reflections (Fig. 2.1(A) a-c). According to Beck *et al.*[3] these four reflection lines can be indexed based on a hexagonal unit cell ($a_0 = 2d_{100}/\sqrt{3}$).

In the XRD pattern of the calcined Si-MCM-41(RT), only the (100) reflection is observed prominently (Fig. 2.1(B)-a). The presence of only (100) reflection in the calcined sample suggests that this material does not possess the well defined hexagonal arrays[23,24] after calcination. However, the long range order in hexagonal symmetry is still retained in the calcined forms of Si-MCM-41(50°C) and Si-MCM-41(110°C), which is indicated by the presence of the four peaks in the XRD patterns (Fig. 2.1(B)-b and c).

In both the as-synthesized and calcined samples, the most intense peak with (100) reflection is shifted to higher d_{100} spacing values with increase in temperature of hydrothermal synthesis from RT to 110°C (Fig. 2.1(A) a-c and Fig. 2.1(B) a-c). Also when as-synthesized samples are compared with calcined ones, it is observed that the most intense

peak with (100) reflection is shifted to lower d_{100} spacing value, as calcination causes condensation of internal SiOH groups giving rise to a contraction of the unit cell[3,25,26].

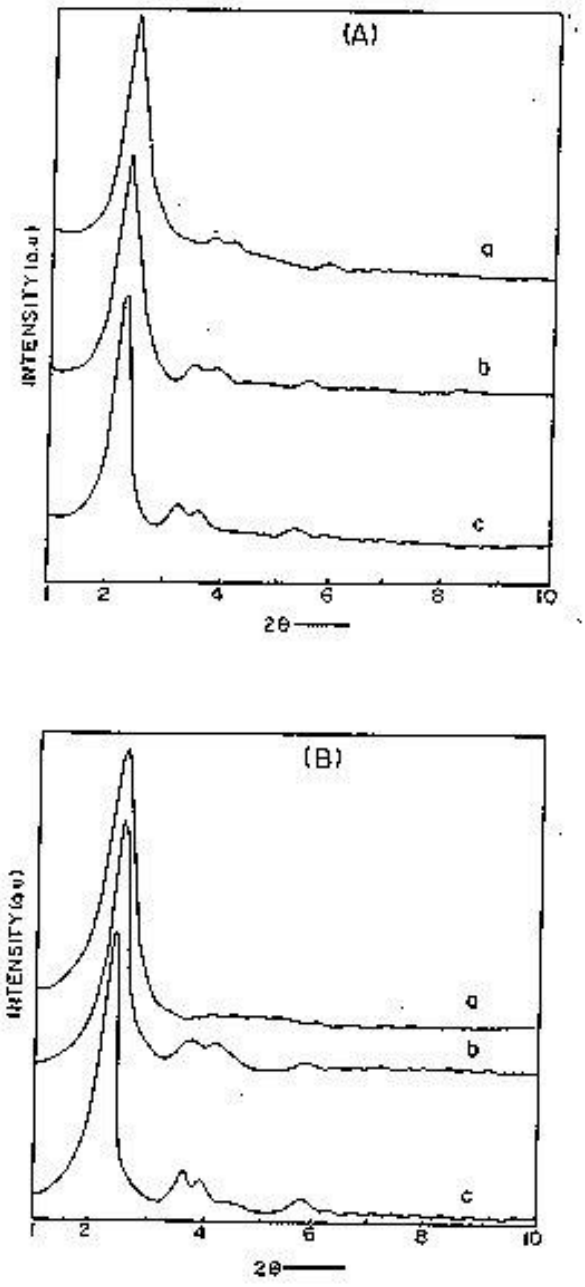

Fig. 2.1 XRD patterns of (A) as-synthesized and (B) calcined samples. (a) Si-MCM-41(RT); (b) Si-MCM-41(50°C) and (c) Si-MCM-41(110°C).

The maximum contraction is observed in the case of Si-MCM-41(RT), which may be due to the poorly ordered arrangement of the mesopores[26] (Table 2.2). A significant increase in the intensity of this peak in calcined samples indicates that an atomic reorganization occurs during the removal of the surfactant molecules in the calcination process[27].

Table 2.2 Data obtained from XRD and N_2-sorption studies

Sample	**d_{100}**	**Unit cell parameter (a_0)**	**S.A. (m^2/g)**	**Average pore diameter (Å)**	**Pore volume (ml/g)**	**Average wall thickness (Å)**
Si-MCM-41(RT) (As-syn.)*	34.91					
Si-MCM-41(RT) (Cal.)	32.89	38.9	468.2	31 (broad)	0.483	7.0
Si-MCM-41(50°C) (As-syn)*	36.48					
Si-MCM-41(50°C) (Cal.)	34.75	40.13	765.5	29	0.5	11.13
Si-MCM-41(110°C) (As-syn.)*	38.37					
Si-MCM-41(110°C) (Cal.)	36.77	42.5	975.0	27	0.631	15.45
Si-MCM-41(150°C) (As-syn.)*	31.98					
Si-MCM-41(150°C) (Cal.)	Amorphous		235	16, 31, 38	0.244	-
Si-MCM-41(150°C)-24h (As-syn.)**	37.86					
Si-MCM-41(150°C)-24h (Cal.)	36.12	41.71	778.2	26, 30	0.837	11.71

*Crystallization period = 96 h.

**Crystallization period = 24 h.

The sample Si-MCM-41(150°C) in its as-synthesized form shows a different XRD pattern (Fig. 2.2-b) with only two diffraction peaks, which matches that of a lamellar phase [3,28]. The higher angle peaks due to (110) and (200) reflections merge together forming one broad peak. On calcination, this sample becomes amorphous, the XRD pattern of which is featureless (Fig. 2.2-a). This is due to the instability of the sample at the high temperature (550°C), required for the removal of surfactant molecules present between the silicate sheets.

However, if the crystallization time is reduced to 24 h, a hexagonal mesophase is obtained. The XRD pattern of as-synthesized form of this sample shows all four peaks (Fig. 2.2-c). This phase remains stable after calcination (Fig. 2.2-d).

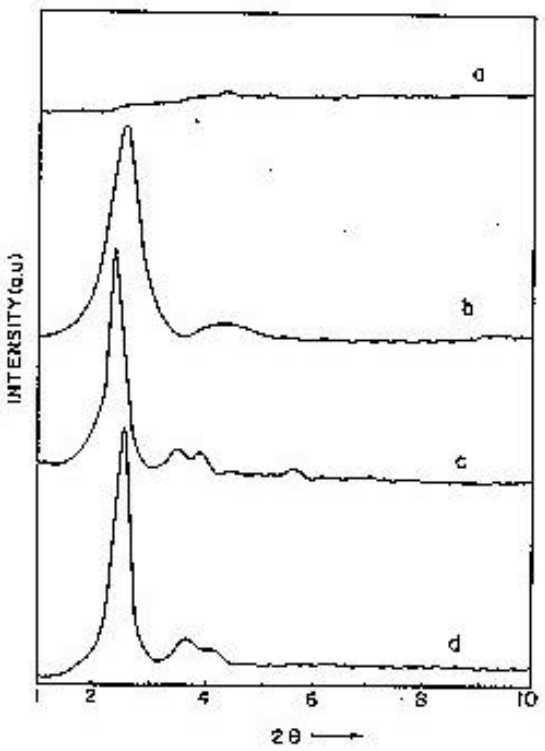

Fig. 2.2 XRD patterns of samples. (a) calcined Si-MCM-41(150°C)-96h; (b) as-syn. Si-MCM-41(150°C)-96h; (c) as-syn. Si-MCM-41(150°C)-24h and (d) calcined Si-MCM-41(150°C)-24h.

The samples synthesized at different temperatures have been characterized further by N_2-sorption studies (Fig. 2.3(A) and Fig. 2.3(B)). According to IUPAC classification, the isotherms of Si-MCM-41(50°C) and Si-MCM-41(110°C) are of type IV[29]. The isotherms exhibit three stages. The first stage is a linear part going through the origin, which is due to monolayer adsorption of nitrogen on the walls of the mesopores ($p/p_0 < 0.2$). The second stage is characterized by a steep increase in adsorption (within the relative pressure p/p_0 range of 0.15 - 0.35) due to capillary condensation in the mesopores. This part shows hysteresis.

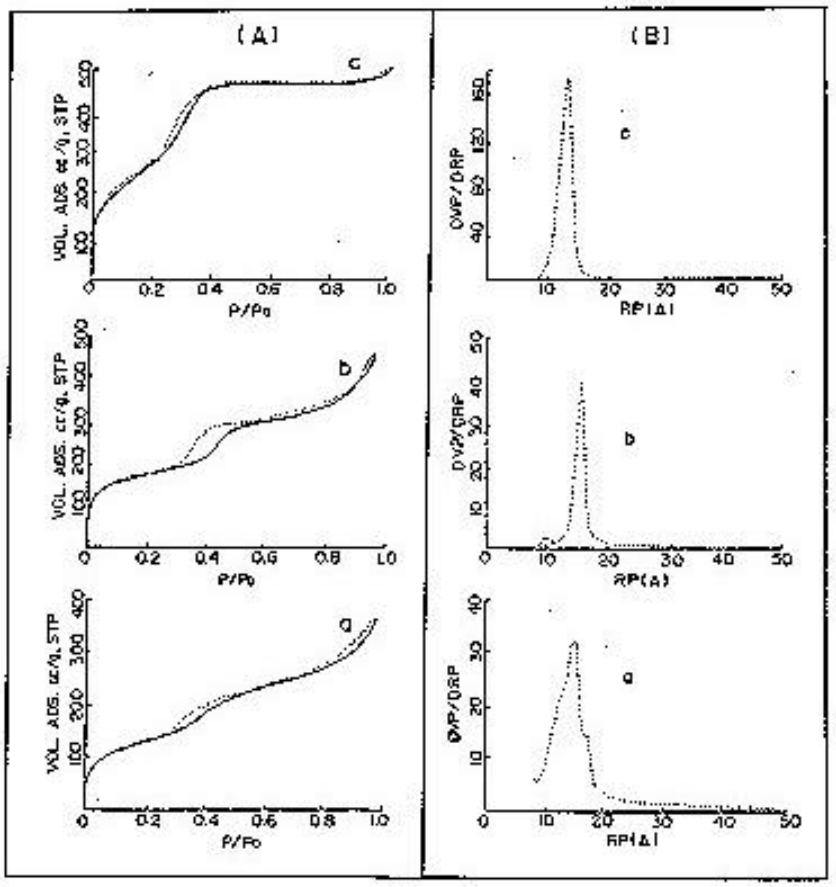

Fig. 2.3 (A) N_2 adsorption-desorption isotherms and (B) pore size distribution of (a) Si-MCM-41(RT); (b) Si-MCM-41(50°C) and (c) Si-MCM-41(110°C).

The p/p_0 value at which the inflection starts is related to the diameter of the mesopores. The sharpness in this step indicates the uniformity of the pore size distribution[30]. The third stage in the adsorption isotherm is an almost horizontal part after the relative pressure p/p_0 of ~0.35 and is due to multilayer adsorption on the outer surface of the particles[30]. In addition, a hysteresis loop at relative pressure $p/p_0 > 0.8$ corresponds to capillary condensation in the interparticle pores[24,29]. In the case of the RT-sample, there is a continuous, slow adsorption of nitrogen after the point of inflection (Fig. 2.3(A)-a) indicating a broad pore size distribution (Fig. 2.3(B)-a). For Samples Si-MCM-41(50°C) and Si-MCM-41(110°C), a linear increase in adsorption at low pressures is observed followed by a steep increase in nitrogen uptake (at a relative pressure of $p/p_0 = 0.31 - 0.41$ and 0.25-0.35 for Si-MCM-41(50°C) and Si-MCM-41(110°C), respectively) due to capillary condensation inside the mesopores (Fig. 2.3.(A)-b,c). The broad hysteresis loop in the isotherm for Si-MCM-41(50°C) reflects disorder in the shape and size of the mesopores. This step of the isotherm is sharper for Si-MCM-41(110°C) indicating a narrow pore size distribution. Thus, as the crystallization temperature increases from RT to 110°C, the step of the isotherm becomes sharper indicating narrower pore size distribution (Fig. 2.3(B)-a-c).

The N_2-adsorption-desorption isotherms and the pore size distribution of the Sample Si-MCM-41(150°C)-96h are presented in Fig. 2.4(A)-a and 2.4(B)-a, respectively. The hysteresis loop is found over a wide range of relative pressures, p/p_0 (0.28-1.00). The shape of the hysteresis loop confirms the formation of a lamellar phase[24,29,]. The pore size distribution becomes broader. However, when the crystallization time is reduced to 24 h (Si-MCM-41(150°C)-24h), a mesoporous phase is obtained (Fig. 2.4(A)-b and 2.4(B)-b). Thus, the XRD results are confirmed by N_2-adsorption-desorption data, which are similar to those reported for MCM-41[3].

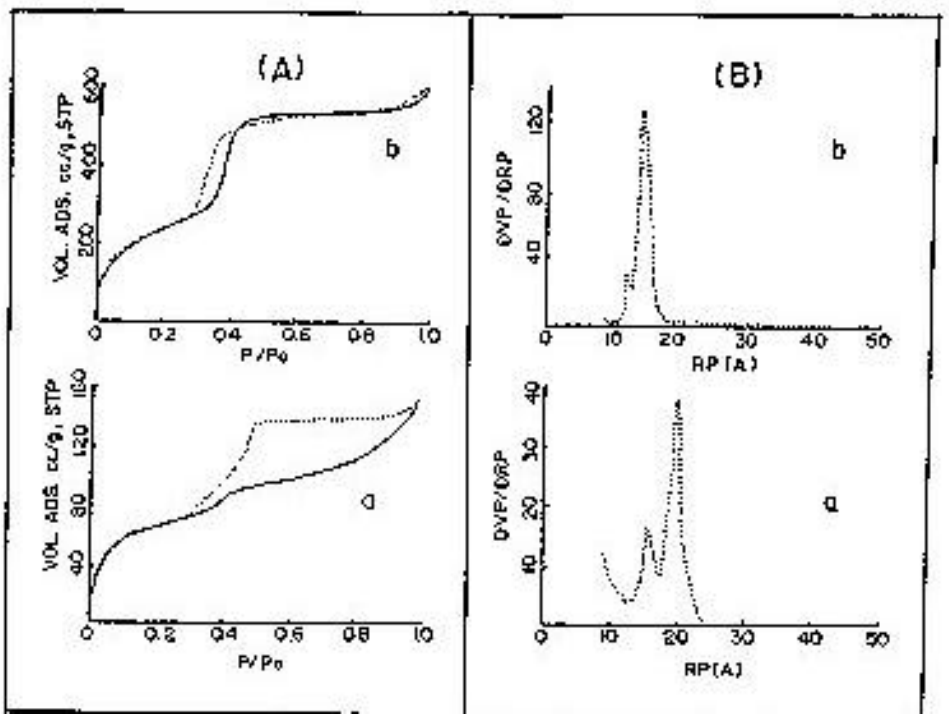

Fig. 2.4 (A) N_2 adsorption-desorption isotherms and (B) pore size distribution of (a) Si-MCM-41(150°C)-96h and (b) Si-MCM-41(150°C)-24h.

Table 2.2 presents a summary of all the parameters obtained by nitrogen sorption and X-ray diffraction. The unit cell parameter (the repeating distance between the pore centres (a_0)) has been calculated[3] by the formula $a_0 = 2d_{100}/\sqrt{3}$. The wall thickness has been calculated by subtracting the pore diameter obtained from N_2-sorption from the unit cell parameter $(a_0)^3$. The slight shift of the most intense peak to higher d_{100} spacing value and decrease in the pore diameter with increase in temperature of hydrothermal synthesis from RT to 110°C is due to increase in the wall thickness of the pores of MCM-41 molecular sieves[31].

The above results indicate that in hydrothermal synthesis of Si-MCM-41 molecular sieves, temperature plays a significant role. An increase of the crystallization temperature from RT to 110°C increases the long-range order in the structure as well as the wall thickness

of the MCM-41 molecular sieves. However, with further increase in the temperature to 150°C, the hexagonal phase changes to a lamellar one under the synthesis conditions.

2.2.2.1(ii) Effect of Crystallization Time

To optimize the crystallization time for the synthesis of Si-MCM-41, the gel was prepared as described in section 2.2.1.1(i), with the molar composition in terms of oxides as :

SiO_2 : 0.086 $(NH_4)_2O$: 0.089 $(CTMA)_2O$: 0.155 $(TMA)_2O$: 40 H_2O.

The gel obtained (pH = 11.2-11.5) was divided into six equal portions, transferred into six autoclaves and was crystallized at different crystallization times at 110°C which has been chosen as an optimum temperature for studying the effect of all the other parameters on synthesis. After the crystallization, the product was filtered, washed with deionized water and dried at 110°C for 5 h. The product was finally calcined at 550°C for 1 h in nitrogen and then for 6 h in air. The formation of the materials has been evaluated by x-ray diffraction and nitrogen sorption studies.

Fig. 2.5 shows the XRD patterns of the calcined samples autoclaved for 24h, 48h, 72h and 96h (designated as Si-MCM-41(24h), Si-MCM-41(48h), Si-MCM-41(72h) and Si-MCM-41(96h), respectively). The most intense peak with (100) reflection is shifted to a higher d_{100} value with increase in crystallization time upto 96h (Fig. 2.5-d). Between 96h and 120h, no significant difference is observed in the XRD patterns, suggesting that the hexagonal structure of the sample is not affected if the sample is crystallized upto 120h (5 days). However, if the crystallization time is increased upto 144h (6 days), the hexagonal phase transforms into the lamellar form which on calcination collapses and shows absence of XRD peaks (similar to Fig. 2.2-a).

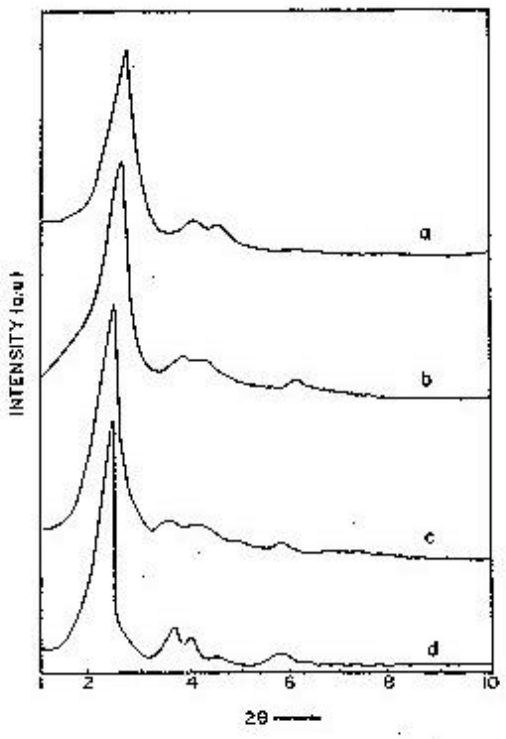

Fig. 2.5 XRD patterns of calcined samples: (a) Si-MCM-41(24h); (b) Si-MCM-41(48h); (c) Si-MCM-41(72h) and (d) Si-MCM-41(96h).

The samples synthesized at 110°C with different crystallization periods have been characterized further by N_2-sorption studies (Fig. 2.6(A) and Fig. 2.6(B)), which support the results obtained from XRD. Table 2.3 presents a summary of all the parameters obtained by nitrogen sorption and X-ray diffraction.

The isotherms are of type IV[29] as expected for MCM-41 molecular sieves[3]. With increase in crystallization time upto 96h, the step observed while filling the mesopores in the relative pressure p/p_0 = 0.25 - 0.4 becomes sharper (Fig. 2.6(A)). Si-MCM-41(24h) and Si-MCM-

41(48h) (figure not given) show a broad pore size distribution due to which it is difficult to determine the wall thickness of these samples.

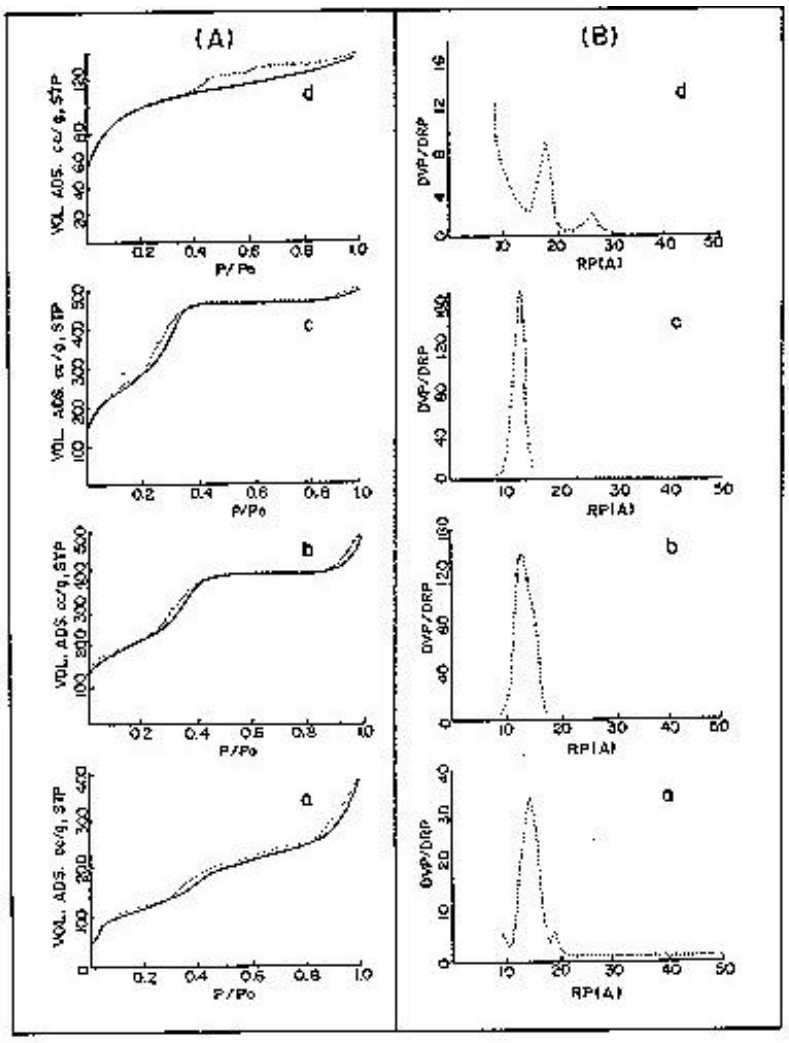

Fig. 2.6 (A) N_2 adsorption-desorption isotherms and (B) pore size distribution of (a) Si-MCM-41(24h); (b) Si-MCM-41(72h); (c) Si-MCM-41(96h) and (d) Si-MCM-41(120h).

Pores with narrow distribution start forming with further increase in crystallization time (Fig. 2.6(B)-b and c). The mean wall thickness of the pores and surface area increase with

crystallization time from 72h to 96h. However, there is a slight decrease in wall thickness at the crystallization time of 120h (Table 2.3).

Table 2.3 Data obtained from XRD and N_2-sorption studies[a]

Sample	D_{100}	Unit cell parameter (a_0)	S.A. (m^2/g)	Average pore diameter (Å)	Pore volume (ml/g)	Average wall thickness (Å)
Si-MCM-41(24h) (As-syn.)	36.78					
Si-MCM-41(24h) (Cal.)	32.22	37.20	433	Between 20-40 (broad)	0.514	-
Si-MCM-41(48h) (As-syn.)	37.72					
Si-MCM-41(48h) (Cal.)	33.95	39.20	551.4	Between 24-36 (broad)	0.593	-
Si-MCM-41(72h) (As-syn.)	38.00					
Si-MCM-41(72h) (Cal.)	35.31	40.77	765.5	30	1.059	10.77
Si-MCM-41(96h) (As-syn.)	38.37					
Si-MCM-41(96h) (Cal.)	36.77	42.46	975.0	27	0.631	15.45
Si-MCM-41(120h) (As-syn.)	38.60					
Si-MCM-41(120h) (Cal.)	36.46	42.10	988.7	27	0.583	15.10
Si-MCM-41(144h) (As-syn.)	33.69					
Si-MCM-41(144h) (Cal.)	Amorphous		337.9	23, 52	0.111	-

[a]Crystallization Temperature = 110°C

However, at longer crystallization time, the hexagonal phase starts transforming to lamellar phase with lack of specific structural features (Fig. 2.6(A)-d and Fig. 2.6(B)-d), showing a sharp reduction in the surface area and pore volume (Table 2.3).

2.2.2.1(iii) Effect of Water Content

Studies were carried out by changing the water content in the synthesis gel prepared by using the procedure of section 2.2.1.1(i). The molar composition of the synthesis gel in terms of oxides was kept the same in all batches, except the water content (gel composition: SiO_2 : 0.086 $(NH_4)_2O$: 0.089 $(CTMA)_2O$: 0.155 $(TMA)_2O$: x H_2O; $20 \leq x \leq 60$.

In the present work, water content with respect to SiO_2 is expressed as H_2O/SiO_2 ratio. Three different samples were prepared from gels with H_2O/SiO_2 of 20, 40 and 60, the samples being designated as Si-MCM-41(20), Si-MCM-41(40) and Si-MCM-41(60), respectively. When the H_2O/SiO_2 ratio was 10 or less than 10, the water content was found to be insufficient to obtain a homogeneous gel and hence crystallization was not attempted.

Samples with almost similar average pore diameters and surface areas could be obtained by varying the crystallization time (from 72-120h) from reaction mixtures with different H_2O/SiO_2 ratios (surface areas of Si-MCM-41(20), Si-MCM-41(40) and Si-MCM-41(60) are 930, 975 and 990 m^2/g, respectively with a nearly same average pore size of ~ 27Å). The XRD patterns of all the three samples revealed the formation of hexagonal materials. Apparently, dilution of the gel did not affect the formation of hexagonal MCM-41 structure (which is mainly determined by the strong electrostatic interaction between the cationic surfactant and anionic silicate species[32]), though it affected the rate of crystallization significantly. More the water content in the gel, longer is the crystallization time required for synthesis. When the H_2O/SiO_2 ratio is increased from 20 to 60 (from Si-MCM-41(20) to

Si-MCM-41(60)), the crystallization time increases from 72 to 120h to obtain a material with similar pore size and surface area.

Scanning electron microscope was used to determine the particle size and morphology of the samples prepared with different water contents. Fig. 2.7 (a-c) presents scanning electron micrographs (SEM) (scanned under identical magnification) of the as-synthesized samples of Si-MCM-41(20), Si-MCM-41(40) and Si-MCM-41(60)), respectively.

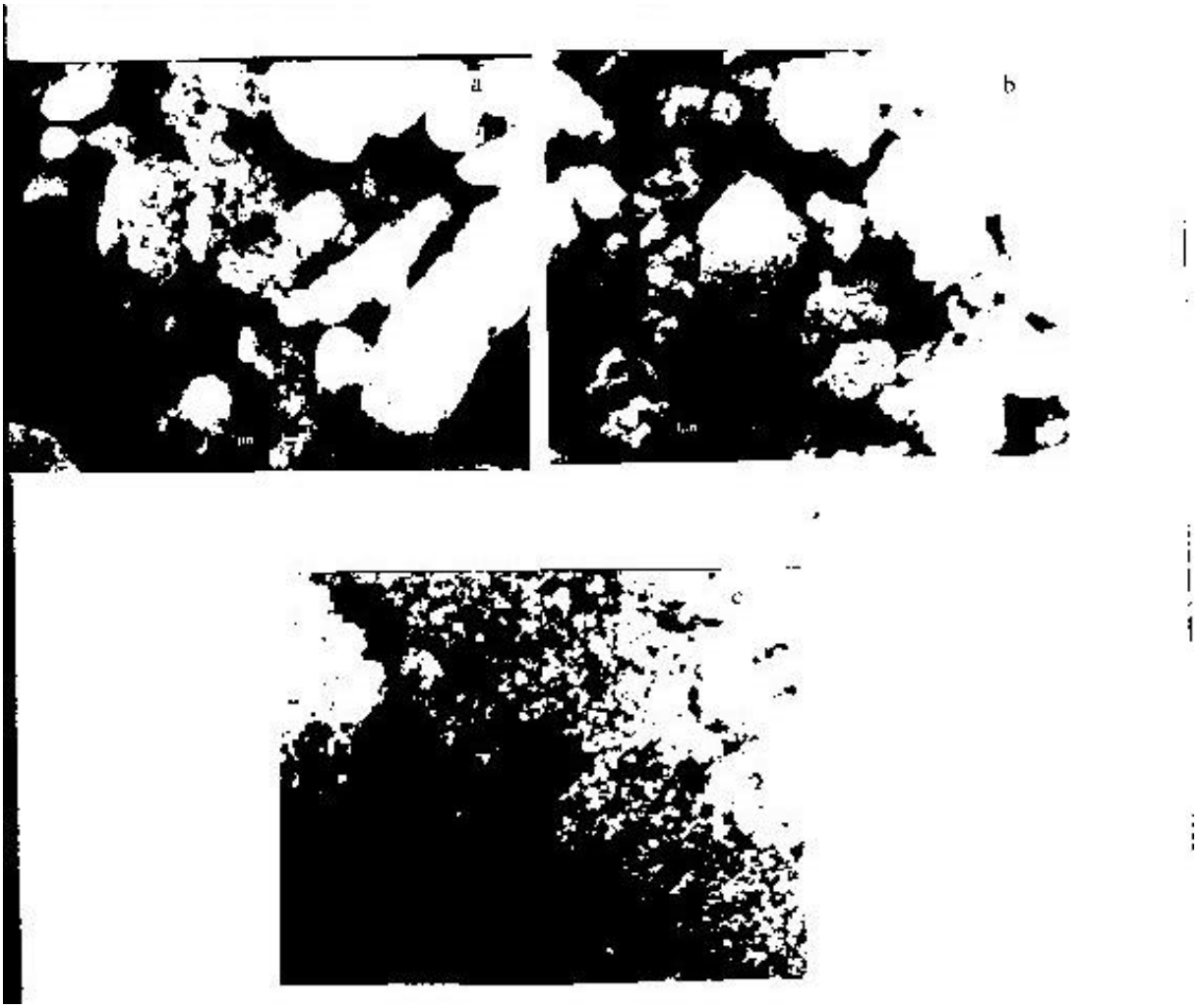

Fig. 2.7 Scanning electron micrographs of samples (a) Si-MCM-41(20); (b) Si-MCM-41(40) and (c) Si-MCM-41(60).

It is seen that there is no specific change in the morphology of the material with change in the water content in the range selected for the present study (H_2O/SiO_2 ratio: 20-60). Micrographs of Si-MCM-41(20) and Si-MCM-41(40) reveal that aggregates of particles (~ 0.1μm – 0.3 μm) with irregular shapes are formed. Si-MCM-41(20) shows indication of some amorphous material, which may be due to lack of homogeneity of the gel having limited quantity of water. In the case of the sample Si-MCM-41(40), individual particles become visible in the aggregates. It is observed that the separation of microcrystalline particles increases with increase in the water content (Fig. 2.7 (a-c)).

2.2.2.1 (iv) Effect of pH

The effect of pH on the formation of MCM-41 was studied by hydrothermal synthesis of a gel with the molar composition in terms of oxides as:

SiO_2 : 0.086 $(NH_4)_2O$: 0.089 $(CTMA)_2O$: 0.155 $(TMA)_2O$: 40 H_2O.

The synthesis gel was obtained by the procedure as described in section 2.2.1.1(i). Four samples were synthesized and designated as Si-MCM-41(pH-8), Si-MCM-41(pH-10), Si-MCM-41(pH-11.5) and Si-MCM-41(pH-12), by varying the pH of the gel, 8, 10, 11.5 and ~ 12, respectively. The pH of the reaction mixture was adjusted to the desired value by addition of dilute sulphuric acid.

Fig. 2.8(a-d) shows the XRD patterns of the calcined Si-MCM-41 type materials prepared from gels of different pH. The d-spacing increases with increase in pH, the d_{100} value being 35.03 Å for Si-MCM-41(pH-8) and 36.78 Å for Si-MCM-41(pH-11.5).

The Si-MCM-41(pH-12) sample in its as-synthesized form shows an XRD pattern with only two diffraction peaks which matches that of a lamellar phase (Fig. 2.8(d))[28]. The higher angle peaks merge with each other forming a broad peak. The d_{100} value (lower angle peak) of the as-synthesized material is slightly smaller than that of the as-synthesized form of

Si-MCM-41(pH-8). On calcination, this sample becomes amorphous as it is unstable at the high temperature (550°C).

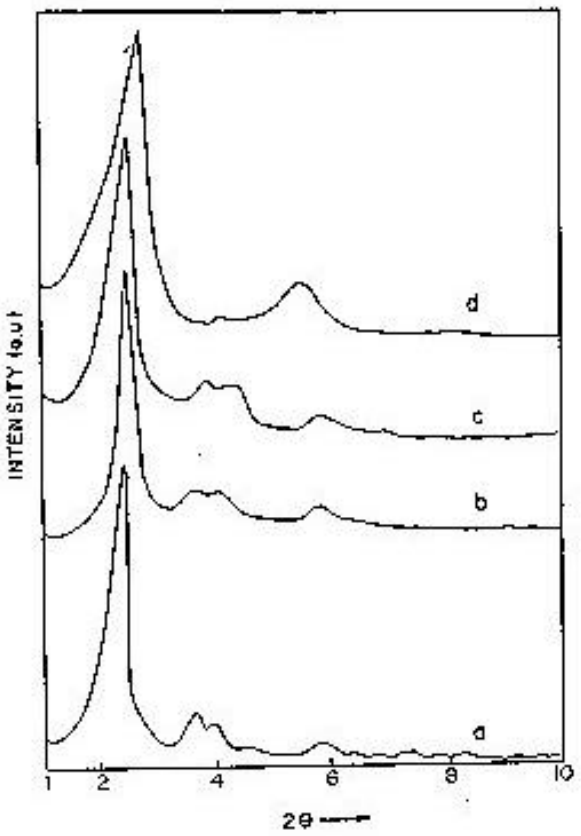

Fig. 2.8 XRD patterns of calcined samples. (a) Si-MCM-41(pH-11.5); (b) Si-MCM-41(pH-10); (c) Si-MCM-41(pH-8) and (d) Si-MCM-41(pH-12).

The samples synthesized with different pH have been characterized further by N_2-sorption studies (Fig. 2.9(A) and Fig. 2.9(B)). The isotherms of the three materials, Si-MCM-41(pH-8), Si-MCM-41(pH-10) and Si-MCM-41(pH-11.5) are of type IV[29] exhibiting the three stages due to monolayer adsorption ($p/p_0 < 0.2$), capillary condensation (p/p_0 0.15-0.75) and multilayer adsorption ($p/p_0 > 0.8$) as discussed earlier. In addition, a hysteresis loop in the range of relative pressure $p/p_0 > 0.8$ corresponds to capillary condensation in the interparticle pores[24,29].

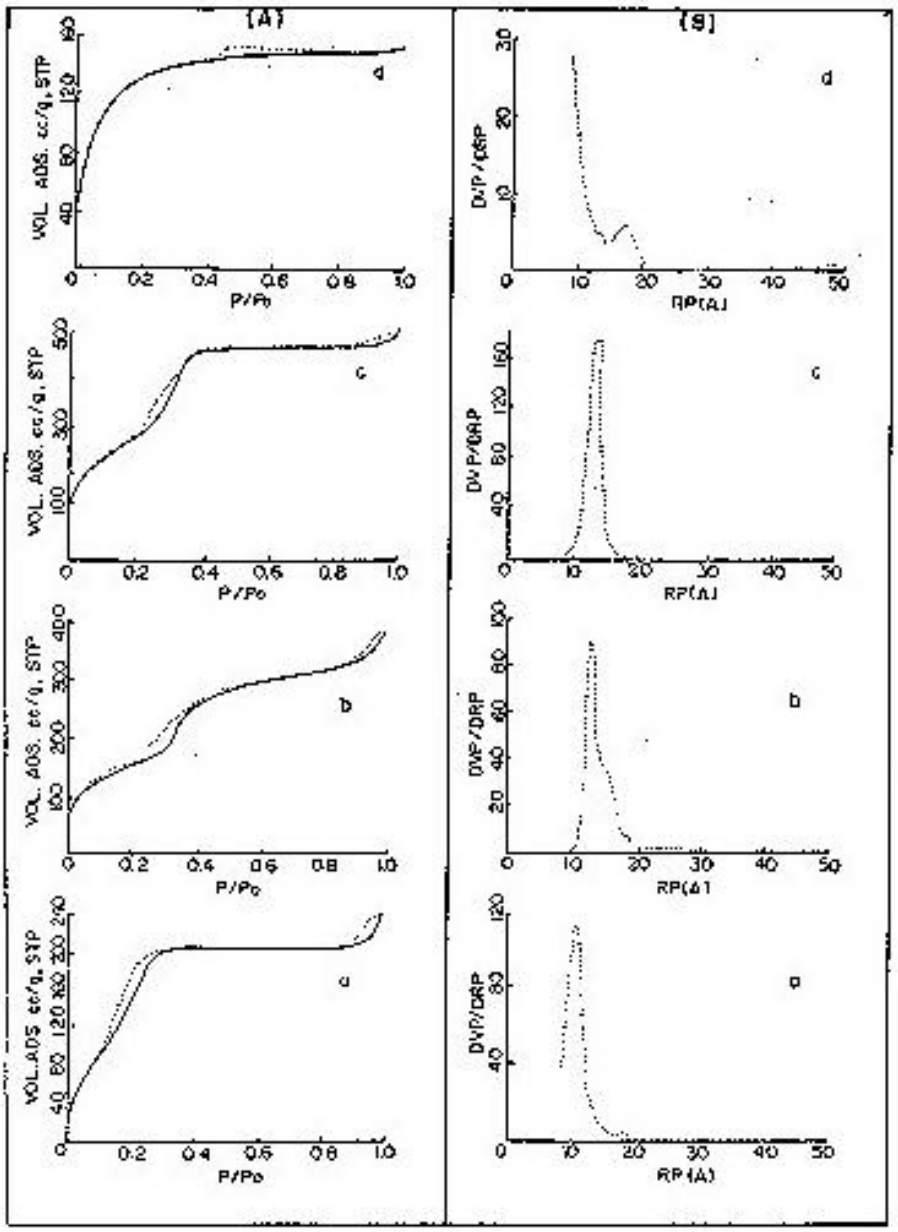

Fig. 2.9 (A) N_2 adsorption-desorption isotherms and (B) pore size distribution of (a) Si-MCM-41(pH-8); (b) Si-MCM-41(pH-10); (c) Si-MCM-41(pH-11.5) and (d) Si-MCM-41(pH-12).

In the case of Si-MCM-41(pH-8) a steep increase in nitrogen uptake due to capillary condensation is observed in p/p_0 range of 0.12-0.25 (Fig. 2.9A)-a), indicating the presence of mesopores with relatively smaller pore diameter. The pore size obtained by the BJH model was found to be of 20-22Å (Fig. 2.9(B)-a). As the pH of the gel is increased further upto

11.5, the steep increase in nitrogen uptake due to capillary condensation is shifted higher p/p_0 values. For Si-MCM-41(pH-10) and Si-MCM-41(pH-11.5), capillary condensation occurs in the p/p_0 ranges of 0.23 - 0.32 and 0.25 - 0.35, respectively (Fig. 2.9(A)-b and c). Accordingly, the mesopores are in the range of 22-24Å and 25-27Å for Si-MCM-41(pH-10) and Si-MCM-41(pH-11.5), respectively (Fig. 2.9(B)-b and c).

The N_2-adsorption-desorption isotherm and the pore size distribution of the sample Si-MCM-41(pH-12) are presented in Fig. 2.9(A)-d and 2.9(B)-d, respectively. The hysteresis loop is found to span a broad range of relative pressures (p/p_0 ~3.7 to ~1.0). The shape of the hysteresis loop confirms the formation of a lamellar phase[24,27]. The pore size distribution becomes wide in the range 16Å-50Å and the BET surface area and pore volume decrease drastically. Table 2.4 presents a summary of all the parameters obtained by nitrogen sorption and X-ray diffraction.

Table 2.4 Data obtained from XRD and N_2-sorption studies

Sample	**d_{100}**	**Unit Cell parameter (a_0)**	**S.A. (m^2/g)**	**Average pore diameter (Å)**	**Pore volume (ml/g)**	**Average wall thickness (Å)**
Si-MCM-41(pH-8) (As-syn.)	37.40	-	-	-	-	-
Si-MCM-41(pH-8) (Cal.)	35.03	40.44	712.5	22	0.458	18.44
Si-MCM-41(pH-10) (As-syn.)	38.38	-	-	-	-	-
Si-MCM-41(pH-10) (Cal.)	36.18	41.77	800.0	25	0.520	16.77
Si-MCM-41(pH-11.5) (As-syn.)	38.37	-	-	-	-	-
Si-MCM-41(pH-11.5) (Cal.)	36.78	42.46	975.0	27	0.631	15.46
Si-MCM-41(pH-12) (As-syn.)	-	-	-	-	-	-
Si-MCM-41(pH-12) (Cal.)	Amorphous		455.4	16, 32 (wide)	0.101	-

It is observed that the surface area, the pore diameter as well as the pore volume of the molecular sieves increases with increase in the pH of the synthesis gel from 8 to 11.5. As the pH increases, the nucleation rate becomes higher forming smaller particles and higher surface area[33]. The observed increase in the pore size with pH depends on two factors, (a) polycondensation of silica species and (b) conformation of the surfactant[34,35]. At high pH, solubility of silica increases rapidly due to which a higher amount of silica is left in the solution at the end of the synthesis[36]. This results in a thinner coating of silica around the surfactant micelle and hence a decrease in the wall thickness (Table 2.4).

2.2.2.2 Effect of the Alkyl Chain Length

The effect of alkyl chain length on the formation of MCM-41 was studied by synthesizing two samples using two surfactant molecules with different carbon chain lengths *viz.*, DTMABr ($C_{12}H_{24}N(CH_3)_3Br$) and CTMACl/OH ($C_{16}H_{33}N(CH_3)_3Cl/OH$). The gel was synthesized by the procedure described in section 2.2.1.1(i). The molar composition of the gel in terms of oxides was as:

$SiO_2 : 0.086\ (NH_4)_2O : 0.089\ (x)_2O : 0.155\ (TMA)_2O : 40\ H_2O;$

where $x = C_{12}H_{24}N^+(CH_3)_3$ *or* $C_{16}H_{33}N^+(CH_3)_3$.

Fig. 2.10 (a and b) shows the XRD patterns of the samples prepared using DTMABr and CTMACl/OH which are designated as Si-MCM-41-D and Si-MCM-41-C, respectively. As the alkyl chain length increases, the d_{100} value also increases (36.33 Å for Si-MCM-41-D and 42.46 Å for Si-MCM-41-C). Besides, the (100) reflection is broader for Si-MCM-41-D than for Si-MCM-41-C (Fig. 2.10-a and b, respectively).

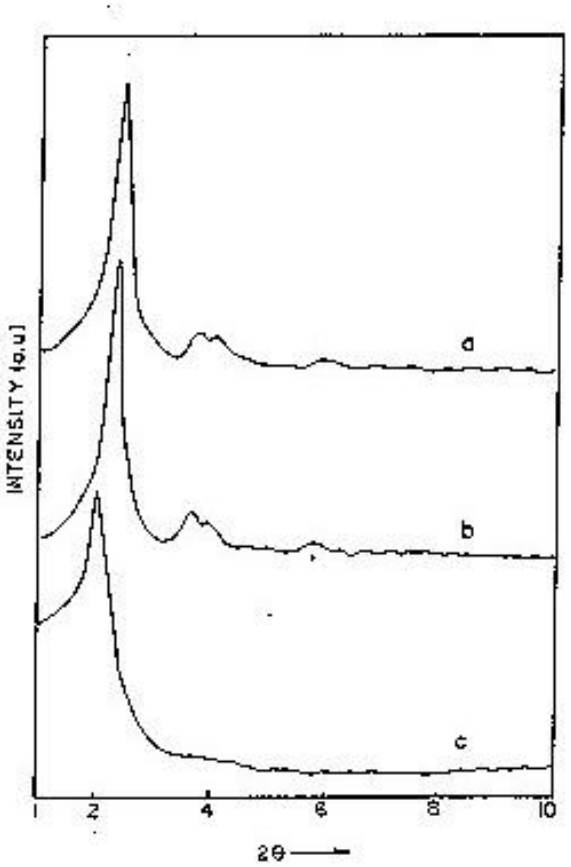

Fig. 2.10 XRD patterns of calcined samples. (a) Si-MCM-41-D; (b) Si-MCM-41-C and (c) Si-MCM-41(MES).

Fig. 2.11(A)-a and b and Fig. 2.11(B)-a and b present the N_2 adsorption-desorption isotherms and the pore size distributions of Si-MCM-41-D and Si-MCM-41-C, respectively. These isotherms also are of type IV[29] and exhibit the three stages already discussed. The second step which characterizes the mesopores in MCM-41 type materials occurs in the p/p_0 range of 0.13-0.23 for Si-MCM-41-D and 0.25-0.35 for Si-MCM-41-C. In addition, a hysteresis loop in the range of relative pressure $p/p_0 > 0.8$ corresponds to capillary condensation within the interparticle mesoporosities[24,29]. This hysteresis loop, observed in the case of Si-MCM-41-C is very small in the relative pressure p/p_0 (0.85 - 1), while in case

of Si-MCM-41-D, it is observed in a wide range of p/p_0 (0.4 – 1) (Fig. 2.11(A)-b and a, respectively).

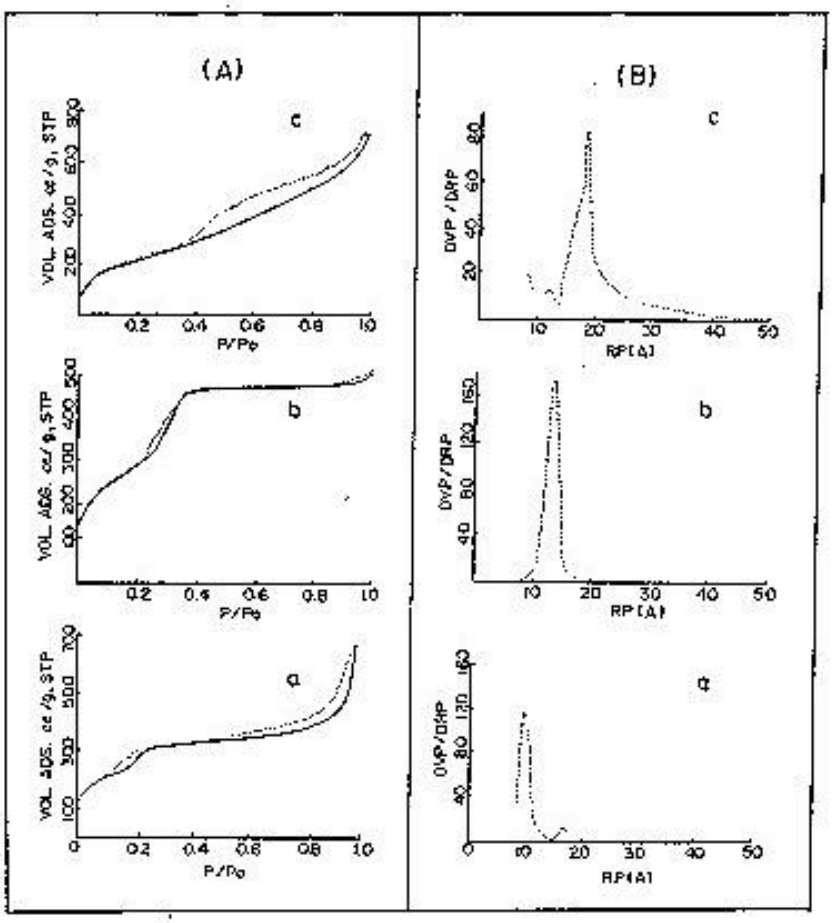

Fig. 2.11 (A) N_2 adsorption-desorption isotherms and (B) pore size distribution of (a) Si-MCM-41-D; (b) Si-MCM-41-C and (c) Si-MCM-41(MES).

A comparison of the hysteresis loops of these two samples in the higher relative pressure region indicates that these two materials differ greatly in textural mesoporosity. This suggests that the interparticle distance in Si-MCM-41-D is larger than those in Si-MCM-41-C. Due to the presence of these bigger interparticle voids, the pore distribution in Si-MCM-41-D is found to be bimodal (Fig. 2.11(B)-a).

2.2.2.3 Effect of the Addition of an Auxiliary Organic

The effect of addition of an auxiliary organic compound on the formation of MCM-41 was studied by adding mesitylene into the gel prepared with the molar composition in terms of oxides as:

SiO_2 : 0.086 $(NH_4)_2O$: 0.089 $(CTMA)_2O$: 0.155 $(TMA)_2O$: MES : 40 H_2O.

The gel was prepared by the same procedure as described in section 2.2.1.1(i) (pH = 11.2-11.5), except that mesitylene (18.28 g) was added at the end and the gel was then transferred to a stainless steel autoclave and heated in an oven at 110°C for 2 days for crystallization. After the crystallization, the product was filtered, washed with deionized water and dried at 100°C for 5 h. The product (designated as Si-MCM-41(MES)) was finally calcined at 540°C for 1 h in nitrogen and then for 6 h in air.

The X-ray diffraction pattern of calcined Si-MCM-41(MES) is shown in Fig. 2.10(c). The pattern exhibits a broad (100) peak spacing (d_{100}) of about 42.85 Å. The shift of the (100) peak to a higher d spacing (compared to Si-MCM-41-C) suggests an increase in pore size by the addition of mesitylene. Only one single peak is obtained indicating structural disorder caused probably by the swelling of micelles. The large scattering at lower angles also suggests the presence of amorphous material in the sample.

Fig. 2.11(A)-c and 2.11(B)-c present the N_2 adsorption- desorption isotherms and the pore size distribution, respectively, of Si-MCM-41(MES). The mesopore filling starts at a higher relative pressure (p/p_0 ~0.35 to ~1.0). The adsorption isotherm shows a change in the shape of the inflection step. It is not as sharp as in case of Si-MCM-41-C (Fig. 2.11(A)-b). The broad hysteresis observed in the isotherm indicates the presence of a broad distribution of pore sizes (Fig. 2.11(B)-c). The maximum number of pores are in the diameter range of 36-38Å. The lower surface area of the sample may be due to the presence of less ordered pores

and the presence of amorphous material. The results obtained for Sample-MES match well those reported in the literature[3, 37].

In aqueous solutions, the critical micellar concentration (cmc), which is the concentration above which monomers spontaneously self-assemble into micelles is a significant parameter for self aggregation of surfactants. The driving force for micellar formation is the transfer of the hydrophobic surfactant chain from water into the nonpolar core of micelles. This force is opposed by steric, polar and electric interactions between the surfactant head groups[38]. The balance between these forces can be accounted for by a molecular packing ratio, R[38,39], which is defined as

$R = V/la,$

where V is the topographic volume of hydrocarbon chain, a = effective area of the surfactant head group and l = effective length of the surfactant chain.

In micellar aqueous solutions hydrophobic molecules like mesitylene which are insoluble in water are solubilized in the interior hydrophobic environment of alkyl chains of the micelles due to the large reduction in the interfacial energy[39]. Solubilization of mesitylene increases the volume (V) of the hydrocarbon chain considerably and hence the packing ratio (R) increases significantly. Consequently, a transition into longer, cylindrical micelles results[38].

2.2.2.4 Effect of Acid and Neutral Medium on Synthesis

Samples were synthesized in acid and neutral medium according to the procedure described in section 2.2.1.2 and 2.2.1.3, respectively and designated as Si-MCM-41(ac) and Sample- HMS, respectively. The x-ray diffraction patterns of Si-MCM-41(ac) and Sample-HMS are shown in Fig. 2.12 (a and b, respectively). The XRD pattern of Si-MCM-41-C is presented in the Fig. 2.12(c). The XRD pattern of calcined Sample-HMS (Fig. 2.12(a)

exhibits a single broad diffraction peak corresponding to a d spacing of about 32.70 Å matching the reported values[17,22]. The single XRD reflection in Sample-HMS has been explained on the basis of control of the formation of these hexagonal materials by weak, nonionic interactions such as hydrogen bonding between the self assembled neutral primary amine micelles (S^0) and neutral inorganic precursors (I^0)[23].

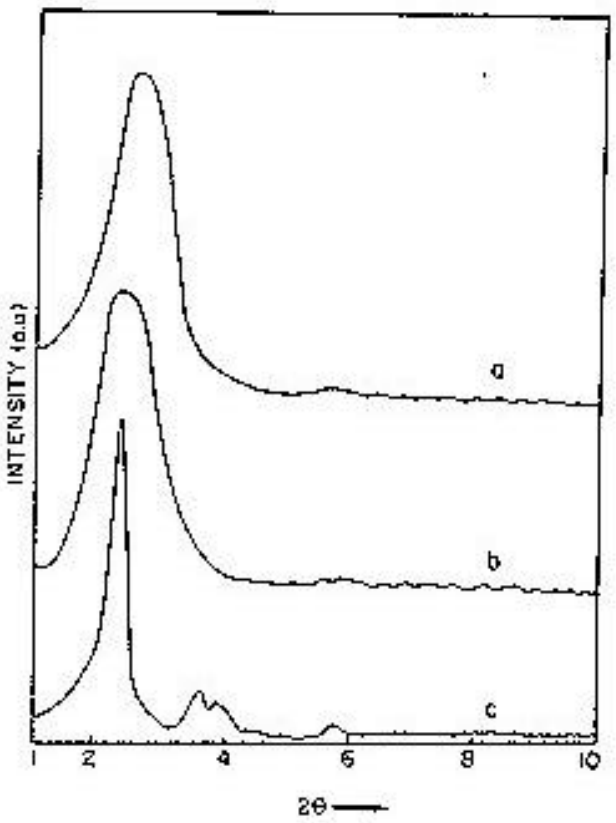

Fig. 2.12 XRD patterns of calcined samples. (a) Sample-HMS; (b) Si-MCM-41(ac) and (c) Si-MCM-41-C.

Similarly, Si-MCM-41(ac) (Fig. 2.12(b)) does not show the (110), (200) and (210) reflections but only one broad (100) reflection which is almost similar to that of HMS. However, this pattern does not match that reported for the MCM-41 sample synthesized by Tanev *et al.*[23] in acid medium.

Fig. 2.13(A)-a and b and Fig. 2.13(B)-a and b present the N_2 adsorption-desorption isotherms and the pore size distribution of Sample-HMS and Si-MCM-41(ac), respectively. The isotherms of both the samples appear nearly similar. The isotherms are of type IV[29] as expected for mesoporous molecular sieves. However, the steep increase in the second stage in adsorption due to capillary condensation in mesopores is not sharp (Fig. 2.13(A) a and b) as in case of the sample synthesized in alkali medium (Si-MCM-41-C; Fig. 2.13(A)-c). Accordingly, the pore size distribution in these samples (Sample-HMS and Si-MCM-41(ac)) is broad (Fig. 2.13(B) a and b) compared to that of Si-MCM-41-C (Fig. 2.13(B)-c).

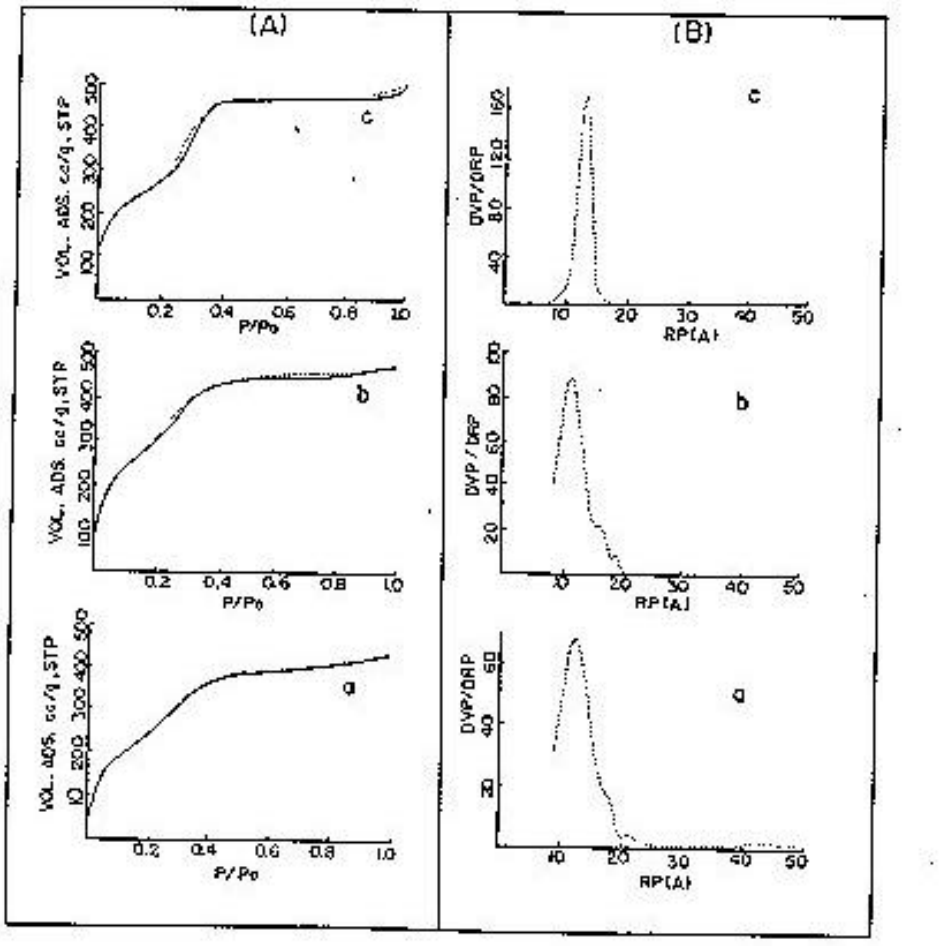

Fig. 2.13 (A) N_2 adsorption-desorption isotherms and (B) pore size distribution of (a) Sample-HMS; (b) Si-MCM-41(ac) and (c) Si-MCM-41-C.

2.3 PART-II: MODIFICATION OF MCM-41

This part describes the synthesis procedures used for modification of MCM-41 by introducing heteroatoms such as aluminium, tin and zirconium into the structure. Other modifications of Si-MCM-41 made by impregnation with Sn and Zr, and Al-MCM-41 by impregnation with Pt are also described.

2.3.1 Synthesis of Al-MCM-41

Al-MCM-41 samples were prepared hydrothermally using a gel with the following molar compositions in terms of oxides:

SiO_2 : x Al_2O_3 : 0.27 $(CTMA)_2O$: 0.13 $(TMA)_2O$: x Na_2O : 60 H_2O;

where $x \leq 0.04$.

The preparation procedure was similar to that of Si-MCM-41 described in section 2.2..1.1(iii), except that sodium hydroxide (0.035 g for Si/Al = 25) dissolved in 8 g water was added to the mixture of sodium silicate and TMAOH and a calculated quantity of $Al_2(SO_4)_3$.18 H_2O (2.52 g for Si/Al = 25) dissolved in 30 g water was added to the final gel, and stirred well. The gel was crystallized as described earlier (110°C for 5 days). Four samples with different Si/Al input ratios of 100, 50, 25 and 12.5 were synthesized. All the samples were calcined at 550°C in nitrogen for 1 h and then in air for 6 h.

The samples synthesized above were characterized by XRD, MAS NMR and adsorption studies. The calcined samples were converted into the catalytically active H-forms by cation exchanging with ammonium nitrate thrice (20 ml of 1M solution/g of the molecular sieve at 95°C for 5 h), dried at room temperature and then calcined at 400°C for 6 h.

2.3.2 Impregnation of Pt on Al-MCM-41

The platinum loading of H-Al-MCM-41 samples was carried out by impregnation with tetraamine platinum (II) nitrate (Aldrich, 99%) to get different Pt loadings (0.1 to 0.5 wt.%). A known quantity of H-Al-MCM-41 sample was added to an aqueous solution of tetraamine platinum (II) nitrate to obtain the desired weight loading. After impregnation, the materials were dried in air at 110°C for 4 h and calcined at 400°C for 3 h in air and reduced at 400°C for 4 h in hydrogen.

2.3.3 Synthesis of Sn-MCM-41

2.3.3(i) Using CTMACl/OH

The molar composition of the synthesis gel in terms of oxides was as follows:

SiO_2 : 0.02 SnO_2: 0.089 $(CTMA)_2O$: 0.155 $(TMA)_2O$: 40 H_2O.

In a typical synthesis, 0.52 g $SnCl_4.5H_2O$ (for Si/Sn = 50) was dissolved in 15 g water and added to 16.7 g of 24.6 % solution of CTMACl/OH with stirring. To this stirred mixture, 2.08 g TMAOH dissolved in 10 g water and 13.6 g TMA silicate were added. The solution was stirred further for 15 minutes. 3.1 g fumed silica was then added slowly in about 10 minutes to the above solution under stirring and the stirring was continued for 1 h after completion of addition. The mixture was then transferred to a stainless steel autoclave and heated at 110°C for 5 days. The solid material was filtered, washed with deionized water and dried at 100°C in air. The product was calcined at 550°C in flowing nitrogen (for 3 h) and in flowing air (for 6 h) to remove the organic material. Four samples containing different Sn contents with Si/Sn input ratios as 200, 150, 100 and 75 were prepared following the general synthesis procedure described above using different quantities of tin tetrachloride ($SnCl_4.5H_2O$).

2.3.3(ii) Using DTMABr

The molar composition of the synthesis gel in terms of oxides was as follows:

SiO_2 : 0.02 SnO_2: 0.089 $(DTMA)_2O$: 0.155 $(TMA)_2O$: 40 H_2O.

In a typical synthesis, 0.52 g $SnCl_4.5H_2O$ (for Si/Sn = 50) was dissolved in 15 g water and added to 4.043 g of DTMABr dissolved in 12.5 g water with stirring. To this stirred mixture, 2.08 g TMAOH dissolved in 10 g water and 13.6 g TMA silicate were added. The solution was stirred further for 15 minutes. 3.1 g fumed silica was then added slowly in about 10 minutes to the above solution under stirring and the stirring was continued for 1 h after completion of addition. The mixture was then transferred to a stainless steel autoclave and heated at 110°C for 5 days. The solid material was filtered, washed with deionized water and dried at 100°C in air. The product was calcined at 550°C in flowing nitrogen (for 3 h) and in flowing air (for 6 h) to remove the organic material. Four samples with Si/Sn input ratios as 200, 150, 100 and 75 were prepared following the general synthesis procedure described above using different quantities of tin tetrachloride ($SnCl_4.5H_2O$).

2.3.3(iii) Synthesis of Sn-silica gel

Sn-silica gel was prepared for comparison of its catalytic activity with Sn-MCM-41 samples. The synthesis of Sn-silica gel (Si/Sn = 50) was done by adding 1.55 g fumed silica to 6.8 g TMA silicate solution with stirring and 0.26 g $SnCl_4.5H_2O$ dissolved in 15.0 g water was added to the above silica gel and stirred for some time. The gel obtained was then dried at 550°C for 6 h

2.3.3(iv) Synthesis of Sn-impregnated MCM-41

One g of calcined dry Si-MCM-41 was added to a solution of 0.123 g $SnCl_4.5H_2O$ in 5.0 g water to obtain Si/Sn = 50. The mixture was then heated on a water bath with frequent stirring till it became dry. The impregnated sample was calcined at 400°C.

2.3.4 Synthesis of Zr-MCM-41

2.3.4 (i) Using CTMACl/OH

The molar compositions of the synthesis gels in terms of oxides were as follows:

SiO_2 : 0-0.02 ZrO_2 : 0.089 $(CTMA)_2O$: 0.155 $(TMA)_2O$: 18 H_2O.

The synthesis of Zr-MCM-41 was carried out in a manner similar to that of Si-MCM-41 as described in section 2.2.1.1(i), except that the required amount of Zr butoxide (0.71 g for Si/Zr = 50, 80 wt.% solution in 1-butanol) dissolved in 5 g isopropanol was added to the final gel and stirred well. The gel was crystallized at 110°C for 5 days and the solid material separated washed and calcined as in the case of Si-MCM-41. Four samples containing different Zr contents (Si/Zr input ratio = 100, 50, 25 and 12.5) were prepared using different quantities of zirconium butoxide [$Zr(O(CH_2)_3CH_3)_4$].

2.3.4(ii) Using DTMABr

The molar compositions of the synthesis gels in terms of oxides were as follows:

SiO_2 : 0-0.02 ZrO_2 : 0.089 $(DTMA)_2O$: 0.155 $(TMA)_2O$: 18 H_2O.

The synthesis of Zr-MCM-41 was carried out in a manner similar to that of Si-MCM-41 as described in section 2.2.1.1(ii), except that the required amount of 0.71 g Zr butoxide for Si/Zr = 50, 80 wt.% solution in 1-butanol) dissolved in 5 g isopropanol was added to the final gel and stirred well. The gel was crystallized at 110°C for 5 days and the solid material separated was washed, dried and calcined as in the case of Si-MCM-41. A total of four samples containing different Zr contents (Si/Zr input ratio = 100, 50, 25 and 12.5) were prepared using different quantities of zirconium butoxide [$Zr(O(CH_2)_3CH_3)_4$].

2.3.4(iii) Synthesis of Zr-impregnated MCM-41

One g calcined dry Si-MCM-41 was added to get a solution of 0.16 g zirconium butoxide in 5-6 g isopropanol to obtain Si/Zr = 25. The mixture was then heated on a water bath with frequent stirring till it became dry. The impregnated sample was dried at 400°C.

2.4 REFERENCES

1. Kresge, C.T., Leonowicz, M.E., Roth, W.J., and Vartuli, J.C., *U.S. Patent*, 5,098,684 (1992).
2. Kresge, C.T., Leonowicz, M.E., Roth, W.J., Vartuli, J.C., and Beck, J.S., *Nature*, **359** (1992) 710.
3. Beck, J.S., Vartuli, J.C., Roth, W.J., Leonowicz, M.E., Kresge, C.T., Schmitt, K.D., Chu, C.T-W., Olson, D.H., Sheppard, E.W., McCullen, S.B., Higgins, J.B., and Schlenker, J.L., *J. Am. Chem. Soc.*, **114** (1992) 10834.
4. Huo, Q., Margolese, D.I., Ciesla, U., Demuth, D.G., Feng, P., Gier, T.E., Sieger, P., Firouzi, A., Chmelka, B.F., Schüth, F., and Stucky, G.D., *Chem. Mater*., **6** (1994) 1176.
5. Stucky, G.D., Monnier, A., Schüth, F., Huo, Q., Margolese, D.I., Kumar, D., Krishnamurthy M., Petroff, P., Firouzi, A., Janicke, M., and Chmelka, B.F., *Mol. Cryst. Liq. Cryst.*, **240** (1994) 187.
6. Schimdt, R., Akporiaye, D., Stöcker, M., and Ellestad, O.H., *J. Chem., Soc., Chem. Commun.*, (1994) 1493.
7. Zhao, D., and Goldfarb, D., *J. Chem. Soc., Chem. Commun.* (1995) 875.
8. Koyoano, K.A., and Tatsumi, T., *Chem. Commun.* (1996) 145.
9. Huo, Q., Margolese, D.I., Ciesla, U., Feng, P., Gier, T.E., Sieger, P., Leon, R, Petroff, P.M., Schüth, F., and Stucky, G.D., *Nature*, **368** (1994) 317.
10. Yanagisawa, T., Schimizu, T., Kuroda, K., Kato, C., *Bull. Chem. Soc. Japan*., **63** (1990) 988.
11. Armengol, E., Cano, M.L., Corma, A., Garcia, H., and Navarro, M.L, *J. Chem. Soc., Chem. Commun.*, (1995) 519.
12. Le, Q.N., *U.S. Patent*, 5 191 134 (1993).
13. Corma, A., Navarro, M.T., and Perez-Pariente, J., *J. Chem. Soc., Chem. Commun*. (1994) 147.
14. Reddy, J.S., and Sayari, A., *J. Chem. Soc., Chem. Commun.* (1995) 2231.
15. Reddy, J.S., Dicko, A., and Sayari, A., in *Synthesis of Porous Materials: Zeolites, Clays and Nanostructures, Marcel Dekker, Inc., New York* (1997) 405.
16. Gontier, S., and Tuel, A., *Stud. Surf. Sci. Catal.*, **105** (1997) 1085.
17. Reddy, K.M., Moudrakovski, I.L., and Sayari, A., *J. Chem. Soc., Chem. Commun*. (1994) 1059.
18. Das, T.K., Chaudhari, K., Chandwadkar, A.J., and Sivasanker, S., *J. Chem. Soc., Chem.*

Commun. (1995) 2495.

19. Chen, C.-Y., Li, H.-X., and Davis, M.E., *Microporous Mater.*, **2** (1993) 17.
20. Luan Z., Cheng, C-F., Zhou, W., and Klinowski, J., *J.Phys. Chem.*, **99** (1995) 1018.
21 Zhang, Y., Wang, J., Tanev, P.T. and Pinnavaia, T.J., *Chem. Commun.* (1996) 979.
22. Conner, W.C., Springuel-Huet, M.A., Fraissard, J., Bonardet, J., McMahon, T., Boudreau, L., and Masciadrelli, J., *Stud. Surf. Sci. Catal.*, **117** (1998) 575.
23. Tanev, P.T., Chibwe, M., and Pinnavaia, T.J., *Nature*, **368** (1994) 321.
24. Chen, X., Huang, l., and Li, Q., *J.Phys. Chem. B*, **101** (1997) 8461.
25. Chen, C.-Y., Burkett, S.L., Li, H.-X., and Davis, M.E., *Microporous Mater.*, **2** (1993) 27.
26. Ryoo, R., Kim, J.M., and Ko, C.H., *Stud. Surf. Sci. Catal.*, **117** (1998) 151.
27. Chang, Z., Zhu, Z. and Kevan L., *J.Phys. Chem. B*, **103** (1999) 9442.
28. Vartuli, J.C., Schmitt, K.D., Kresge, C.T., Roth, W.J., Leonowicz, M.E., McCullen, S.B., Hellring, S.D., Beck, J.S., Schlenker, J.L., Olson, D.H., and Sheppard, E.W., *Stud. Surf. Sci. Catal.*, **84** (1994) 53.
29. Gregg, S.J., and Sing, K.S.W., *Adsorption, Surface Area and Porosity, Academic Press* London, Ch. 4 (1982).
30. Luan Z., He, H., Zhou, W., Cheng, C-F., and Klinowski, J., *J. Chem. Soc., Faraday Trans.*, **91(7)** (1995) 2955.
31. Feuston, B.P., and Higgins, J.B., *J. Phys. Chem.*, **98** (1994) 4459.
32. Lin, H.-P., Cheng S., and Mou, C.-Y., *Chem. Mater.*, **10** (1998) 581.
33. Sierra, L., and Guth, J.-L., *Microporous and Mesoporous Materials*, **27** (1999) 243.
34. Iler, R.K., *The Chemistry of Silica, Wiley, New York*, 1979.
35. Gellan, A., Rochester, C.H., *J. Chem. Soc.,Faraday Trans.*, **181** (1985) 2235.
36. Di Renzo, F., Coustel, N., Mendiboure, M., Cambon, H., and Fajula, F., *Stud. Surf. Sci. Catal.*, **105** (1997) 69.
37. Galarneau, A., Deaplantier, D., Dutartre, R., and Di Renzo, F., *Microporous and Mesoporous Materials*, **27** (1999) 297.
38. Øye, G, Sjöblom, Stöcker, M., *Microporous and Mesoporous Materials*, **27** (1999) 171.
39. Israelachvili, J.N., Mitchell, D.J., and Ninham, B.W., *J. Chem. Soc., Faraday. Trans.*, **272** (1976) 1525.
40. Aamodt, M., Landgren, M., Jönsson, B., *J. Phys. Chem.*, **96** (1992) 945.

Chapter III

CHARACTERIZATION

3.1 INTRODUCTION

Zeolites and other porous materials need to be characterized to elucidate their structural features, pore architecture and catalytic behaviour. A complete characterization of molecular sieves requires information from a number of physical, chemical and spectroscopic techniques. Mesoporous molecular sieves are characterized by techniques such as XRD, sorption, TEM, TGA/DTA, FTIR etc.[1-3]. Among these, x-ray diffraction is of primary importance which provides information on the phase purity and some evidence for heteroatom incorporation[4-6]. Since mesoporous molecular sieves lack strict crystallographic order on an atomic level, their wall structure can not be determined from crystallographic data. However, the x-ray diffraction pattern of MCM-41 shows low angle peaks, which are reflections from the quasi-regular arrangement of mesopores with hexagonal symmetry. The sorption capacity data provide surface area, pore volume and pore size[7-9]. TEM is an established technique to obtain the topographic information of mesoporous materials[10]. A combination of X-ray diffraction, sorption studies and TEM of mesoporous molecular sieves provides a reasonable idea about the structure of these materials. Similar to microporous molecular sieves, other techniques like thermal methods (TG/DTA), FTIR, MAS NMR etc. are also useful in the characterization of these molecular sieves. The applications of these techniques have been discussed in Chapter I.

Samples of MCM-41, synthesized as described in Chapter II, have been characterized using various physico-chemical techniques. This chapter summarizes the results of the physico-chemical characterization of Si-MCM-41 and modified MCM-41 samples. The discussion is focused on XRD, thermal analysis, N_2-adsorption-desorption, transmission electron microscopy (TEM), scanning electron microscopy (SEM), Fourier Transform infrared spectroscopy (FTIR), UV-visible spectroscopy, MAS NMR spectroscopy, temperature programmed desorption of

pyridine, Pt-dispersion by H_2 chemisorption, Mössbauer spectroscopy and electron spin resonance (ESR) spectroscopy of these materials.

3.2 EXPERIMENTAL

3.2.1 X-ray Diffraction

The crystalline phase identification and phase purity of the as-synthesized and calcined samples were determined by X-ray diffraction spectra which were scanned either on a Philips diffractometer or a Siemans instrument using a monochromatic CuK_{α} radiation (λ = 1.5406Å; 40 kV, 25mA) with a 0.02 step size and a 1.2 s step time. The samples were prepared as thin layers on glass slides.

3.2.2 Chemical Analysis

The chemical compositions of the samples were determined by a combination of wet chemical methods, atomic absorption spectrometry (Hitachi, Model Z 800) and wavelength dispersive x-ray fluorescence spectrometer (Rigaku 3070 E) with Rh target energized at 50 kV and 40 mA. For XRF measurements borate fusion technique was used to prepare glassy beads of standards and samples. A calibration curve was made using standards. For the analysis of Si and Al, a pentaerythrital (PET) crystal was used whereas for the analysis of Zr and Sn, lithium fluride (LiF) crystal was utilized. For all the analyses, K_{α} lines were selected and pulses were collected for 40 sec. A background correction was applied.

3.2.3 XPS

XPS measurements were carried out using V. G. Scientific ESCA-3-MK II x-ray photoelectron spectrometer with AlK$_\alpha$ X-ray source. The binding energy values were measured with reference to the carbon peak at 285.0 eV.

3.2.4 Sorption

The sorption capacities for H_2O, n-hexane and benzene were measured gravimetrically using a vacuum electrobalance (Cahn Instrument) and a glass vacuum unit (Mc-Bain Baker balance) at p/p_0 = 0.5 at 25°C. The sample (~ 35 mg) was pressed into a small pellet and weighed into an aluminium bucket. The system was connected to high vacuum and the sample was activated in vacuum (10^{-5} Torr) at 400°C for 4h. The sample was then cooled to room temperature under high vacuum. The sorbate vapours were admitted into the sample at a constant pressure and temperature and the weight gained was recorded continuously as a function of time. After completion of the experiment, the sample was evacuated and heated to 400°C at 10^{-5} Torr and used for the next measurement.

Surface areas and pore diameters of the samples were determined from N_2-adsorption-desorption isotherms using a commercial volumetric adsorption apparatus (Omnisorp 100 CX, Coulter Corporation, USA). Approximately 100-150 mg of the calcined sample was degassed at 400°C for 5h at 10^{-5} Torr, prior to surface area measurements. The sample was then cooled to 77K using liquid nitrogen and the sorption of nitrogen was carried out at different equilibrium pressures. The anhydrous weight of the sample was used in the surface area calculations. To obtain the surface area, the results were fitted into the equation,

$$S_{BET} = V_m \times N \times A_m$$

Where, V_m is the monolayer volume,

N is the Avagadro's number and

A_m is the cross sectional area of the adsorbent.

The pore size distribution and pore diameters were calculated using the Barret-Joyner-Halenda (BJH) model[11]. The above model was chosen since it has been derived for nonintersecting cylindrical pores[12] (as in MCM-41 type materials). However, as the model uses the Kelvin equation, the validity of which is questionable for pores of diameter less than 50Å[11], systematic errors might be present in the estimated pore diameters (Table 3.1, 3.3 and 3.4). However, the reported trend in the pore diameters for the different samples is expected to be the same.

3.2.5 Transmission Electron Microscopy (TEM)

The samples were embedded in Epon 812 epoxy resin, which was then cured. The epoxy blocks were ultramicrotomed at room temperature. The ultrathin sections ranging in thickness from 80 to 100 nm were prepared using a Reichert microtome. The thin sections were examined by TEM. The TEMs used for these studies were either JEOL 2000 FX or Philips CM-20 equipped with a high resolution ultrathin polepiece. Images were recorded on conventional sheet films.

3.2.6 Scanning Electron Microscopy

The crystallite size and morphology of the as-synthesized and calcined samples were determined by a scanning electron microscope (Model JEOL JSM 5200) equipped with energy dispersive X-ray analysis (EDAX). The samples were sputtered with gold to prevent surface charging and to protect from thermal damage from the electron beam.

3.2.7 Thermal Analysis

TGA/DTA analyses of the as-synthesized samples were carried out using a computer controlled thermal analyzer (Setaram, France, Model TG-DTA 92). Approximately 35 mg of the sample was used in each experiment and inert ∝-alumina was used as the reference sample. A linear rate of heating of 10°C min^{-1} from room temperature to 1000°C in air flow (30 ml min^{-1}) was employed to find out the temperature of decomposition of the organic additives, the thermal stability of the molecular sieves and weight loss.

3.2.8 Infrared Spectroscopy

Samples mixed in nujol were used for framework IR analysis. Fourier transform infrared (FTIR) spectra were recorded with a Shimadzu FTIR spectrometer (Model 8300). FTIR spectra of the molecular sieves in the framework region (450 cm^{-1} to 1300 cm^{-1}) were obtained in the diffuse reflectance mode.

3.2.9 Pyridine sorption

The nature of the hydroxyl groups on MCM-41 samples was characterized by FTIR spectroscopy. Thin wafers of the samples weighing about 5-6 mg/cm^2 area were made by pressing at a pressure of 5 $ton/inch^2$. The wafer was placed inside the controlled environmental chamber of the transmittance cell, which was connected to a high vacuum system. The sample was evacuated to 10^{-6} Torr at 400°C for 3 hrs and cooled to 100°C before recording the spectrum. Then the sample was allowed to adsorb pyridine at an equilibrium pressure of 10 mm of Hg for 30 minutes and the loosely adsorbed and free vapour of pyridine was removed by evacuating for 1h successively at 100, 200, 300 and 400°C before recording the spectrum again. The spectrum

was recorded with 4 cm^{-1} resolution after averaging over 500 scans using Nicolet 60 SX B FTIR spectrometer.

3.2.10 Solid State MAS NMR Spectroscopy

The solid state magic-angle spinning (MAS) NMR spectroscopic studies were carried out on a Bruker MSL-300 FT NMR spectrometer. For the MAS NMR studies, the finely powdered samples were placed in 7.0 mm O.D. zirconia rotors and spun at 2.5-3.3 kHz. For ^{27}Al signal, aluminium nitrate (1M aqueous solution) was used as the reference compound. The ^{119}Sn signal was referred to the isotropic peak of SnO_2 taken as δ = - 604 ppm (w.r.t. tetramethyl tin), while tetraethyl orthosilcate (δ = 82.4 ppm from tetra methyl silane) was used as the reference compound for ^{29}Si. The resonance frequencies of ^{119}Sn, ^{13}C and ^{29}Si were 111.8, 75.5 and 59.6 MHz, respectively.

For the ^{13}C CP/MAS experiments, the Hartmann-Hahn match conditions were adjusted using adamantane. The ^{13}C signal of the CH_2 group of adamantane was taken as a secondary reference (δ = 28.7 ppm from TMS). The resonance frequency of ^{13}C was 75.5 MHz.

3.2.11 Temperature Programmed Desorption

Temperature programmed desorption of pyridine was studied on H-Al-MCM-41 and other samples under chromatographic conditions[13]. The data were collected using a Perkin Elmer Sigma 3B gas chromatograph with a flame ionization detector. Nitrogen was used as the carrier gas (flow rate: 40 cm^3/min).

3.2.12 Pt-dispersion Measurement by H_2 Chemisorption

The platinum dispersion measurements of H-Al-MCM-41 with 0.5% Pt impregnated samples with different Si/Al ratios were carried out by hydrogen chemisorption at ambient temperature[14]. About 3 g of the calcined catalyst was loaded in a pyrex-glass U-shaped sample holder. The sample was reduced at 350°C for 2h and degassed at 500°C for 5 h under vacuum (10^{-5} Torr). Under the same vacuum, the sample was cooled to the ambient temperature. High purity hydrogen was adsorbed in the equilibrium pressure range between 5 to 200 Torr. After this, the sample was evacuated at 10^{-5} Torr at ambient temperature to remove the weakly adsorbed hydrogen. A second adsorption isotherm was carried out at ambient temperature in the same pressure range as the first one. The difference between the two adsorption isotherms after extrapolating to zero pressure provides the amount of chemisorbed hydrogen[14]. The Pt-dispersion was estimated assuming dissociative adsorption of hydrogen on the metal.

3.2.13 UV-visible Spectroscopy

The UV-vis diffuse reflectance spectra of the samples were obtained using a Shimadzu (Model UV-2101 PC) spectrometer using barium sulphate as the reference.

3.2.14 Mössbauer spectroscopy

Mössbauer spectra of Sn-MCM-41-C(133), Sn-MCM-41-C(83) and Sn-MCM-41-C(42) samples were recorded at 77K and at 300K. Two series of measurements were performed. In the first one, the spectra of the three samples were recorded in the calcined state at two temperatures. In the second series, *in situ* spectra were obtained on a selected sample (Sn-MCM-41-C(83)) in order to study the effects of reduction (620K and 670K for 2h in H_2 flow) and oxidation (520K for 2h in flow of air) on the state of tin. The isomer shift values reported are

relative to SnO_2 at 300K. For the deconvolution, a Lorentzian line shape was assumed and none of the positional parameters was constrained. The estimated accuracy of positional data is ± 0.03 mm/s.

Similarly Mössbauer spectra of two Sn-MCM-41-D samples (Sn-MCM-41-D(85) and Sn-MCM-41-D(43)) were also recorded at 77 K and at 300 K. *In situ* spectra were obtained on Sn-MCM-41-D(43) sample in order to study the effects of reduction (620 K for 2h in H_2 flow) and oxidation (520K for 2h in flow of air) on the state of tin.

3.2.15 Electron Spin Resonance (ESR) Spectroscopy

The ESR spectra of calcined Si-MCM-41 and Zr-MCM-41 samples were recorded on a Bruker EMX spectrometer operating at X-band frequency and 100 kHz field modulation. The samples were taken in specially designed Suprasil quartz tubes (4.5 mm o.d.) having a provision for evacuation and adsorption of gases. The measurements at 77K were carried out using a quartz insert dewar. Spectral manipulations and simulations were done using Bruker WINEPR and Simfonia software packages. Microwave frequency was calibrated using a frequency counter fitted in the microwave bridge (Bruker ER 041XG-D) and the magnetic field was calibrated by a (ER 035M NMR) Gaussmeter.

For ESR studies, the samples were initially evacuated (10^{-5} Torr) and dehydrated by gradually raising the temperature of the sample from 298K to 673K in about 4 - 5h and then kept at the required temperature for a further period of 16h. These dehydrated samples were then subjected to hydrogen reduction by treating with dry hydrogen (20 ml/min) at higher temperatures (673K, 773K and 873K) for 6h.

Chemical reductions were done under argon atmosphere by reacting the dehydrated samples with $LiAlH_4$ in anhydrous distilled THF, at 298K, for 6h. The mixtures containing Zr-MCM-41 were then transferred to 4.5 mm o.d. quartz ESR tubes taking care to avoid contact with atmospheric oxygen.

The activated samples of Zr-MCM-41 were sealed in glass vials and reduced by exposing to γ-radiation generated from a ^{60}Co source at 77K (total dose = 1.38 Mrad at a dose rate of 0.2 Mrad/h).

3.3 RESULTS AND DISCUSSION

3.3.1 Al-MCM-41

This section gives detailed information on characterization data of the Si-MCM-41 (designated as Si-MCM-41-B) and Al-MCM-41 samples with different Si/Al ratios synthesized using cetyltrimethylammonium bromide (CTMABr) as the surfactant. The details of the preparations of these samples discussed in the following sections are presented in Chapter II (section 2.3.1).

3.3.1(i) X-ray diffraction

The XRD patterns of the calcined Al-MCM-41 samples with different Si/Al ratios and the pure silica Si-MCM-41-B are presented in Figure 3.1. The spectra showed XRD patterns identical to that reported for MCM-41 materials[1-3]. Kresge *et al.*[1] indexed these peaks for a hexagonal unit cell, the parameter of which was calculated from the equation $a_0 = 2d_{100}/\sqrt{3}$. On calcination of samples, the peak is shifted to lower d_{100} spacing value probably due to condensation of internal Si-OH groups giving rise to a contraction of the unit cell[9]. The unit cell

parameter and d-spacing of the Al-MCM-41 samples and Si-MCM-41-B are given in Table 3.1. The slight increase in d-spacing and unit cell parameters of Al-MCM-41 compared to its pure silica analog (Table 3.1) suggests the presence of aluminium in the framework.

Fig. 3.1 XRD patterns of calcined samples. (a) Si-MCM-41-B; (b) Al-MCM-41(44); (c) Al-MCM-41(23) and (d) Al-MCM-41(14).

The increase in unit cell parameter on Al incorporation is probably due to the replacement of shorter Si-O bonds by longer Al-O bonds in the structure[15]. It is also observed that alongwith an

increase in the unit cell parameter, the (100) diffraction peak becomes broader and less intense with increasing aluminium content, probably, because of the change of the T-O-T bond angle due to aluminium incorporation, causing a distortion in the long range ordering of the hexagonal mesoporous structure. Similar effects have been observed by earlier workers also[1,16].

3.3.1(ii) Chemical analysis

Chemical analyses of Al-MCM-41 samples obtained from XRF are presented in Table 3.1. It is observed that the Si/Al output ratio is less than the input ratio. However, the output ratio in the sample Al-MCM-41(14) is slightly higher than the input ratio.

Table 3.1 Physicochemical properties of Al-MCM-41 samples

Samples	**Si/Al ratio**		**d_{100} spacing**		**Surface area (m^2/g)**	**Pore volume (ml/g)**	**Pore diameter (Å)**
	Input in gel	**Calcined sample**	**As-syn.**	**Calcined**			
Si-MCM-41-B	-	-	36.40	33.00	990	0.60	23
Al-MCM-41(86)	100	86.3	36.48	33.19	1013	0.69	23
Al-MCM-41(44)	50	43.9	37.72	34.48	1025	0.76	24
Al-MCM-41(23)	25	23.3	38.72	35.39	1072	0.79	25
Al-MCM-41(14)	12.5	14.3	39.76	36.48	1098	0.82	26

3.3.1(iii) Sorption

The BET surface areas and pore volumes of the Al-containing samples are presented in Table 3.1. As explained in Chapter II for Si-MCM-41 samples, the N_2-adsorption isotherms of Al-MCM-41 samples also show type IV[11] pattern with three stages: monolayer adsorption of

nitrogen on the walls of mesopores ($p/p_0 < 0.2$), the part characterized by a steep increase in adsorption due to capillary condensation in mesopores with hysteresis ($p/p_0 = 0.15 - 0.3$), and multilayer adsorption on the outer surface of the particles[11]. The pore diameters increase with increasing Al content of the samples. The pore volumes calculated (at $p/p_0 = 0.5$) from N_2-sorption, n-hexane and benzene adsorption are nearly similar (Table 3.2).

Table 3.2 Pore volume, acidity and Pt dispersion of the samples

Sample	Pore volume (ml/g)			Acidity (mmol/g)[b]	Dispersion D (H/Pt)[c]
	N_2[a]	n-Hexane	Benzene		
Si-MCM-41-B	0.60	0.68	0.64	-	-
Al-MCM-41(86)	0.69	0.70	0.75	0.035	0.74
Al-MCM-41(44)	0.76	0.73	0.72	0.060	0.69
Al-MCM-41(23)	0.79	0.74	0.75	0.098	0.78
Al-MCM-41(14)	0.82	0.76	0.77	0.152	0.64

[a]Calculated from N_2 adsorption isotherm at liquid nitrogen temperature.

[b]Pyridine desorbed beyond 100°C.

[c]Pt-content was 0.5 wt.% for all samples.

3.3.1(iv) Temperature Programmed Desorption of Pyridine

The acidities of the H-Al-MCM-41 samples were characterized by the TPD of pyridine. The acid strengths appear to be rather moderate as nearly all the pyridine desorbed below 300°C. The acidities (mmol/g) based on the pyridine desorbed by the samples beyond 100°C are presented in Table 3.2. As the aluminium content increases, the total acidity increases in the samples (Al-MCM-41(86) < Al-MCM-41(44) < Al-MCM-41(23) < Al-MCM-41(14)).

3.3.1(v) Pt-Ddispersion

The Pt dispersion values of the Pt-H-Al-MCM-41 samples determined by hydrogen chemisorption are presented in Table 3.2. The Pt dispersions were almost similar for all the samples (64% to 78%).

3.3.1(vi)Transmission Electron Microscopy (TEM)

Fig. 3.2 presents the transmission electron micrographs of the Si-MCM-41-B and Al-MCM-41(23) samples. The micrographs show a reasonably regular array of channels in hexagonal arrangement as reported earlier[1-3]. In both samples the repeat distance between the channels is about 25 Å, which is consistent with the position of the first peak in the x-ray diffraction pattern of this material (d_{100} $\sqrt{3}/2$). The distance between the channels is also consistent with the estimated pore size of about 25 Å calculated from N_2 sorption measurement of the material.

3.3.1(vii) Scanning Electron Microscopy

Scanning electron micrographs of Al-MCM-41(23) sample is presented in Fig. 3.3. The micrographs reveal agglomerates of small particles of the size between 0.1 – 0.3 μm.

3.3.1(viii) TGA/DTA

TGA and DTA profiles of as-synthesized Si-MCM-41-B, Al-MCM-41(86) and Al-MCM-41(23) samples, are presented in Fig. 3.4(A) and 3.4(B), respectively. The TGA curves record a continuous weight loss upto ~ 750°C, amounting to ~ 53%. DTA curves (Fig 3.4(B)) of all the three samples reveal five distinct stages: characterized by a small endothermic peak (27-130°C) due to loss of loosely bound water from the pores and four exothermic peaks (between 200 to

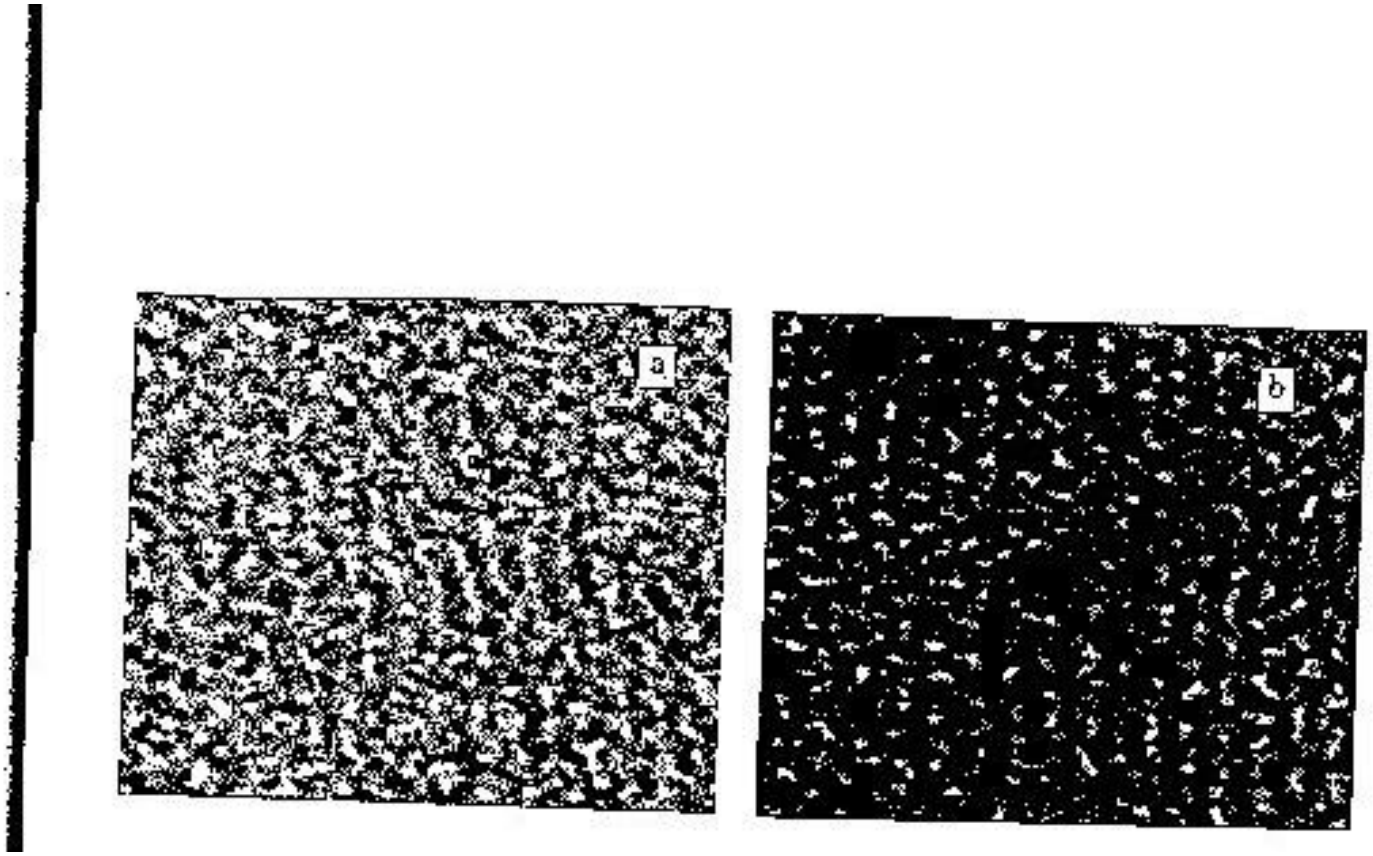

Fig. 3.2 Transmission electron micrographs of (a) Si-MCM-41-B and (b) Al-MCM-41(23).

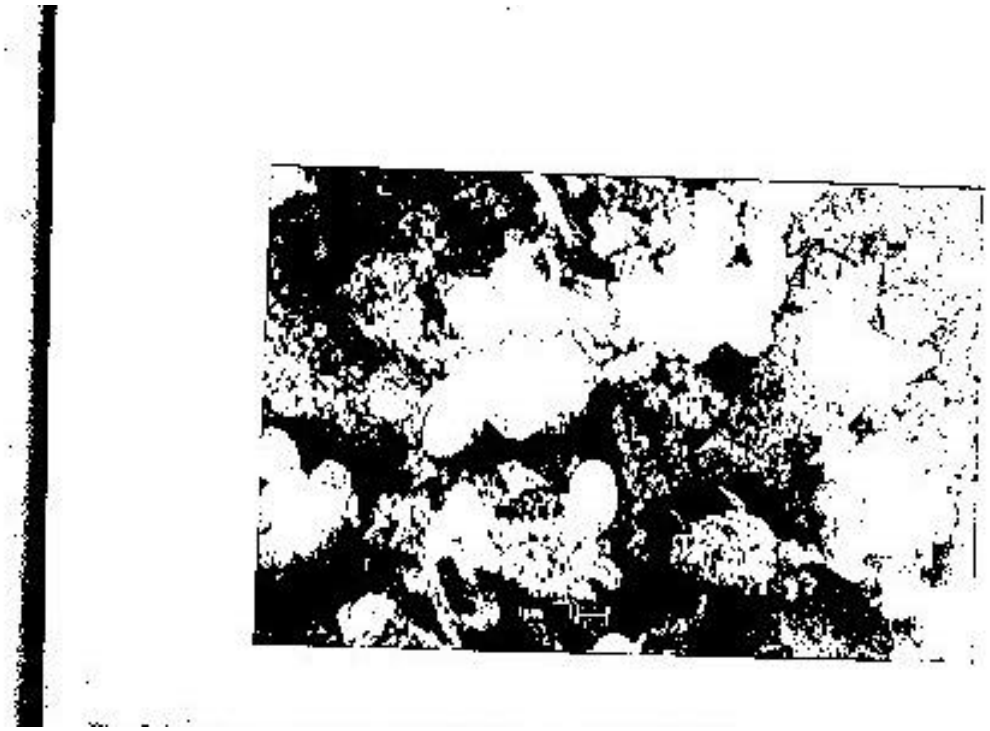

Fig. 3.3 Scanning electron micrograph of Al-MCM-41(23).

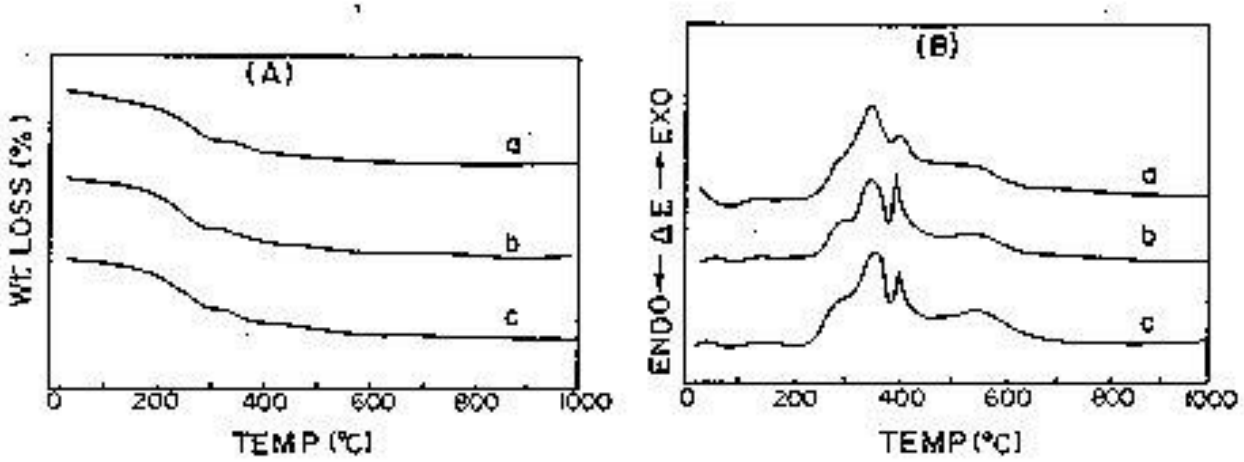

Fig. 3.4 (A) TGA profiles and (B) DTA profiles of as-synthesized (a) Si-MCM-41-B; (b) Al-MCM-41(86) and (c) Al-MCM-41(23).

650°C) indicating the combustion and decomposition of the embedded organic species (C_{16}TMA and TMA) in air.

The isomorphous substitution of Si by Al in these mesoporous materials (Al-MCM-41(86) and Al-MCM-41(23), Fig. 3.4(B)) does not appear to cause a significant change in the dehydration step (1st step). The weight loss for all the three samples is ~ 5.0% in the temperature range of 27-126°C. This is contrary to the observation of Chandwadkar *et al.*[17] (in the case of NaY) that, dehydration of the zeolite becomes faster and occurs at lower temperature with reduction of aluminium content (*i.e.* with decrease in charge balancing sodium ions). This effect was reported to be related to the greater strength of the bonds between the water and Na^+ cations[18]. In the case of MCM-41 type materials, organic templates act as charge balancing cations instead of alkali metal ions and no change in the dehydration peak maximum (T_{max}) is noticed on Al incorporation. The T_{max} of 2nd to 4th steps shifts slightly towards higher

temperatures (by 2-5°C) with increase in aluminium content due the formation of more relatively stronger bonds of the organic species with Al.

The TGA-DTA data reveal that nearly all the template is lost (accompanied by water loss due to condensation of silanol groups) from the pore system at a temperature of ~ 600°C. The last (relatively broad) step in the range of 500-650°C is probably due to condensation of the remaining silanol groups and combustion of the difficult to burn carbonaceous material[19]. As-synthesized Si-MCM-41, Al-MCM-41(86) and Al-MCM-41(23) samples contained ~ 48% template, revealing the existence of large pore volumes. The low and nearly similar starting temperature of template decomposition and the rapid weight loss confirm the openness of the pore system of all the substituted samples. While about 60% of the total template is lost in the 2nd and 3rd steps upto a temperature of ~ 400°C, the remaining template is lost at higher temperatures. Burning of the template is accompanied by the formation of coke, which is slowly removed in the last step. From the thermo-analytical curve, it appears that all the samples are highly porous and incorporation of Al has no significant effect on the decomposition behaviour of the template. In contrast, some zeolites, for instance ZSM-5 and beta[20,21] show a distinct influence of isomorphous substitution on the temperature of template decomposition.

Busio *et al.*[22] found a linear relationship between Al content and high temperature (300-500°C) weight loss, as long as the Al content did not exceed 3 wt.%. For $SiO_2/Al_2O_3 < 18$, only a limited no. of Al species were associated with surfactant molecules, which could be due to the extra-framework Al[21,23] acting as charge compensating cations[24]. In contrast, our results do not show any clear correlation between Al content and weight loss due to organic species, which is in agreement with the findings of Janicke *et al.*[25]. The multistep decomposition of the organics

could also be due to the existence of different acid site strengths and distributions, as a result of different Si-O-Al (IV) environment

3.3.1(ix) FTIR

The mid-infrared region from 400-1300 cm^{-1} contains vibrations due to the framework structure of zeolites[26]. Similarly, mesoporous molecular sieves also show series of bands that are characteristics of the SiO_4 tetrahedral unit and its modification by introduction of metal ions (Fig. 3.5). The IR spectra of lattice vibration of as-synthesized and calcined Si-MCM-41 and Al-MCM-41 are presented in Fig. 3.5(A) and 3.5(B), respectively. The spectra show five main absorption bands between the regions 1210-1245, 1055-1090, 960-970, 790-805 and 440-465 cm^{-1}, similar to amorphous fumed silica[16,27,28] (Fig. 3.5). The T-O-T lattice vibrations are found to shift to lower wavenumbers for Al-MCM-41 probably due to the incorporation of Al into the channel walls, as Al-O bond is longer than Si-O bond[26].

The band in the region 1210 to 1245 cm^{-1} is due to external asymmetric stretching vibrations of five membered Si-O rings[29], which is an evidence for the presence of 5 membered rings in the walls of MCM-41 structure. This band becomes less intense in the calcined samples indicating probably a rearrangement of the wall structure due to high temperature treatment[30]. In a molecular dynamics simulation study, Feuston and Higgins[31] have reported the presence of maximum number of 5 membered rings in the walls of MCM-41 in addition to other rings (4, 6, 7, 3 and 8)

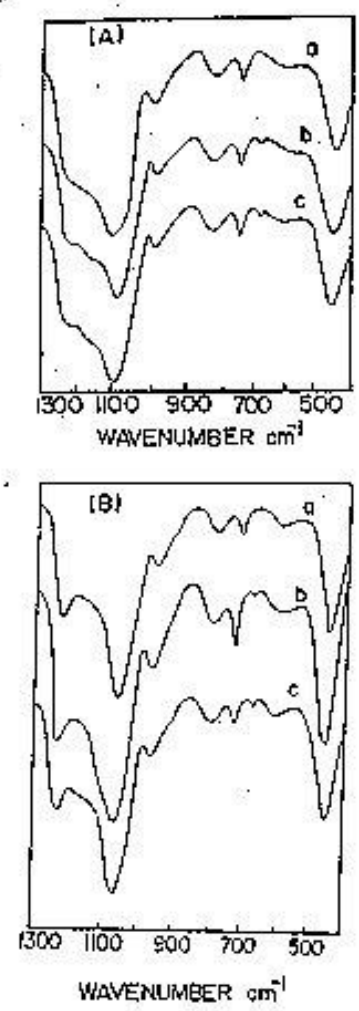

Fig. 3.5 FTIR spectra of (A) as-synthesized and (B) calcined (a) Si-MCM-41-B; (b) Al-MCM-41(44) and (c) Al-MCM-41(23).

The band in the region 1060-1090 cm^{-1} due to internal asymmetric stretching mode of SiO_4 (TO_4) skeleton appears to be the strongest band in the spectra of all silicates. The broadening of this band on calcination may be due to superimposition of many bands ascribable to TO_4 arising from different T-O-T angles. In the case of amorphous silica, silicalite-1 and TS-1, the strongest

band is observed at 1100 (± 1) cm^{-1}, whereas in case of as-synthesized Si-MCM-41and Al-MCM-41 samples, this band is significantly shifted to a lower wavenumber (1066 cm^{-1}). This may be due to the stretching of Si-O bond by long chain surfactant molecules forming micelles around which the SiO_4 species are wound during formation of the mesoporous molecular sieves. Such Si-O bond stretching is not observed in the case of microporous molecular sieves, the structure of which is formed around a single, small template molecule. Interestingly, this band at ~ 1066 cm^{-1} of mesoporous molecular sieves is found to be shifted to the higher wavenumber i.e. ~ 1085 cm^{-1} on removal of the surfactant molecules during calcination. This suggests that contraction of Si-O bond takes place during calcination, which has also been confirmed by XRD characterization[1].

All IR spectra exhibit one common feature, a band at ~ 970 cm^{-1}. The correct interpretation of this vibrational band has been a matter of extensive studies. Fig. 3.5 shows that with incorporation of metal ions, the intensity of this band marginally increases. This band is generally considered as a proof for the incorporation of the heteroatom into the framework[32]. Camblor et al.[32] have proposed that the band at 960 cm^{-1} is due to the Si-O stretching vibrations of Si-OH groups present at defect sites. This vibration has also been detected in Ti- and V-containing silica molecular sieves[33]. However, this band is observed in Si-MCM-41 too. Hence it can not be taken as an evidence for the incorporation of the heteroatom into the framework of the mesoporous molecular sieves.

3.3.1(x) Pyridine Sorption

In the Fig. 3.6(A), curves a-d, the spectra of Al-MCM-41(44) sample activated *in situ* at 100, 200 ,300 and 400°C and then cooled to 100°C are presented.

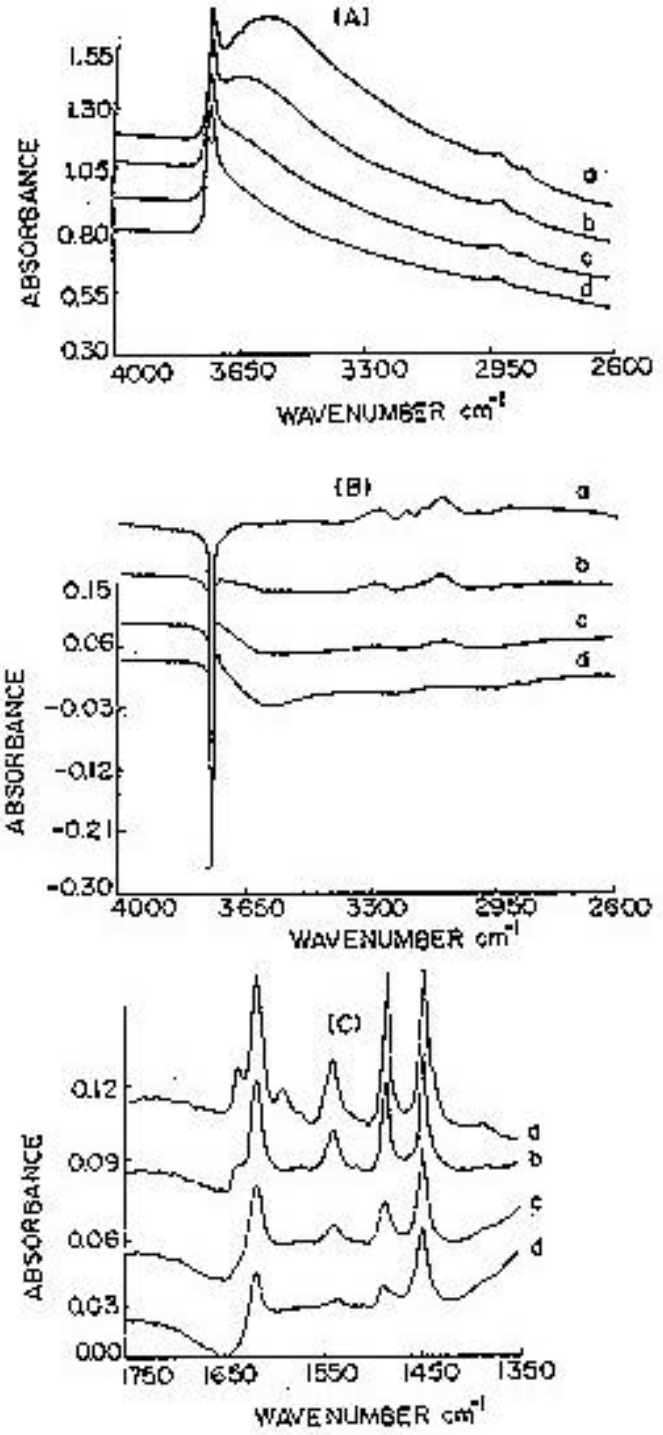

Fig. 3.6 IR spectra of H-Al-MCM-41(44) after evacuation at (a) 100°C; (b) 200°C; (c) 300°C and (d) 400°C: (A) Spectra of OH groups; (B) Spectra of adsorbed pyridine in the NH region and (C) Spectra of adsorbed pyridine showing Brönsted and Lewis acidity.

The two prominent bands at 3735 and 3600 cm^{-1} are ascribed to structural silanol (Si-OH) groups and physisorbed water, respectively[34,35]. As the temperature of activation increases, the band at 3600 cm^{-1} disappears and that at 3735 cm^{-1} appears predominantly superimposed on a very broad band in the region 3750 to 3300 cm^{-1}. This broad band is attributed to hydrogen bonded hydroxyl groups[36]. These hydroxyl bands are formed on defect sites due to structural imperfections or by dealuminated sites. The hydroxyl groups directly related to tetrahedral incorporation of Al^{3+} into MCM-41 framework were not observed. Such bridging hydroxyl groups are characterized by sharp bands in the region 3650-3550 cm^{-1}. Jentys *et al.*[35] have reported similar observations.

Adsorption of pyridine is routinely used for the estimation of acidity of catalysts[37]. Fig. 3.6(B) and 3.6(C) present the different spectra of adsorbed pyridine on Al-MCM-41(44). As the temperature of desorption increases from 100 to 400°C (curves a-d), the disappearance of N-H stretching vibrational bands in the region 3300-2900 cm^{-1} can be seen in the Fig. 3.6(B). It is associated with the increase in intensity of silanol bands at 3735 cm^{-1} and that of a broad band around 3600 cm^{-1}. The latter may be due to bridged Al^{3+} cations. In the Fig. 3.6(C), the bands due to pyridine adsorption on Brönsted and Lewis acid sites are observed[37]. The bands at 1639 and 1545 cm^{-1} are characteristic of pyridinium ion on the Brönsted acid sites and at 1621, 1595 and 1454-1445 cm^{-1} are characteristic of pyridine coordinately adsorbed on Lewis acid sites in the sample. The band at 1491 cm^{-1} can occur in either case. As the temperature of desorption increases from 100°C to 400°C (Fig. 3.6(C), curves a-d), the intensity of the pyridinium ion bands decreases rapidly compared to those of coordinately bound pyridine.

3.3.1(xi) ^{29}Si MAS NMR

^{29}Si MAS spectra obtained for two Al-MCM-41 samples (Al-MCM-41(44) and Al-MCM-41(23)) are compared in Fig.3.7 with that of Si-MCM-41 in the as-synthesized (Fig. 3.7(a-c)) and the calcined (Fig. 3.7(d-f)) forms.

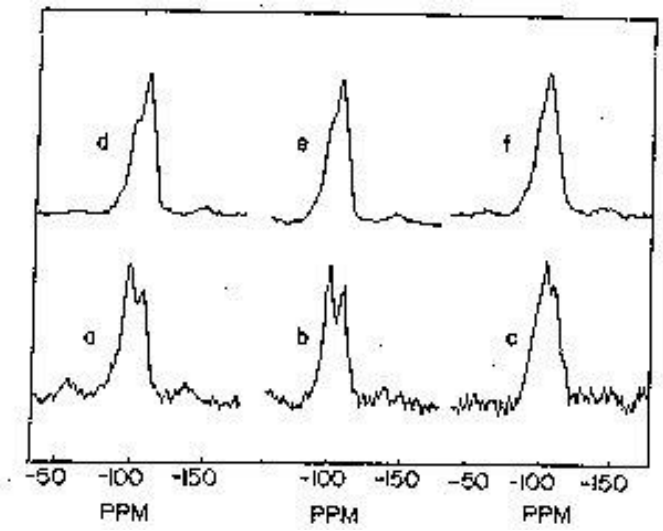

Fig. 3.7 ^{29}Si MAS NMR spectra of the samples. As-synthesized (a) Si-MCM-41-B; (b)Al-MCM-41(44) and (c) Al-MCM-41(23) and calcined (d) Si-MCM-41-B; (e)Al-MCM-41(44) and (f) Al-MCM-41(23).

The as-synthesized samples show two broad resonances with chemical shifts at δ = ~ -102 and - 112 ppm which can be assigned to the Q_3 and Q_4 silicon environments, respectively. The broadness of the ^{29}Si signals has been attributed to the large distribution of the T-O-T angles[3]. It is evident from these spectra that aluminium substitution does not give rise to any additional ^{29}Si peaks. The lack of high sensitivity for ^{29}Si signals is indicative of the very long spin lattice relaxation time associated with the MCM-41 system. Nevertheless, a comparison of the ^{29}Si MAS spectra recorded under identical conditions for the as-synthesized samples (Fig. 3.7 (a-c))

indicates that the Q_3 signal at δ = ~ - 102 ppm is slightly more for the Al-MCM-41 samples than for the Si sample in keeping with the larger surface areas of the former (Table 3.1). As expected, due to dehydroxylation, the intensity of the Q_3 sites decreases on calcination of the samples (Fig. 3.7(d-f)).

3.3.1(xii) ^{27}Al MAS NMR

The MAS ^{27}Al NMR spectra of as-synthesized and calcined Al-MCM-41 are presented in Fig. 3.8. The as-synthesized samples show only a single signal with δ = 54 ppm due to the presence of Al in tetrahedral coordination. The peak at 0 ppm corresponding to octahedral Al species is not noticeable. The ^{27}Al signals of the Al-MCM-41 samples are found to be broader than the signals generally observed for zeolitic Al presumably due to the presence of greater distortions in the tetrahedral environment in mesoporous materials.

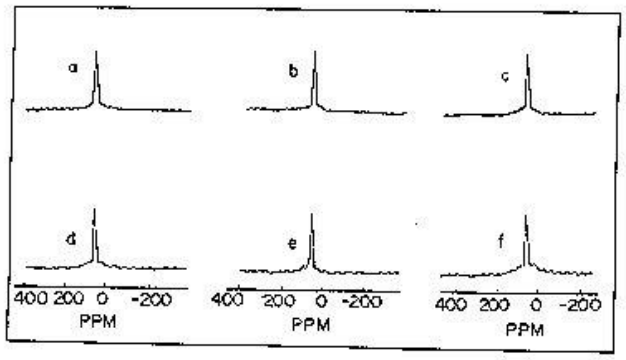

Fig. 3.8 ^{27}Al MAS NMR spectra of the samples. As-synthesized (a) Al-MCM-41(44); (b) Al-MCM-41(23) and (c) Al-MCM-41(14) and calcined (d) Al-MCM-41(44); (e) Al-MCM-41(23) and (f) Al-MCM-41(14).

On calcination, an additional signal with very low intensity is seen at ~ 32 ppm attributable to Al^{3+} ions in nontetrahedral coordination in the case of the sample with the highest Al content (Al-MCM-41(14)) (Fig. 3.8(f)).

3.3.2 Sn-MCM-41 and Zr-MCM-41

This section presents in detail the characterization of Sn- and Zr-containing MCM-41 samples synthesized (Chapter II, section 2.3.3 and 2.3.4, respectively) with two different surfactant molecules, CTMACl/OH and DTMABr designated as M-MCM-41-C(X) and M-MCM-41-D(X), respectively, where C and D represent M-MCM-41 synthesized using CTMACl/OH and DTMABr, respectively. M is Sn or Zr, and X is the Si/M output ratio.

3.3.2(i) X-ray Diffraction

The XRD patterns of the calcined Sn-MCM-41-C and Sn-MCM-41-D samples with different Si/Sn ratios and the pure silica Si-MCM-41-C and Si-MCM-41-D are given in Figure 3.9 (A and B) and the XRD patterns of Zr-MCM-41-C and Zr-MCM-41-D samples are shown in Fig. 3.10 (A and B, respectively). As seen in the case of Si-MCM-41 samples (Chapter II) and Al-MCM-41 samples (Section 3.3.1(i)), the XRD patterns of these samples (except for the sample Zr-MCM-41(23)), show one major peak along with three small peaks indexed for a hexagonal unit cell. However, in the XRD pattern of the calcined Zr-MCM-41(23), only the (100) reflection is observed (Fig. 3.10(A)-b). The retention of only one peak at the lowest angle indicates that on calcination only the short range symmetry is present in the structure[38].

On calcination, an additional signal with very low intensity is seen at ~ 32 ppm attributable to Al^{3+} ions in nontetrahedral coordination in the case of the sample with the highest Al content (Al-MCM-41(14)) (Fig. 3.8(f)).

3.3.2 Sn-MCM-41 and Zr-MCM-41

This section presents in detail the characterization of Sn- and Zr-containing MCM-41 samples synthesized (Chapter II, section 2.3.3 and 2.3.4, respectively) with two different surfactant molecules, CTMACl/OH and DTMABr designated as M-MCM-41-C(X) and M-MCM-41-D(X), respectively, where C and D represent M-MCM-41 synthesized using CTMACl/OH and DTMABr, respectively. M is Sn or Zr, and X is the Si/M output ratio.

3.3.2(i) X-ray Diffraction

The XRD patterns of the calcined Sn-MCM-41-C and Sn-MCM-41-D samples with different Si/Sn ratios and the pure silica Si-MCM-41-C and Si-MCM-41-D are given in Figure 3.9 (A and B) and the XRD patterns of Zr-MCM-41-C and Zr-MCM-41-D samples are shown in Fig. 3.10 (A and B, respectively). As seen in the case of Si-MCM-41 samples (Chapter II) and Al-MCM-41 samples (Section 3.3.1(i)), the XRD patterns of these samples (except for the sample Zr-MCM-41(23)), show one major peak along with three small peaks indexed for a hexagonal unit cell. However, in the XRD pattern of the calcined Zr-MCM-41(23), only the (100) reflection is observed (Fig. 3.10(A)-b). The retention of only one peak at the lowest angle indicates that on calcination only the short range symmetry is present in the structure[38].

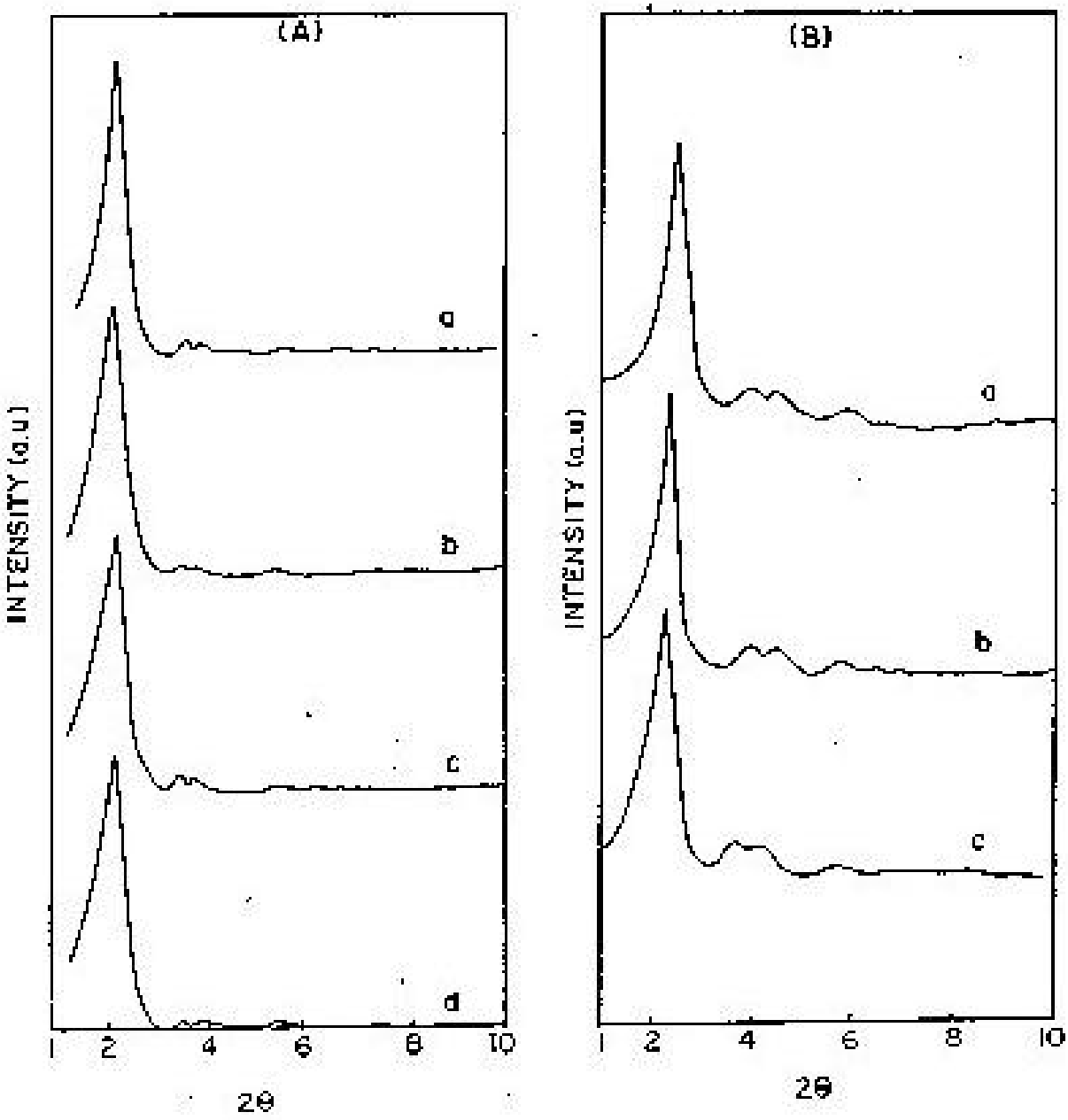

Fig. 3.9 (A) XRD patterns of calcined (a) Si-MCM-41-C; (b) Sn-MCM-41-C(133); (c) Sn-MCM-41-C(83) and (d) Sn-MCM-41-C(42) and (B) XRD patterns of calcined (a) Si-MCM-41-D; (b) Sn-MCM-41-D(85) and (c) Sn-MCM-41-D(43).

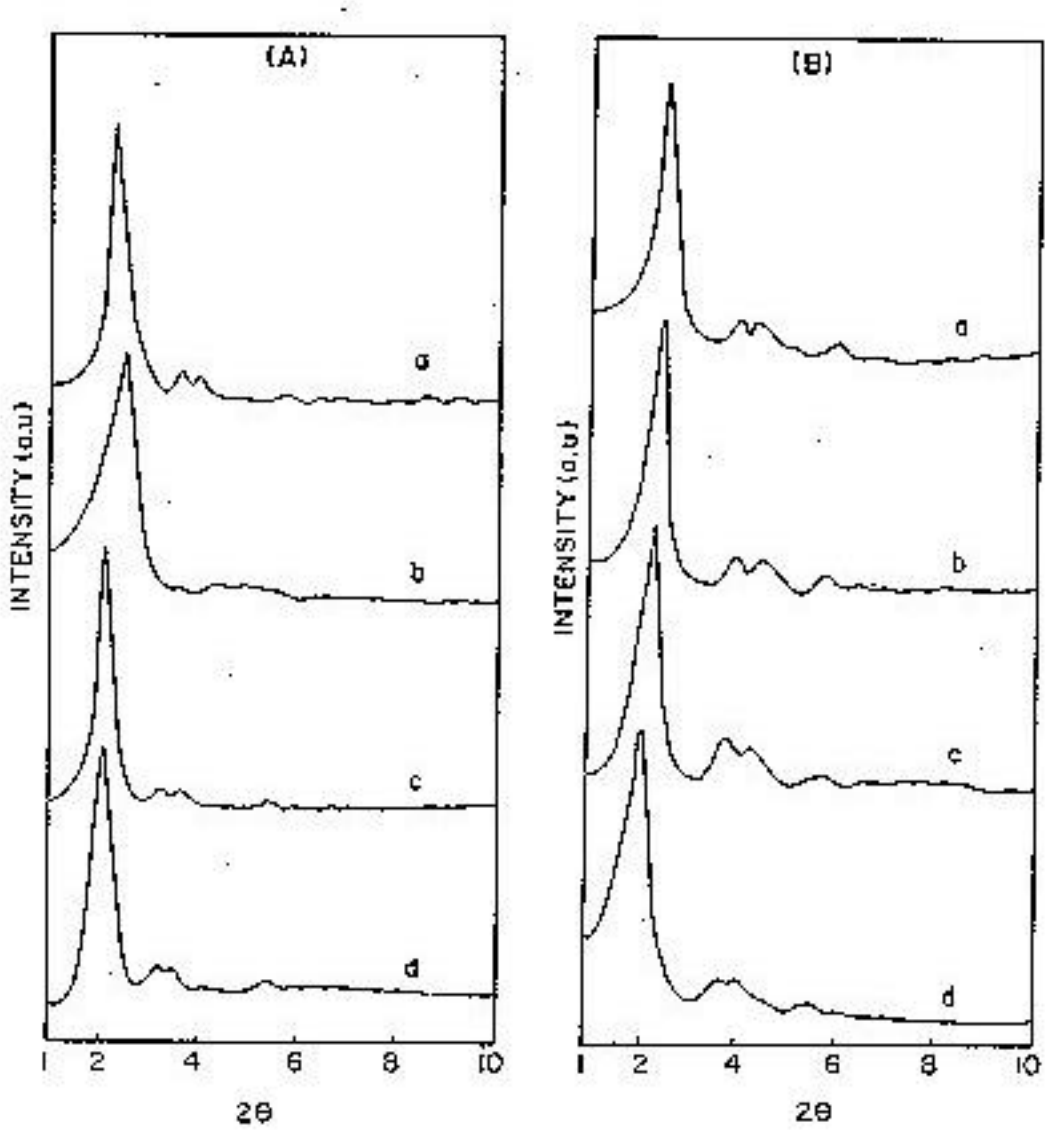

Fig. 3.10 (A) XRD patterns of calcined (a) Si-MCM-41-C; (b) Zr-MCM-41-C(55); (c) Zr-MCM-41-C(39) and (d) Zr-MCM-41-C(23) and (B) XRD patterns of calcined (a) Si-MCM-41-D; (b) Zr-MCM-41-D(59); (c) Zr-MCM-41-D(42) and (c) Zr-MCM-41-D(33).

The unit cell parameter and d-spacing of the Sn-MCM-41 and Si-MCM-41 are given in Table 3.3, while those of Zr-MCM-41 are given in Table 3.4.

Table 3.3 Composition and physicochemical characteristics of the Sn-MCM-41-C and Sn-MCM-41-D samples

Sample	SiO_2/MO_2 (mole ratio)			XRD d_{100} (Å)	Unit cell (a_0) parameter in Å	BET surface area (m^2/g)[a]	Average pore diameter (Å)[a]
	Gel	Product					
		Chemical analysis	XPS				
Si-MCM-41-C	-	-	-	36.77	42.5	975	27.0
Si-MCM-41-D	-	-	-	36.33	41.9	1000	22, 35
Sn-MCM-41-C(178)	200	178	176	38.38	44.31	978	28.5
Sn-MCM-41-C(133)	150	133	129	39.39	45.48	990	29.6
Sn-MCM-41-C(83)	100	83	81	39.58	45.70	1031	30.2
Sn-MCM-41-C(42)	50	42	42	39.66	45.80	1082	30.5
Sn-MCM-41-D(85)	100	85	82	37.42	43.2	1025	20, 34
Sn-MCM-41-D(43)	50	43	41	38.14	44.0	1052	20, 32
Sn-impregnated MCM-41	-	50	48	-	-	-	-
Sn-silica gel	50	50	47	-	-	-	-

[a]Calculated from N_2 sorption isotherm at liquid nitrogen temperature.

Table 3.4 Composition and physicochemical characteristics of the Zr-MCM-41-C and Zr-MCM-41-D samples

Sample	SiO_2/MO_2 (mole ratio)			XRD d_{100} (Å)	Unit cell (a_0) Parameter in Å	BET Surface area (m^2/g)[a]	Pore diameter (Å)[a]
	Gel	Product					
		Chemical analysis	XPS				
Si-MCM-41	-	-	-	36.77	42.5	975	27.0
Si-MCM-41-D	-	-	-	36.33	41.9	999.9	22, 35
Zr-MCM-41-C (96)	100	96	93	38.38	44.3	968	28
Zr-MCM-41-C (55)	50	55	51	39.76	45.9	942	30
Zr-MCM-41-C (39)	25	39	44	40.88	47.2	889	31
Zr-MCM-41-C (23)	12.5	23	20	33.69	38.9	766	25
Zr-MCM-41-D(102)	100	102.3	-	38.21	44.1	1023	22, 33
Zr-MCM-41-D(59)	50	58.9	-	38.92	44.9	1046	22, 32
Zr-MCM-41-D(42)	25	42.0	-	39.35	45.4	1101	24, 31
Zr-MCM-41-D(33)	12.5	33.0	-	37.97	43.8	1054	24

[a]Calculated from N_2 adsorption isotherm at liquid nitrogen temperature.

Incorporation of metal results in a slight increase in d-spacing and unit cell parameters of M-MCM-41-C compared to its pure silica analog (Table 3.3 and Table 3.4) suggesting the presence of metal in the framework. The increase in unit cell parameter on metal incorporation is probably due to the larger size of metal ions compared to Si^{4+}. It is also observed that the unit cell parameter increases with increasing metal content. A similar increase has been observed by earlier workers with aluminium[3,15], titanium[39] and vanadium[40] containing MCM-41.

On calcination, the peak is shifted to lower d_{100} spacing value probably due to condensation of internal Si-OH groups during calcination giving rise to a contraction of the unit cell[3]. Also the intensity of this peak significantly increases in calcined samples, which indicates the occurrence of an atomic rearrangement during the removal of the surfactant molecules in calcination process[30].

It has been observed that the d-spacing values are slightly less for M-MCM-41-D samples than the corresponding M-MCM-41-C samples (Table 3.3 and Table 3.4), as the latter samples have been synthesized using CTMACl/OH, with a longer alkyl chain (C_{16}), while the former have been synthesized using DTMABr with an alkyl chain of 12 C-atoms. These results are similar to those reported earlier[3].

3.3.2(ii) Chemical Analysis and XPS

The results of the chemical analysis of the Sn-MCM-41-C and Sn-MCM-41-D samples are presented in Table 3.3. The chemical compositions determined by chemical analysis and XPS analysis are similar. The x-ray photoelectron spectra of the samples show typical doublets for Sn $3d_{3/2}$ and $3d_{5/2}$ electrons with binding energies of 496.3 and 488.0 eV, respectively,[41] indicating the presence of Sn^{4+} at the surface. The surface chemical compositions were calculated from the intensities of the Sn 3d and Si 2s peaks[41] and given in Table 3.3. The good correspondence between the compositions from chemical and XPS methods confirms that the Sn^{4+} ions are uniformly distributed in the surface and the bulk in the samples. Further, no loss of Sn occurred on extraction with dil HCl (1.1M) suggesting the absence of Sn^{2+} ions in the samples.

The XRF analyses and XPS results of Zr-MCM-41-C samples are given in Table 3.4. The chemical compositions determined by chemical analysis and XPS analysis are nearly similar.

The x-ray photoelectron spectra of the samples show typical doublets for Zr $3d_{3/2}$ and $3d_{5/2}$ electrons with binding energies of 178.7 and 181.1 eV, respectively indicating the presence of Zr^{4+} at the surface. The surface chemical compositions were calculated from the intensities of the Zr 3d and Si 2s peaks[42] and given in Table 3.4. The good correspondence between the compositions from chemical and XPS methods confirms that the Zr^{4+} ions are uniformly distributed in the surface and the bulk in the samples. In contrast to Zr-MCM-41-C, in all the Zr-MCM-41 samples, the Zr contents were less than those introduced in the synthesis gel (Table 3.4), the difference being more marked at higher Zr contents.

3.3.2(iii) Sorption

The BET surface areas, average pore diameters and pore volumes calculated from N_2-sorption isotherms of Sn-MCM-41-C & Sn-MCM-41-D and Zr-MCM-41-C & Zr-MCM-41-D samples are presented in Table 3.3 and Table 3.4, respectively. According to IUPAC classification, the isotherms are of type IV[11] (presented for Zr-MCM-41-C and Zr-MCM-41(D) in Fig. 3.11 and 3.12, respectively). The isotherms exhibit three stages (see Chapter II, Section 2.2.2.1). The second stage is characterized by a steep increase in adsorption within the relative pressure p/p_0 range between 0.15 - 0.35 due to capillary condensation in mesopores. This part shows hysteresis. The position of p/p_0 at which inflection starts is related to the diameter of the mesopores. The sharpness in this step indicates the uniformity of the pore size distribution[11]. In the case of both M-MCM-41-C (M = Sn or Zr), this step of isotherm shifts slightly towards higher relative pressure p/p_0 with increase in metal content of the sample (except sample Zr-MCM-41-C(23) and Zr-MCM-41-D(33), Fig. 3.11(A)-d) and Fig. 3.12(A)-d), respectively),

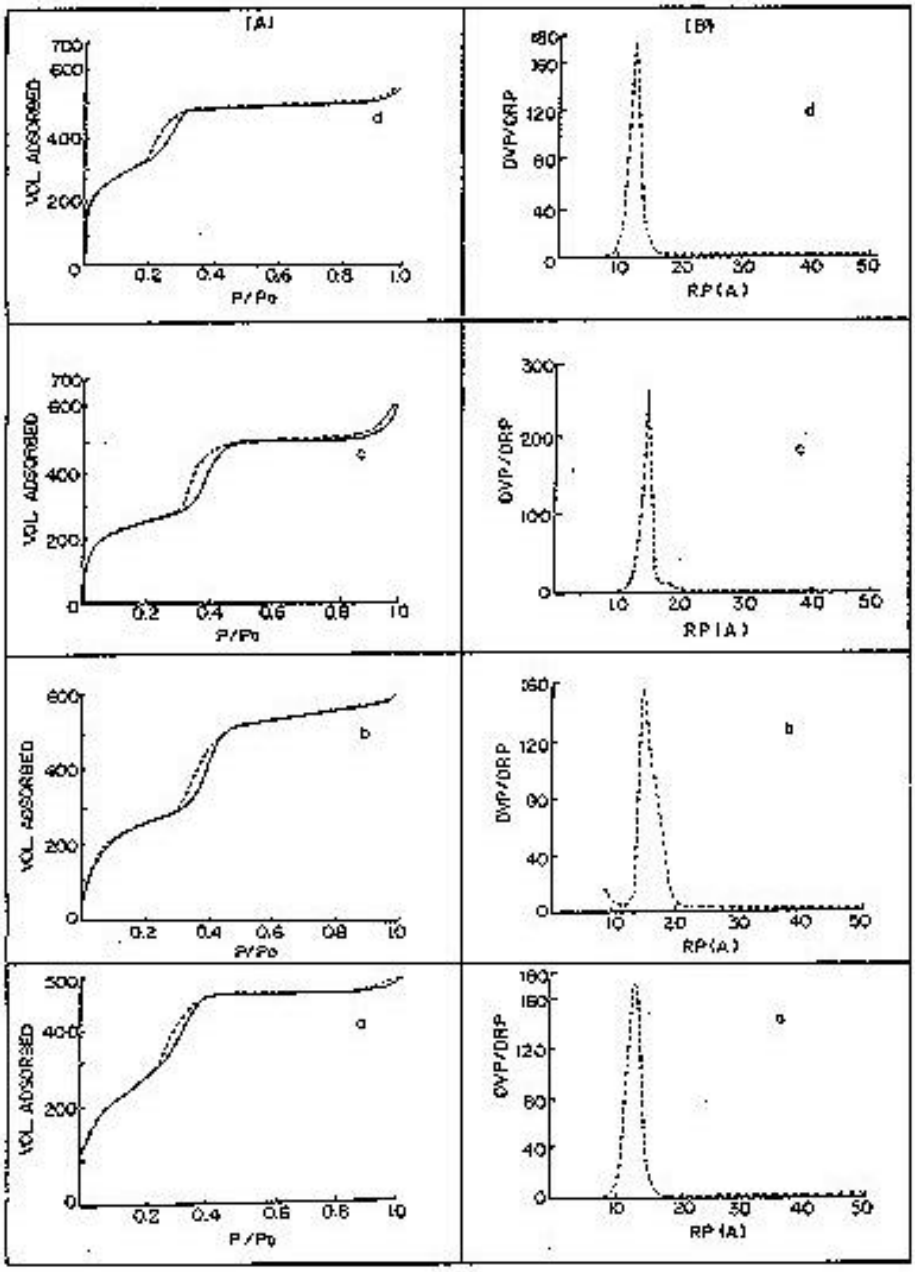
[A]
[B]
VOL ADSORBED
P/Po
DVP/DRP
RP(A)
a
b
c
d

Fig. 3.11 (A) N_2-adsorption-desorption isotherms and (B) Pore size distribution of (a) Si-MCM-41-C; (b) Zr-MCM-41-C(55); (c) Zr-MCM-41-C(39) and (d) Zr-MCM-41-C(23).

indicating increase in the pore size. However, the broadening of the hysteresis loop increases with increase in the metal content (Fig. 3.11(A) from b to c and Fig. 3.12(A) from b to c). This may be due to changes in the shape of the mesopore shape.

The hysteresis loop in the range of $p/p_0 > 0.8$ due to capillary condensation in the interparticle mesopores[11] observed in the case of Sn-MCM-41-C and Zr-MCM-41-C samples is very small (Fig. 3.11(A), shown for Zr-MCM-41-C samples). In the case of Sn-MCM-41-D and Zr-MCM-41-D samples, the hysteresis loop is observed in a wide range of p/p_0 (0.4 – 1) (Fig. 3.12(A), shown for Zr-MCM-41-D samples). A comparison of the hysteresis loops of these two sets of samples at higher relative pressure region indicates that these two materials prepared with different templates differ greatly in textural mesoporosity. Thus, due to the presence of internal pores (22-24 Å) and the interparticle voids (> 30 Å) the pore distribution in M-MCM-41-D samples is found to be bimodal (Fig 3.12(B)).

The pore diameters increase with increasing metal (Sn or Zr) content of the samples. The pore volumes of Sn-MCM-41 samples calculated (at $p/p_0 = 0.5$) from N_2-sorption, n-hexane and benzene adsorption are similar (Table 3.5). The amounts of H_2O adsorbed are however smaller[42].

Table 3.5 Adsorption capacity and the pore volume of the samples

Sample	Sorption capacity (mass %)[a]			Pore volume (ml/g)		
	H_2O	n-Hexane	Benzene	n-Hexane	Benzene	N_2[b]
Si-MCM-41-C	13.8	45.1	56.1	0.684	0.642	0.631
Si-MCM-41-D	12.3	40.2	48.2	-	-	0.83
Sn-MCM-41-C(178)	15.7	46.7	58.03	0.709	0.664	-
Sn-MCM-41-C(133)	17.5	47.0	60.5	0.713	0.692	0.664
Sn-MCM-41-C(83)	19.5	49.2	62.4	0.747	0.714	-
Sn-MCM-41-C(42)	20.1	50.3	63.1	0.763	0.722	0.733
Sn-MCM-41-D(85)	13.4	42.0	49.2	-	-	1.11
Sn-MCM-41-D(43)	13.8	42.9	50.2	-	-	1.32

[a]Gravimetric adsorption (Cahn electrobalance) at $p/p_0 = 0.5$ and 298K.

[b]Calculated from N_2 adsorption isotherm at liquid nitrogen temperature.

3.3.2(iv) Transmission Electron Microscopy (TEM)

Fig. 3.13-a, b and c present the transmission electron micrographs of Si-MCM-41-C, Sn-MCM-41-C(83) and Zr-MCM-41-C(39), respectively, while Fig. 3.14-a and b present transmission electron micrographs of Si-MCM-41-D and Zr-MCM-41-D(42), respectively. All the micrographs reveal show a reasonably regular array of channels in hexagonal arrangement. In the case of Si-MCM-41-C, the repeat distance between the channels in Si-MCM-41-C, Sn-MCM-41-C(83) and Zr-MCM-41-C(39) is about 37, 40 and 47 Å, respectively, which is consistent with the position of the first peak in the x-ray diffraction pattern of this material ($d_{100}\sqrt{3}/2$).

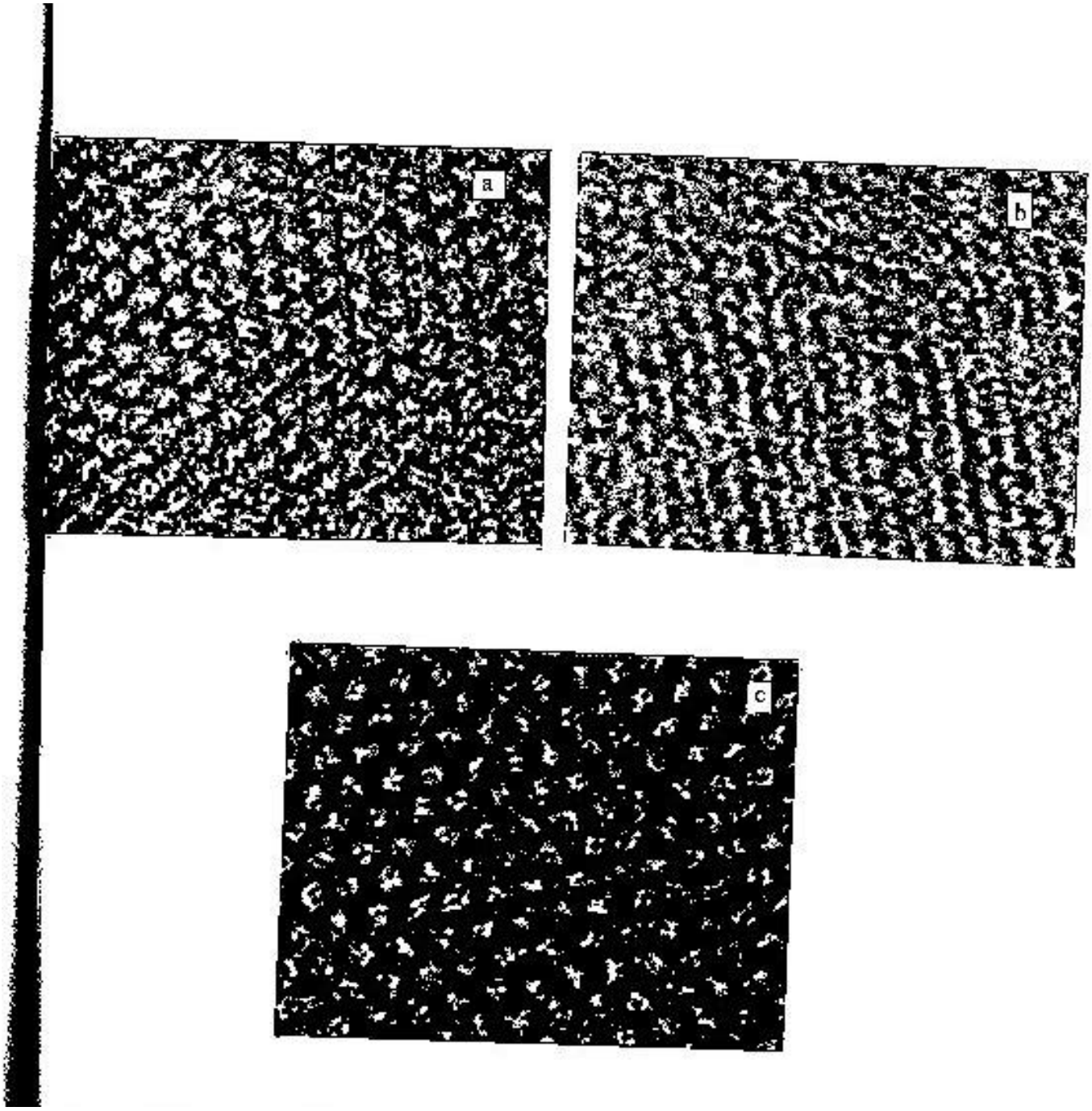

Fig. 3.13 Transmission electron micrographs of (a) Si-MCM-41-C; (b) Sn-MCM-41-C(83) and (c) Zr-MCM-41-C(39).

The channel size is also consistent with the estimated pore size (of about 28, 31 and 32 Å for Si-MCM-41-C, Sn-MCM-41-C(83) and Zr-MCM-41-C(39), respectively) calculated from N_2 sorption measurement.

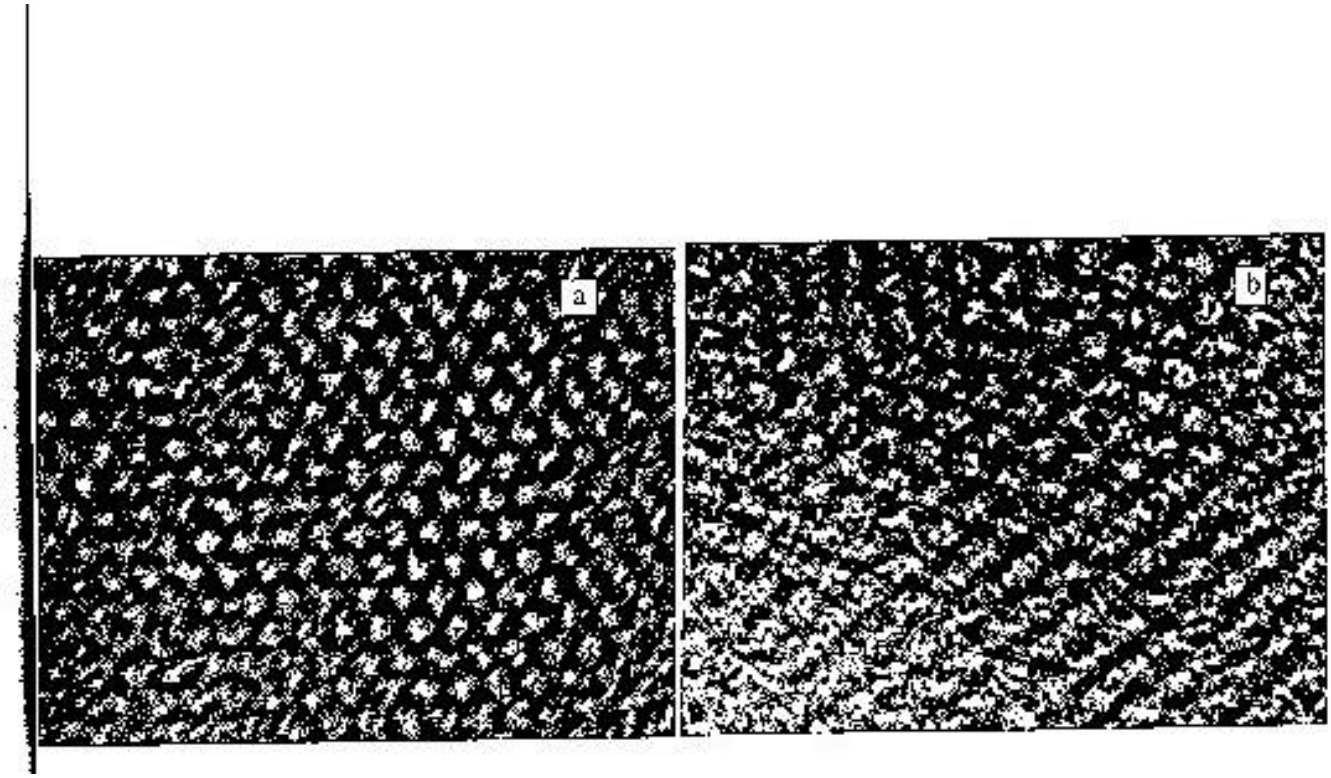

Fig. 3.14 Transmission electron micrographs of (a) Si-MCM-41-D and (b) Zr-MCM-41-D(42).

The repeat distance between the channels is about 42 and 45 Å for Si-MCM-41-D and Zr-MCM-41-D(42), respectively (Fig. 3.14), which is similar to the unit cell value. The channel size is also consistent with the estimated pore size (of about 22 Å) calculated from N_2 sorption measurement.

3.3.2(v) Scanning Electron Microscopy (SEM)

Scanning electron micrographs of Sn-MCM-41-C(83) and Zr-MCM-41-C(39) samples are presented in Fig. 3.15 (SEM picture of Si-MCM-41-C is presented in Ch. II, section 2.2.2.1(iii), Fig. 2.7(B)-Si-MCM-41(40)), and those of Si-MCM-41-D, Sn-MCM-41-D(85) and Zr-MCM-41-D(42) samples are presented in Fig. 3.16. Little change in the morphology of the samples is noticed after heteroatom incorporation. The micrographs reveal agglomerates of small particles (0.1– 0.3 μm).

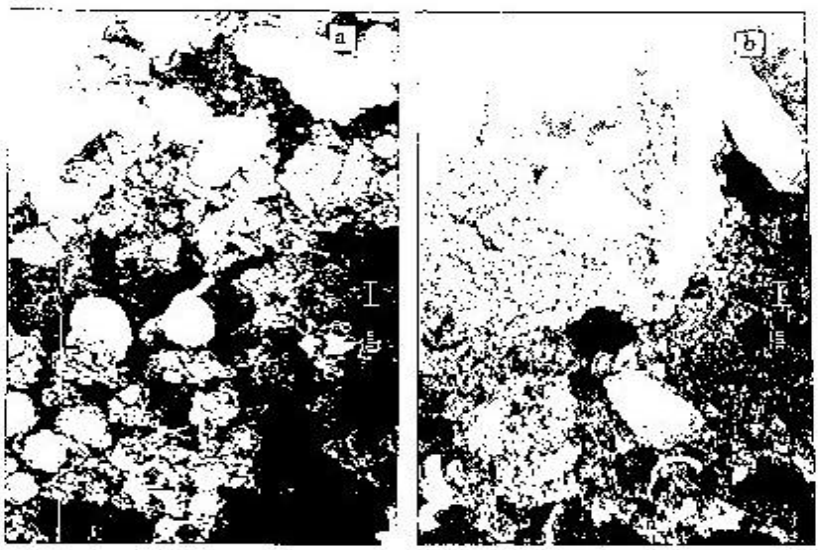

Fig. 3.15 Scanning electron micrographs of (a) Sn-MCM-41-C(83) and (b) Zr-MCM-41-C(39).

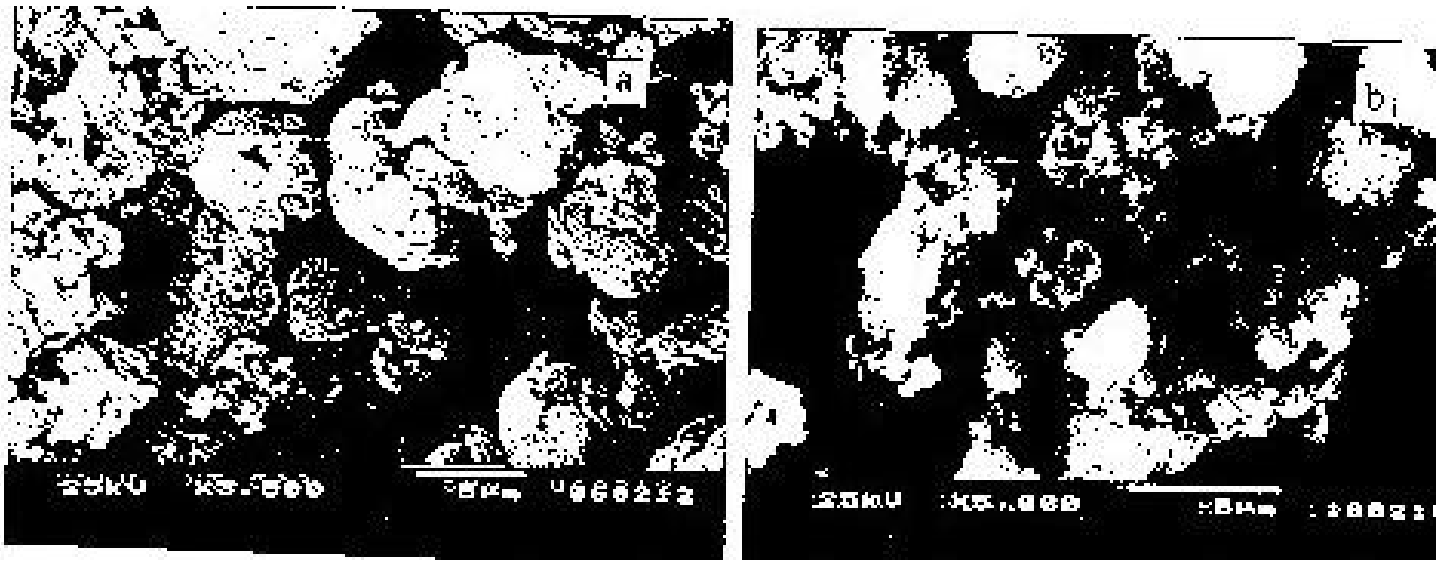

Fig. 3.16 Scanning electron micrographs of (a) Si-MCM-41-D and (b) Zr-M-41-D(42).

3.3.2(vi) TGA-DTA

Fig. 3.17(A) and 3.17(B) present the TGA and DTA curves of Si-MCM-41-C, Zr-MCM-41-C(96), Zr-MCM-41-C(39), respectively. All the samples show five step weight loss similar to Al-MCM-41 samples (Fig. 3.17(B)). The first step (below 130°C) in the TGA profile of Si-MCM-41-C sample is due to weight loss (~ 6.0 wt.%) from the desorption of physisorbed water held in the pores. The large (~ 25%) weight loss in the temperature range of 130 - 320°C followed by smaller weight losses of 9.5%, 5.1% and 4.4% in the temperature range of 300 - 650°C is mainly due to oxidative decomposition of templates and also loss of water molecules due to condensation of silanol groups.

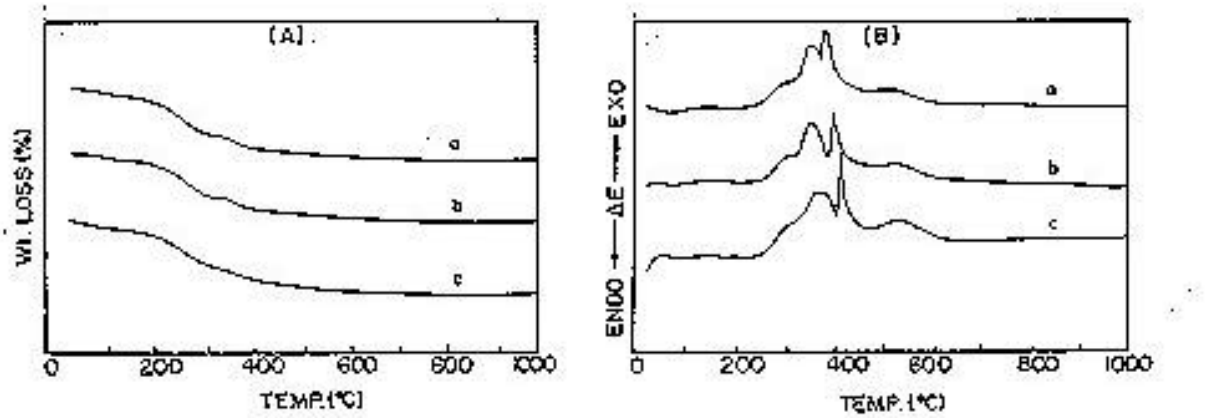

Fig. 3.17 (A) TGA profiles and (B) DTA profiles of as-synthesized (a) Si-MCM-41-C; (b) Zr-MCM-41-C(96) and (c) Zr-MCM-41-C(39).

The weight loss is almost similar for both Zr-MCM-41 and Si-MCM-41-C due to dehydration of water (1st step). The T_{max} for 2nd to 4th steps is shifted to higher temperatures (~ 10°C) with increase in Zr content with the exotherms becoming slightly sharper. The total weight loss due to oxidative decomposition of associated templates (and water from silanol groups) also remain almost same (~ 43.0%; upto 650°C).

Fig. 3.18(A and B) shows the TGA-DTA curves of Si-MCM-41-D, Zr-MCM-41-D(102) and Zr-MCM-41-D(42) samples. The DTA curves of these samples also show five steps of weight loss (Fig. 3.18(B)). The weight loss due to oxidative decomposition of associated templates also remains nearly the same (~ 35%) for all the samples upto 650°C. The lower weight loss (by ~ 8 %) on changing the organic template (from CTMACl to DTMABr) is due to the smaller size of the template. If we assume the size of the polar end ($-N^+(CH_3)_3$) of the template molecules, their

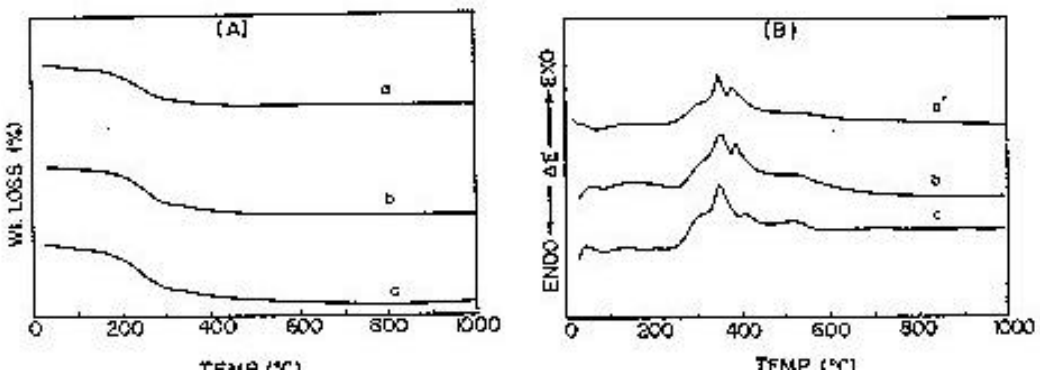

Fig. 3.18 (A) TGA profiles and (B) DTA profiles of as-synthesized (a) Si-MCM-41-D; (b) Zr-MCM-41-D(102) and (c) Zr-MCM-41-D(42).

packing densities and the length of the micellar units to be similar, then the weight loss due to template loss should be related to the molecular weight of the surfactant (formula weight for $CTMA^+$ = 284 and $DTMA^+$ = 228). Our observations on weight loss are in conformity with the above idea.

Fig. 3.19 and Fig. 3.20 present the thermoanalytical curves of Sn-MCM-41 samples prepared using CTMACl/OH and DTMABr, respectively. The DTA curves (Fig. 3.19(B) and 3.20(B)) of the two Sn systems are not as well separated as in the Al or Zr system. It is observed that for Si-MCM-41-C, Sn-MCM-41-C(83) and Sn-MCM-41-C(42), the weight loss due to dehydration of

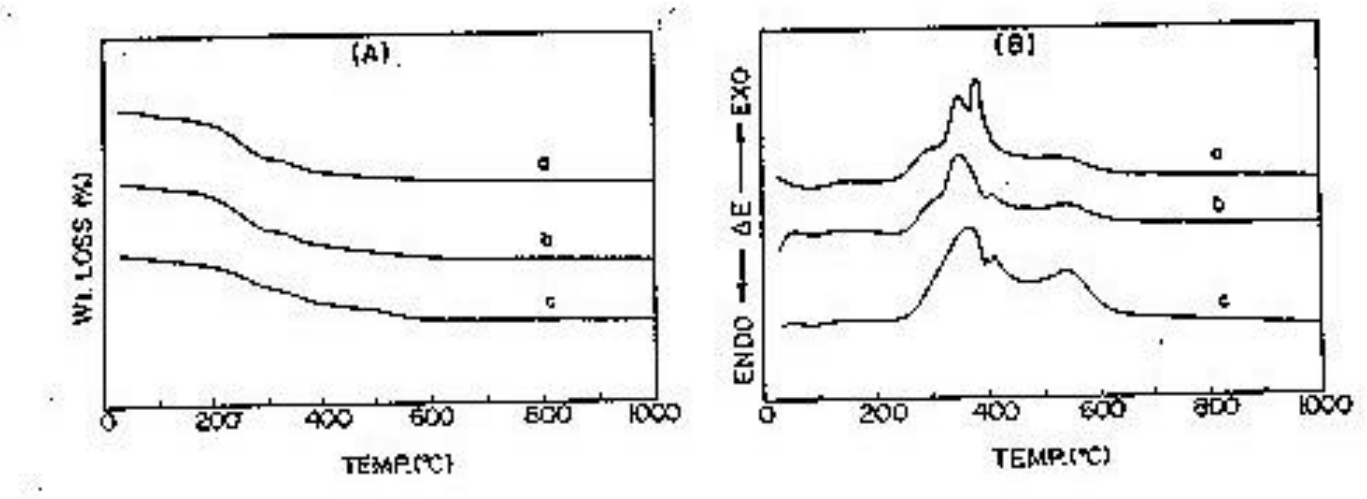

Fig. 3.19 (A) TGA profiles and (B) DTA profiles of as-synthesized (a) Si-MCM-41-C; (b) Sn-MCM-41-C(83) and (c) Sn-MCM-41-C(42).

water molecules is ~ 4% and loss due to template combustion is in the range of 45-50%. The weight loss for template combustion in the case of Si-MCM-41-D, Sn-MCM-41D(85) and Sn-MCM-41-D(43) (exotherms, from step 2 to step 5 upto ~ 650°C) is ~ 35%. This is again attributed to template size effect. On isomorphous substitution of Si by Sn, an increase in T_{max} is also observed for both sets of samples.

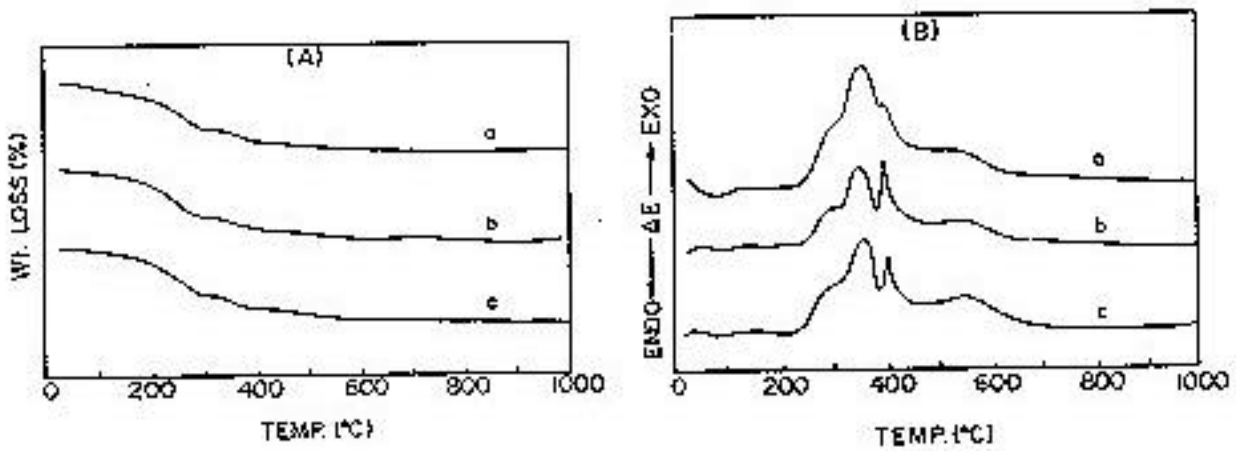

Fig. 3.20 (A) TGA profiles and (B) DTA profiles of as-synthesized (a) Si-MCM-41-D; (b) Sn-MCM-41-D(85) and (c) Sn-MCM-41-D(43).

3.3.2(vii) FTIR

The FTIR spectra of as-synthesized and calcined M-MCM-41-C and M-MCM-41-D samples are presented in Fig. 3.21. The values of some major absorption bands are compiled in Table 3.6.

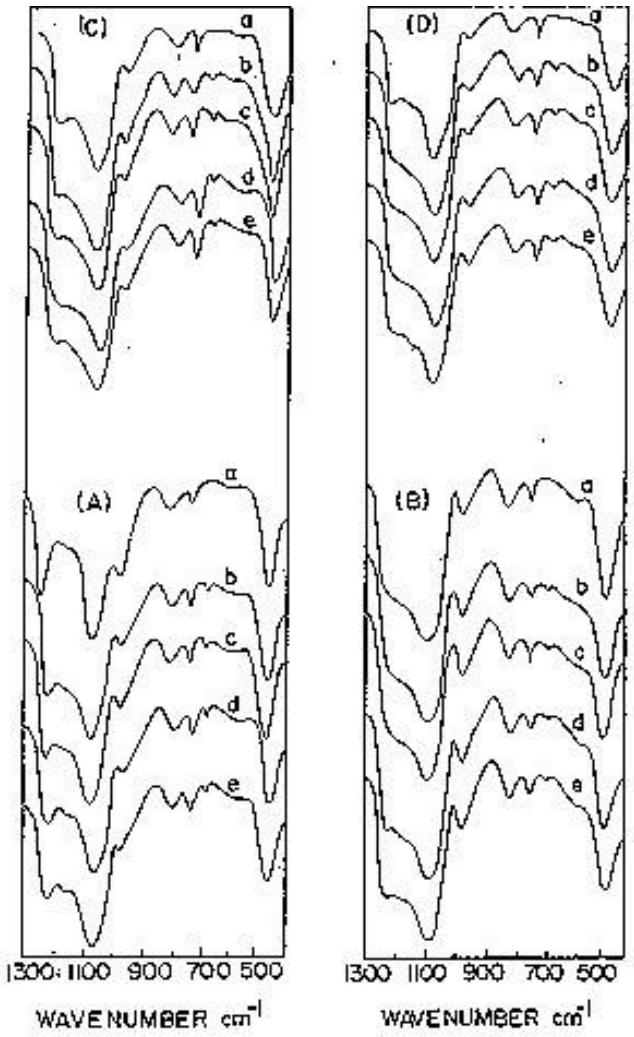

Fig. 3.21 FTIR spectra of (A) as-synthesized and (B) calcined (a) Si-MCM-41-C; (b) Zr-MCM-41-C(55); (c) Zr-MCM-41-C(39); (d) Sn-MCM-41-C(83) and (e) Sn-MCM-41-C(42), (C) as-synthesized and (D) calcined (a) Si-MCM-41-D; (b) Zr-MCM-41-D(59); (c) Zr-MCM-41-D(42); (d) Sn-MCM-41-D(85) and (e) Sn-MCM-41-D(43).

Table 3.6 FTIR absorption frequencies of Samples

Sample	Wavenumber (cm^{-1})	
	As-synthesized	***Calcined***
Fumed silica	1101	-
Si-MCM-41-C	1067	1089
Zr-MCM-41(55)	1065	1086
Zr-MCM-41(39)	1062	1086
Sn-MCM-41(83)	1061	1084
Sn-MCM-41(42)	1059	1082
Si-MCM-41-D	1074	1085
Zr-MCM-41-D(59)	1067	1084
Zr-MCM-41-D(42)	1064	1082
Sn-MCM-41-D(85)	1065	1084
Sn-MCM-41-D(43)	1063	1082

As explained in the case of Al-MCM-41 samples (Section 3.3.1(ix)), the spectra show five main absorption bands between the regions 1210 - 1245 (due to external asymmetric stretching vibrations of five membered Si-O rings[29], which is an evidence for the presence of 5 membered rings in the walls of MCM-41 structure), 1055-1090 (broad and strongest band; due to internal asymmetric stretching mode of SiO_4 (TO_4) skeleton), 960-970, 790-805 and 440-465 cm^{-1}, similar to amorphous fumed silica[16,27,28] (Fig. 3.21). The band due to T-O-T lattice vibration is shifted to lower wavenumbers for M-MCM-41 probably due to the incorporation of metal ion into the channel walls as the M-O bonds are longer than Si-O bond[16].

Fig. 3.21 shows that the strongest band (1060-1090cm^{-1}) in the case of as-synthesized Si-MCM-41-D and M-MCM-41-D samples, is slightly shifted towards higher wavenumbers. This shift is in accordance with the length of the alkyl chain in the surfactant molecule, the

micelles of the smaller template molecules (DTMABr) causing less stretching of Si-O bonds than in the case of Si-MCM-41-C and M-MCM-41-C (synthesized using surfactant molecules containing longer alkyl chains (C_{16})).

3.3.2(viii) UV-visible Spectroscopy

The diffuse reflectance spectra of calcined Sn-MCM-41-C and Sn-MCM-41-D samples reveal absorption at 208 ± 5 nm (Fig.3.22(A)). The intensity of this absorption band increases with increase in Sn content in the samples and reveals the presence of well dispersed Sn^{4+} (presumably in tetrahedral coordination). In addition to this band, an additional band at ~ 230 nm is observed in the case of Sn-MCM-41-C(42), Sn-MCM-41-D(85)and Sn-MCM-41-D(43) (Fig. 3.22(A), spectra c, d and e, respectively), indicative of the presence of small amounts of poorly dispersed (probably hexa coordinated) Sn species at high Sn contents. These observations are similar to those made by Mal *et al*. in the case of Sn-MFI molecular sieves[43]. For comparison, the spectra of pure SnO_2 and Sn-impregnated MCM-41 are also included in Fig. 3.22(A),(curves f and g). Both Sn-impregnated MCM-41 and SnO_2 show broad absorption at 280 ± 5 nm which may be assigned to hexacoordinated polymeric Sn-O-Sn type of species.

The dispersion of Zr(IV) cations in the silica matrix was also studied by UV-visible spectroscopy. Fig. 3.22(B) presents the UV-visible spectra of the calcined Zr-MCM-41-C and Zr-MCM-41-D samples, alongwith that of Si-MCM-41 and pure ZrO_2 samples. All the Zr containing samples exhibit a band around 210 nm attributable to a O $\rightarrow$ Zr(IV) charge transfer transition. This band in neat ZrO_2 occurs at 240 nm (Fig. 3.22(B), spectrum f). A shift of this band towards higher energy side is perhaps due to monoatomic dispersion of zirconium in

Zr-MCM-41 samples. Similar shift in the charge transfer band was observed by others also in Ti containing MCM-41 samples[44,45]. The band broadens with increasing Zr content in the samples.

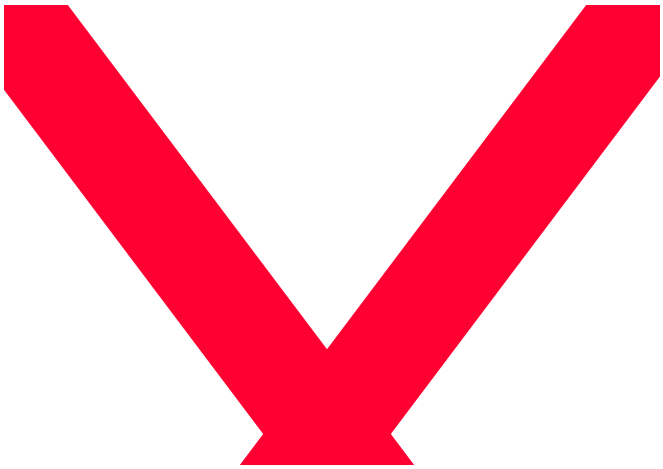

Fig. 3.22 Diffuse reflectance UV-vis spectra of (A) calcined (a) Si-MCM-41-C; (b) Sn-MCM-41-C(83); (c) Sn-MCM-41-C(42); (d) Sn-MCM-41-D(85); (e) Sn-MCM-41-D(43); (f) Sn-impregnated MCM-41 and (g) SnO_2 and (B) calcined (a) Si-MCM-41-C, (b) Zr-MCM-41-C(55), (c) Zr-MCM-41-C(39), (d) Zr-MCM-41-C(23); (e) Zr-MCM-41-D(33) and (f) ZrO_2.

3.3.2(ix) ^{29}Si MAS NMR

The ^{29}Si MAS spectra obtained for Sn-MCM-41 and Zr-MCM-41-D systems are compared with that of Si-MCM-41 in the as-synthesized as well as the calcined forms (Fig. 3.23 and 3.24, respectively). The as-synthesized samples show broad resonances with chemical shifts at δ = ~ -102 and -112 ppm which are assigned to the Q_3 and Q_4 silicon environments, respectively.

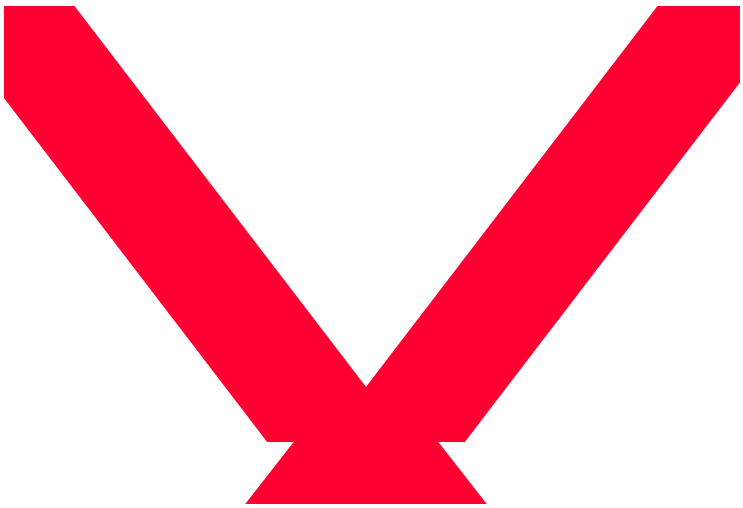

Fig. 3.23 ^{29}Si MAS NMR spectra of as-synthesized (a) Si-MCM-41-C; (b) Sn-MCM-41-C(83) and (c) Sn-MCM-41-C(42) and calcined (d) Si-MCM-41-C; (e) Sn-MCM-41-C(83) and (f) Sn-MCM-41-C(42).

The broadness of the ^{29}Si signals has been attributed to the large distribution of the TOT angles[3]. The lack of high sensitivity for ^{29}Si signals is indicative of the long spin lattice relaxation time associated with the MCM-41 system. It is evident from these spectra that tin or zirconium substitution does not give rise to any additional ^{29}Si peaks. As expected, due to dehydroxylation, the intensity of the Q_3 sites decreases on calcination of the samples.

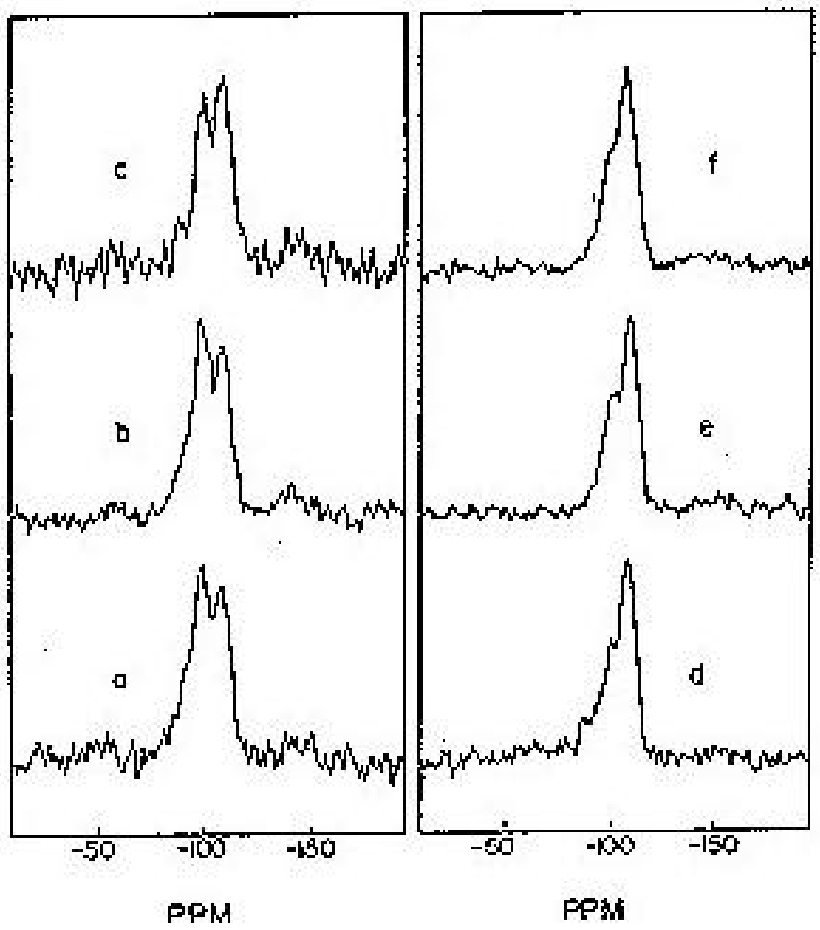

Fig. 3.24 ^{29}Si MAS NMR spectra of as-synthesized (a) Si-MCM-41-D; (b) Zr-MCM-41-D(59) and (c) Zr-MCM-41-D(42) and calcined (d) Si-MCM-41-D; (e) Zr-MCM-41-D(59) and (f) Zr-MCM-41-D(42).

3.3.2(x) ^{13}C NMR.

The ^{13}C CP/MAS NMR spectra of Sn-MCM-41, Si-MCM-41 and CTMACl are presented in Fig. 3.25. A comparison of the ^{13}C CP/MAS NMR spectra of the uncalcined MCM-41 and Sn-MCM-41 samples (Fig. 3.25(a-c)) with that of $CTMA^+$ cations in solution shows (Fig. 3.25 (d)) that $CTMA^+$ cations remain intact inside the pores of the molecular sieves. The ^{13}C NMR spectra of the $CTMA^+$ in solution and uncalcined Sn-MCM-41 are similar, except for minor

changes in the chemical shifts and resolution. The maximum shift (δ = ~ 1.4 ppm) is observed for the terminal methyl carbon.

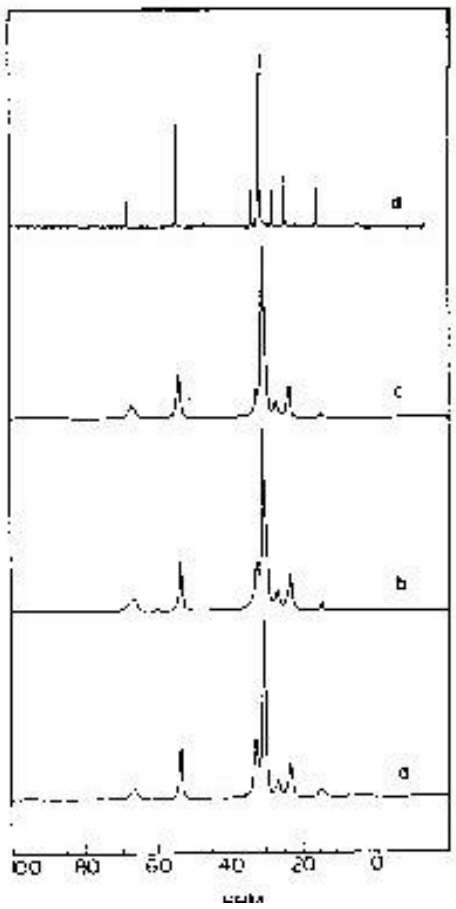

Fig. 3.25 ^{13}C CP/MAS NMR spectra of as-synthesized (a) Si-MCM-41-C; (b) Sn-MCM-41-C(83); (c) Sn-MCM-41-C(42) and (d) aqueous solution of $CTMA^+$ ions.

The methyl carbon is shifted to a higher field when the surfactant is in the zeolite channel. The peak at δ = 66 ppm can be assigned to the methylene carbon of the cetyl chain bonded to the nitrogen atom. The three methyl groups bonded to nitrogen atoms resonate at 53 ppm. The signals between 22 ppm and 32 ppm are from the different methylene carbon atoms in the cetyl

chain. A comparison of the ^{13}C CP/MAS NMR spectrum of Sn-MCM-41 (Fig. 3.25 (b) and (c) with that of Si-MCM-41 (Fig. 3.26 (a)) reveals negligible peak broadening for the =N-CH_2 (at δ = 66 ppm) and the =N-CH_3 (at δ = ~ 54 ppm) carbons in the former sample compared to the latter one. A broadening of these lines has been correlated by earlier workers with the negative charge on the framework of transition metal incorporated MCM-41[46]. It appears, therefore, that the incorporation of Sn occurs mainly as Sn^{4+} ions, which do not change the charge on the framework unlike the incorporation of di- and trivalent metal cations such as Co and Fe.

3.3.2(xi) ^{119}Sn MAS NMR

Though the natural abundance and the magnetogyric ratio of ^{119}Sn are higher than that of ^{29}Si, the detection of Sn in stannosilicates is not easy due to the low incorporation, long spin lattice relaxation times and to some extent the large chemical shift anisotropy (CSA). Nevertheless, an attempt has been made to record the static and MAS spectra of Sn-MCM-41 samples, the results of which are presented in Fig. 3.26. The ^{119}Sn spectrum of pure SnO_2 (static) (Fig. 3.26 (a)) and a 5% (w/w) mixture of SnO_2 in Si-MCM-41 (Fig. 3.26 (d)) are also presented for comparison. The overall sensitivity of the ^{119}Sn in Sn-MCM-41 is low, especially under magic angle spinning conditions. The better sensitivity obtained for the samples recorded in the static mode than under MAS conditions is due to the large amount of sample (~ 4 times) that could be accommodated in the sample tube (10 mm o.d., ~ 5 cm length) in the static measurements. Isotopic chemical shifts of δ = ~ - 677 ppm and δ = - 710 ppm, respectively, are observed for Sn-MCM-41(83) and Sn-MCM-41(42). Under the same experimental conditions, the chemical shift of octahedrally coordinated tin in pure SnO_2 shows a chemical shift of δ = -604 ppm (Fig. 3.26 (d)). Thus, the chemical shift values obtained for Sn-MCM-41 samples can be attributed to the tetrahedral coordination of the Sn^{4+} ions.

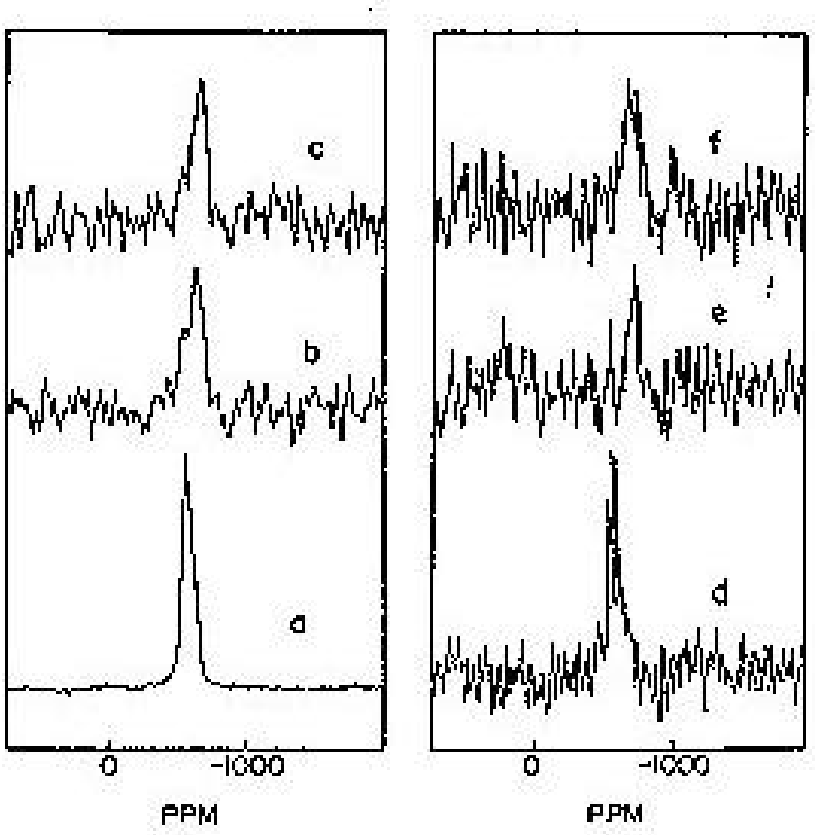

Fig. 3.26 ^{119}Sn static NMR spectra of (a) SnO_2; (b) Sn-MCM-41-C(83) and (c) Sn-MCM-41-C(42) and MAS NMR spectra of (d) 5% (w/w) mixture of SnO_2 and Si-MCM-41-C; (e) Sn-MCM-41-C(83) and (f) Sn-MCM-41-C(42).

3.3.2(xii) Mössbauer spectroscopy of Sn-MCM-41 samples

Mössbauer spectra of the tin containing samples (Sn-MCM-41-C(133), Sn-MCM-41-C(83) and Sn-MCM-41-C(42), a, b and c, respectively) are shown in Fig. 3.27(A) and the parameters obtained from the corresponding fits are collected in Table 3.7. Besides the regular Mössbauer parameters (isomer shift (IS), and quadruple splitting (QS), respectively) the corresponding $d\ln(A_{300}/A_{77})/dT$ values were also determined (A is the spectral area of the given component relative to the base line at 300K or 77K).

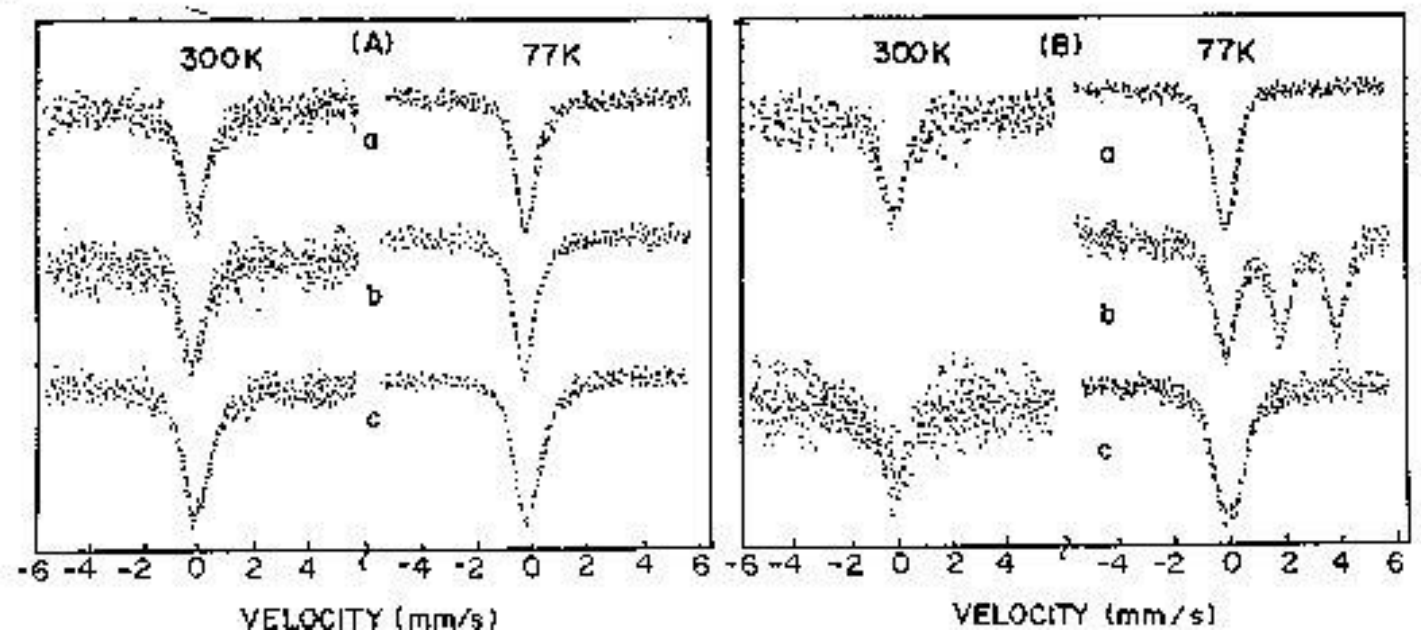

Fig. 3.27 (A) ^{119}Sn Mössbauer spectra of Sn-MCM-41-C samples at 300K and 77K (a) Sn-MCM-41-C(133); (b) Sn-MCM-41-C(83) and (c) Sn-MCM-41-C(42) and (B) In situ ^{119}Sn Mössbauer spectra obtained on (a) Sn-MCM-41-C(83); (b) Sn-MCM-41-C(83) treated in hydrogen at 670K for 2h and (c) as b, Sn-MCM-41-C(83) treated in air at 520 K for 2h.

The sample Sn-MCM-41-C(83) exhibiting the largest $d\ln(A_{300}/A_{77})/dT$ value was selected for further *in situ* reduction/oxidation studies. Spectra obtained after reduction at 670K and calcination 520K are shown in Fig. 3.27(B) and the corresponding IS, QS and dlnA/dT values are presented in the second half of Table 3.7.

Samples Sn-MCM-41-C(133) and Sn-MCM-41-C(82) exhibit rather low isomer shift values (close to -0.2 mm/s). Similar IS values were reported on tin containing zeolites[47,48]. This low value is probably characteristic of tetrahedrally coordinated Sn^{4+}. For this assignment it may be recalled that the value of the isomeric shift of tin is a result of contributions from p- and s- electrons. An increase of the p-symmetry results in a decrease of the isomer shift.

Table 3.7 Mössbauer parameters of the Sn-MCM-41-C samples

Sample	Treatment	Compo-nent	Temperature				$d\ln(A_{300}/A_{77})/dt \times 10^{-2}$
			300K		77K		
			Is	QS	Is	QS	
Sn-MCM-41-C(133)	Calcined	Sn^{4+}	-0.24	0.22	-0.21	0.31	0.665
Sn-MCM-41-C(83)	Calcined	Sn^{4+}	-0.26	0.37	-0.21	0.32	0.863
Sn-MCM-41-C(42)	Calcined	Sn^{4+}	-0.10		-0.09	0.47	0.496
Sn-MCM-41-C(83)	Calcined	Sn^{4+}	-0.26	0.37	-0.21	0.32	0.863
	670K/ H_2	Sn^{4+}			-0.21	0.33	0.783
		Sn^{2+}			2.77	1.95	1.22
	520K/ air	Sn^{4+}	-0.12	0.56	-0.10	0.57	0.627
	620K/H_2	Sn^{4+}			-0.15	0.56	
		Sn^{2+}			2.96	2.21	

Compared to octahedral bonding as in SnO_2[49], tetrahedral bonding requires a larger contribution from p-electrons. Thus, it appears that the Sn ions in Sn-MCM-41-C(133) and Sn-MCM-41-C(83) are present mostly in tetrahedral coordination, suggesting that a major part of tin is present as isomorphous substituent for Si.

The sample with the largest tin content, Sn-MCM-41-C(42) exhibits an intermediate IS value (-0.1 mm/s), lying in-between the previously considered -0.2 mm/s and 0.0 mm/s values, the latter being characteristic for SnO_2 with octahedral coordination. Thus, it appears likely that the -0.1 mm/s IS value is due to the presence of both types of coordinations, i.e. the tetrahedral (framework substituted) and the octahedral (extra-framework), in comparable amounts in Sn-MCM-41-C(42). It is also worth mentioning that the QS value obtained for Sn-MCM-41-C(42) is the largest among the values obtained for the samples, attesting further to the presence of extra-framework SnO_2.

The comparison of dlnA/dT values is also worthy of consideration. Although the values scatter to a certain extent (which might also be partly attributed to differences in sample thickness, etc.), sample Sn-MCM-41-C(42) exhibits the lowest $dln(A_{300}/A_{77})/dT$ value, attesting for the strongest average Sn-O bond in this sample (the stronger the bond, the smaller is the dlnA/dT value[49]). Again, this feature can probably be attributed to the contribution of SnO_2 which has a low $dln(A_{300}/A_{77})/dT$ value[49].

Besides the IS = - 0.2 mm/s value, sample Sn-MCM-41(83) exhibits the largest dlnA/dT value. This large value is attributed to the presence of isomorphically substituted tin to a large extent in the MCM-41 structure; thus, this sample was selected for further studies on the effects of reduction and oxidation treatments on the state of substituted Sn^{4+}. The treatment in a flow of hydrogen at 670K resulted in partial reduction; more than a half of the Sn^{4+} was reduced to the Sn^{2+} state. The IS and QS parameters are close to those characteristic of the so called red modification of SnO, or those of hydroxo-complexes of Sn^{2+} [50]. In addition, the dlnA/dT value obtained for the Sn^{2+} component is considerably large. Thus, the Sn^{2+} component is probably present in a loosely bound form (e.g. in a hydroxylated state, forming Si-O-Sn^{2+}-OH groups).

The subsequent oxidation treatment in air at 520K resulted in the full reoxidation to Sn^{4+} state. However, the original tetrahedral coordination does not appear to be restored, as suggested by the increase in IS and QS values (Table 3.7). Most probably SnO_2 is formed to a significant extent, due to the redox treatment, since the IS and QS values are shifted towards the characteristic values of this compound. Correspondingly, a decrease of $dln(A_{300}/A_{77})/dT$ value of Sn^{4+} is also noticed. Table 3.7 contains IS and QS values of Sn-MCM-41-C(83) which was reduced at a lower temperature (620K). It is observed that if the temperature of the hydrogen

treatment is reduced from 670K to 620K, it results in slight difference in the IS and QS values of the Sn^{2+} component.

Fig. 3.28(A) presents Mössbauer spectra and the Table 3.8 presents corresponding Mössbauer parameters for two Sn-MCM-41-D(85) and Sn-MCM-41-D(43) samples, while spectra of Sn-MCM-41-D(43) obtained after 620K reduction and 573K oxidation are shown in Fig. 3.28(B) and the corresponding IS, QS and dlnA/dT values are presented in Table 3.8.

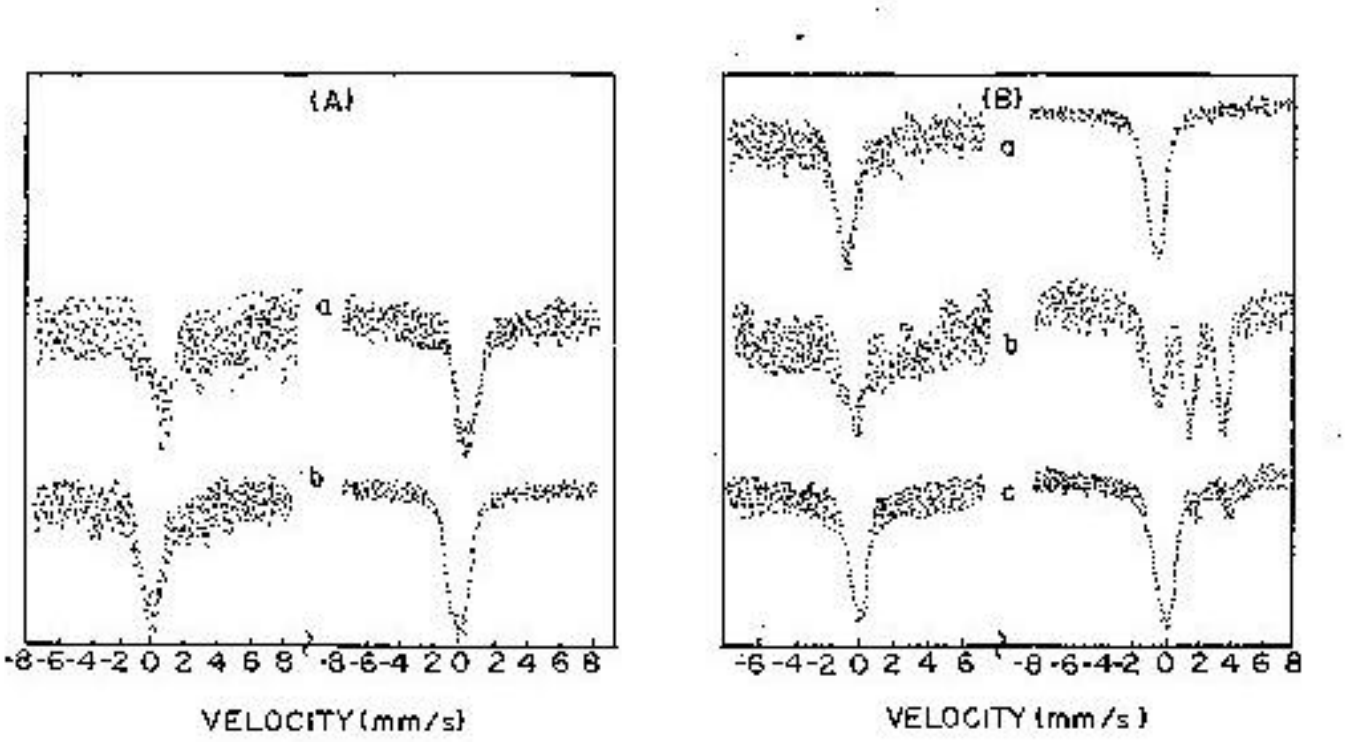

Fig. 3.28 (A) ^{119}Sn Mössbauer spectra of Sn-MCM-41-D samples at 300K and 77K (a) Sn-MCM-41-D(85) and (b) Sn-MCM-41-D(43) and (B) In situ ^{119}Sn Mössbauer spectra obtained on (a) Sn-MCM-41-D(43); (b) Sn-MCM-41-C(43) treated in hydrogen at 620K for 2 h and (c) as b, Sn-MCM-41-C(43) treated in air at 573K for 2h.

Table 3.8 Mössbauer parameters of the Sn-MCM-41-D Samples

Sample	Treatment	Compo-nent	Temperature				$Dln(A_{300}/A_{77})/dt \times 10^{-2}$
			300K		77K		
			Is	QS	Is	QS	
Sn-MCM-41-D(85)	Calcined	Sn^{4+}	-0.10	0.17	-0.13	0.66	0.617
	620K/H_2	Sn^{4+}			-0.05	0.45	
		Sn^{2+}			3.08	2.11	
Sn-MCM-41-D(43)	Calcined	Sn^{4+}	-0.12	0.46	-0.15	0.65	0.686
	620K/H_2	Sn^{4+}	-0.09	0.15	-0.05	0.56	0.374
		Sn^{2+}	3.21	1.83	3.06	2.17	1.106
	573K/air	Sn^{4+}	-0.04	0.5	-0.02	0.64	0.479
		Sn^{2+}	3.35	1.64	3.15	2.06	0.667

Both samples exhibit an IS value (- 0.1 mm/s, Table 3.8) lying in between – 0.2 mm and 0.0 mm/s values, which indicates that samples contain both types of coordination *i.e.*, tetrahedral (framework substituted) and octahedral (extraframework). The overall comparison of the Mössbauer data between these two series of samples (Series C and D) does not reveal much difference in the IS and QS values. It seems that the use of the two different surfactants in the synthesis does not result in different species, which can be distinguished by the Mössbauer method.

From the Mössbauer data of both the series, two observations can be made:

1. The isomer shift values of Sn^{4+} are dominantly in the negative velocity range below 0.0 mm/s, indicating a large contribution from Sn^{4+} (tetrahedral coordination).

2. The dlnA/dT values are significantly larger than observed for SnO_2 (dlnA/dT for SnO_2 is 0.1^{50}), suggesting weak binding of Sn. Thus these ions are probably bound to Si in the

MCM-41 (Sn-O-Si bond is weaker than Sn-O-Sn).

These two points suggest that Sn^{4+} probably mainly occupies positions in the walls of MCM-41.

Finally, it is worth comparing the present Mössbauer data obtained on tin containing MCM-41 with those obtained on medium pore MFI, MEL and large pore MTW tin silicalites[48]. In general, similarities such as the presence of tetrahedrally coordinated Sn^{4+}, and reducibility of a certain amount of Sn^{4+} to Sn^{2+} in the structure[48] are noticed. On the other hand, the MCM-41 structure exhibits a smaller ability for stabilizing the Sn^{2+} state. For instance, all the Sn^{2+} was reoxidized to Sn^{4+} by the 520 K treatment in air, while in the other medium pore zeolites the presence of Sn^{2+} was observed in significant amounts after similar treatments (this stabilization of Sn^{2+} was attributed to formation and stabilization of Si-O-Sn-O groups[48]). In the MCM-41 structure the formation of similar groups is probably less pronounced, although the formation of hydroxylated Si-O-Sn^{2+}-OH groups may occur after reduction treatments.

3.3.2(xiii) ESR spectroscopy of Zr-MCM-41-C Samples

Calcined samples of Zr-MCM-41-C are ESR silent both at 298K and 77K. However, on evacuation (10^{-5} Torr; above 623K for 5h) a weak, isotropic signal centered at $g_{av} = 2.0023$, with a peak-to-peak linewidth of 6 G, appears. The intensity of the signal is proportional to the treatment temperature. The spectrum becomes anisotropic (with $g_{\parallel} = 2.0013$ and $g_{\perp} = 2.0028$) at 873K. Representative ESR spectra of Zr-MCM-41-C(39) revealing the effect of thermo-evacuation are shown in Figure 3.29. The origin of these signals is attributed to the presence of electrons trapped in oxygen vacancies (i.e., framework defects).

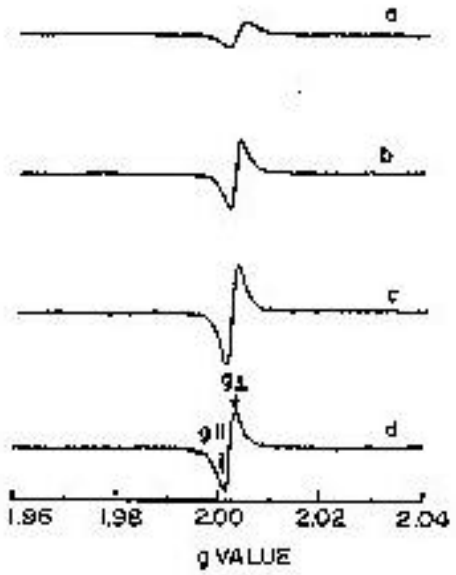

Fig. 3.29 ESR spectra of Zr-MCM-41-C(39) after evacuation at different temperatures. (a) 623K; (b) 723K; (c) 823K and (d) 873K.

Zr-MCM-41-C samples, after reduction with dry hydrogen at 673K, exhibit spectra corresponding two types of species I and II, at 77K. Species I is characteristic of a Zr(III) ion with a $4d^1$ electronic configuration (S = ½) and species II corresponds to a superoxide anion with a rhombic g symmetry (g_1 = 2.0310, g_2 = 2.0076, g_3 = 2.0010). Reduction experiments at different temperatures indicate that species I could be generated in high yields at 873K. Si-MCM-41-C samples after interaction with dry hydrogen do not show any ESR signals and hence, conform the origin of species I and II as due to the heteroatom, zirconium only. During these ESR studies, interaction of Zr(III) ions (species I) with atmospheric oxygen could not be completely avoided. This interaction resulted in the formation of zirconium(IV) superoxide radical ions, $Zr^{IV}(O_2^{\cdot -})$ (species II). Figure 3.30 shows ESR spectra, at 77K, of Zr-MCM-41 samples with varying Si/Zr ratio. The signals corresponding to species I and II are marked. The intensity of the signal due to species I increases with higher zirconium content.

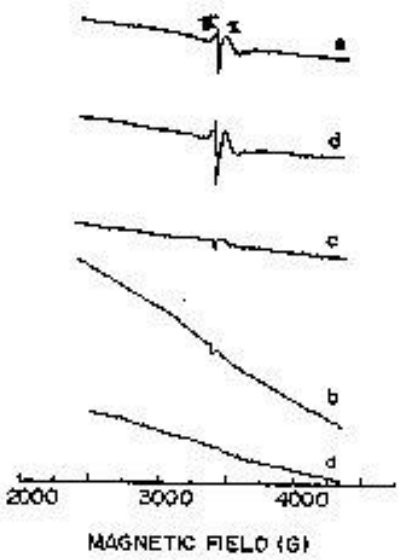

Fig. 3.30 ESR spectra of MCM-41 samples after treatment with dry hydrogen. (a) Si-MCM-41-C; (b) Zr-MCM-41-C(96); (c) Zr-MCM-41-C(55); (d) Zr-MCM-41-C(39)and (e) Zr-MCM-41-C(23).

Zr-MCM-41-C samples were also reduced by $LiAlH_4$. The ESR spectra of the reduced samples are shown in Figure 3.31. The spectra are almost similar to those of hydrogen reduced samples (Figure 3.30). It appears that Zr(IV) is reduced to a greater extent by $LiAlH_4$ than by dry hydrogen.

In samples Zr-MCM-41-C(39) and Zr-MCM-41-C(23), Zr(III) ions (species I) are highly unstable towards molecular oxygen. Upon exposing the reduced samples to air the signals due to species I decrease and those of species II ($Zr^{IV}(O_2^{\cdot-})$) increase. Interestingly, the behaviour of species I in Zr-MCM-41-C(96) and Zr-MCM-41-C(55) is different. Species I in those samples is stable even after 16h of contact with air. This observation indicates the presence of two types of Zr sites in Zr-MCM-41-C samples.

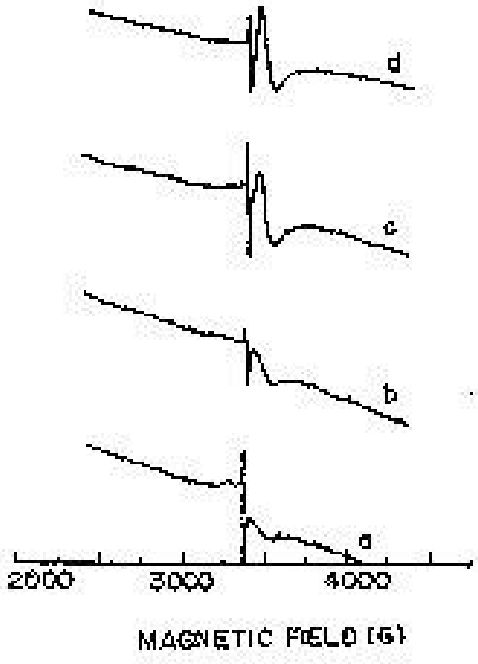

Fig. 3.31 ESR spectra of Zr-MCM-41 samples after reaction with $LiAlH_4$ in dry THF. (a) Zr-MCM-41-C(96); (b) Zr-MCM-41-C(55); (c) Zr-MCM-41-C(39) and (d) Zr-MCM-41-C(23).

In samples containing lower amounts of zirconium *i.e*., Zr-MCM-41-C(96) and Zr-MCM-41-C(55), the heteroatom is mostly incorporated in the framework structure of MCM-41, replacing Si ions, and the substituted zirconium (probably in the walls) cannot be oxidized easily with molecular oxygen at 298K. On the other hand, the samples Zr-MCM-41-C(96) and Zr-MCM-41-C(55) contain Zr both in substitutional locations (type I') and on the surface of the pores (type I"). The latter type of Zr(III) ions (type I"), are highly reactive and readily form $Zr^{IV}(O_2^-)$ (species II) on exposure to the atmosphere. The signals due to types I' and I'' are marked in Figure 3.32. The substitutional Zr(III) ions (type I') are characterized by rhombic g values (g_1 = 1.876, g_2 = 1.943 and g_3 = 1.970) while the surface ions (type I") are characterized by axial g values ($g_{||}$ = 1.899 and $g_{\perp}$ = 1.961).

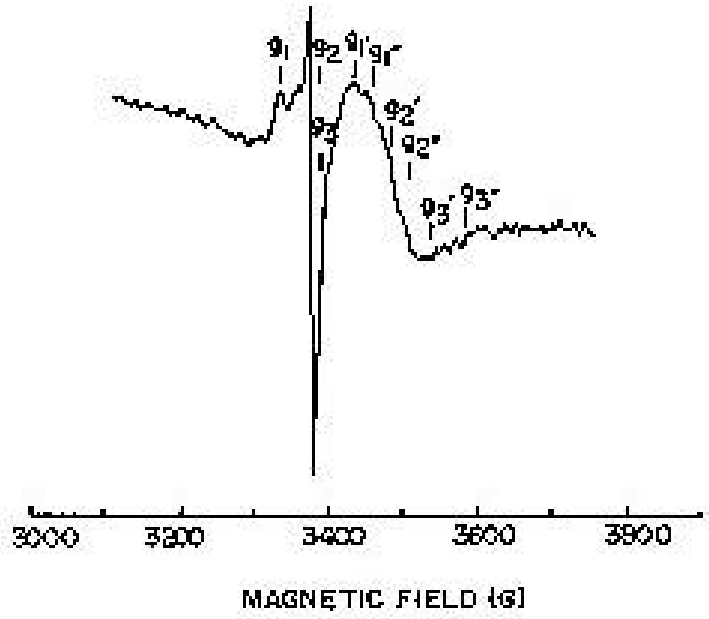

Fig. 3.32 ESR spectra of Zr-MCM-41-C(39) after treatment with dry hydrogen. The signals corresponding to the two types of Zr(III) sites are indicated.

Reduction of zirconium containing samples by γ-ray irradiation, at 77K, yields spectra typical of Zr(IV) superoxide radicals (species II). Figure 3.33(a) shows the ESR spectrum for Zr-MCM-41-C(23) samples irradiated and measured at 77K. Formation of two types of superoxide radicals (type II' with g_1 = 2.0319, g_2 = 2.0093 and g_3 = 2.0024 and type II" with g_1 = 2.0131, g_2 = 2.0098 and g_3 = 2.0045) are evident from Figure 3.33(a). Upon annealing the sample, species II' almost disappears and the spectrum (Figure 3.33(b)) corresponds mostly to species II". Impregnated samples with the same Zr content show a similar spectral pattern indicating that species II' and II" are due to two different types of surface superoxide anion radicals of Zr(IV). As observed in the chemically reduced samples, even on γ-ray irradiation the Zr ions undergo reduction initially from +4 to +3 state. Subsequent oxidation of Zr(III) ion due to interaction with atmospheric oxygen results in Zr(IV) superoxo radical ions. The superoxo

radical species II' could also be generated by interacting the Zr-MCM-41-C(39) and Zr-MCM-41-C(23) samples with 50% H_2O_2 solution.

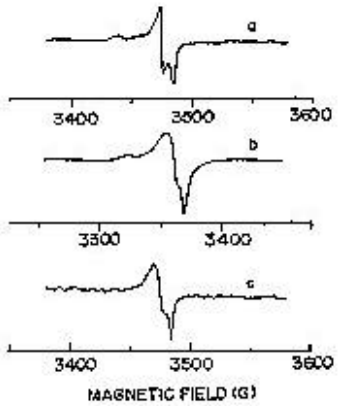

Fig. 3.33 ESR spectra of γ-ray irradiated samples. (a) Zr-MCM-41(23) irradiated and measured at 77K; (b) annealed and measured at 298K and (c) Zr impregnated Si-MCM-41 after irradiation at 77K.

Table 3.9 lists the ESR spin Hamiltonian parameters of different species generated by chemical oxidation and γ-ray irradiation. The calcined Zr-MCM-41-C samples show ESR signals on thermoevacuation at $g_{\|} = 2.0013$ and $g_{\perp} = 2.0028$. The origin of these signals could be due to the following: (a) presence of organic molecules used as structure directing agents in the synthesis of MCM-41 samples, (b) hydrocarbons adsorbed from the vacuum system (vacuum grease or oil) and (c) F-centers (i.e., electrons trapped in the oxygen vacancies at the surface of the pores). The presence of unburned template molecules is ruled out as the samples were calcined at 823K prior to the thermo-evacuation studies. Also necessary care was taken to avoid any adsorption of hydrocarbons from the vacuum system.

Table 2. ESR Spin Hamiltonian Parameters

System	Treatment	g_1	g_2	g_3	Assignment	Reference
Zr-MCM-41	$H_2/LiAlH_4$	1.943	1.970	1.876	Zr(III); Type I'	Present work
		1.961	1.961	1.899	Zr(III); Type I"	Present work
		2.001	2.008	2.031	$Zr(O_2^-)$; Type II'	Present work
Zr-MCM-41	γ-irradiation	2.0024	2.0093	2.0319	$Zr(O_2^-)$; Type II'	Present work
		2.0045	2.0098	2.0131	Superoxo species; Type II'	Present work
Zirconia/ Zirconia-Hydroxide	Thermal evacuation	1.978	1.978	1.953	Zr(III)	51, 52
		2.0036	2.0096	2.0336	$Zr(O_2^-)$	53-55
TS-1	CO/H_2	1.968	1.968	1.933	Ti(III)	56
Ti-MCM-41	γ-irr	1.967	1.967	1.901	Ti(III)	57

Hence, the paramagnetic signals observed in the calcined Zr-MCM-41-C samples on thermo-evacuation are attributed to the F-centers. In support to the formation of these colour centers we have also noticed a change in the colour of the samples from white to gray on thermal treatment. Formation of such defect centers was reported earlier on the surfaces of oxide materials,[58] zirconia[51,52] and zirconium hydroxide-oxide[58]. In zirconia and zirconium hydroxide-oxide systems Zr(III) ions (with $g_{\|} = 1.953$ and $g_{\perp} = 1.978$) were also formed in addition to the defect centers on thermo-evacuation[51,52,58]. However, in Zr-MCM-41, thermal treatments does not result in Zr(III) ions. This indicates the stabilizing role of the support silica and the difference in the redox behaviour of zirconium in Zr-MCM-41-C and neat zirconia samples.

However, the reduction of zirconium in Zr-MCM-41-C, from +4 to +3 state is achieved by reaction with dry hydrogen or $LiAlH_4$. ESR studies reveal at least two locations for Zr: substitutional sites in pore walls (type I') and at the surface of the pores (either as substitution

sites or as anchored/surface bound ZrO_2 (type I")). In samples Zr-MCM-41-C(96) and Zr-MCM-41-C(55), zirconium is isomorphously incorporated in the location of Si inside the pore walls while in samples Zr-MCM-41-C(39) and Zr-MCM-41-C(23), it occupies the surface of the pores in addition to the substitutional sites inside the pore walls. Type I' centers are characterized by a rhombic g tensor (g_1 = 1.876, g_2 = 1.943 and g_3 = 1.970) and type I" centers are characterized by an axial g tensor ($g_{||}$ = 1.899 and $g_{\perp}$ = 1.961). When Zr(IV) with a higher ionic radius (0.79 Å) occupies the Si location (ionic radius of Si = 0.41 Å), the local symmetry is distorted and hence, results in a rhombic g anisotropy. It is also interesting to note that the g values for Zr(III) ions (both type I' and I") in Zr-MCM-41-C samples are different from those observed for pure zirconia samples ($g_{||}$ = 1.953 and $g_{\perp}$ = 1.978)[51, 52]. The deviation is mainly due to a change in the molecular symmetry and also indicate the monoatomic dispersion of surface zirconia. The diffuse reflectance UV-visible spectra also provide evidence for monoatomic dispersion of surface zirconia by showing the ligand to metal charge transfer band at a higher energy (210 nm) compared to neat ZrO_2 (Section 3.3.2(viii)).

It is interesting to compare the spin Hamiltonian parameters of Zr(III) with Ti(III) in silicate molecular sieves. Both the ions are isoelectronic but the unpaired electron of Ti(III) occupies a 3d metal orbital while that of Zr(III) occupies a 4d orbital. Prakash *et al.*[56] have reported that Ti in titanosilicate molecular sieves TS-1 and titanium aluminophosphate molecular sieves (TAPO-5, TAPO-11, TAPO-31 and TAPO-36)[57] could be reduced by treating with CO or H_2. But Ti in MCM-41 structure could not be reduced by H_2 even at 650K, though reduction could be achieved by γ-irradiation[58]. Our observations reveal that Zr in MCM-41 could be reduced by H_2 at temperatures above 673K. The signals for Ti(III) ions occurred at $g_{\perp}$ = 1.968 and $g_{||}$ =1.933 in TS-1[56] and at $g_{\perp}$ = 1.967 and $g_{||}$ = 1.901 in γ-irradiated Ti-MCM-41 structures[57]. The deviation

of g values (especially $g_{||}$) for Zr(III) from those of Ti(III) ions is worth noting. The energy level ordering of d orbitals in tetrahedral and octahedral crystal field environments are shown in Figure 3.34.

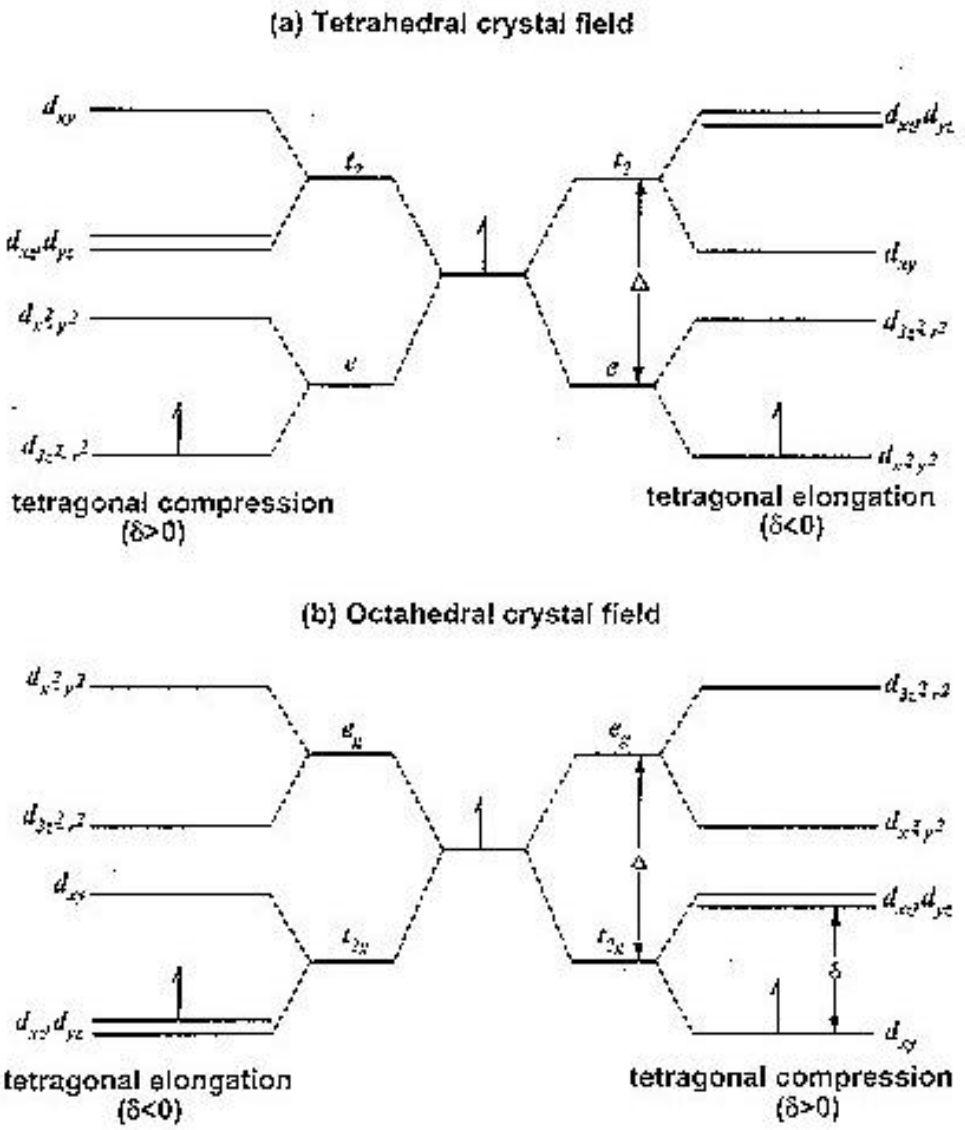

Fig. 3.34 The energy level ordering of d orbitals in tetrahedral and octahedral crystal field environments.

In a tetrahedral crystal field, a d^1 ion has the E state in the ground level. A further tetrahedral distortion removes the orbital degeneracy of the ground state as shown in Figure 3.34(a). If the distortion is positive (i.e., tetragonal compression), the $d_{3z^2-r^2}$ will lie lower. Conversely, if the distortion is negative (i.e., tetragonal elongation), the $d_{x^2-y^2}$ state lies lower. Considering the distortion axis as the z-direction, the expressions for the g components are

$g_{||} = 2.0023$ and $g_{\perp} = 2.0023 - (6\lambda/\Delta)$ for a positive distortion ($\delta > 0$) and

$g_{||} = 2.0023 - (8\lambda/\Delta)$ and $g_{\perp} = 2.0023 - (2\lambda/\Delta)$ for a negative distortion ($\delta < 0$).

In the former case (with $\delta > 0$), $g_{\perp} < g_{||} \approx 2.0023$ and in the latter (with $\delta < 0$), $g_{||} < g_{\perp} < 2.0023$, both the g components are smaller than 2.0023.

In an octahedral crystal field T_{2g} is the ground state (Figure 3.34). Thus, the ground state retains some orbital angular momentum even in the zero-order. ESR signal is not observed for d^1 ions in purely octahedral symmetry. If the tetragonal distortion is positive, spin doublet d_{xy} orbital is the ground state and in such a case, the g components are expressed as follows:

$g_{||} = 2.0023 - (8\lambda/\Delta)$, $g_{\perp} = 2.0023 - (2\lambda/\delta)$.

Hence, both the g values are predicted to be less than 2.0023 for d^1 ions in an octahedral crystal field with $0 < \delta >> \lambda$ and $\Delta >> \delta$. However, $g_{\perp}$ is larger than $g_{||}$. The g values of Zr(III) in Zr-MCM-41 deviate much from the free spin g value and at the same time $g_{||} < g_{\perp}$. These observations suggest that Zr has a distorted octahedral geometry. A smaller $g_{||}$ value for Zr(III) compared to Ti(III) is due to the differences in their spin orbit coupling constants of Ti (154 cm^{-1}) and Zr (cm^{-1}).

The stability and location of Zr(III) centers (species I) were examined by exposing the reduced samples to atmospheric oxygen. The Zr(III) ions in samples A and B (having lower Zr

contents), were resistive towards reoxidation, at 298K, even after more than 16h of exposure to air. These centers in samples A and B are, therefore, attributed to the isomorphous substituted locations inside the walls of MCM-41 structure (type I'). Conversely, samples C and D (having higher contents of Zr) were unstable and formed Zr(IV)-superoxo species soon after exposing to atmospheric oxygen. This indicates that Zr in samples C and D is mainly present at the surface of the pores (in extraframework or substitutional locations; type I"). The studies on samples containing various amounts of zirconium indicate that zirconium at a level of 2 mol% can be substituted for Si in the framework structure of MCM-41.

Exposure of Zr-MCM-41 and Zr impregnated Si-MCM-41 samples to γ-radiation results in the formation of two types superoxo species (type II' and II"). Type II' species with higher g anisotropy are unstable on annealing the sample, while type II" having lower g anisotropy are stable. The g parameters of type II' are almost similar to the superoxo ion observed in the reduced samples. Hence it is proposed that Zr(IV) is initially reduced to Zr(III) by γ-radiolysis and then these surface Zr(III) centers on interaction with atmospheric oxygen result in Zr(IV)-superoxo anions. The interaction of aerial oxygen with defect centers can also generate superoxide ions. These are supposed to have lower g anisotropy. Formation of such superoxo anions on the silica surface is well known. The origin of type II" species is associated with the defect sites. A comparison of spin Hamiltonian parameters for type II' superoxoanions with those of pure zirconia and titania is interesting. The superoxide ions formed upon irradiation of TiO_2 highly dispersed on porous Vycor glass showed signals at $g_1 = 2.0268$, $g_2 = 2.0088$ and $g_3 = 2.0036$. The superoxide ions at the surface of ZrO_2 are characterized by $g_1 = 2.0336$, $g_2 = 2.0096$ and $g_3 = 2.0036$[53,54,60]. The similarity in g components of type II' species ($g_1 = 2.0319$, $g_2 = 2.0093$ and $g_3 = 2.0024$) and those on ZrO_2 reveals that the type II' centers are those associated

with surface Zr(IV) ions. Type II' species were not observed in hydrogen or $LiAlH_4$ reduced samples. The g_1 parameter of the superoxo anion is sensitive to the ion and its oxidation state it is bound to[53]. Assuming that the z direction corresponds to the internuclear axis and the y direction to the orbital hosting the unpaired electron, the expression for the g parameters of the superoxide anion to first order in λ', Δ and E are written as

$g_{xx} = 2.0023$

$g_{yy} = 2.0023 + 2\lambda'/E$ and

$g_{zz} = 2.0023 + 2\lambda'/\Delta$.

Here, λ' is the spin-orbit coupling constant for the oxygen atom and E and Δ are the energy separations between $2p\sigma$ & $2p\pi y^*$ and $2p\pi x^*$ & $2p\pi y^*$, respectively. Although the oxidation state of titanium and zirconium in the superoxo species is the same, the difference in the g value is attributed to the difference in the covalency parameter as well as the energy separation between $2p\pi x^*$ and $2p\pi y^*$ orbitals. Probably the Zr-O bond is less covalent than the Ti-O bond and hence results in higher g_1 value for $Zr(O_2^{-\cdot})$ than for $Ti(O_2^{-\cdot})$ species. The probable locations of zirconium in mesoporous MCM-41 samples and the reduction mechanism are presented in Scheme 1.

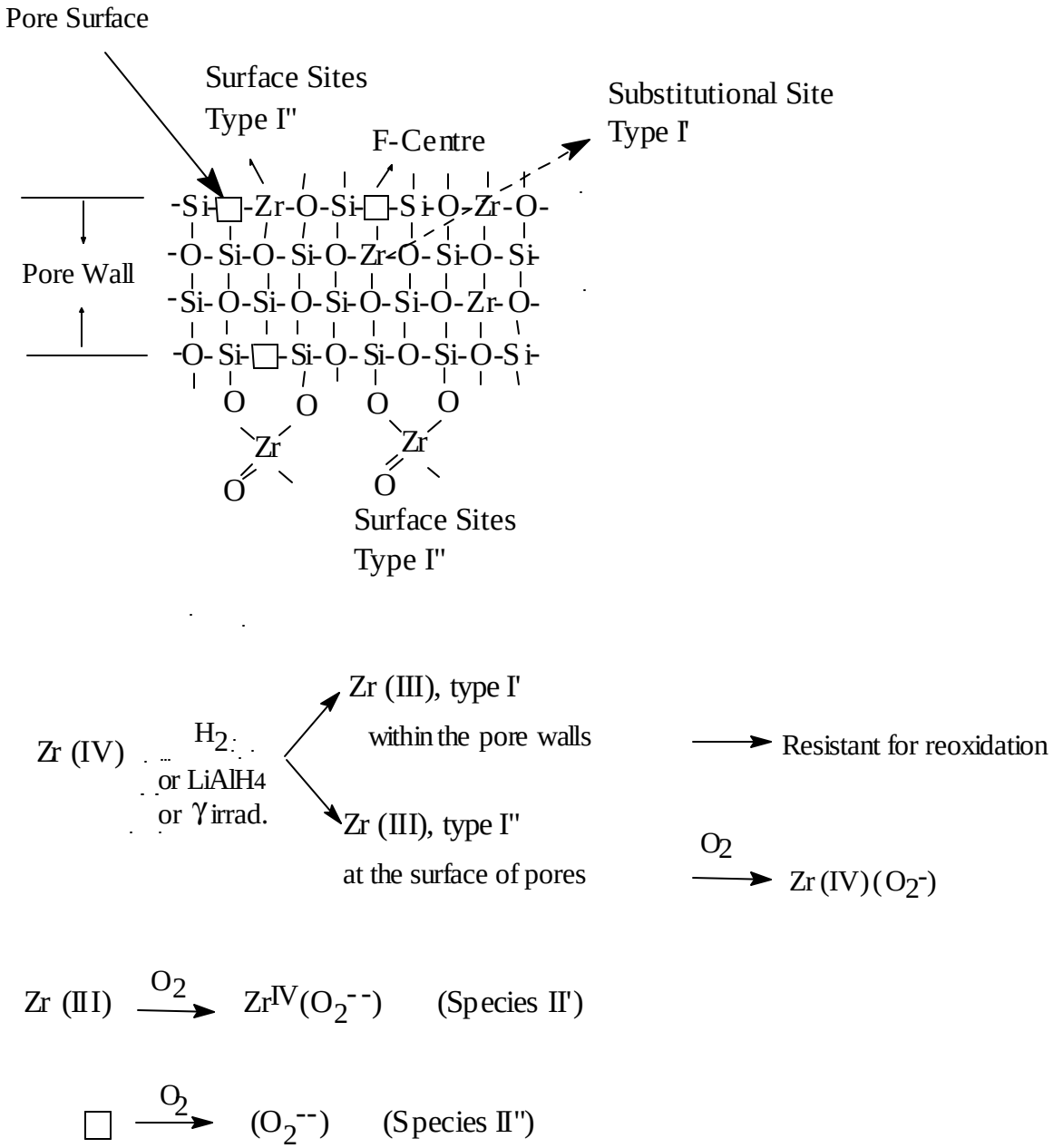
Pore Surface
Surface Sites
Type I"
Substitutional Site
Type I'
F-Centre
Pore Wall
Surface Sites
Type I"
Zr (IV)
H2
or LiAlH4
or γ irrad.
Zr (III), type I'
within the pore walls
Zr (III), type I"
at the surface of pores
Resistant for reoxidation
O2
Zr (IV) (O2-)
Zr (III)
O2
ZrIV(O2--)
(Species II')
O2
(O2--)
(Species II")

Scheme I

3.4 REFERENCES

1. Kresge, C.T., Leonowicz, M.E., Roth, W.J., and Vartuli, J.C., *U.S. Patent* 5098684 (1992).
2. Kresge, C.T., Leonowicz, M.E., Roth, W.J., Vartuli, J.C., and Beck, J.S., *Nature*, **359**, 710 (1992).
3. Beck, J.S., Vartuli, J.C., Roth, W.J., Leonowicz, M.E., Kresge, CT., Schmitt, K.D., Chu, C.T-W., Olson, D.H., Sheppard, E.W., McCullen, S.B., Higgins, J.B., and Schlenker, J.L., *J. Am. Chem. Soc.*, **114** (1992) 10834.
4. Cheng, C.F., He, H., Zhou, W., and Klinowski, J., *Chem. Phys. Lett.*, **244** (1995) 117.
5. Corma, A., Navarro, M.T., and Perez-Pariente, J., *J. Chem. Soc., Chem. Commun.*, (1994) 147.
6. Tatsumi, T., and Koyano, K.A., *Microporous Mater.*, **10** (1997) 259.
7. Chen, C.Y., Li, H.Y., and Davis, M.E., *Microporous Mater.*, **2** (1993) 27.
8. Schmidt, R., Hansen, E.W., Stöcker, M., Akporiaye, D., and Ellestad, O.H., *J. Am. Chem. Soc.*, **117** (1995) 4049.
9. Tanev, P.T., and Pinnavaia, T.J., *Chem. Mater.*, **8** (1996) 2068.
10. Chenite, A., Page, Y.L., Sayari, A., *Chem. Mater.*, **7** (1995) 1015.
11. Gregg, S.J., and Sing, K.S.W., in *"Adsorption, Surface Area and Porosity", Academic Press* London (1982) Ch. 4.
12. Barrett, E.P., Joyner, L.G., and Halenda, P.H., *J. Am. Chem. Soc.*, **73** (1951) 373.
13. Nayak, V.S., *Ph.D. Thesis, University of Poona, Poona, India* (1982).
14. Smirniotis, P.G., and Ruckenstein, E., *Appl. Catal.* **123**, 59 (1995).
15. Borade, R.B., and Clearfield, A., *Catal. Lett.* **31**, 267 (1995).
16. Chen, X., Huang, L., Ding, G., and Li, Q., *Catal. Lett.* **44,** 123 (1997).
17. Chandwadkar, A.J., and Kulkarni, S.B., *J. Therm. Anal.*, **19** (1980) 313.
18. Mishin, V., Piloyan, G.A., Klychko-Gurvich, A.L., and Rubinshtein, A.M., *Bull Akal. Sci., USSR*, **22** (1973) 1298.
19. Biz, S., and Occelli, M., *Catal. Rev.-Sci. Eng.*, 40 (1998) 329.
20. Kosslick, H., Tuan, V.A., Fricke, R., Jedamzik, J., and Lanh, H.D., *J. Therm. Anal.*, **37** (1991) 2631.

21. Minachev, Ch., Weyda, H., Minko, V., Penchev, V., and Lechert, J., *J. Therm. Anal.*, **37** (1992) 571.
22. Busio, M., Janchen, J., and van Hooff, J.H.C., *Microporous Mater.*, **5** (1995) 211.
23. Schimdt, R., Akporiaye, D., Stocker, M., Ellestad, O., *Stud. Surf. Sci. Catal.*, 84 (1994) 61.
24. Borade, R.B., and Clearfield, A., *Synthesis of Porous Materials: Zeolites, Clays and Nanostructures (Eds.: M.L. Occelli and H. Kessler), Marcel Dekker Inc., New York* (1997).
25. Janicke, M., Kumar, D., Stucky, G.D., and Chmelka, B.F., *Stud. Surf. Sci. Catal.*, **84** (1994) 243.
26. Flanigen, E.M., Intrazeolite Chemistry and Catal; Pabo, J.A., *Eds.: AS Monograph Series 171; American Chem. Soc.*; Washington, DC (1976) 80.
27. Chen, C-Y., Li, H-X., and Davis, M.E., *Microporous Mater.*, **2** (1993)17.
28. Chen, C-Y., Li, H-X., and Davis, M.E., *Microporous Mater.*, **2** (1993)27.
29 Szostak, R., *"Molecular Sieves: Principles of Synthesis and Identification"* Van Nostrand Reinfold, New York (1989).
30. Chang, Z., Zhu, Z. and Kevan L., *J.Phys. Chem. B*, **103** (1999) 9442.
31. Feuston, B.P., and Higgins, J.B., *J. Phys. Chem.*, **98** (1994) 4459.
32. Camblor, M.A., Corma, A., and Perez-Pariente, J., *J. Chem. Soc., Chem. Commun.*, (1993) 557.
33. Thangaraj, A., Kumar, R., Mirajkar, M.P., and Ratnasamy. P., *J. Catal.*, **130** (1991) 1.
34. E. Gallei, and D. E. Seuback, *J. Catal.*, **37** (1975) 474.
35. A. Jentys, N.H. Pham and H. Vinek, *J. Chem. Soc., Faraday Trans.*, **92** (1996) 3287-3291.
36. G.L. Woolery, L.B. Alemany, R.M. Dessaue and A.W. Chester, *Zeolites*, **7** (1987) 11.
37. Di Renzo, F., Coustel, N., Mendiboure, M., Cambon, H., and Fajula, F., *Stud. Surf. Sci. Catal.*, **105** (1997) 69.
38. Ryoo, R., Kim, J.M., and Ko, C.H., *Stud. Surf. Sci. Catal.*, **117** (1998) 151.
39. Tanev, P.T., Chibwe, M., and Pinnavaia, T.J., *Nature*, **368** (1994) 321.
40. Reddy, K.M., Moudrakovski, I., and Sayari, A., *J. Chem. Soc. Chem. Commun*. 1059 (1994).

41. Mal, N.K., Ramaswamy, V., Ganapathy, S., and Ramaswamy, A.V., *Appl. Catal. A: General,* **125** (1995) 233.
42. Beck, J.S., Chu, C.T.W., Kresge, C.T., Leonowicz, M.E., Roth, W.J., and Vartuli, J.C., *U.S.Patent* 11390 (1991).
43. Mal, N.K., and Ramaswamy, A.V., *J. Mol. Catal.,* **105** (1996) 149.
44. Tuel A,, Gontier S., and Teissier R., *J. Chem. Soc. Chem. Commun.* (1996) 651.
45. Gontier, S., and Tuel., A., *Appl. Catal. A: General*, **143** (1996) 125.
46. Caravlho, W.A., Paula, B.V., Wallau, M., and Schuchardt, U., *Zeolites* **18** (1997) 408.
47. Fejes, P., Nagy, J.B., and Vanko, Gy., *Appl. Catal. A: General,* **145** (1996) 155.
48. Lazar, K., Szeleczky, N.K., Mal, N.K., and Ramaswamy, A.V., *Zeolites* **19** (1997)**,** 123.
49. Parish, R.V., in *Mössbauer Spectroscopy Applied to Inorganic Chemistry* **Vol.1** (Ed. G.J. Long) Plenum Press, New York (1984) 527.
50. Greenwood, N.N., and Gibb, T.C., *Mössbauer Spectroscopy, Chapman and Hall Ltd, London* (1971) 388.
51. Liu, H.; Feng, L., Zhang, X., and Xue, Q., *J. Phys. Chem.*, **99** (1995) 332.
52. Bobricheva, I.V., Stavitsky, I.A., Yermolaev, V.K., Kotsarenko, V.P., Shmachkova, V.P., and Kochubey, D.I., *Catal. Lett.*, **56** (1998) 23.
53. Geobaldo, F., Bordiga, S., Zecchina, A., Giamello, E.; Leofanti, G., and Petrini, G., *Catal. Lett.*, **16** (1992) 109.
54. Che, M., and Giamello, E., *Stud. Surf. Sci. Catal.*, **57 B** (1990) 265.
55. Anpo, M., Che, M., fubini, B., Garrone, E., Giamello, E., and Pagamini, M.C., *Topics Catal.*, **8** (1999) 189.
56. Prakash, A.M., and Kevan, L., *J. Catal.*, **978** (1998) 586.
57. Prakash, A.M., Kevan, L., Zahedi-Niaki, M.H., Kaliaguine, S., *J, Phys. Chem.*, **103** (1999) 831.
58. Torralvo, M. J., and Alario, M. A. *J. Catal.*, **86** (1984) 473.
59. Luan, Z., and Kevan, L., *J.Phys. Chem. B*, **101** (1997) 2020.
60. Goodman, B.A., and Raynor, J.B., In *Adv. Inorg. Chem. Radiochem*.; Eds.; H.J. Emeleus, A.G. Sharpe; Academic Press, New York, **13** (1970) 135.

CHAPTER IV

CATALYTIC ACTIVITY

GENERAL INTRODUCTION

Heterogeneous catalysts are used in a number of reactions in chemical industries as they are noncorrosive, ecofriendly, easy to handle and reusable. The reactivities and selectivities of molecular sieves as catalysts are determined by active sites arising from an imbalance in charge between the silicon and the aluminium ions in the framework. The active sites in solid acid catalysts arise mainly from the Brönsted acidity associated with the presence of framework trivalent aluminium or other trivalent ions. Purely siliceous materials have electrically neutral frameworks and consequently no Brönsted acidity. Lewis acidity is an electron acceptor property which arises from the trigonally coordinated aluminium atom in the structure of the molecular sieves.

Acidity in mesoporous molecular sieves can be generated either by isomorphous substitution of trivalent cations such as Al for Si, or by incorporating an acidic component such as $AlCl_3$ or a heteropolyacid. The Al-analogs of MCM-41 have been investigated as solid acid catalysts in a number of acid catalyzed reactions in petroleum refining processes, alkylation of bulky aromatic compounds etc. [1-4].

Since the discovery of the remarkable catalytic activity of TS-1[5] in the selective oxidation of organic substrates by H_2O_2, the field of transition metal modified zeolites has grown tremendously[6,7]. In addition to its hydrophobicity, the major role of the zeolite matrix is the stabilization of isolated redox centres. However, the small pore size of these molecular sieves limit the accessibility of their active sites only to small substrate molecules. The discovery of mesoporous molecular sieves has provided a good solution to these limitations. The Ti and V containing MCM-41 molecular sieves have been found to be active in a variety of liquid phase oxidation reactions involving bulky molecules[8-10].

This chapter presents the catalytic activities of the acid catalyst Al-MCM-41 and the selective oxidation catalysts Sn and Zr containing MCM-41 molecular sieves prepared in the present investigation (Chapter II).

Part I of the present chapter describes the catalytic use of platinum impregnated H-Al-MCM-41 as an acid catalyst in the hydroisomerization of n-hexane, H-Al-MCM-41 in the alkylation of benzene with long chain olefins and the Beckmann rearrangement of cyclohexanone oxime to caprolactam.

Part II reports the selective oxidation properties of Sn-MCM-41 and Zr-MCM-41 molecular sieves. Sn-MCM-41 has been evaluated for catalytic activity in the hydroxylation of phenol, 1-naphthol and epoxidation of norbornene and Zr-MCM-41 has been tested for the hydroxylation of 1-naphthol and epoxidation of norbornene.

4.1 PART I: ACID CATALYZED REACTIONS OVER Al-MCM-41

4.1.1 HYDROISOMERIZATION OF N-HEXANE

4.1.1.1 Introduction

The hydroconversion of n-paraffin components of light naphtha into branched isomers is an important process in the petroleum refining industry to obtain high octane gasoline blendstocks[11,12]. Platinum or palladium impregnated zeolites are known to give high isomerization selectivities at medium conversions and are the most common n-alkane hydroconversion catalysts. However, due to the strong acidity of these catalysts, their use is characterized by significant hydrocracking to undesirable alkanes at high conversion levels. This section of the chapter presents the n-hexane hydroconversion activity of Pt-loaded aluminosilicate MCM-41 molecular sieves.

4.1.1.2 Experimental methods

4.1.1.2(i) Preparation of the Catalysts

The details of the methods of preparation of Al-MCM-41 molecular sieves with different Si/Al ratios (designated as Al-MCM-41(86), Al-MCM-41(44), Al-MCM-41(23) and Al-MCM-41(14) and their modification have been presented in Chapter II, while the characterization of these catalysts has been described in Chapter III.

4.1.1.2(ii) Reaction Procedure

The catalytic reactions were carried out in a down flow fixed bed tubular glass reactor (i.d. = 15 mm; length = 30 cm) at atmospheric pressure using about 2 g of the catalyst in the presence of hydrogen. n-Hexane was fed using a syringe pump and H_2 was introduced using a mass flow controller. The top section of the reactor (~ 20 cm long) above the catalyst bed (~ 3 cm long) which was packed with ceramic beads acted as the preheating section. The reactor was placed inside a temperature controlled vertical furnace (Geomécanique, France). The thermocouple tip was centred at the middle of the catalyst bed. The catalyst was compacted in a hydraulic press, the pellets were broken and then sieved to 16-20 mesh size prior to use. n-Hexane used was > 99% pure (S.D. Fine Chemicals Pvt. Ltd., Bombay). The conditions of the reactions were, temp. = 300-400°C, WHSV(h^{-1}) = 0.5 to 5.0, H_2/n-C_6 (mole) = 2 to 9. The catalyst was dried *in situ* in a flow of N_2 (20 ml/min) at 450°C for 6 h, cooled to 350°C and reduced for 2 h in H_2 (20 ml/min) prior to start of run. The reaction products (which were in the gaseous state) were analyzed using a Hewlett-Packard gas chromatograph (5880 A) with a capillary column (cross-linked methyl silicone gum, HP1, 50 m $\times$ 0.2 mm i.d.) and a flame ionization detector (FID).

4.1.1.3 Results and Discussion

4.1.1.3(i) Transformation of n-hexane

Hydroisomerization of alkanes is generally carried out over bifunctional catalysts, often containing platinum. The metal component aids in increasing the rate of isomerization, besides lowering catalyst deactivation. The reactivity of n-alkanes increases as the carbon number increases but the selectivity towards isomerization decreases[13]. The hydroisomerization of n-hexane has already been studied over Pt-loaded zeolites such as Pt-Y[14], Pt-beta[15] and Pt-mordenite[16]. There is a general consensus on the mechanism of alkane hydroisomerization. n-Alkane molecules are adsorbed at dehydrogenation/ hydrogenation sites where n-alkenes are formed. These migrate and interact with acid sites and secondary carbenium ions are generated, which further rearrange to more stable tertiary carbenium ions. Finally, the tertiary carbenium ions abstract hydride ions from hydrocarbon molecules and transform into olefins. These are then hydrogenated at the metallic sites into isoalkanes[17,18].

The hydroconversion of n-hexane was carried out in a fixed bed down flow glass reactor at atmospheric pressure in the temperature range of 300-400°C over Pt-H-Al-MCM-41 samples containing different amounts of Pt (0.1-0.5 wt.%). At the conditions of the investigation, the major reactions were isomerization and cracking; negligible cyclization and aromatization were observed. Small amounts of alkenes (1-2%) were also detected in the products. The activities of catalysts (Fig. 4.1-4.6) are expressed as conversion (%) and turn over frequencies (TOF, s^{-1}) based on the number of acid sites as estimated from temperature programmed desorption of pyridine (Table 3. 2). A decrease in n-hexane conversion (and TOF) was observed with duration of run (time on stream, TOS) over all the catalysts.

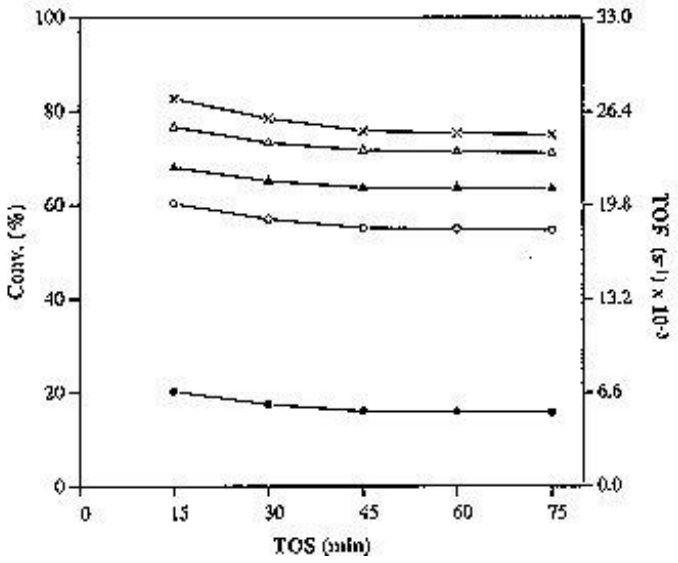

Fig. 4.1 Influence of time on stream (TOS) on activity of catalyst. Catalyst: Pt(0.3%)-Al-MCM-41(23); WHSV (h^{-1}) = 1.0; H_2/n-hexane (mole) = 3.5; (●) 300°C, (o) 325°C, (σ) 350°C, (Δ) 375°C and (×) 400°C.

Though the deactivation rate was significant during the first few minutes (Fig. 4.1), the activity of the catalyst became reasonably stable after about 45 minutes. Hence the data were collected at a time on stream (TOS) of 45 minutes during further studies of the reaction. A certain amount of initial deactivation has also been reported by other workers during the isomerization of n-alkanes over Pt-catalysts[14,19], which is expected at atmospheric pressure conditions.

4.1.1.3(ii) Influence of Pt content

The influence of Pt content on the hydroisomerization of n-hexane over Pt-H-Al-MCM-41 (Si/Al = 23.3) (Pt-H-form of Al-MCM-41(23)) at different temperatures is presented in Fig. 4.2 (a).

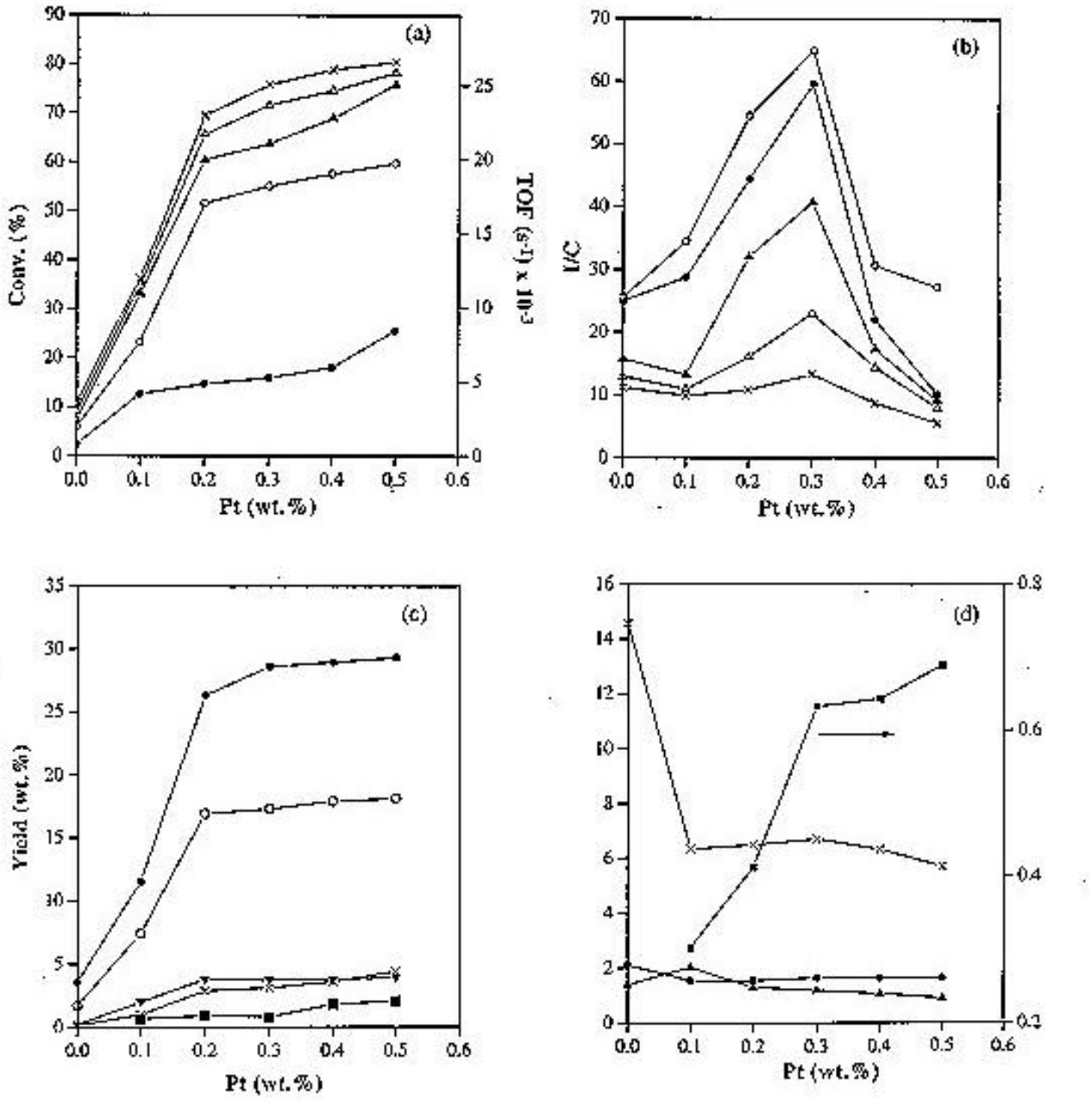

Fig. 4.2 Influence of Pt-content on n-hexane isomerization. Catalyst: Pt-Al-MCM-41(23) with different Pt contents; WHSV (h^{-1}) = 1.0; H_2/n-hexane (mole) = 3.5; TOS = 45 min. (a) and (b): (•) 300°C, (o) 325°C, (σ) 350°C, (Δ) 375°C and (×) 400°C; (c): (•) 2-MP, (o) 3-MP, (σ) 2,3-DMB, (×) 2,2-DMB and (■) C_1-C_5 products; (d): (•) 2-MP/3-MP, (σ) 2,3-DMB/2,2-DMB, (×) MP/DMB and (■) C_1+C_5/C_3.

The incorporation of Pt increases the activity of H-Al-MCM-41 several fold (Fig. 4.2 (a)). The conversion increases rapidly with increasing Pt content upto about 0.2% and slowly thereafter. This behaviour is typically noticed when a bifunctional mechanism is the major contributor to the reaction[17,20,21]. The selectivity of the catalysts for the isomerization reaction can be evaluated by the relative amount of the isomerization and cracking products formed in the reaction, which can be conveniently expressed by the I/C (Isomerization/Cracking) ratio.

The influence of Pt content on the selectivity to isomerization is shown in Fig. 4.2 (b). The I/C ratio increases with increase in Pt content and reaches a maximum at about 0.3 wt.% Pt (I/C = 65 at a conversion of ~ 55% at 325°C). The C_1-C_5 fraction increases with increasing Pt content (Fig. 4.2 (c)) primarily due to an increase in the hydrogenolysis activity which is confirmed by the increase in the C_1+C_5/C_3 ratio (Fig. 4.2 (d)). Apparently, the enhanced hydrogenolysis activity is the main reason for the decrease in I/C ratio beyond 0.3% Pt. The distribution of isohexanes is shown in Fig. 4.2 (c) and the ratios of the products are presented in Fig. 4.2 (d). When Pt is present (even 0.1%) the ratios of the monomethyl pentanes (2-MP/3-MP) (1.52 to 1.65) are close to the expected equilibrium value of 1.57[17] suggesting the rapid equilibration of the two isomers; in the absence of Pt, the equilibrium is not attained (2-MP/3-MP = 2.2). The ratios of methyl pentanes/dimethyl butanes (MP/DMB) are, however, far from the equilibrium value (3.51), being ~ 6 when Pt is present and 14.8 when absent, due to the difficulty in the isomerization of the methylpentane to dimethyl butanes. The 2,3-DMB/2,2-DMB ratios decrease (2.0 to 0.84) with increasing Pt content and reach the equilibrium value of 0.86 at 0.5 % Pt. The results suggest that the metal function, besides acting as the hydrogenation-dehydrogenation agent, probably also assists the isomerization of the cation, though it is not clear how.

4.1.1.3(iii) Influence of Si/Al ratio

The influence of Al content in the Pt-H-Al-MCM-41 samples was studied at 325°C and 350°C with catalysts having different Si/Al ratios (Si/Al ratios of 86.3, 43.9, 23.3 and 14.3 for samples Al-MCM-41(86), Al-MCM-41(44), Al-MCM-41(23) and Al-MCM-41(14), respectively) impregnated with 0.3 wt.% Pt. The conversion decreases with decrease in Al content *i.e.* the higher the Si/Al ratio, the lower is the conversion (Fig. 4.3 (a) and Fig. 4.3 (c)). The activity of a commercial silica-alumina cracking catalyst (LA-LPV; Ketjen; S.A. = 650 m^2/g) at 325°C and 350°C is also presented in Fig. 4.3 (a) and 4.3 (c). The amorphous silica alumina sample is relatively less active for the given Al content, probably due to a poor distribution of Al. Both cracking and isomerization are enhanced with increasing Al content. However, the I/C ratio peaks for the sample with an intermediate Si/Al value at 23.3 (Al-MCM-41(23)). Though the reasons for this behaviour are not clear, it is probably connected with the presence of some very strong acid centres in samples with low and high Si/Al ratios. While strong acidity in the Si-rich samples (Al-MCM-41(86); Si/Al = 86.3) may be due to the extreme isolation of Al-ions, it could be due to the presence of small amounts of extra framework Al species in the Al rich sample (Al-MCM-41(14); Si/Al = 14.3).

It is also possible that the above behaviour is due to the different n_{Pt}/n_A (n_{Pt} = no. of exposed Pt atoms and n_A = no. of acid sites) in the samples. For example, when the n_{Pt}/n_A is large, hydrogenolysis activity will be predominant. When it is very small, the acid activity (cracking) will prevail; isomerization (bifunctional reaction) selectivity will be maximum when the ratio of the two functions is optimum. The distribution of the light products from the samples is not typical of either hydrogenolysis or cracking, as more (moles of) C_4 and C_5 hydrocarbons are present than can be accounted for by yields of C_1 and C_2 hydrocarbons.

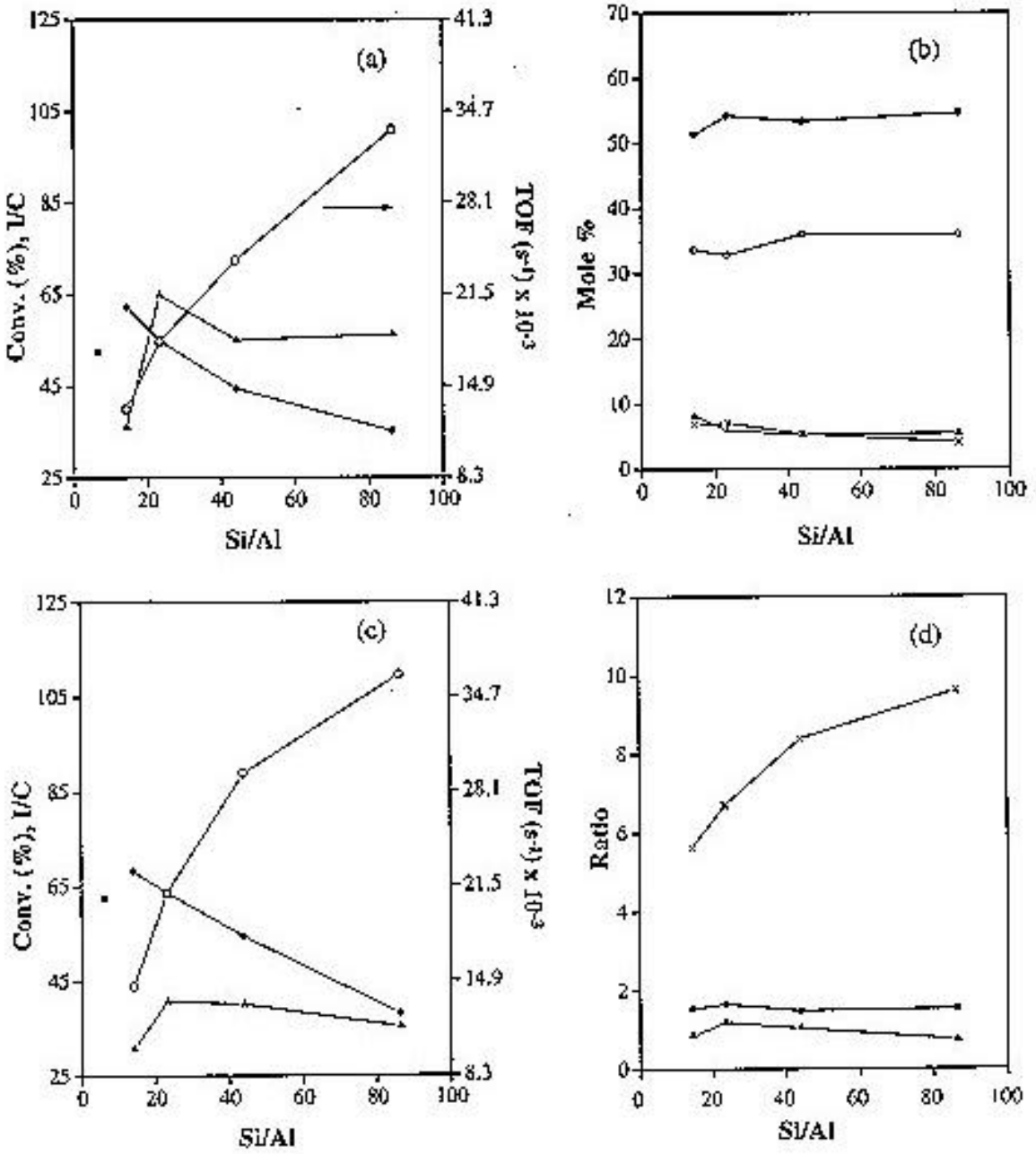

Fig. 4.3 Influence of Al content on n-hexane isomerization. Pt-Al-MCM-41(86 to 14); Pt content = 0.3%; WHSV (h^{-1}) = 1.0; H_2/n-hexane (mole) = 3.5; TOS = 45 min; (a) Temp. = 325°C, (●) Conv.(%), (o) TOF (s^{-1}) and (σ) I/C; (b) Temp. = 325°C, (●) 2-MP, (o) 3-MP, (σ) 2,3-DMB and (×) 2,2-DMB; (c) Temp. = 350°C, (●) Conv.(%), (o) TOF (s^{-1}), (σ) I/C and (■) amorphous SiO_2-Al_2O_3, % conversion; (d) Temp. = 325°C, (●) 2-MP/3-MP, (σ) 2,3-DMB/2,2-DMB and (×) MP/DMB.

Similar imbalance has also been reported by earlier workers[16] and attributed to the occurrence of alkylation-cracking reactions during alkane transformations over metal loaded zeolites. Earlier, Guisnet *et al.*[22] have reported while studying Pt-H-Y that acid activity becomes important when n_{Pt}/n_A is < 0.03 and hydrogenolysis activity becomes important when n_{Pt}/n_A is > 0.4. Unlike in the case of Y, it is difficult to estimate the number of acid sites in H-Al-MCM-41 based only on the Al content. Besides, the acid sites in H-Al-MCM-41 are much weaker than those in zeolites[23]. It is therefore difficult to arrive at the exact n_{Pt}/n_A ratios for our catalysts. Our studies on the TPD of pyridine over the Pt-H-Al-MCM-41 samples revealed that most of the pyridine desorbed before 300°C attesting to the weak nature of the acid centres. An estimate of the acid sites based on pyridine desorbed beyond 100°C is presented in Table 3.2. Assuming that each acid site desorbs a single of pyridine molecule (Table 3.2) and assuming an average Pt dispersion of 70%, we obtain n_{Pt}/n_A values in the range of 0.06 to 0.42 for Si/Al (86.3 to 14.6) in the samples at constant Pt (0.3%) and in the range 0.036 to 0.18 for Al-MCM-41(23) with different Pt contents (0.1 to 0.5%). Both sets of studies (Si/Al and Pt content variations) suggest a maximum isomerization selectivity for Al-MCM-41(23) with 0.3% Pt with an n_{Pt}/n_A ratio of 0.11 (Fig. 4.3 (a) and Fig. 4.2 (b)). This value is within the limits reported by Guisnet *et al.*[22]

4.1.1.3(iv) Influence of temperature

The influence of temperature on n-hexane transformation over Al-MCM-41(23) with different Pt contents is presented in Fig. 4.4 (a). Though the activities of the catalysts increase with temperature, the increase is moderate beyond 350°C. This is mainly due to the near attainment of equilibrium for the isomerization reaction at higher temperatures. The theoretical equilibrium conversion (isomerization) values (based on data of ref. 24) are also presented in the Figure 4.4 (a). The conversion recorded is generally lower than the equilibrium values even at temperatures above 350°C.

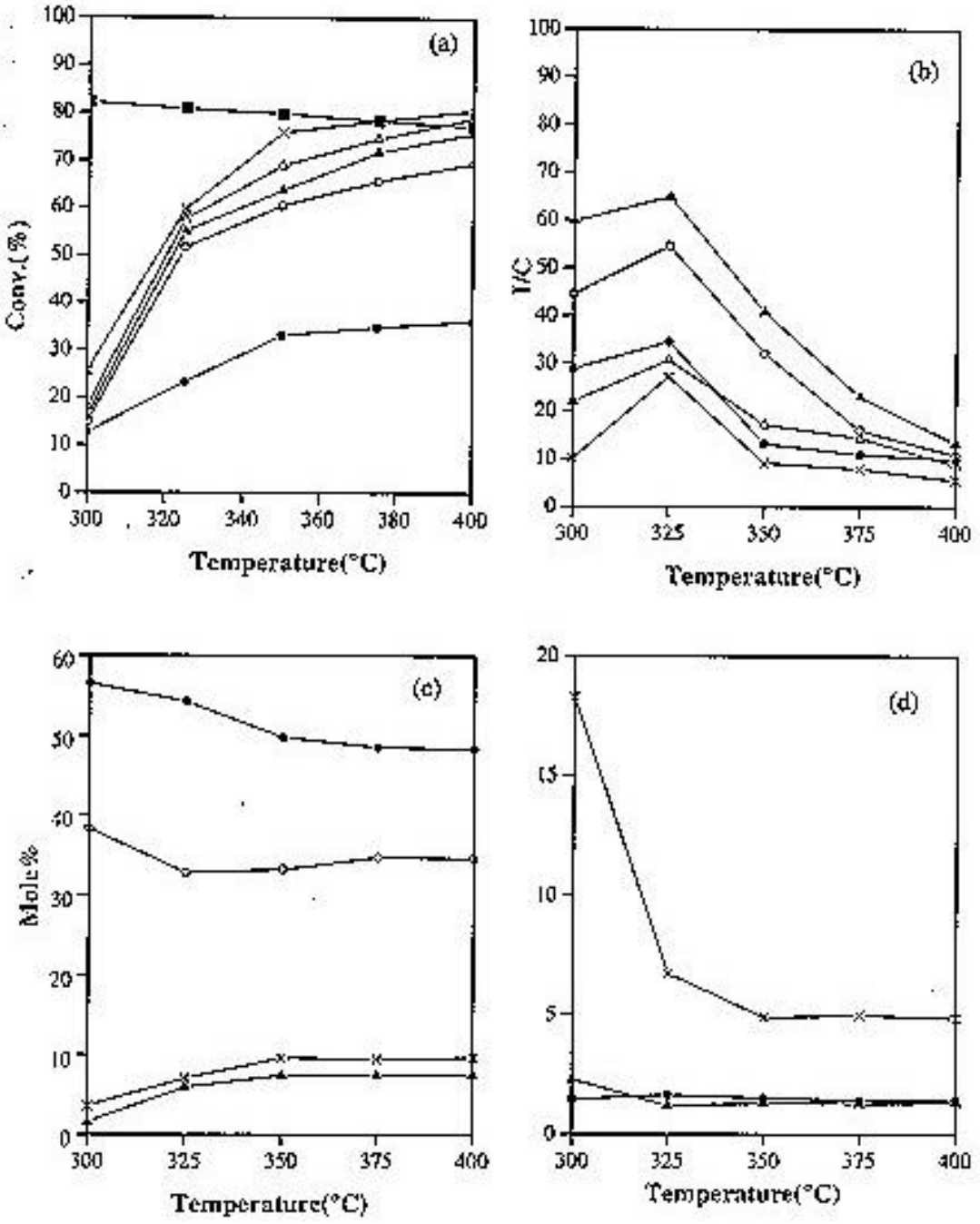

Fig. 4.4 Influence of temperature on n-hexane isomerization. Pt(0.3%)-Al-MCM-41(23); WHSV (h^{-1}) = 1.0; H_2/n-hexane (mole) = 3.5; TOS = 45 min; (a) and (b) (•) 0.1 wt.% Pt, (o) 0.2 wt.% Pt, (σ) 0.3 wt.% Pt, (Δ) 0.4 wt.% Pt and (×) 0.5 wt.% Pt; (c) (•) 2-MP, (o) 3-MP, (σ) 2,3-DMB and (×) 2,2-DMB; (d) (•) 2-MP/3-MP, (σ) 2,3-DMB/2,2-DMB and (×) MP/DMB. The equilibrium conversion (■) values are presented in (a).

The activation energies (E_a) for isomerization calculated for the different samples based on the data collected below 325°C (at low conversions away from the equilibrium values) were in the range 22 - 31 Kcal.mole^{-1} (22 Kcal.mole^{-1} for 0.2% Pt and 31 Kcal.mole^{-1} for 0.5% Pt). The E_a values for cracking (and hydrogenolysis) were in the range 15 – 22 Kcal.mole^{-1} in the entire temperature range (22 Kcal.mole^{-1} for 0.2% Pt and 15 Kcal. mole^{-1} for 0.5% Pt). These E_a values for isomerization and cracking are similar to the values reported by earlier workers[19,21,25]. However, at higher conversions (> 325°C), the E_a values for isomerization were lower (5 - 10 Kcal.mole^{-1}). This is attributed to the near attainment of equilibrium at these conditions.

The I/C ratio goes through a maximum for all the catalysts with different Pt contents (Fig. 4.4 (b)). The maximum I/C obtained is 65% at 325°C (conversion ~ 55%) with the sample impregnated with 0.3 wt.% Pt. The presence of an optimum temperature suggests that the bifuncional activity of the catalyst overrides the other reactions (monofunctional hydrogenolysis or cracking) at this temperature. The break up of the individual components and their ratios at 0.3 % Pt content are presented in Fig. 4.4 (c) and Fig. 4.4 (d). The 2-MP/3-MP ratio is nearly constant at ~ 1.6 at all the temperatures revealing the attainment of equilibrium between the two isomers. The dimethylbutane fraction in the product increases sharply at 325°C and remains nearly constant (rela tive to other isomers) (Fig. 4.4 (c)). This results in a sharp decline in the MP/DMB ratios at 325°C. The ratio (4.8) however is still far from the equilibrium value (of 3.5) even at 400°C. However, the 2,3/2,2 DMB ratio is close to the equilibrium value of 0.86. This confirms that the nonattainment of the equilibrium between the mono and dimethyl isomers is mainly due to the successive cracking of the dibranched isomers.

4.1.1.3 (v) Influence of space velocity

As the contact time (1/WHSV) increases, n-hexane conversion increases, but the I/C ratio decreases (Fig. 4.5 (a)). The decrease in I/C is a result of the increase in cracking reactions favoured by the longer residence of the adsorbed intermediates at the surface at the low feed rates. Plots of the yields of the different isomers against conversion (Fig.4.5 (c)) suggest that methyl pentanes are the primary products and the dimethyl butanes are the secondary products. The sequence of reactions is: n-hexane $\Rightarrow$ methyl pentanes $\Rightarrow$ dimethyl butanes. Eventhough 2,2-DMB is the thermodynamically more favoured product at the conditions of the study, its formation (directly from methyl pentanes or from 2,3-DMB) is kinetically less favoured due to the difficulty in transforming a more stable tertiary carbocation (c-c$^+$-c-c-c or c-c-c$^+$-c) into a less stable secondary carbocation (c-c-c$^+$-c)[17].

The data from the above experiments suggest a first order kinetics for the conversion of n-hexane. This conclusion is arrived at based on the linear heat relationship (Fig.4.5 (d)) between V/F and ln [1/(1-$\in$)]; k = (1/T)ln [1/(1-$\in$)] where P = V/F, V = volume of the catalyst, F = feed rate per second and $\in$ = fractional conversion[26].

4.1.1.3(vi) Influence of H_2/nC_6 mole ratio

The influence of H_2/nC_6 mole ratio is shown in Fig. 4.6 (a). Increasing the mole ratio from 2 to 9 (P_{H2} = 0.67 to 0.90) at a constant feed rate of nC_6 decreases the conversion. The decrease in activity with increasing partial pressure of H_2 can be a result of the rapid hydrogenation of the intermediate olefins and carbocations preventing their further reaction. This is clear from a comparison of data obtained from contact time and the H_2 partial pressure studies. For e.g., at a conversion of about 19%, the MP/DMB ratio is 8.0 in contact time variation experiments (P_{H2} = 0.78), while it is 18 at a similar conversion (18%; P_{H2} = 0.90).

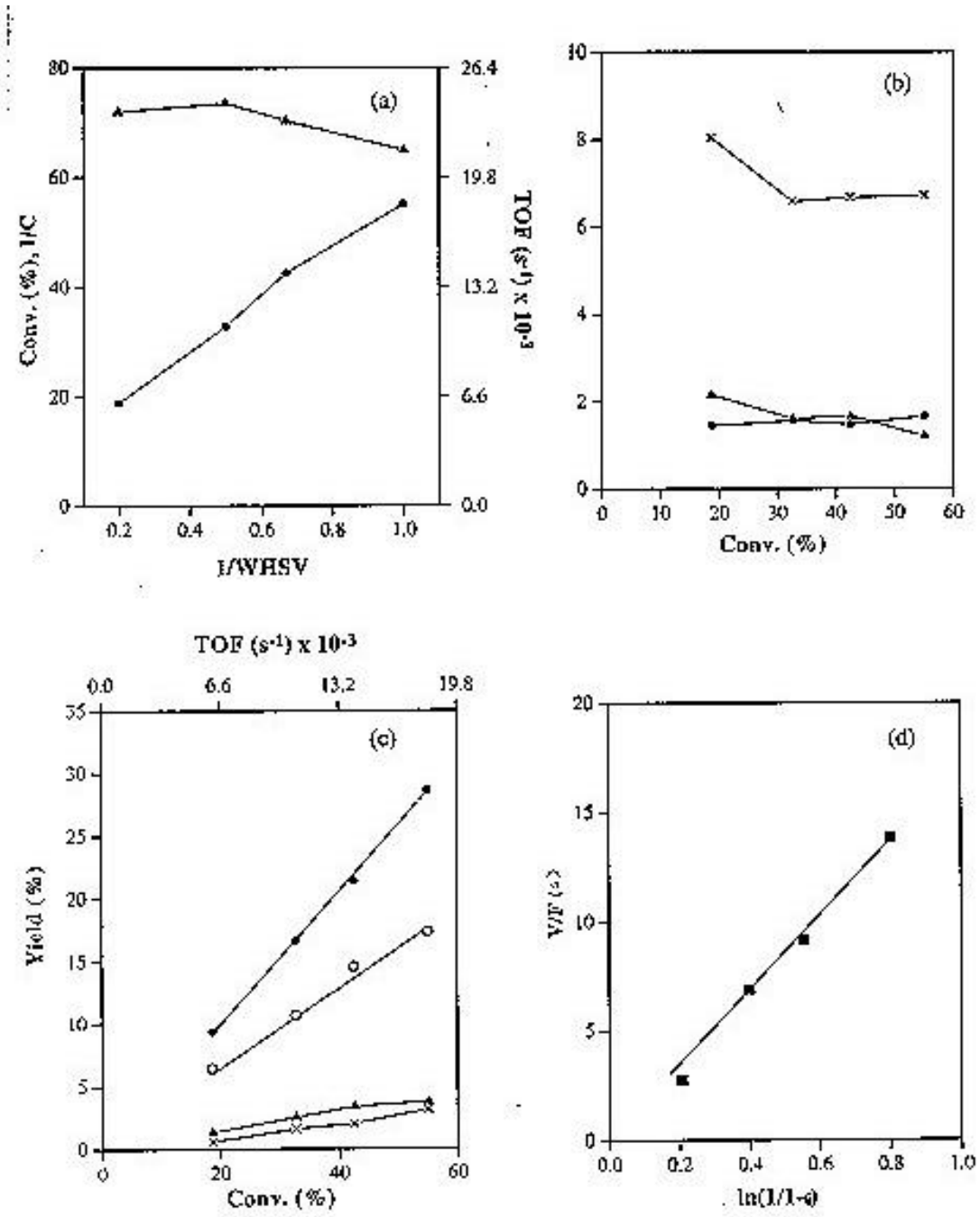

Fig. 4.5 Influence of space velocity on n-hexane isomerization. Pt(0.3%)-Al-MCM-41(23); Temp. = 325°C; WHSV (h^{-1}) = 1.0; H_2/n-hexane (mole) = 3.5; TOS = 45 min; (a) (•) Conv. (%) and TOF (s^{-1}); (σ) I/C; (b) (•) 2-MP/3-MP, (σ) 2,3-DMB/2,2-DMB and (×) MP/DMB; (c) (•) 2-MP, (o) 3-MP, (σ) 2,3-DMB and (×) 2,2-DMB; (d) V/F Vs [ln 1/1-∈]; first order kinetics.

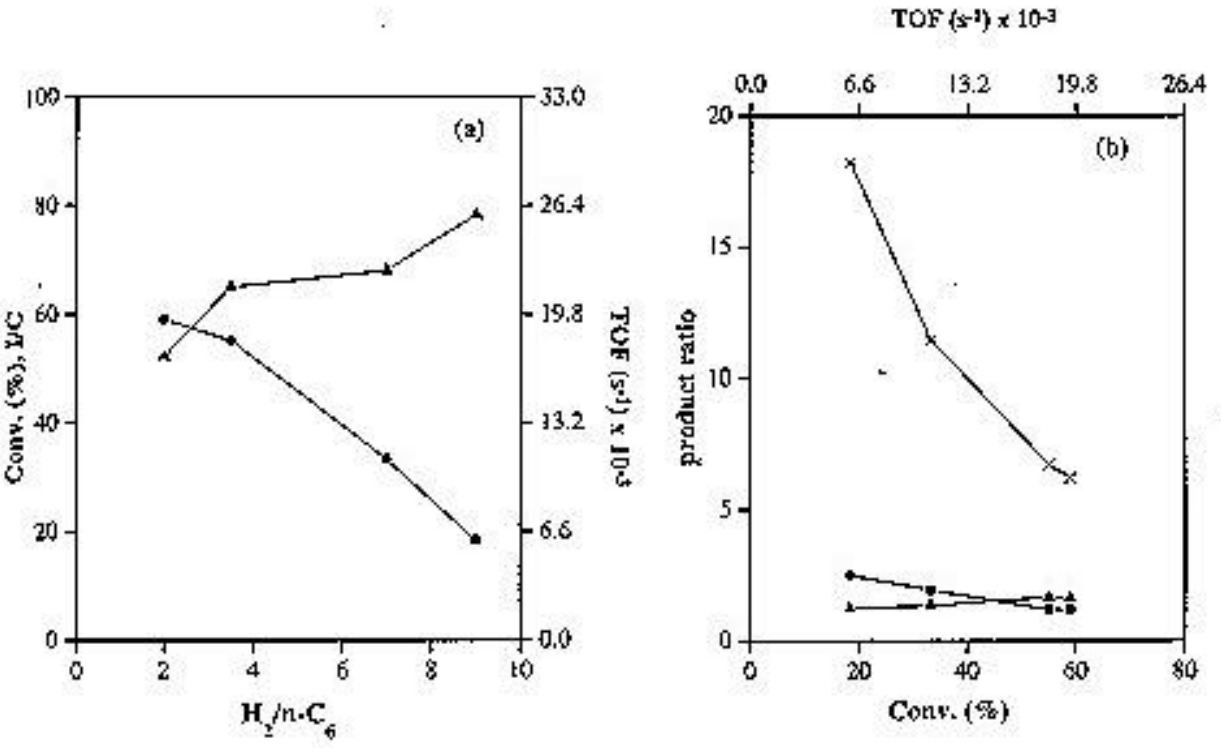

Fig. 4.6 Influence of H_2/n-C_6 (mole) ratio on n-hexane isomerization. Pt(0.3%)-Al-MCM-41(23); Temp. = 325°C; TOS = 45 min; H_2/n-hexane (mole) = 3.5; (a) (•) Conv. (%) and (σ) I/C; (b) (•) 2-MP/3-MP, (σ) 2,3-DMB/2,2-DMB and (×) MP/DMB.

4.1.2 ALKYLATION OF BENZENE WITH LINEAR OLEFINS

4.1.2.1 Introduction

Alkylaromatic compounds have numerous industrial applications, one of the important applications being their use in the preparation of biodegradable synthetic detergents. Linear alkyl benzenes (LAB), which are valuable industrial chemicals used in the manufacture of detergents are usually mixtures of C_{10}-C_{13} alkyl benzenes obtained by alkylation of benzene with long chain olefins (C_{10} to C_{13}) over Friedel-Crafts type catalysts such as $AlCl_3$, BF_3, H_2SO_4, anhydrous HF etc.[27]. These long chain olefins are produced by the dehydrogenation

of C_{10}-C_{13} paraffins obtained from kerosene by molecular sieve separation process. An important by-product obtained during the production of LAB is HAB (heavy alkyl benzenes), which is a valuable source of synthetic lube oils for special lubrication purposes. In the alkylation of benzene with long chain alkenes (C_{10}-C_{13}), a mixture of alkylbenzenes with the phenyl group attached to different C-atoms is obtained. The more preferred isomeric component in detergent manufacture is the 2-phenyl (2-ϕ) isomer, which possesses better emulsibility characteristics than the others. The typical structures of the compounds present in LAB and HAB are shown below.

LAB

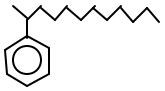

2-Phenylalkane

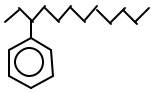

3-Phenylalkane (and other isomers)

HAB

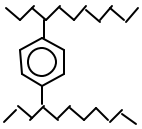

Dialkylbenzene

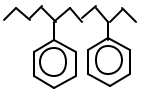

Diphenylalkane

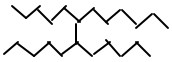

Dimer

The proportion of the three components in HAB depends on the alkylation conditions, the catalyst and the diolefin content in the olefin mixture.

Homogeneous acid catalysts are difficult to handle, to separate from the products, and to regenerate. Besides, they cause pollution and equipment corrosion. Hence, efforts have been put to replace these by non-corrosive solid catalysts such as acidic zeolites[28-31]. The alkylation of benzene with long chain olefins has been reported over heteropolyacids[28], clays[29], pillared clays[30] and ZSM-12[31]. The alkylation of benzene with 1-hexene, 1-octene,

1-dodecene and a mixture of C_{10}-C_{13} olefins over a number of medium and wide pore zeolites has also been reported[32]. It has been observed that hexagonal mesoporous silica (HMS) supported $AlCl_3$ gives enhanced selectivity for the formation of the 2-ϕ isomer[33]. It has been shown that when alkylation of benzene was carried out with ethylene on MCM-41, a product containing 99.9 wt.% ethylbenzene which was free from xylenes was obtained[34]. Perego et al[35] have reported liquid phase alkylation of toluene with propylene to produce cymenes. In the present work the alkylation of benzene with a commercial olefin mixture (C_{10}-C_{13}) over mesoporous Al-MCM-41 is reported.

4.1.2.2 Experimental methods

4.1.2.2(i) Preparation of Catalysts

The alkylation of benzene with olefins was tested on two catalysts H-Al-MCM-41(44) and H-Al-MCM-41(14). The details of the methods of preparation of these catalysts have been given in Chapter II and the characterization of these catalysts has been explained in Chapter III.

4.1.2.2(ii) Reaction Procedure

The reaction was carried out in a commercial fixed bed reactor supplied by Autoclave Engineers, USA. The reactor id. was ~ 12 mm. The feed mixture (benzene + olefin mixture) was injected using a high pressure syringe pump. The olefin content of the mixed olefins was 11.2%, the rest being paraffins. The typical composition of the feed mixture is given in Table 4.1. 5 g charge of catalyst in the form of crushed granules (10-12 mesh) was used. The length of the catalyst bed was about 4 cm. The liquid feed entered from the top of the reactor and flowed past the catalyst. The studies consisted of testing the catalysts at different temperatures between 150 and 180°C and weight ratio of benzene/olefin of 5:1.

Table 4.1 Composition of the feed mixture

Compound	Carbon number	Concentration (wt.%)
Paraffin	C_{10}	14.7
	C_{11}	32.7
	C_{12}	20.8
	C_{13}	14.2
Olefins	C_{10}	1.4
	C_{11}	3.9
	C_{12}	3.3
	C_{13}	2.6

A pressure of 15 bar was used for keeping the benzene in the liquid state over the catalyst. To keep the system at the required pressure, a small flow of N_2 (10 ml / min) was maintained. The space velocity (WHSV (h^{-1})) used was = 1. The reaction conditions were chosen to keep the reactant benzene in the liquid state and to achieve a high conversion of the olefins over most of the catalysts. A steady state was reached in about 1h. The products were analyzed using a Hewlett-Packard gas chromatograph (5880 A) with a capillary column (HP 1, cross-linked methyl silicone gum 50 m $\times$ 0.2 mm). As the components in the product possess widely different molecular weights and boiling points, multiple analysis using a split capillary column (50 m HP 5, 0.2 mm i.d.) and a short packed column (10% UCM 982; HP) used in simulated distillation of petroleum oils (ASTM Method 2887) were used in the analysis. Three G.C. analyses were done for each sample; two using a capillary column for LAB and olefin contents. The simulated distillation analysis was done to estimate the relative LAB and HAB contents and to obtain the oligomer and alkylate break up in the HAB fraction (Fig. 4.7).

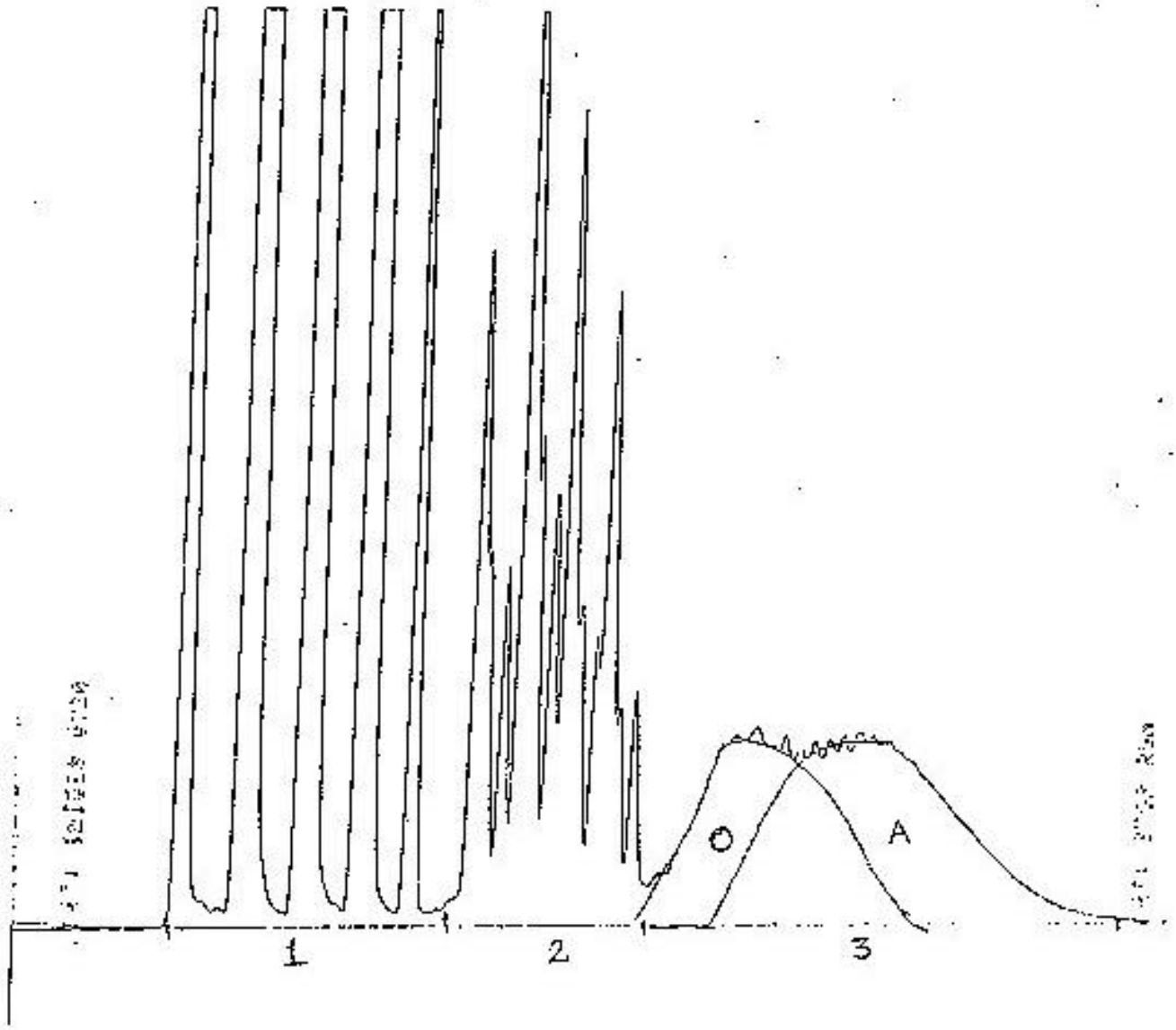

Fig. 4.7 Typical gaschromatogram of a sample obtained under simulated distillation conditions. (1) paraffins; (2) LAB; (3) HAB; (O) oligomers and (A) alkylates.

4.1.2.3 Results and discussion

The influence of temperature on the conversion of the olefins (C_{10} to C_{13}) in the olefin/paraffin mixture is presented in Fig. 4.8. In the case of both the MCM-41 samples (H-Al-MCM-41(44) and H-Al-MCM-41(14), the conversion increases as expected with temperature, the increase being more pronounced for the low-alumina (H-Al-MCM-41(44)) sample. The activity of this sample is quite low (~ 40%) at 150°C and increases to about 80% at 170°C. In case of the high Al sample (H-Al-MCM-41(14)), the conversion increases only marginally from ~ 78% to ~ 82% at 170°C. The smaller conversion increase with temperature in the case of the high Al sample may be due to pore diffusion effects becoming important at higher conversion.

The products of the alkylation of benzene with long chain olefins may be conveniently divided into two fractions, the LAB (linear alkyl benzene) and HAB (heavy alkyl benzene) fractions. The LAB fraction is mainly monoalkylated aromatics while the HAB fraction is mostly made up of dialkylated aromatics and oligomers (mainly dimers). Some diphenyl alkanes formed from the small amounts (< 0.5%) of diolefins in the olefin feed may also be present in HAB.

The relative amounts of HAB and LAB fractions in the product as a function of temperature for the two MCM-41 samples are presented in Fig. 4.9. The yield of HAB goes through a maximum at about 160°C. The initial increase may be due to rapid alkylation while the decrease at higher temperature may be due to the instability of the larger molecules and the onset of cracking and disproportionation reactions. The amount of HAB formation is relatively more over the less acidic MCM-41 (H-Al-MCM-41 (44)) sample than over H-Al-MCM-41 (14).

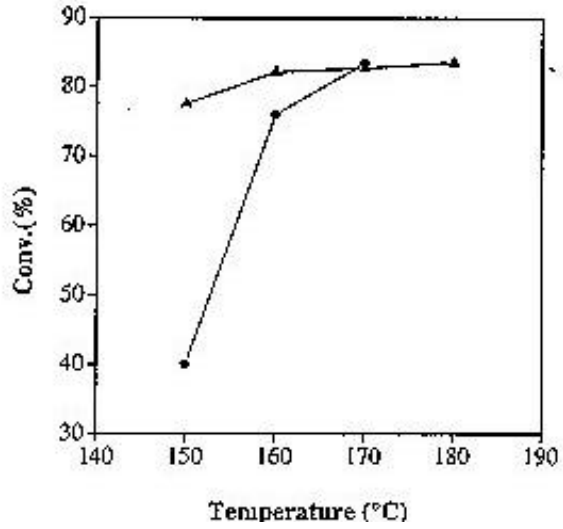

Fig. 4.8 Influence of temperature on the conversion of olefins. Pressure = 10 bar; WHSV (h^{-1}) = 1; N_2 flow = 10 ml/min, (•) H-Al-MCM-41(44) and (σ)H-Al-MCM-41(14).

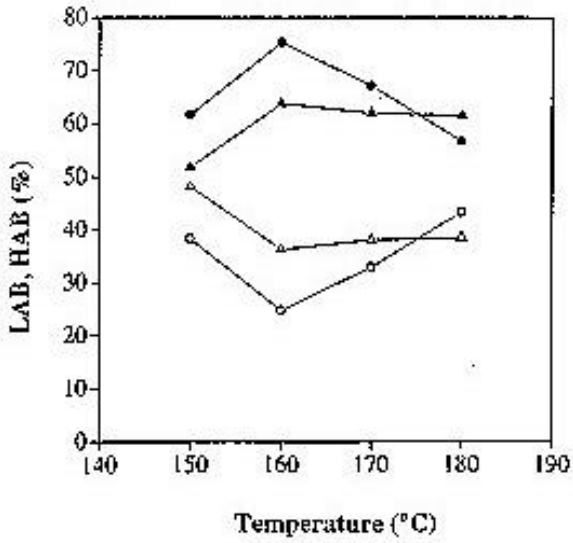

Fig. 4.9 Influence of temperature on LAB and HAB fractions. Pressure = 10 bar; WHSV (h^{-1}) = 1; N_2 flow = 10 ml/min, (•) H-Al-MCM-41(44), HAB; (σ) H-Al-MCM-41(14), HAB; (o) H-Al-MCM-41(44), LAB and (Δ)H-Al-MCM-41(14), LAB.

As the mixed olefins are mixtures of positional isomers, not only all the isomeric alkylbenzenes (except 1-phenyl) are obtained for each olefinic carbon (C_{10} to C_{13}), but also the HAB is made up of mixed oligomers and mixed polyalkyl benzenes (with alkyl groups of different carbon numbers). The dimeric olefins will be in the molecular range of C_{20} to C_{26} while the dialkyl benzenes will be in the molecular range of C_{26} to C_{32}. However due to the large number of positional and skeletal isomers, the boiling points of the two types of compounds merge and it is difficult to separate them individually. When G.C. analysis is carried out by the simulated distillation method, distinct peaks for the dimeric products and the dialkylbenzenes can be seen (Fig. 4.7). The two components of HAB have been separated by deconvolution and their relative amounts have been estimated (Fig. 4.10).

The influence of temperature on the relative amounts of the alkylate and oligomer fractions is presented in Fig. 4.11. It is noticed again that the alkylate yield goes through a maximum with increasing temperature. The formation of the alkylates is more over the Al rich sample. The larger amount of HAB and lower alkylate yield from the H-Al-MCM-41 (44) sample suggest that oligomerization reactions are relatively more over the Al deficient sample than over the Al-rich sample.

The alkylation of benzene with olefins goes through a carbonium ion mechanism[36,37]. In the case of long chain olefins, many secondary carbonium ions are possible. For example, in the case of dodecene, six carbonium ions are possible. The relative stabilities of these increase as the C-number increases, the least stable being the primary ion (1-position). Due to its low stability, the 1-phenyl isomer was not detected in the products. On the basis of the relative stabilities of the others (all secondary), one would expect the isomer content to increase with the position of the carbon towards the centre of the chain.

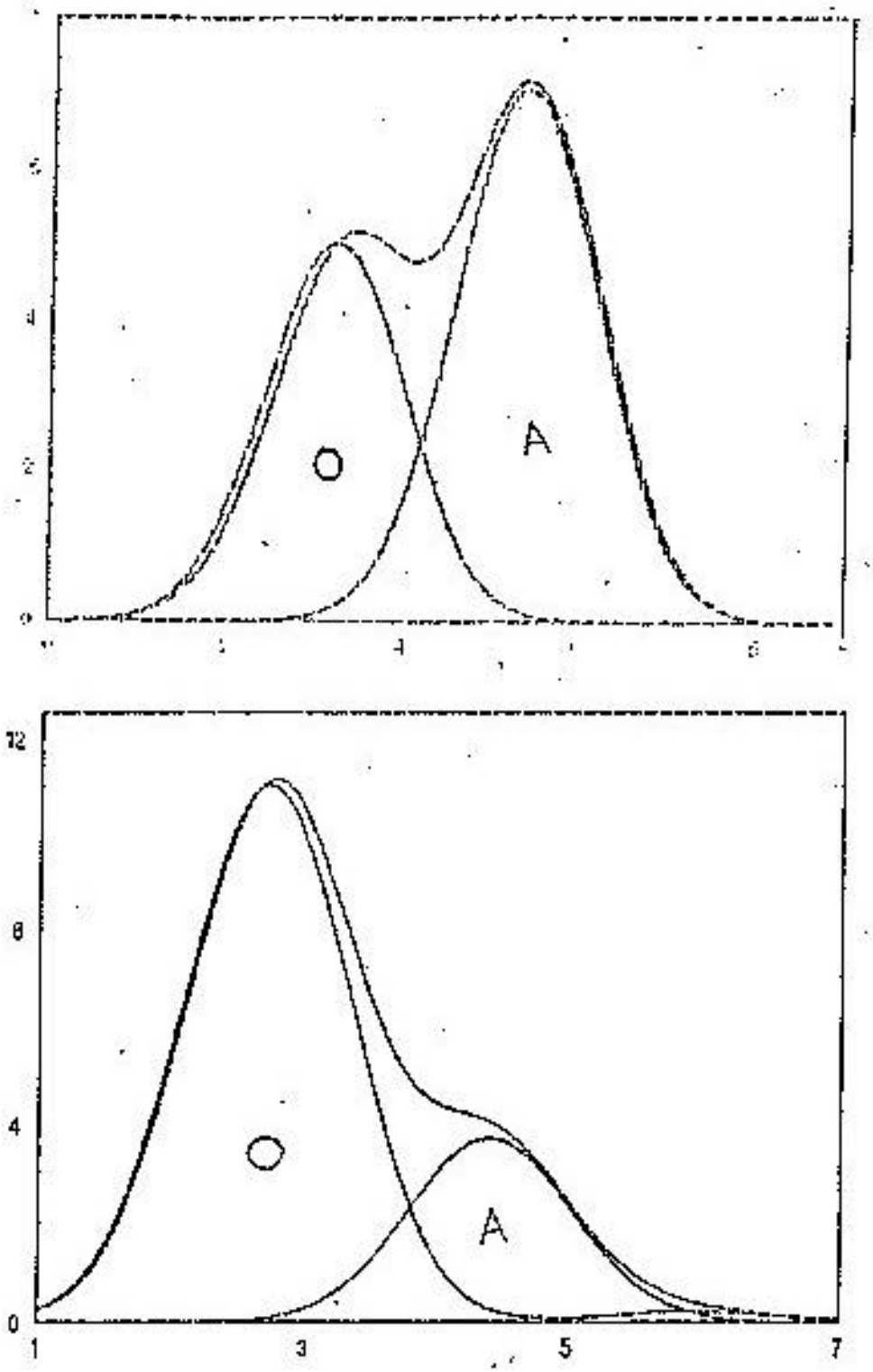

Fig. 4.10 G.C. profiles of HAB; examples of deconvolutions of gas chromatograms. (O) olefin oligomers and (A) dialkyl benzenes

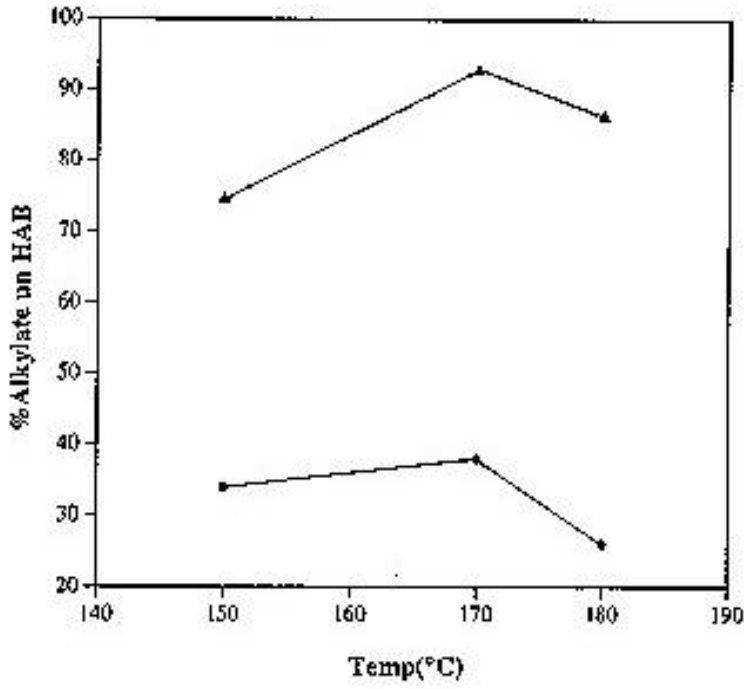

Fig. 4.11 Influence of temperature on alkylate fraction in HAB. Pressure = 10 bar; WHSV (h^{-1}) = 1; N_2 flow = 10 ml/min, (●) H-Al-MCM-41(44), and (○) H-Al-MCM-41(14).

As a result, the ratios of the 2-ϕ (2-phenyl alkane) to the 5-ϕ or 6-ϕ alkanes (5-phenyl or 6-phenyl) are less than 1 when thermodynamic equilibrium is reached. This has been reported to be so in alkylation of 1-dodecene over HF and RE-Y[36] (2-ϕ / 6-ϕ ~ 0.8) implying the attainment of thermodynamic equilibrium in these cases. In the present study, the 2-ϕ / 5-ϕ ratios were always higher (> 1 for C_{10}-C_{13} olefins) than those observed over HF and Re-Y suggesting non-attainment of equilibrium (Table 4.2).

Table 4.2 Alkylation of Benzene with 1-Dodecene

Catalyst	Product distribution					2-f /6-f ratio
	2-ϕ[a]	3-ϕ	4-ϕ	5-ϕ	6-ϕ	
SiO_2-Al_2O_3[a]	33.4	21.9	14.8	15.6	14.2	2.4
RE-Y[a]	17.6	19.1	19.8	22.0	21.5	0.8
HF[b]	20	17	16	23	24	0.8
H-Al-MCM-41 (44)[c]	25.2	18.6	18.1	19.9	18.1	1.4

[a]S. Sivasanker and Thangaraj, J. Catal. 138, 386 (1992); Ref. 38

[b]Data of Olson (ref 39): Temp. = 289 ± 3 K

[c]Product from C_{12} olefin fraction.

The olefin mixture used in these studies were obtained by dehydrogenation at elevated temperatures (> 450°C). At these conditions, the equilibrium content of the terminal olefins is more than the internal olefins. During alkylation at lower temperatures (150-180°C), two possibilities exist: 1) the olefins equilibrate to the thermodynamic composition at the reaction temperature prior to undergoing alkylation and 2) rapid alkylation takes place first and the alkylates isomerize over the catalyst into an equilibrium composition. Higher 2-ϕ contents have been reported by earlier workers during the alkylation of 1-dodecene over some catalysts such as SiO_2-Al_2O_3, Amberlyst 15, H-montmorillonite[39] and $AlCl_3$. In the case of the above solid catalysts, their weaker acidity was suggested to be responsible for the larger formation of the 2-ϕ isomer, while in the case of $AlCl_3$, it was attributed to steric and solvation effects stabilizing the 2-phenylarenium ion[40]. The non-attainment of equilibrium in

the present study is probably due to the weaker acidity of the catalysts (similar to SiO_2-Al_2O_3).

The influence of temperature and C-number of the olefins on the 2-ϕ / 5-ϕ ratios for the different olefin carbon numbers are presented in Fig. 4.12 and 4.13, respectively. It is noticed that the 2-ϕ / 5-ϕ ratio increases with increase in the C-number at all the temperatures. This suggests a greater difficulty in attainment of equilibrium with increase in the carbon number. The 2-ϕ / 5-ϕ ratio decreases continuously with increase in temperature for the C_{10} fraction but goes through a maximum for the other fractions. The general decrease noticed at higher temperatures is probably due to greater approach towards equilibrium compositions at higher temperatures. The reason for the maxima is not clear and not easy to explain in the absence of olefin distribution data.

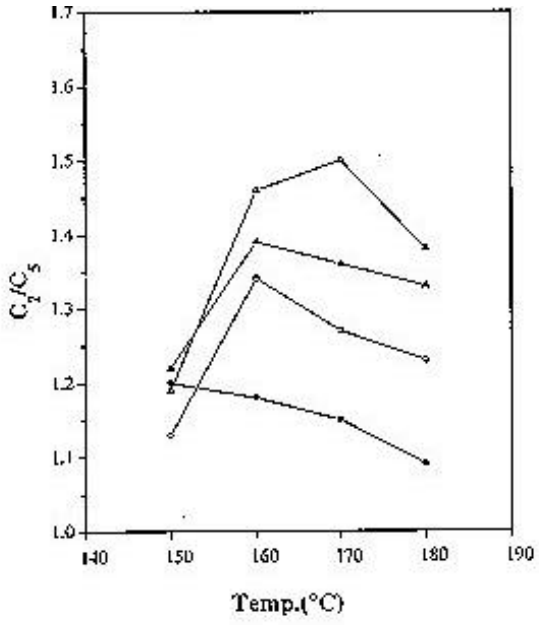

Fig. 4.12 Influence of temperature on 2-ϕ /5-ϕ ratio. Pressure = 10 bar; WHSV (h^{-1}) = 1; N_2 flow = 10 ml/min, (•) H-Al-MCM-41(14), C_{10}; (σ) H-Al-MCM-41(14), C_{11}; (o) H-Al-MCM-41(14), C_{12} and (Δ) H-Al-MCM-41(14), C_{13}.

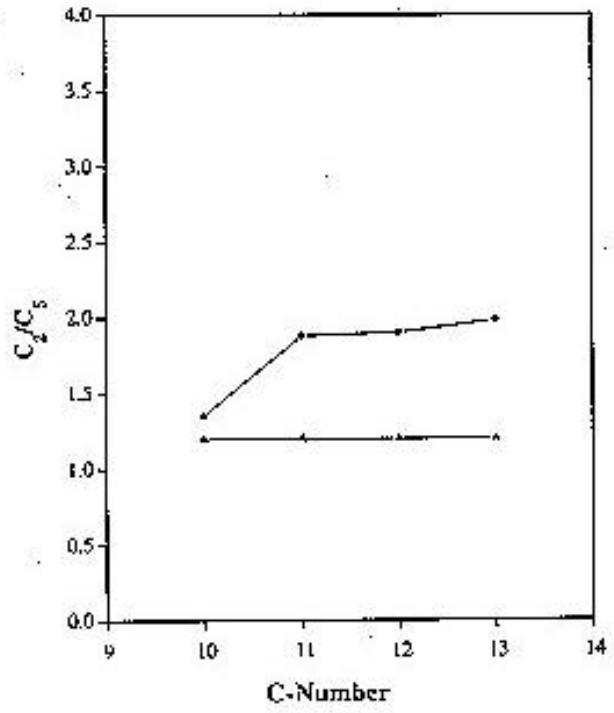

Fig. 4.13 Influence of C-Number on C_2 /C_5 ratio. Pressure = 10 bar; WHSV (h^{-1}) = 1; N_2 flow = 10 ml/min, (•) H-Al-MCM-41(44), C_2 /C_5, 150°C ; (σ) H-Al-MCM-41(14), C_2 /C_5, 150°C.

4.1.3 BECKMANN REARRANGEMENT OF CYCLOHEXANONE OXIME

4.1.3.1 Introduction

Liquid phase Beckmann rearrangement of cyclohexanone oxime to ε-caprolactam, which is the monomer of nylon-6, is carried out industrially using concentrated sulphuric acid as the catalyst[41]. Although the process is highly selective even at a low reaction temperature, it has several disadvantages such as the requirement of a large amount of ammonia to neutralize the sulphuric acid during the separation of ε-caprolactam from the product mixture, the large amount of low value ammonium sulphate (formed in larger amount than ε-caprolactam) and

corrosion and environmental pollution caused by the use of fuming sulphuric acid. To overcome these problems, many research groups have attempted to carry out vapour phase Beckmann rearrangement using solid acid catalysts like silica-alumina[42], zeolite Y[43,44], mordenite[43,45], ZSM-5[46], TS-1[47], ZSM-11 and TS-2[48]. Use of such solid acid catalysts in the rearrangement is favoured for economic and environmental reasons.

It has been suggested that the strong Brönsted acidity of the zeolite catalyst enhances the formation of ε-caprolactam[44]. However, a majority of researchers have noticed that weak or intermediate strength acid sites or even neutral silanol groups present on the external surface of the zeolites are effective for this rearrangement[49-52] while strong acid sites accelerate the formation of by-products[53,.54]. Decrease in acidity and increasing the silanol groups has been reported to enhance the formation of ε-caprolactam. It is well known that the mesoporous material MCM-41 possessing a hexagonal array of pores[55,56], has a large amount of surface SiOH groups[57] and its acidity is considerably weak[58,59]. Considering this characteristic property of the structure of mesoporous molecules, Dai *et al.*[60] have studied the Beckmann rearrangement of cyclohexanone oxime using methanol and hexanol as diluents and it has been revealed that the protonic form of mesoporous molecular sieves exhibited high activities. In the present work, we report the conversion of cyclohexanone oxime to ε-caprolactam on Si-MCM-41 and H-Al-MCM-41 with different Al contents in acetonitrile solvent.

4.1.3.2 Experimental methods

4.1.3.2(i) Preparation of Catalysts

The details of preparation of the Al-MCM-41 molecular sieves with different Si/Al ratios (designated as Al-MCM-41(44), Al-MCM-41(23) and Al-MCM-41(14)) and their

modification have been given in Chapter II, while the characterization of these catalysts has been explained in Chapter III.

4.1.3.2(ii) Reaction Procedure

The catalytic reactions were carried out in a down flow fixed bed tubular glass reactor (i.d. = 15 mm; 30 cm length) at atmospheric pressure using about 2 g of the catalyst. The catalyst was compacted in a hydraulic press, the pellets were broken and then sieved to 16-20 mesh size prior to use. The top section of the reactor (~ 20 cm long) above the catalyst bed (~ 3 cm long) which was packed with ceramic beads acted as the preheating section. The reactor was placed inside a temperature controlled vertical furnace (Geomécanique, France). The thermocouple tip was centred at the middle of the catalyst bed. A solution of cyclohexanone oxime (20 wt.%) in acetonitrile was fed using a syringe pump. The inert gas (nitrogen gas; 20 ml/min) was introduced using a mass flow controller. Cyclohexanone oxime used was 97% pure (Aldrich). The conditions of the reactions were, temp. = 300-400°C, WHSV(h^{-1}) = 1. The catalyst was dried *in situ* in a flow of N_2 (20 ml/min) at 450°C for 6 h, cooled to 350°C prior to start of run. The reaction products were collected in a receiver after cooling with ice cold water and analyzed using a Hewlett-Packard gas chromatograph (5880 A) with a capillary column (cross-linked methyl silicone gum, HP1, 50 m × 0.2 mm id) and a flame ionization detector (FID).

4.1.3.3 Results and discussion

The main reactions that occur during the rearrangement of cyclohexanone oxime to ε-caprolactam are:

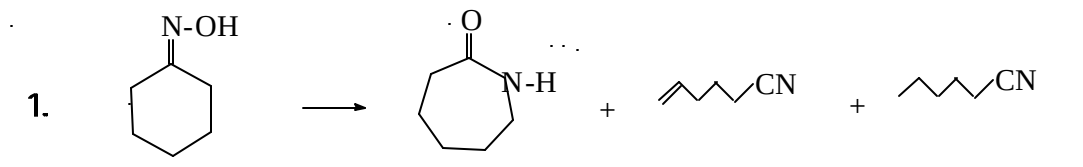

Cyclohexanone Oxime ε-Caprolactam 5-Cyanopent-1-ene 5-Cyanopentane

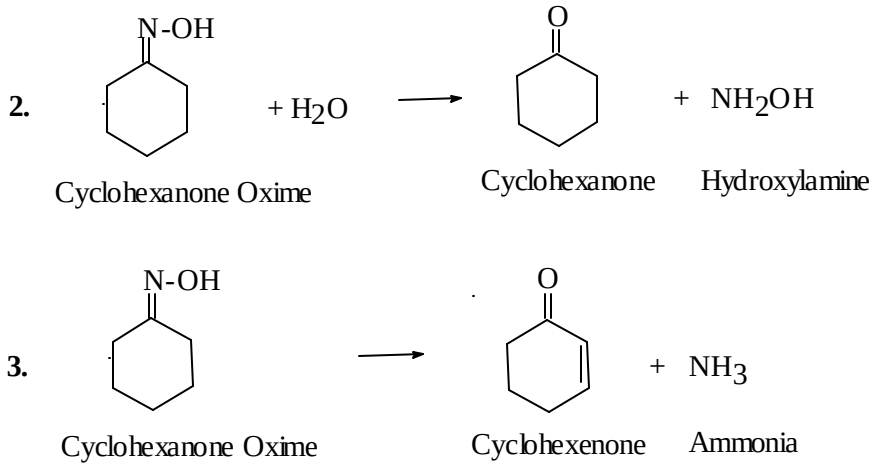

Table 4.3 presents the product distribution in the reaction over different catalysts with acetonitrile as the solvent. The major product was found to be the rearranged product ε-caprolactam.

Table 4.3 Product distribution in Beckmann rearrangement[a]

Catalyst	**Conv. (Wt.%)**	**Selectivity (Wt.%)**				
		Capro-lactam	**Cyano-pentane**	**5-Cyano-pentene**	**Cyclo-hexenone**	**Cyclo-hexanone**
Si-MCM-41	> 99.0	32.4	-	6.8	36.4	24.4
Al-MCM-41(44)	> 99.0	48.3	11.1	-	16.6	24.0
Al-MCM-41(23)	> 99.0	65.6	8.4	-	12.3	13.6
Al-MCM-41(13)	> 99.0	87.6	3.8	-	4.3	4.3

[a]Reaction conditions: Temp. = 360°C; WHSV (h^{-1}) = 1; TOS = 3 h; Cyclohexanone oxime: Acetonitrile = 1:5 (Wt.%); Feed rate = 4ml/h; N_2 flow rate = 20 ml/min.

The conversion of cyclohexanone oxime remained nearly constant (± 2%) with time on stream (TOS) upto 5 h over all the catalysts at all the temperatures studied (300-390°C).

However, the selectivity to ε-caprolactam gradually increased with TOS and reached a maximum at about 3 h. The variations in selectivity as a function of duration of run over the different catalysts are presented in Fig. 4.14. Selectivity variations with TOS for Al-MCM-41(14) and Si-MCM-41 at different temperatures are plotted in Fig. 4.15. Both sets of data reveal maximum caprolactam selectivity at TOS of ~ 3h. Hence, data were collected at a TOS of 3 h during further studies. The initial increase in selectivity is probably due to deactivation of the strong acid sites. Interestingly, the dependence of selectivity on TOS is different from the observation of earlier workers who have reported a continuous increase in selectivity with time[47].

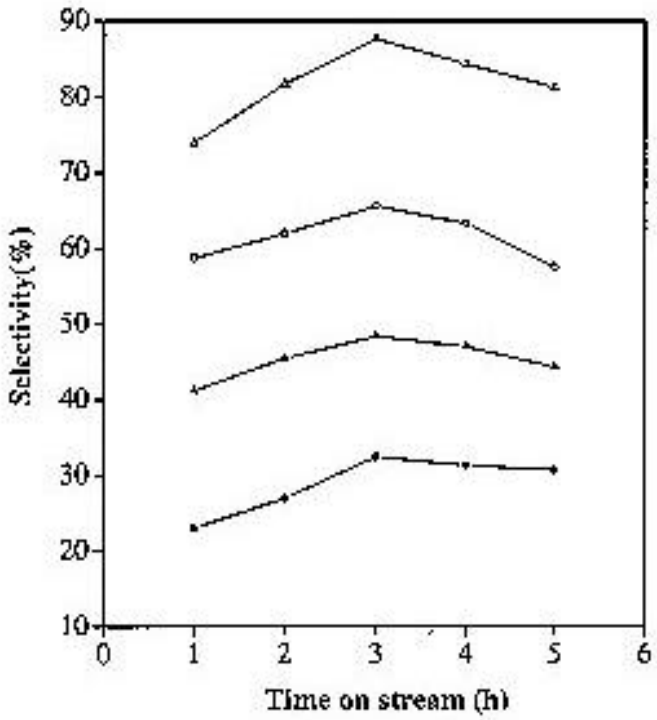

Fig. 4.14 Effect of time on stream (TOS) on selectivity for caprolactam. Conditions: Temp. = 360°C; WHSV (h^{-1}) = 1; Cyclohexanone oxime:acetonitrile = 1:5 (wt.%); N_2 flow rate = 20 ml/min.; (•) Si-MCM-41; (σ) H-Al-MCM-41(44); (o) H-Al-MCM-41(23)); (Δ)H-Al-MCM-41(14).

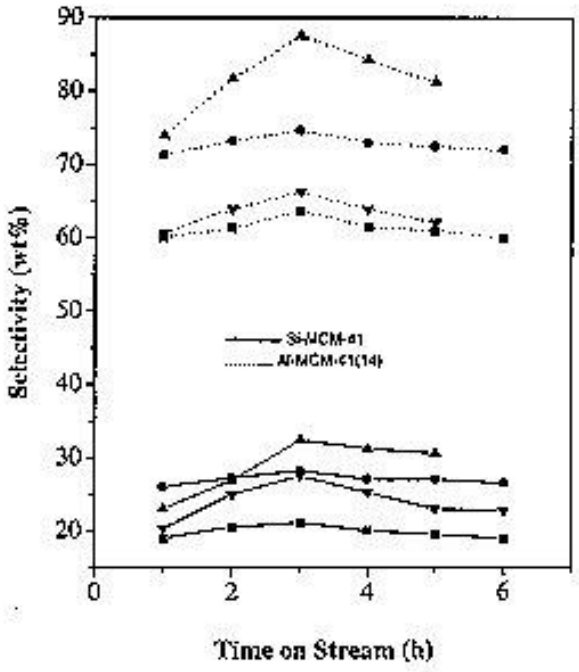

Fig. 4.15 Effect of time on stream (TOS) on selectivity for caprolactam at different temperatures. Conditions: WHSV (h^{-1}) = 1; Cyclohexanone oxime: acetonitrile = 1:5 (Wt.%); N_2 flow rate = 20 ml/min.; (■)300°C; (●) 330°C; (σ) 360°C and (τ) 390°C.

4.1.3.3(i) Influence of temperature

The effect of temperature on the selectivity of cyclohexanone oxime to ε-caprolactam over different catalysts is presented in Figure 4.16. The transformation of the oxime was rapid over the catalysts and reached nearly 100% at temperatures > 330°C over all the catalysts (Fig. 4.16). The rearrangement was studied in the temperature range 300-400°C. As reported in the literature[60], the conversions were nearly stable (upto 5 h) at the temperatures studied. The selectivity for ε-caprolactam increased upto 360°C and decreased beyond 360°C. At 360°C, the lactam yield on the catalyst with Si/Al = 14 was 87%.

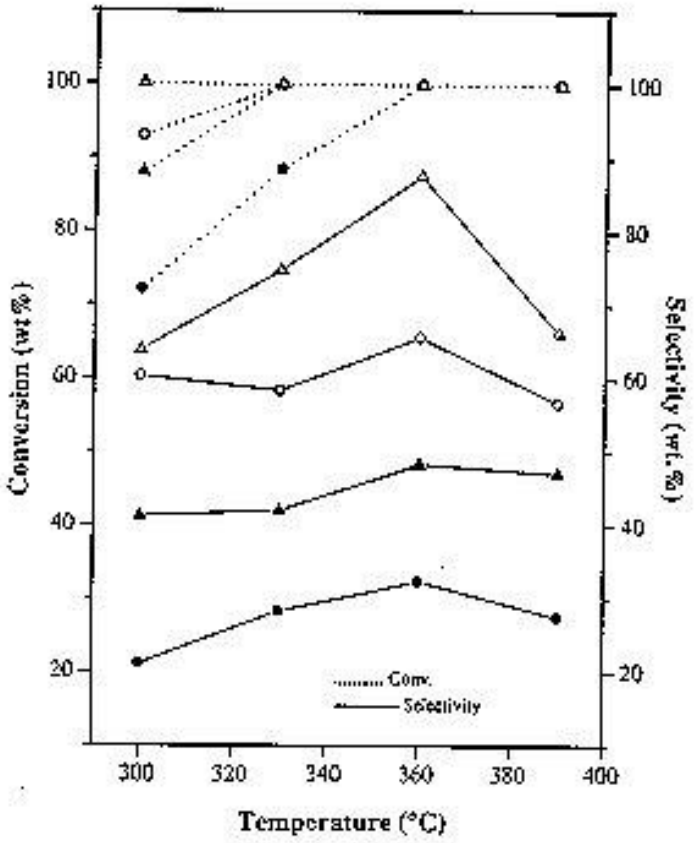

Fig. 4.16 Effect of temperature on conversion of cyclohexanone oxime and selectivity for caprolactam. Conditions: TOS = 3 h; WHSV (h^{-1}) = 1; Cyclohexanone oxime: acetonitrile = 1:5 (Wt.%); N_2 flow rate = 20 ml/min.; (•) Si-MCM-41; (σ) H-Al-MCM-41(44); (o) H-Al-MCM-41(23); (Δ)H-Al-MCM-41(14).

The decrease in selectivity at higher temperatures is probably due to the decomposition of the ε-caprolactam on the catalyst surface and increase of the side reactions[51]. The product break up at different temperatures over two typical catalysts Al-MCM-41(14) and Si-MCM-41 are presented in Fig. 4.17. The yield of the byproducts decreases with temperature with a concomitant increase in caprolactam production upto almost 360°C, beyond which they increase again. The yields of cyclohexanone and cyclohexenone are very high over silicalite.

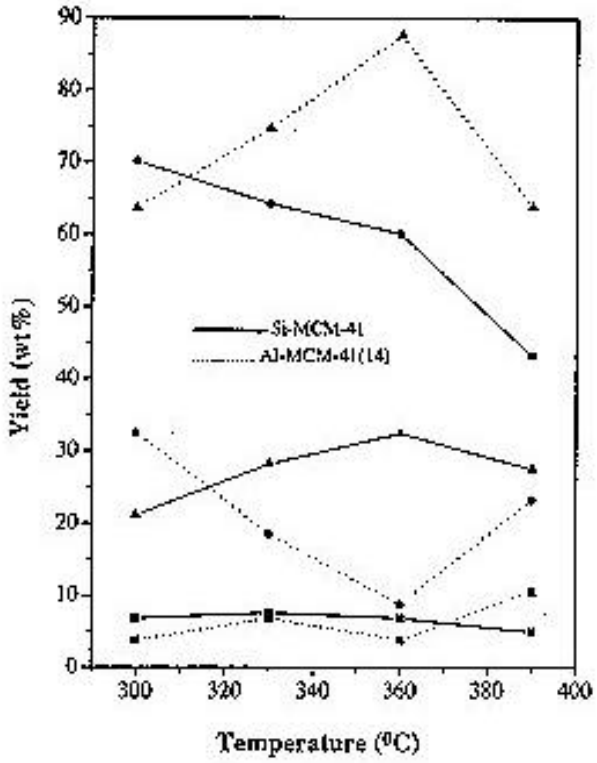

Fig. 4.17 Break up of products at different temperatures. Conditions: WHSV (h^{-1}) = 1; Cyclohexanone oxime: acetonitrile = 1:5 (wt.%); TOS = 3 h; N_2 flow rate = 20 ml/min.; (■) cyanopentane + 5-cyanopentene; (●) cyclohexanone + cyclohexenone and (σ) caprolactam.

4.1.3.3 (ii) Influence of Space Velocity

The influence of contact time on conversion and caprolactam selectivity at 360°C is presented in Fig. 4.18 (a) and 4.18 (b), respectively. Increasing the contact time increases the conversion over the catalysts (Fig. 4.18 (a)). In the case of Al-MCM-41(14), the conversion increases to nearly 100%, even at the lowest contact time investigated. The selectivity for caprolactam goes through a maximum at an intermediate contact time (~ 0.53 h).

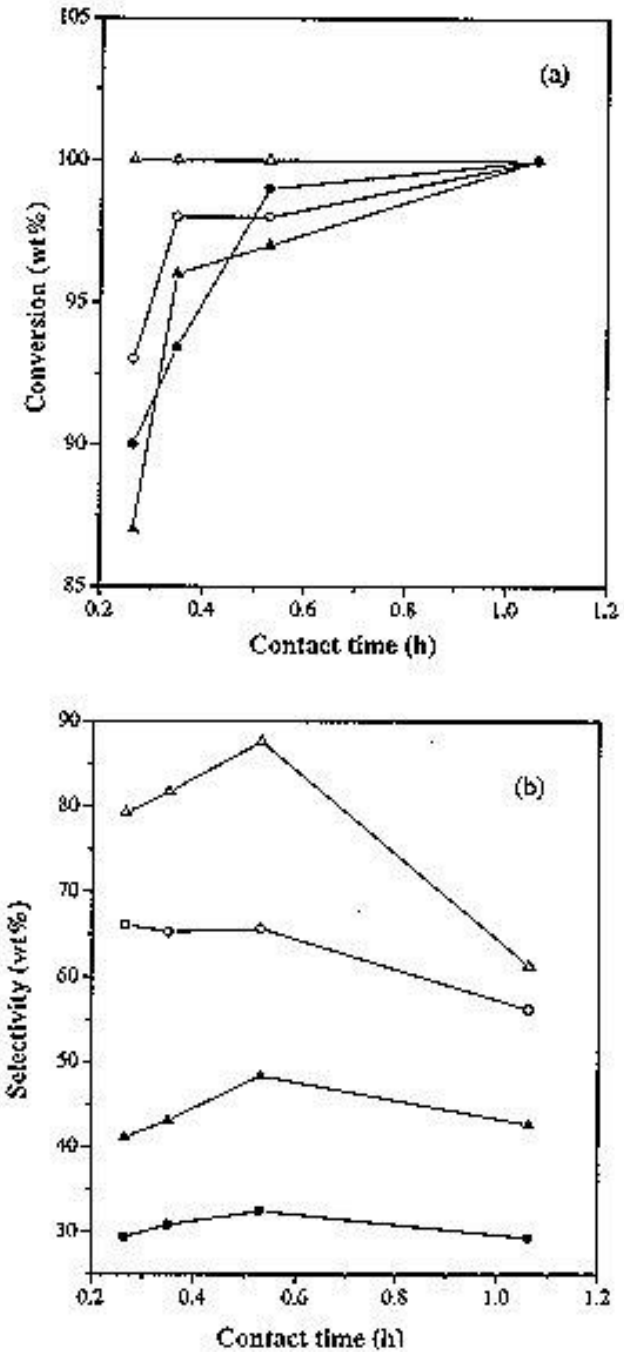

Fig. 4.18 Effect of contact time on (a) conversion and (b) selectivity. Conditions: Temp. = 360°C; Cyclohexanone oxime: aceto nitrile = 1:5 (Wt.%); TOS = 3 h; N_2 flow rate = 20 ml/min.; (●) Si-MCM-41; (σ) H-Al-MCM-41(44); (o) H-Al-MCM-41(23) and (Δ)H-Al-MCM-41(14).

The product distribution at different contact times over the Si-MCM-41 and Al-MCM-41(14) are presented in Fig. 4.19. It is noticed that the yield of caprolactam increases rapidly with contact time while the byproducts decrease upto a contact time of about 0.53 h. At higher contact time, the caprolactam yield decreases. A rapid increase in yield of cyclohexanone and cyclohexenone is also noticed beyond 0.53 h in the case of Al-MCM-41(14).

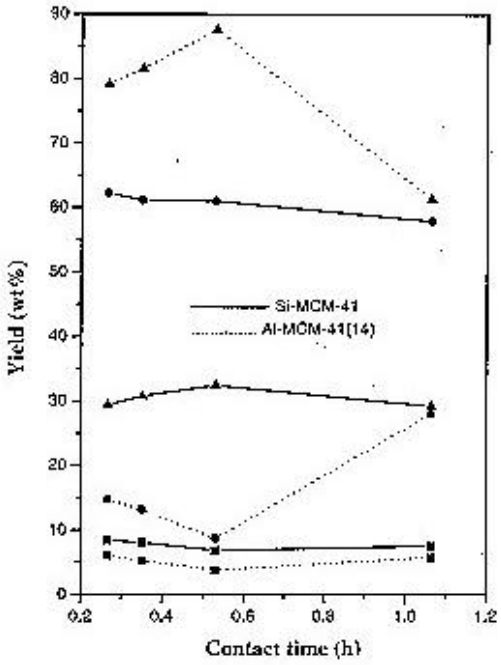

Fig. 4.19 Effect of contact time on product distribution. Conditions: Temp. = 360°C; Cyclohexanone oxime: acetonitrile = 1:5 (Wt.%); TOS = 3 h; N_2 flow rate = 20 ml/min.; (v) cyanopentane + 5-cyanopentene; (●) cyclohexanone + cyclohexenone and (σ) caprolactam.

4.1.3.3 (iii) Influence of Si/Al ratio

The effect of Al content in the H-Al-MCM-41 samples was investigated over the catalysts having different Si/Al ratios (Si/Al of 44, 23 and 14). The selectivity of ε-caprolactam was more over the Al-MCM-41 samples than Si-MCM-41. It increased with increase in Al content (Fig. 4.20). Maximum ε-caprolactam with a high selectivity of 87.6% was formed over the catalyst with a Si/Al = 14. It was observed that the yield of the byproducts decreased with increasing Al content in the catalysts (Table 4.3). Apparently, the silanol groups present on Si-MCM-41 are not sufficiently acidic to catalyze the rearrangement though they are able to catalyze the formation of the byproducts.

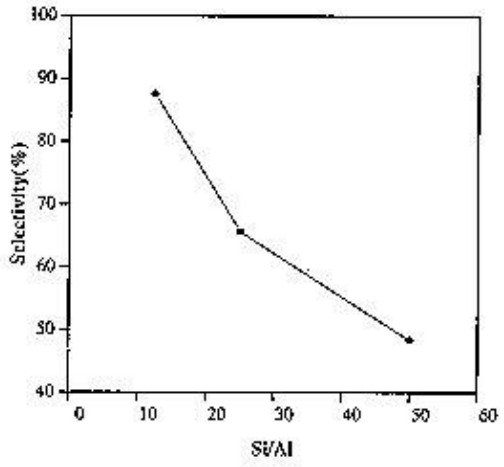

Fig. 4.20 Effect of Al content selectivity for caprolactam. Conditions: Temp. = 360°C; WHSV (h^{-1}) = 1; TOS = 3 h; Cyclohexanone oxime: acetonitrile = 1:5 (wt.%); N_2 flow rate = 20 ml/min.

More hydrolysis products are obtained over Si-MCM-41 probably due to the reaction of the surface –OH groups with the oxime. This observation is also different from that of earlier workers who observed an increase in selectivity with decreasing Al content[47] in the case of MFI type materials.

4.2 PART II: OXIDATION REACTIONS

4.2.1 Introduction

The catalytic properties of zeolites in selective oxidation reactions are well known.[61]. Due to the remarkable properties of TS-1 in oxidation reactions at low temperatures with dilute H_2O_2 as an oxidant[6,61,62], the synthesis of Ti-containing large pore zeolites and mesoporous materials has received considerable attention[63-67]. Simultaneously, other cations like V^{4+}, Cr^{3+}, Mo^{6+}, Mn^{3+} etc[68-73] have been incorporated in the mesoporous molecular sieves and used in oxidation reactions. The Ti and V containing MCM-41 molecular sieves have been used in a variety of oxidation reactions of bulky molecules using either H_2O_2 or TBHP as oxidant[74-79]. A few reports describe the synthesis and basic characterization of mesoporous silica modified by metals like Cr[70,71], Mo[72] or Mn[73]. Cr-MCM-41[71] has been found to be catalytically active in the hydroxylation of phenol, 1-naphthol and oxidation of aniline with aqueous H_2O_2.

In the present work, we report catalytic oxidation reactions over Sn-MCM-41 and Zr-MCM-41 molecular sieves. Sn-MCM-41 has been evaluated for catalytic activity in the hydroxylation of phenol, 1-naphthol and epoxidation of norbornene and Zr-MCM-41 has been tested for the hydroxylation of 1-naphthol and epoxidation of norbornene.

4.2.2 Experimental

Catalytic activity tests were carried out using a batch reactor at atmospheric pressure (at 80°C). Aqueous H_2O_2 (25 wt.% solution) was used in the hydroxylation of phenol and 1-naphthol while TBHP (70% aqueous solution, Aldrich) was used in the epoxidation of norbornene. In a standard run of phenol hydroxylation, 1 g phenol, 10 g water and 0.1 g catalyst were taken in a 50 ml round bottomed flask equipped with a condenser and heated at 80°C in an oil bath with stirring. H_2O_2 was added (phenol/H_2O_2 mole ratio = 3) to the

reaction mixture and the reaction was continued for 24 hours. The oxidation of 1-naphthol was carried out by taking 0.5 g reactant, 10 g acetonitrile and 0.1 g catalyst in a 50 ml round bottomed flask attached with a condenser and heated at 80°C in an oil bath. The oxidant (H_2O_2) was added to the reaction mixture and the reaction was carried out for 24 h. In the epoxidation of norbornene, 0.5 g of norbornene dissolved in 10 g of acetonitrile was taken in a 50 ml round bottomed flask equipped with a condenser and 0.1 g of the catalyst was added to it. The reaction mixture was heated at 70°C in an oil bath with stirring. TBHP (norbornene/TBHP = 1.5) was added to the above mixture. The reaction was continued for 24 h and the products were removed from the flask at different intervals. The products were analyzed in a GC (HP-5880A) equipped with a methyl-silicon gum capillary column (HP1, 50m long and 0.2 mm i.d.) and a flame ionization detector (FID).

4.2.3 Results and discussion

4.2.3.1 Hydroxylation Reactions

The Sn-MCM-41 samples possess selective oxidation properties when peroxides are used as oxidants. The hydroxylation of phenol and 1-naphthol were carried out over four Sn-MCM-41 samples containing different amounts of Sn. For comparison, the reactions were carried out over Sn-impregnated MCM-41 and Si-MCM-41 (Table 4.4 and 4.5). The inactivity of the Sn-free material (Si-MCM-41) suggests that Sn-ions are responsible for activity. This is also confirmed by the increase in conversion with increase in Sn-content of the samples (Tables 4.4 and 4.5). In both the hydroxylation reactions the activity of the Sn-impregnated MCM-41 was much less than those of the Sn-MCM-41 samples (Tables 4.4 and 4.5). This is probably due to the larger activity of the Sn^{4+} incorporated in the framework than the impregnated Sn species. Interestingly, it is noticed that the Turn Over Numbers (TON; no. of reactant molecules converted per Sn atom in 24h; Tables 4.4 and 4.5) decrease

with increasing Sn content. If all the Sn ions were equally active and monoatomically dispersed in the samples, one would expect a constancy in the TON for all the samples. The possible explanation for the decrease is that, more than one type of Sn species is present in the samples, and the proportion of the less active Sn species increases with Sn content in the samples (Samples Sn-MCM-41-C(178) to Sn-MCM-41-C(42)). Both UV-vis and Mössbauer studies suggest the presence of octahedral coordinated Sn (besides Sn in tetrahedral coordination) in samples containing more Sn. Part of the Oh Sn could also exist as poorly dispersed SnO_2. The TON values are smaller for 1-naphthol than for phenol in spite of the larger amount of the H_2O_2 used for the hydroxylation of the former due to greater difficulty of the reaction. The major product in 1-naphthol hydroxylation is 1,4 - naphthoquinone produced from the subsequent oxidation of the primary 1,4 - dihydroxy product. In the case of phenol, the activities of the Sn-MCM-41 samples are similar to those reported for VS-2 by earlier workers[80,81]. For example, a TON of 133 has been reported by Prasad and Ramaswamy[80] for VS-2 with Si/V = 79, comparable to the value (110) observed by us for Sn-MCM-41(C) with Si/Sn = 82. Though the ratios of the yields of the p/o-products ((PBQ+HQ)/CAT) is similar (~1) to those reported for titano- and vanadosilicates[82] in aqueous medium, more benzoquinone is formed over the Sn-MCM-41 samples suggesting the deeper oxidation ability of the active Sn-species.

It is noticed that the activity of the samples synthesized from DTMABr (Sn-MCM-41-D samples) are similar to those prepared from CTMACl/OH (Sn-MCM-41-C samples; Table 4.4 and Table 4.5). Apparently the method of preparation does not affect the activity of the catalysts.

The results of the hydroxylation of 1-naphthol over Zr-MCM-41 samples are presented in Table 4.6. The samples prepared using surfactants CTMACl/OH and DTMABr are equally active. Going by the TON values, Zr-MCM-41 samples are less active than the Sn-MCM-41

samples. The H_2O_2 selectivities are also slightly lower for Zr catalysts. Examining the product distribution pattern, they are similar to those observed over the Sn-catalysts, though a little more naphthoquinones are produced over the Zr samples. Again, as in the case of Sn samples, the activity of the impregnated catalysts is very small.

Table 4.4

Activity of the Sn-MCM-41-C and Sn-MCM-41-D samples in the hydroxylation of phenol[a]

Sample	Phenol conv. (mol %)	H_2O_2 select. (mol %)	TON[b]	Product distribution (mass %)[c]		
				PBQ	CAT	HQ
Sn-MCM-41-C(178)	14.8	50.0	170.5	30.0	55.4	14.6
Sn-MCM-41-C(133)	17.4	55.8	150.5	26.4	57.4	16.2
Sn-MCM-41-C(83)	20.2	65.3	110.3	25.2	57.5	17.3
Sn-MCM-41-C(42)	22.8	72.3	64.8	23.8	57.8	18.4
Sn-MCM-41-D(85)	19.8	64.3	110.6	25.4	56.8	17.8
Sn-MCM-41-D(43)	22.5	71.7	65.4	23.4	58.4	18.2
Sn-impregnated MCM-41	1.0	3.9	3.4	50.0	25.0	25.0
Si-MCM-41	No detectable activity					
Sn-silica-gel	1.3	5.2	4.4	55.2	24.8	20.0
SnO_2	0.5	2.0	0.1	53.5	24.3	22.2
VS-2 (SI/V = 79)[d]	25.8	58.7	133.7	2.3	55.5	42.2

[a]Reaction conditions: phenol = 1 g; phenol/H_2O_2 = 3; catalyst = 0.1 g; solvent (water) = 10 g; temp. = 80°C; reaction time = 24 h.

[b]Turn over number (number of molecules of phenol converted per atom of Sn in 24 hours).

[c]PBQ = *para*-benzoquinone; CAT = catechol; HQ = hydroquinone.

[d]Data of Prasad and Ramaswamy (Ref. 80).

An important aspect of the study of oxidation reactions over metallosilicate molecular sieves is proving that the reaction is truly heterogeneous. We believe that the heterogeneous pathway is the major component in all the reactions reported in this section. Thus conclusion has been arrived from the nondetectability of dissolved Sn or Zr in the liquid products and the negligible conversions observed over the impregnated catalysts which are expected to be more susceptible to leaching than the metallosilicates with more firmly anchored metal ions.

Table 4.5

Activity of the Sn-MCM-41-C and Sn-MCM-41-D samples in the hydroxylation of 1-naphthol[a]

Sample	1-naphthol Conv. (mole %)	H_2O_2 Select. (mole %)	TON[b]	Product distribution (wt %)		
				1,4 naphtho-quinone	1,4 dihydroxy naphtha-lene	1,2 dihydroxy naphtha-lene
Sn-MCM-41-C(178)	14.2	40.0	53.4	88.0	7.7	4.3
Sn-MCM-41-C(133)	15.3	42.3	43.2	84.3	11.1	4.6
Sn-MCM-41-C(83)	17.1	46.9	30.5	83.0	12.3	4.7
Sn-MCM-41-C(42)	18.9	55.6	17.5	82.1	13.1	4.8
Sn-MCM-41-D(85)	16.6	46.4	30.3	86.2	9.7	4.1
Sn-MCM-41-D(43)	18.3	50.8	17.4	85.1	10.4	4.5
Sn-impregnated MCM-41	1.0	4.5	1.1	50.0	50.0	-
Si-MCM-41	No detectable activity					
Sn-silica-gel	1.2	2.8	1.3	58.3	25.0	16.7
SnO_2	0.5	1.2	0.03	60.0	20.0	20.0

[a]Reaction conditions: 1-naphthol = 0.5 g; 1-naphthol/H_2O_2(mole) = 1.5; catalyst = 0.1 g; solvent (acetonitrile) = 10 g; temp. = 80°C; reaction time = 24 h.

[b]Turn over number (number of molecules of 1-naphthol converted per atom of Sn in 24 h).

Table 4.6

Activity of the Zr-MCM-41-C and Zr-MCM-41-D samples in the hydroxylation of 1-naphthol[a]

Sample	1-naphthol	H_2O_2	TON[b]	Product distribution (wt %)		
	Conv. (mole %)	Select. (mole %)		1,4 naphtho-quinone	1,4 dihydroxy naphtha-lene	1,2 dihydroxy naphtha-lene
Zr-MCM-41-C(96)	10.18	29.4	20.6	95.4	1.9	2.7
Zr-MCM-41-C(55)	14.2	41.4	16.9	94.3	2.6	3.1
Zr-MCM-41-C(39)	17.8	51.5	15.2	92.6	3.7	3.7
Zr-MCM-41-C(23)	16.6	47.4	8.7	90.5	4.2	5.3
Zr-MCM-41-D(102.3)	9.8	29.2	21.3	97.7	1.4	0.9
Zr-MCM-41-D(58.9)	11.6	34.2	14.7	96.9	1.8	1.3
Zr-MCM-41-D(42)	16.5	48.2	15.1	94.7	3.4	1.9
Zr-MCM-41-D(33)	17.1	49.5	12.5	92.8	4.4	2.8
Zr-impregnated (25)[c]	1.0	2.3	0.6	50.0	50.0	0.00

[a]Reaction conditions: 1-naphthol = 0.5 g; 1-naphthol/H_2O_2(mole) = 1.5; catalyst = 0.1 g; solvent (acetonitrile) = 10 g; temp. = 80°C; reaction time = 24 h.

[b]Turn over number (number of molecules of 1-naphthol converted per atom of Zr in 24 h).

[c]Zr impregnated MCM-41 with Si/Zr = 25.

4.2.3.2 Epoxidation

The Sn-MCM-41-C samples were also active in the epoxidation of norbornene with tertiary butyl hydroperoxide (TBHP) (Table 4.7). The reaction was nearly complete after 10 h. Continuing the reaction upto 24 h increased the conversion only marginally (28.2% at 10 h and 29.7% at 24 h in case of Sn-MCM-41(178). This is attributed to the near exhaustion of

the peroxide after 10 h through consumption in the reaction and decomposition. Similar results were also obtained over the other samples. Again the TON values decrease with increase in the Sn content of the samples. This was earlier attributed to the larger amount of the less active Oh Sn-species in samples with more Sn. The ratio of TON (at 24 h) of Sn-MCM-41(42) and Sn-MCM-41-C(178) (TON of Sn-MCM-41-C(42) / TON of Sn-MCM-41-C(178)) is about 0.41 for the epoxidation which is comparable to the values of 0.38 and 0.33 for the hydroxylation of phenol and naphthol, respectively (Tables 4.4 and 4.5). The reasonable similarity in values is interesting and could suggest that the relative activities of the different Sn-sites are similar for the different reactions.

The oxidation of norbornene on Zr-MCM-41 gives exo and endo epoxides which open further during the reaction to give alcohols. Conversions of 26 to 30% are observed in the epoxidation of norbornene over Zr-MCM-41 within 6 h with 62-63% selectivity for the exo epoxide (Table 4.8). The conversion increases slightly with an increase in Zr content in the sample (Table 4.8). The exo/endo epoxide ratio increases slowly with increase in run duration probably due to an interconversion reaction leading to the more stable product.

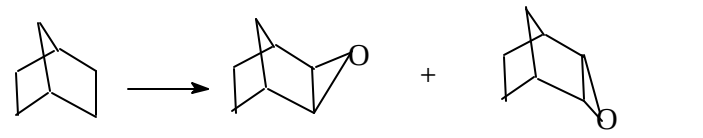

Norbornene Epoxy norbornene (Exo) Epoxy norbornene (Endo)

Table 4.7

Activity of Sn-MCM-41-C samples in epoxidation of Norbornene [a]

Sample	Reaction Time (h)	Norbornene Conv. (mol.%)	TON[b]	Product Distribution			
				Exo 2,3-epoxy norbornene	Endo 2,3-epoxy norbornene	Exo + Endo norborneol	Others
Sn-MCM-41-C(178)	4	10.5	15.1	86.0	4.0	4.7	5.3
	10	28.2	16.2	85.3	3.8	4.5	6.4
	24	29.7	7.1	78.2	3.3	11.6	6.9
Sn-MCM-41-C(133)	10	38.9	16.8	82.8	3.8	5.6	7.8
Sn-MCM-41-C(83)	10	45.6	12.7	80.3	4.2	6.0	9.5
Sn-MCM-41-C(42)	10	47.2	6.7	78.0	6.3	6.8	8.9
Sn-impregnated MCM-41	10	2.0	0.3	71.6	6.9	13.0	8.5

[a]Reaction conditions : Norbornene = 0.5 g; Norbornene/TBHP (mole) = 1.5; Catalyst = 0.1g; Solvent (acetonitrile) = 10 g; Temp. = 80°C.
[b]Turn over number (number of molecules of Norbornene converted per atom of Sn per hour).

Table 4.8

Activity of Zr-MCM-41-C and Zr-MCM-41D samples in epoxidation of Norbornene [a]

Sample	Reaction Time (h)	Norbornene Conv. (mol.%)	TON[b]	Product Distribution			
				Exo 2,3-epoxy norbornene	Endo 2,3-epoxy norbornene	Exo + Endo norborneol	Others
Zr-MCM-41-C(96)	6	18.1		84.6	2.8	8.8	3.8
	10	31.8		78.9	3.2	12.6	5.3
	24	38.4		72.7	3.8	17.5	6.0
Zr-MCM-41-C(55)	10	37.9		80.4	3.9	13.2	2.5
Zr-MCM-41-C(39)	10	46.5		84.7	4.2	9.8	1.3
Zr-MCM-41-C(23)	10	41.7		64.8	9.6	19.8	5.8
Zr-MCM-41-D(102)	6	24.9	13.8	75.5	3.2	11.2	10.1
	10	49.8	16.6	71.7	3.8	14.9	9.6
	24	51.9	7.2	69.0	3.9	17.1	10.0
Zr-MCM-41-D(59)	10	49.5	9.6	58.9	7.5	13.2	14.4
Zr-MCM-41-D(42)	10	56.9	8.0	62.8	7.1	13.6	16.5
Zr-MCM-41-D(33)	10	28.4	3.2	83.5	1.8	7.7	7.0
Zr-impregnated (25)[c]	10	2.0	0.2	50.0	25.0	25.0	-

[a]Reaction conditions: Norbornene = 0.5 g; Norbornene/TBHP (mole) = 1.5; Catalyst = 0.1g; Solvent (acetonitrile) = 10 g; Temp. = 80°C.

[b]Turn over number (number of molecules of Norbornene converted per atom of Zr per hour).

[c]Zr impregnated MCM-41 with Si/Zr = 25.

4.4 REFERENCES

1. Beck, J.S., and Vartuli, J.C., *Current Opinion in Solid State and Materials Science* **1** (1996) 76.
2. Climent, M.J., Corma, A., Iborra, S., Navarro M.C., and Primo, J., *J. Catal*., **161** (1996) 783.
3. Girgis, M.J., and Tsao, Y.P., *Ind. Engg. Chem. Res.*, **35** (1996) 386.
4. Mokaya, R., Jones, W., Moreno, S., and Poncelet, G., *Catal. Lett.*, **49** (1997) 87.
5. Taramasso, M., Perego, G., and Notari, B., *U.S. Patent*, 4, 578, 521 (1983).
6. Ramaswamy, A.V., and Sivasanker, S., *Catal. Lett*., **22** (1993) 239.
7. Notari, B., *Catal. Today*, **18** (1993) 170.
8. Kresge, C.T., Leonowicz, M.E., Roth, W.J., and Vartuli, J.C., *U.S. Patent*, 5, 250, 282 (1993).
9. Corma, A., Navarro, M.T., and Perez-Pariente, J., *J. Chem. Soc., Chem. Commun.*, (1994) 147.
10. Reddy, K.M., Moudrakovski, I.L., and Sayari, A., *J. Chem. Soc., Chem. Commun.*, (1994) 1059.
11. Ciapetta, F.G., and Wallace, D.N., *Catal. Rev.*, **5** (1971) 67.
12. Cusher, N.A., Greenouch, P., Rolfe, J.P.K., and Weiszmann, J.A., in *"Handbook of Petroleum Refining Processes" (R.A. Meyers, Ed.), McGraw-Hill, New York*, ch. 5 (1986).
13. Farneth, W.E., and Gorte, R.J., *Chem. Rev*., **95** (1995) 615.
14. Gianetto, G. E., Perot, G.R., and Guisnet M.R., *Ind. Eng. Chem. Prod. Res. Dev.*, **25** (1986) 481.
15. Leu, L.J., Hou, L.-Y., Kang, B-D, Li, C., Wu, S-T., and Wu, J-C., *Appl. Catal.*, **69** (1991) 49.
16. Guisnet, M., Fouche, V., Belloum, M., Bournonville, J.P., and Travers, C., *Appl. Catal.*, **71** (1991) 283.
17. Chen, J.K., Martin, A.M., Kim, Y.G., and John, V.T., *Ind. Eng. Res.*, **27** (1988) 401.
18. Guisnet, M., Fouche, V., Belloum, M., Bournonville, J.P., and Travers, C., *Appl. Catal.*, **71** (1991) 295.
19. Ravishankar, R., and Sivasanker, S., *Appl. Catal. A: General*, **142** (1996) 47.
20. Weisz, P.B., *Adv. Catal.*, **13** (1962) 137.

21. Jacobs, P.A., Uytterhoeven, J.B., Steijns, M., Foment, G., and Weitkamp, J., *Proc. 5th Int. Conf. On Zeolites, Naples, ed. L.V.C. Rees (Heyden, London* (1980) 607.
22. Guisnet, M., Alvarez, F., Giannetto G., and Perot, G., *Catal. Today,* **1** (1987) 433.
23. Kim, J-Ho, Tanabe, M., and Niwa, M., *Micro. Mater*., **10** (1997) 85.
24. Stull, D.R., Westrum Jr., E.F., and Sinke, G.C., in *"The Chemical Thermodynamics of Organic Compounds"* John Wiley & Sons, Inc., New York (1969).
25. Germain, J.E., in "Catalytic Conversion of Hydrocarbons", Academic Press, London, 1969.
26. Miale, J.N., Chen, N.Y., and Weisz, P.B., *J. Catal.,* **b**, 278 (1966).
27. Pujado, P.R.,in *"Handbook of Petroleum Refining Process"* (R.A. Meyers Ed.) McGraw-Hill.New York (1986).
28. Sebulsky, R.T., and Henke, A.M., *Ind. Eng. Chem. Process Dev*., **10** (1971) 271.
29. Berna, T., Jose, L., Moreno, D., and Alfonso, *EP Appl.*, 0, 353, 813 (1991).
30. He, Ming-Yuan, Zhonghui, L., and Enze, M., *Catal. Today*, **2** (1988) 321.
31. Young, L.B., *US Pat*., 4, 301, 317 (1981).
32. Sivasanker, S., Thangaraj, A., Abdulla R.A., and Ratnasamy, P., *Proc. 10th Int. Cong. Catal., 1992,* Elsevier Science Publishers (1993) 397.
33. Price, P.M., Clark, J.H., Martein K., Macquarrie, D.J., and Bastock, T.W., *R. Soc. Chem.*, **216** (1998) 229.
34. Meima, G.R., van der Aalst, M.J.M., Samson, M.S.U., Garces, J.M., and Lee, J.G., *"Catalysis on Solid Acids and Bases"* (Weitcamp, J., Lücke, B., (Eds.) Proc. DGMK-Conference (1996) 125.
35. Perego, C., Amarilli, S., Caroti, A., Flego C., Pazzuconi, G., Rizzo C., and Bellusi G., *Microporous and Mesoporous Materials*, **27** (1999) 345.
36. Venuto, P.B., Hamilton, L.A., and Landis, P.S., *J. Catal.*, **5** (1960) 21.
37. Patinkin, S.H., and Friendman, B.S., in "Friedel-Crafts and Related Reactions" (G. Olah Ed.) Publishers, New York, **II** Int. (1964) Chap 14, p. 3,.
38. S. Sivasanker, and Thangaraj, A., *J. Catal.*, **138** (1992) 386.
39. Olson, A.C., *Ind. Eng. Chem*., **52** (1960) 833.
40. Alul, H.R., and McEwan, G.J., *J. Org. Chem.*, **32** (1967) 3365.
41. Kent, J.E., and Riegel, S., *Handbook of Industrial Chemical, 8th edn.*, van Nostrand, New York (1983) 402.
42. Venuto, P.B., and Landis, P.S., *Adv. Catal.*, **18** (1968) 259.

43. Landis, P.S., and Venuto, P.B., *J. Catal.,* **6** (1966) 245.

44. Aucejo, A., Burguet, M.C., Corma,A., and Fornés, V., *Appl. Catal.,* **22** (1986) 187.

45. Bell, W.K., and Chang, C.D., *EP* 056, 698 (1985).

46. Sato, H., Ishii, K., Hirose, K., and Nakamura, Y., *Stud. Surf. Sci. Catal.,* **28** (1986) 755.

47. Thangaraj, A., Sivasanker, S., and Ratnasamy, P., *J. Catal.,* **137** (1992) 252.

48. Reddy, J.S., Ravishankar, R., Sivasanker, S., and Ratnasamy, P., *Catal. Lett.,* **17** (1993) 139.

49. Dai, L.-X., Hayasaka, R., Iwaki, Y., Koyano, K.A., and Tatsumi., T., *Chem. Commun.*, (1996) 1071.

50. Yashima, T., Miura, K., and Komatsu, T., *Stud. Surf. Sci. Catal.,* **84** (1994) 1897.

51. Singh, P.S., Bandopadhyay, R., Hegde, S.G., and Rao, B.S., *Appl. Catal. A: General,* **136** (1996) 249.

52. H. Sato, K. Hirose and M. Kitamura and Y. Nakamura, *Stud. Surf. Sci. Catal.,* **49** (1989) 1213.

53. H. Sato, S. Hasabe, H. Sakurai, K. Urabe and Y. Izumi, *Appl. Catal.,* **29** (1987) 107.

54. T. Ushikub and K. Wada, *J. Catal*., **148** (1994) 138.

55. Kresge, C.T.; Leonowicz, M.E.; Roth, W.J.; Vartuli, J.C. *U.S. Patent,* 5,098,684 (1992).

56. Kresge, C.T.; Leonowicz, M.E.; Roth, W.J.; Vartuli, J.C.; Beck, J.S. *Nature,* **359** (1992) 710.

57. Beck, J.S., Vartuli, J.C. Roth, W.J., Leonowicz, M.E., Kresge, C.T., Schmitt, K.D., Chu, C.T.W., Olson, D.H., Sheppard, E.W. McCullen, S.B., Higgins, J.B., and Schlenker, J.L., *J. Am. Chem. Soc.*, **114** (1992) 10835.

58. Busio, M., Jänchen, J., and van Hooff, J.H.C., *Microporous Mater.*, **5** (1995) 211.

59. Corma, A., Fornes, V., Navarro, M.T., and Perez-Pariente, J., *J.Catal.*, **148** (1994) 569.

60. Dai, L.-X, Koyama, K., and Tatsumi, T., *Catal Lett*., **53** (1998) 211.

61. Notari, B., *Catal. Today*, 18 (1993) 163.

62. Clerici, M.G., *Appl. Catal.*, 68 (1991) 249.

63. Camblor, M.A., Corma, A., Perez-Pariente, J., *Zeolites,* 13 (1993) 82.

64. Tuel, A., *Zeolites,* **15** (1995) 228.

65. Tuel, A., *Zeolites*, **15** (1995) 236.

66. Dartt, C.B., Davis, M.E., *Appl. Catal., A: General*, **143** (1996) 53.

67. Franke, O., Rathouski, J., Schulz-Ekloff, G., Starek, J., and Zukal, Z., *Stud. Surf. Sci. Catal.*, **84** (1994) 77.

68. Reddy, K.M., Moudrakovski, I.L., and Sayari, A., *J. Chem. Soc., Chem. Commun.*, (1994) 1059.

69. Luan Z., Xu, J., He, H., Klinowski, J., Kevan, L., *J.Phys. Chem.*, **100** (1996) 19595.

70. Zhang, W., Pinnavaia, T.J., *Catal. Lett.*, **38** (1996) 261.

71. Ulagappan, N., and Rao, C.N.R., *J. Chem. Soc., Chem. Commun.*, (1996) 665.

72. Zhang, W., Wang, J., Pinnavaia, T.J., Tanev, P.T., *J. Chem. Soc., Chem. Commun.*, (1996) 979.

73. Zhao, D., and Goldfarb, D., *J. Chem. Soc., Chem. Commun.* (1995) 875.

74. Sayari, A., *Chem. Mater.*, **8** (1996) 1840.

75. Corma, A., Navarro, M.T., and Perez-Pariente, J., *J. Chem. Soc., Chem. Commun.*, (1994) 147.

76. Corma, A., Navarro, M.T., Perez-Pariente, and Sanchez, F., *Stud. Surf. Sci. Catal.*, **84** (1994) 147.

77. Pinnavaia, T.J., Tanev, P.T., Wang, J., and Zhang, W., *Mater. Res. Soc. Symp. Proc.*, **371** (1995) 53.

78. Tanev, P.T., Chibwe, M., and Pinnavaia, T.J., *Nature*, **368** (1994) 317.

79. Reddy, J.S., and Sayari, A., *Appl. Catal.A. General*, **148** (1996) 7.

80. Rao, P.R.H. Prasad, and Ramasway, A.V., *Appl. Catal. A: General* **93** (1993) 123.

81. Sheldon, R.A., Wallau, M., Arends, I.W.C.E. and Schuchardt, U., *Acc. Chem. Res.*, **31** (1998) 485.

Chapter V

SUMMARY AND CONCLUSIONS

5.1 INTRODUCTION

M41S is a family of mesoporous molecular sieves having well defined mesopores, diameters of which can be tailored to the desired value (18-100Å). MCM-41 is one of the members of the M41S family possessing a hexagonal array of uniform pores. The template molecules used for synthesis of mesoporous molecular sieves are self assembled surfactant molecules around which silicate species are wound building the mesostructure. To impart catalytic activity to the neutral siliceous mesoporous molecular sieves, it is modified by introduction of heteroatoms in the structure. There have been several publications and patents reported on modified MCM-41 molecular sieves such as Al-MCM-41, Ti-MCM-41, V-MCM-41, Mo-MCM-41 etc. The aim of the present investigation is to study the behaviour of Al^{3+}, Sn^{4+} and Zr^{4+} species in the structure of MCM-41 and their catalytic applications.

5.2 SYNTHESIS

MCM-41 molecular sieves were synthesized hydrothermally using three different templates, CTMACl/OH, CTMABr and DTMABr. The kinetics of crystallization of MCM-41 was studied in alkaline medium using the surfactant CTMACl/OH to optimize the synthesis conditions. The various parameters studied were, temperature (RT-150°C), crystallization time (24 h–144 h), water content (H_2O/SiO_2 (mole) = 20-60) and pH (8-12). It is observed that the optimum conditions of temperature, crystallization time and pH for a sample with the molar composition, SiO_2 : 0.086 $(NH_4)_2O$: 0.089 $(CTMA)_2O$: 0.155 $(TMA)_2O$: 40 H_2O; are 110°C, 96 h and 11.5, respectively.

CTMACl/OH is found to be a better surfactant than DTMABr, as it imparts better textural mesoporosity to the material/catalyst. Addition of mesitylene increases the pore diameter (from 27Å to 36-38Å) of the molecular sieve. Samples synthesized in acid and neutral medium possess broader pore size distributions (18-36Å) than those synthesized from alkaline medium (27Å).

Al-MCM-41 samples with different Si/Al ratios (Si/Al input ratios: 100, 50, 25 and 12.5) were synthesized by using CTMABr as a surfactant, while Sn-MCM-41 and Zr-MCM-41 samples with different Si/M ratios (M = Sn or Zr; Si/Sn input ratios: 200, 150, 100, and 50 and Si/Zr input ratios: 100, 50, 25 and 12.5) were synthesized using CTMACl/OH and DTMABr as surfactants.

5.3 CHARACTERIZATION

XRD and N_2-sorption studies show that the characteristics of the synthesized Al-MCM-41 samples are in agreement with the reported ones; the samples possess very high surface areas (> 1000m^2/g) with mesopores of size, ~ 24-25Å. Unit cell increase with Al content suggests the incorporation of Al in the framework. Temperature programmed desorption of pyridine on Al-MCM-41 sample shows that these materials possess Al^{3+} ions in tetrahedral coordination and are moderately acidic. TEM of Al-MCM-41 reveals a regular array of pores in a hexagonal arrangement. TGA/DTA of Al-MCM-41 samples reveal that there is no significant difference in the weight loss of Si-MCM-41 and Al-MCM-41 samples. FTIR of the samples show that the band due to internal asymmetric stretching (1100 cm^{-1}) is shifted significantly to lower wavenumbers (~1064 cm^{-1}) due to the stretching of Si-O bond. Pyridine adsorption on Al-MCM-41 sample suggests that Al-MCM-41 possesses both Brönsted as well as Lewis acid sites.

With increase in temperature of evacuation, Brönsted acidity is lost more rapidly than Lewis acidity. ^{29}Si MAS NMR study of Al-MCM-41 samples reveals the presence of Q_3 and Q_4 species in as-synthesized samples. The intensity of Q_3 sites decreases on calcination of the samples. ^{27}Al MAS NMR study reveals the presence of tetrahedral aluminium in both as-synthesized and calcined samples, while an additional signal for nontetrahedral Al is seen on calcination in the sample with higher Al content.

Sn^{4+} and Zr^{4+} ions can be incorporated in the framework of MCM-41 by hydrothermal synthesis methods using surfactants like CTMACl/OH (M-MCM-41-C) and DTMABr (M-MCM-41-D). XRD patterns of all the M-MCM-41 (M is either Sn or Zr) samples are also similar to that of Si-MCM-41. N_2-sorption studies of the M-MCM-41-C samples reveal that the pore size increases with incorporation of the metal (Sn and Zr), while the pore size distribution is found to be bimodal (mesopores of 22-24Å and 30-35Å in diameter) in the case of M-MCM-41-D samples. TEM pictures of Sn-MCM-41 and Zr-MCM-41 samples show a regular array of pores in a hexagonal arrangement. The total weight loss from M-MCM-41-C is more than that from M-MCM-41-D samples, which may due to the larger template molecules present in the former. FTIR spectra of the samples reveal that the band due to internal asymmetric stretching (1100 cm^{-1}) is shifted significantly to lower wavenumber (1058- 1064 cm^{-1}) due to stretching of the Si-O bond. UV-vis spectra suggest that the Sn^{4+} ions in Sn-MCM-41 samples are present mostly in a tetrahedral environment, though the samples with higher Sn content contain octahedral Sn^{4+} ions also. The Uv-vis spectra of Zr-MCM-41 samples exhibit a band at ~210 nm due to discrete Zr^{4+} ions, which broadens with increasing Zr content in the samples. ^{13}C NMR spectroscopy of Sn-MCM-41 samples indicate the absence of

significant broadening of the ^{13}C signal of the =N-CH_2 and =N-CH_3 groups revealing the absence of a charged framework suggesting the incorporation of Sn as Sn^{4+} ions. The ^{29}Si NMR spectra of M-MCM-41 samples reveal the presence of large amount of Q_3 species [$Si(OSi)_3OH$]; the species are probably mainly present at the surface of the pores. The intensity of Q_3 sites decreases on calcination of the samples.

Mössbauer studies of Sn-MCM-41 samples reveal that the ions undergo reversible redox $Sn^{4+} \leftrightarrow Sn^{2+}$ transformation on treatment with H_2 (at 670K) or air (at 520K). Stabilization of both Sn^{4+} and Sn^{2+} is allowed in the MCM-41 structure and variation of the bonding strength upon the treatment for both Sn^{2+} and Sn^{4+} is reflected in the corresponding dlnA /dT values.

ESR technique reveals that zirconium ions in Zr-MCM-41 samples are reduced by reacting with dry hydrogen, $LiAlH_4$ and γ-ray irradiation. While Zr is mostly in the substitutional locations in Zr-MCM-41 samples with Si/Zr = 96 and 55, it also occupies the surface sites in samples with Si/Zr = 39 and 23. The surface sites are highly reactive towards oxygen and form zirconium(IV)-superoxo species. The redox behaviour of Zr in MCM-41 is probably responsible for its reactivity in liquid phase oxidation of organic molecules with alkyl peroxides.

5.4 CATALYSIS ON MCM-41

The modified MCM-41 molecular sieves were further catalytically evaluated in a number of reactions. Three reactions *viz.*, hydroisomerization of n-hexane, alkylation of benzene with long chain olefins and the Beckmann rearrangement of cyclohexanone oxime to caprolactam were performed on the acid catalyst, Al-MCM-41. The selective

oxidation reactions, namely, the hydroxylation of phenol and 1-naphthol and epoxidation of norbornene were studied on Sn-MCM-41 and Zr-MCM-41 molecular sieves.

n-Hexane hydroisomerization was carried out on Pt-loaded (0.1-0.5 wt.%) H-Al-MCM-41 with different Si/Al ratios (output ratios between 14.3 - 86.3). The influence of different parameters such as time on stream (TOS), temperature, Pt-content, Al-content, contact time and the $H_2/n\text{-}C_6$ ratio were investigated at atmosphere pressure. At the conditions of the investigation, the major reaction was isomerization with negligible amount of cyclization and aromatization. There is a decrease in n-hexane conversion with duration of run (TOS) over all the catalysts, which is due to the deactivation of the catalyst. However, the activity of the catalyst becomes stable after about 45 minutes. The incorporation of Pt increases the activity of H-Al-MCM-41 several fold. The conversion increases rapidly with increasing Pt content upto 0.2wt.% and slowly thereafter. This is a typical behaviour of bifunctional catalysts. The I/C (isomerization/cracking) is maximum at about 0.3 wt.% Pt. The decrease in I/C ratio with further increase in Pt loading is due to enhanced hydrogenolysis activtiy. Conversion increases with increase in Al content. Both cracking and isomerization are enhanced with increase in Al content. However, the I/C ratio is maximum for the sample with an intermediate Si/Al value of 23.3. Though the activites of the catalysts increase with temperature, the increase is moderate beyond 350°C which is mainly due to the near attainment of equilibrium for the isomerization reaction at higher temperatures. As the contact time increases, n-hexane conversion increases, but the I/C ratio decreases, due to increase in cracking. Increasing the $H_2/n\text{-}C_6$ mole ratio from 2 to 9 at a constant feed rate

of n-C_6 decreases the conversion as a result of the rapid hydrogenation of the intermediate olefins and carbocations.

Thus it is concluded that the isomerization of n-hexane takes place with high selctivites over Pt-Al-MCM-41 samples due to the weak to moderate acidity of the material. The conversion follows a first order kinetics. The isomerization selectivity is maximum at around 0.3 wt.% Pt on the catalyst, H-Al-MCM-41(Si/Al output ratio 23.3) at around 325°C. The ratios of monomethyl pentanes (2-MP/3-MP) are close to the equilibrium value of 1.57, due to the rapid equilibrium of the two isomers. However, the MP/DMB ratios are far from the equlibrium value due to the difficulty in the isomerization of methylpentane to dimethyl butanes.

Alkylation of benzene with a commercial olefin mixture (C_{10}-C_{13}) over H-Al-MCM-41 has been performed with two catalysts, H-Al-MCM-41(44) and H-Al-MCM-41(14)) at a pressure of 15 bar with a space velocity (WHSV) = 1 h^{-1}. Two classes of products were formed, LAB (linear alkyl benzene) and HAB (heavy alkyl benzene containing dialkyl benzenes and olefin oligomers). Conversion increases with increase in the temperature from 150°C to 170°C. The yield of HAB goes through a maximum at about 160°C. The amount of HAB formed is relatively more over the less acidic H-Al-MCM-41(44) sample due to larger oligomer content. The formation of dialkylbenzenes is more over the Al rich sample (H-Al-MCM-41(14)). The ratios of 2-phenyl alkane (2-ϕ) to 5-phenyl alkane or 6-phenyl alkane (5-ϕ or 6-ϕ) are higher (> 1) than those observed over HF or ReY suggesting nonattainment of equilibrium which may be due to the weaker acidity of the catalysts. The 2-ϕ/5-ϕ ratio increases with increase in C-number of the

olefin at all temperatures suggesting a greater difficulty in attainment of equilibrium with increase in the C-number.

Liquid phase Beckmann rearrangement of cyclohexanone oxime to ε-caprolactam was carried out on Si-MCM-41 and H-Al-MCM-41 with different Al contents (Si/Al output ratios between 14.3 – 44) in acetonitrile solvent. The conversion of cyclohexanone oxime remained constant with TOS upto 5 h over all the catalysts at all the temperatures studied (300-390°C). In the case of both Si-MCM-41 and H-Al-MCM-41 catalysts, the selectivity for ε-caprolactam increases with TOS and reaches a maximum at about 3h. Transformation of the oxime is rapid and reaches ~ 100% at temperatures above 330°C over all the catalysts. The selectivity for ε-caprolactam increases upto 360°C and decreases at higher temperatures, which might be due to the decomposition of ε-caprolactam on the catalyst surface and increase of the side reactions. At 360°C, the lactam yield over H-Al-MCM-41(14) is 87%. Increasing the contact time (0.2- 1h) increases the conversion, while the selectivity for ε-caprolactam goes through a maximum at an intermediate contact time (0.53h). The selectivity for ε-caprolactam is more over H-Al-MCM-41 than Si-MCM-41. It increases with increase in the Al content. It is concluded that the silanol groups present on Si-MCM-41 are not sufficiently acidic to catalyze the rearrangement. The moderate acidity of Al-MCM-41 samples favours the rearrangement. The optimum conditions (for maximum selectivity of ε-caprolactam) are; temp. = 360°C, TOS = 3h and contact time = 0.53h.

Sn-MCM-41 and Zr-MCM-41 samples prepared using two different surfactants, CTMACl/OH and DTMABr were tested for catalytic activity in oxidation reactions. The

activity of both the samples (M-MCM-41-C and M-MCM-41-D) are similar. Apparantly the method of preparation does not affect the activity of the catalyst.

In the hydroxylation of phenol and 1-naphthol over Sn-MCM-41 samples and of 1-naphthol on Zr-MCM-41 using H_2O_2 as an oxidant, it was observed that conversion increases with the metal content in the sample. The inactivity of Si-MCM-41 in the reactions suggests that the metal ions are responsible for activity. In both hydroxylation reactions, the activity of metal impregnated MCM-41 is much less than those of the M-MCM-41 samples, which may be due to the larger activity of the M^{4+} incorporated in the framework than the impregnated species. However, the TON dereases with increase in the Sn content, which may be due to the presence of more than one type of metal species in the samples, the proportion of the less active metal species increasing with metal content.

The M-MCM-41 (Sn-MCM-41-C, Zr-MCM-41-C and Zr-MCM-41-D) samples are also active in the epoxidation of norbornene with TBHP. Maximum conversion is obtained within 10h with maximum selectivity for the exo epoxide. As in the case of hydroxylation reactions, the TON values decrease with increase in metal content of the sample. The reasonable similarity in values of TON for the two different reactions suggests that the relative activities of the different metal sites are similar for hydroxylation and epoxidation.